



HAL
open science

**Modélisation de la multi-fissuration des matériaux
quasi-fragiles par couplage d'un modèle
d'endommagement anisotrope microplan et d'une
formulation des discontinuités fortes dans la méthode
des éléments finis enrichis**

Svnp Sri Hari Santosh Kakarla

► **To cite this version:**

Svnp Sri Hari Santosh Kakarla. Modélisation de la multi-fissuration des matériaux quasi-fragiles par couplage d'un modèle d'endommagement anisotrope microplan et d'une formulation des discontinuités fortes dans la méthode des éléments finis enrichis. Génie civil. Université Paris-Saclay, 2020. Français. NNT : 2020UPASN013 . tel-03197956

HAL Id: tel-03197956

<https://theses.hal.science/tel-03197956>

Submitted on 14 Apr 2021

HAL is a multi-disciplinary open access archive for the deposit and dissemination of scientific research documents, whether they are published or not. The documents may come from teaching and research institutions in France or abroad, or from public or private research centers.

L'archive ouverte pluridisciplinaire **HAL**, est destinée au dépôt et à la diffusion de documents scientifiques de niveau recherche, publiés ou non, émanant des établissements d'enseignement et de recherche français ou étrangers, des laboratoires publics ou privés.

From anisotropic damage to multiple
cracks by coupling a microplane
model and a strong discontinuity
formulation in the Embedded Finite
Element Method

Thèse de doctorat de l'université Paris-Saclay

École doctorale n°579 Sciences mécaniques et énergétiques, matériaux
et géosciences (SMEMAG)

Spécialité de doctorat: génie civil

Unité de recherche : Université Paris-Saclay, CEA, Service d'études mécaniques et
thermiques, 91191, Gif-sur-Yvette, France.

Référent : ENS Paris-Saclay

Thèse présentée et soutenue à Cachan le 19/06/2020, par

M. Santosh KAKARLA

Composition du Jury

Pr Delphine BRANCHERIE Professeure, UTC Compiègne	Présidente
Pr Jean Baptiste COLLIAT Professeur, Université de Lille	Rapporteur
Pr Panagiotis KOTRONIS Professeur, EC Nantes	Rapporteur
Dr Ludovic JASON Ingénieur chercheur HDR de l'Université Paris Nanterre, CEA	Examineur
Pr Frédéric RAGUENEAU Professeur, ENS Paris-Saclay	Examineur
Dr Cédric GIRY Maître de conférences, ENS Paris-Saclay	Co-encadrant & Examineur
Dr Giuseppe RASTIELLO Ingénieur chercheur, CEA	Co-encadrant & Examineur
Dr Benjamin RICHARD Chef de Laboratoire HDR, IRSN	Directeur de thèse

This page is intentionally empty

Résumé Français

Dans un contexte d'évaluation des structures en béton armé, il est d'usage d'estimer certaines propriétés de l'ouvrage étudié. En particulier, la durabilité à l'échelle du matériau, l'aptitude au service et enfin, la tenue structurale sont des fonctions qui doivent être évaluées. L'ensemble de ces propriétés définit la performance de l'ouvrage considéré. Cette performance doit être maintenue au cours du temps afin de se prémunir du risque de défaillance non maîtrisé. Toutefois, évaluer la performance d'un élément de structure à un instant donné nécessite le recours à des approches numériques permettant la description, voire la prédiction, des principaux mécanismes dissipatifs qui sont susceptibles de se produire au sein d'un élément de structure en béton armé sous chargement. Par ailleurs, il est attendu de cette description que des quantités locales caractérisant la fissuration soient accessibles numériquement. Par exemple, on peut citer la tortuosité, l'espacement ou encore les ouvertures associés à la fissuration.

Il existe plusieurs méthodes numériques efficaces dans la littérature pour modéliser l'enclenchement et la propagation de fissures dans les milieux continus. Cependant, simuler l'enclenchement de multiples fissures, les interactions entre ces fissures et les effets de fermeture pendant un chargement cyclique reste un problème ouvert.

L'objectif principal de ces travaux de thèse est le développement d'un cadre numérique dans lequel les multiples fissures dans le béton peuvent être décrites de manière explicite, pour que des quantités locales caractérisant la fissuration soient obtenues sans recourir à une technique de post-traitement. En particulier, nous proposons, (i) un modèle constitutif qui prend en compte la phase d'endommagement diffus dans le béton, (ii) un modèle numérique pour décrire la formation et la propagation de fissures multiples pendant le chargement cyclique et (iii) un cadre de transition au sein duquel les deux approches sont couplées pour modéliser l'ensemble du processus de localisation des déformations.

Afin de décrire le comportement du béton sous chargements cycliques, nous devons prendre en compte la dégradation de la rigidité, l'effet unilatéral et l'anisotropie induites par la fissuration. Dans la littérature, plusieurs modèles comme les modèles élasto-plastiques [REYNOUARD, 1974, WILLAM and WARNKE, 1975, OTTOSEN and SCORDELIS, 1977], les modèles de fissuration diffuse (*smearred crack*) [NGO and SCORDELIS, 1967, ?], les modèles d'endommagement [MAZARS, 1984, LEMAITRE and MAZARS, 1982], les modèles microplan [BAŽANT and OH, 1985, BAŽANT, 1984], etc. , sont développés pour décrire des fissures dans le béton sur la base d'approches phénoménologiques. Parmi ces formulations, on choisit d'utiliser un modèle microplan. Selon la théorie des microplans, on suppose une relation entre les vecteurs des contraintes sur les microplans et le tenseur des contraintes à un point donné du milieu. Le principe des travaux virtuels est alors utilisé pour calculer le tenseur des contraintes à partir d'une intégration sur une sphère/cercle de quantités définies aux microplans.

Par ailleurs, les modèles à cinématique discontinue permettent de prédire la rupture dans les matériaux quasi-fragiles en incorporant des discontinuités de déformation/déplacement dans le

milieu continu. Dans l'approche par discontinuité forte, une discontinuité est introduite dans le champ de déplacement. Dans la littérature, il existe deux familles de modèles suivant cette approche: (i) EFEM [ORTIZ et al., 1987, OLIVER, 1996a, ALFAIATE et al., 2001, ARMERO and EHRLICH, 2006], Embedded Finite Element Method, où des degrés de liberté supplémentaires sont intégrés dans les éléments finis localisés et des degrés de liberté globaux du modèle d'éléments finis restent inchangés et (ii) XFEM [BELYTSCHKO and BLACK, 1999, DOLBOW and BELYTSCHKO, 1999, MOES et al., 1999, SUKUMAR et al., 2001], eXtended Finite Element Method, où des degrés de liberté supplémentaires sont pris en charge par les nœuds des éléments finis localisés. Ainsi, des degrés de liberté globaux supplémentaires sont ajoutés. Parmi ces modèles, nous avons choisi la méthode EFEM pour modéliser les fissures explicitement en raison de son coût de calcul qui reste maîtrisé.

Plusieurs approches qui réalisent une transition d'une description implicite de la fissuration à une description explicite de la fissuration ont été proposées [MAZARS and PIJAUDIER-CABOT, 1996, JIRÁSEK and ZIMMERMANN, 2001, ?, COMI et al., 2002]. Dans ces travaux, l'approche par équivalence énergétique est retenue pour introduire une fissure cohésive dans la zone de dommages localisés. Selon cette approche, nous introduisons des discontinuités fortes (fissures cohésives) dans les éléments finis lorsqu'un certain critère de transition est atteint [COMI et al., 2007, ROTH et al., 2015, WU et al., 2014]. Les paramètres des lois cohésives (énergie de rupture, niveau de traction au point de transition) sont calibrés à partir de l'équivalence entre la dissipation d'énergie du processus de rupture décrit par un modèle de microplan et celle de la loi cohésive. L'équilibre à travers l'élément fini fissuré est alors assuré en utilisant des conditions de continuité du vecteur des tractions (une condition par fissure). Ceci est nécessaire pour déterminer les degrés de liberté supplémentaires et pour pouvoir appliquer la technique de condensation statique au niveau des éléments finis traversés par une discontinuité.

Dans ce cadre, le cas des fissures multiples peut être traité de manière simple. En effet, le principal avantage de l'utilisation du modèle des microplans est que l'on peut formuler des critères de transition basés sur les variables des microplans, ce qui est prometteur pour la représentation de phénomènes directionnels comme la multi-fissuration, qui ne sont pas naturels à décrire dans le cadre de la méthode EFEM.

Les méthodologies proposées sont illustrées à l'aide de plusieurs cas de tests élémentaires permettant de reproduire des états de contrainte et de déformation complexes. Enfin, nous évaluons la capacité des modèles proposés à simuler la formation et la propagation de fissures dans les structures en béton et en béton armé.

Acknowledgments

The authors declare that they have no known competing financial interests or personal relationships that could have appeared to influence the work reported in this thesis. S. Kakarla and G. Rastello were supported by the SEISM Institute (<http://www.institut-seism.fr>).

This page is intentionally empty

Contents

Résumé Français	i
Acknowledgments	iii
List of Figures	ix
List of Tables	xv
1 Introduction	1
1.1 Context	1
1.2 Motivation	1
1.3 Structure of the manuscript	3
2 State-of-the-art literature review	5
2.1 Mechanical phenomenology of concrete	5
2.2 Thermodynamic framework	8
2.3 Description of cracking in concrete	9
2.3.1 Implicit description of cracking	9
2.3.1.1 Elasto–plastic models	9
2.3.1.2 Damage models	10
2.3.1.3 Smearred crack models	12
2.3.1.4 Microplane models	13
2.3.1.5 Regularization techniques	17
2.3.2 Explicit description of cracking	18
2.3.2.1 Cohesive crack models	18
2.3.2.2 Discontinuous kinematics models	19
2.3.2.3 Embedded finite element method	20
2.3.2.4 Nodal enrichment method	21

2.4	Transition from implicit to explicit descriptions of cracking	24
2.4.1	Experimental motivation	24
2.4.2	Numerical transition methodologies	25
2.4.2.1	Weak energetic equivalence enforcement	25
2.4.2.2	Strong energetic equivalence enforcement	26
2.5	Summary	26
3	Strong discontinuity kinematics and embedded finite element method	29
3.1	Introduction	29
3.2	Kinematics of strong discontinuity	29
3.3	Strong discontinuity approach	30
3.4	Boundary value problem	31
3.5	Embedded finite element method	33
3.5.1	Enhanced assumed strain method	33
3.5.2	Numerical resolution	36
3.5.2.1	Incremental iterative scheme	36
3.5.2.2	Path-following technique	38
3.5.2.3	Staggered solution scheme: operator split method	39
3.5.3	Representative example: uniaxial tension-compression test	40
3.6	Multiple cracks in EFEM	42
3.6.1	Motivation	42
3.6.2	Kinematics and boundary value problem	42
3.6.3	Enhanced assumed strain method – multiple local enhancements	44
3.6.4	Numerical resolution - two embedded cracks	46
3.6.5	Numerical examples: multiple cracks	47
3.6.5.1	Two phase tensile test: orthogonal cracks	47
3.6.5.2	Willam’s test: non-orthogonal cracks	49
3.7	Conclusions	53
4	Microplane microdamage model	57
4.1	Introduction	57
4.2	Framework of microplane models	58
4.2.1	Projection of strain tensor	58
4.2.2	Derivation of stress tensor	59
4.2.2.1	Using principle of virtual work	59
4.2.2.2	Using thermodynamic framework	60
4.3	Microplane microdamage model	60

4.3.1	Thermodynamic framework	61
4.3.2	Secant stiffness	64
4.3.2.1	Microplane elastic constants	64
4.3.2.2	Effect of ν on $\dot{\phi}_V^\alpha$	65
4.3.3	Tangent stiffness	66
4.3.4	Loss of ellipticity of the rate equilibrium problem	67
4.4	Numerical implementation of the microplane microdamage model	68
4.4.1	Integration of microplane quantities	69
4.4.2	Energetic regularization	69
4.5	Numerical case studies	71
4.5.1	Uniaxial tensile loading	71
4.5.1.1	Problem setting	71
4.5.1.2	Global and local responses	72
4.5.1.3	Numerical localization analysis	74
4.5.2	Parametric studies	77
4.5.2.1	Influence of the number of microplanes	77
4.5.2.2	Influence of parameter β	77
4.5.3	Mesh dependency studies	79
4.5.3.1	Problem setting	80
4.5.3.2	Results	80
4.6	Discussion on advantages of the microplane microdamage model	82
4.7	Conclusions	84
5	Microplane microdamage model to strong discontinuity model transition approach	85
5.1	Introduction	85
5.2	Energy equivalence based transition approach	86
5.2.1	General framework	86
5.2.2	Example in 1D setting: bar in tension	87
5.3	Microplane microdamage model to strong discontinuity transition approach	88
5.3.1	Formulation	88
5.3.2	Algorithm for microplane microdamage model to EFEM transition approach	89
5.4	Numerical aspects of microplane microdamage to strong discontinuity formulation transition approach	91
5.4.1	Numerical validation of the transition approach in the case of a single crack	91
5.4.2	Mesh dependency of various transition criteria	92
5.5	Microplane damage to multiple cracks transition	93
5.5.1	Formulation	93

5.5.2	Algorithm	95
5.5.3	Numerical studies involving multiple crack formation	96
5.5.3.1	Orthogonal cracks case	96
5.5.3.2	Non-orthogonal cracks case	97
5.6	Conclusions	102
6	Structural case studies	107
6.1	Double notched specimen under tensile loading	107
6.1.1	Description of the test	107
6.1.2	Numerical simulations	107
6.2	Shear wall tests	116
6.2.1	Description of the test	116
6.2.2	Numerical simulations	116
6.2.2.1	Monotonic loading	117
6.2.2.2	Non–reverse cyclic loading	122
6.3	Conclusions	126
7	Conclusions	127
7.1	Conclusions	127
7.2	Perspectives	128
	Appendix Elastic coefficients of the microplane microdamage model	133
	Appendix Modified traction-separation law	137
	Bibliography	141

List of Figures

1.1	Schematic representation of the strain localization process [HUESPE and OLIVER, 2011]	2
1.2	Shear wall [French research project, Ceos.fr] under cyclic loading	3
2.1	Uniaxial behavior of concrete in tension [TERRIEN, 1980]	6
2.2	Dilatancy of concrete during uniaxial compression loading: evolution of the transversal deformation (a) and evolution of the effective Poisson's ratio (b) [RAMTANI, 1990]	6
2.3	Uniaxial behavior of concrete under compression loading [RAMTANI, 1990]	7
2.4	Unilateral effect in concrete [LA BORDERIE, 1991]	7
2.5	Normalised biaxial strength envelopes for concrete [LEE et al., 2004]	8
2.6	Elasto-plastic model for concrete: plastic strain and elastic unloading [DRAGON and MROZ, 1979]	10
2.7	Smearred crack model: crack plane aligned with the maximum principal stress direction	12
2.8	Fixed crack model: misalignment of crack plane with the maximum principal stress direction	13
2.9	Rotating crack model: rotation of the crack plane along with the maximum principal stress direction	14
2.10	Fixed multi-directional crack model: opening of the second crack plane after certain rotation of the maximum principal stress direction	14
2.11	Framework of the microplane models: spherical microplane models	15
2.12	Cohesive crack approach [de BORST et al., 2004]	19
2.13	Illustration of weak and strong discontinuities	20
2.14	Illustration of embedded finite element method	21
2.15	Enrichment in XFEM: nodes enriched using asymptotic function (red squares) and nodes enriched using Heaviside function (blue circles) [BELYTSCHKO et al., 2009]	22
2.16	Enrichment function: EFEM (right) and XFEM (left) [JIRÁSEK and BELYTSCHKO, 2002]	24
2.17	Experimental investigation of fracture growth (localized damage/crack opening) in a single notched beam: set up (a) and simultaneous behavior of crack openings and AE energy dissipation with loading steps (b) [ALAM and LOUKILI, 2017]	25

3.1	Strong discontinuity kinematics - a body (\mathcal{B}) crossed by discontinuity Γ_d	31
3.2	EFEM - a finite element ($\mathcal{B}_e^h \in \mathcal{E}$) with a discontinuity Γ_d	35
3.3	FE discretization of the specimen ($1\text{ m} \times 1\text{ m}$) and the expected crack orientations under vertical loading–unloading (a) and the considered material parameters (b)	40
3.4	Time evolution of the applied loading - vertical loading–unloading	41
3.5	Global and local responses of the vertical loading–unloading test: force–displacement curve (a) and traction–separation law - opening of horizontal crack (b)	42
3.6	Extension of strong discontinuity kinematics - a body (\mathcal{B}) with multiple intersecting discontinuities Γ_{d_1} and Γ_{d_2}	43
3.7	Extended EFEM - a finite element ($\mathcal{B}_e^h \in \mathcal{E}_1 \cap \mathcal{E}_2$) with multiple intersecting discontinuities Γ_{d_1} and Γ_{d_2}	45
3.8	FE discretization of the specimen ($1\text{ m} \times 1\text{ m}$) and the expected crack orientations - horizontal loading after vertical loading-unloading	48
3.9	Force–displacement curve - horizontal loading: standard EFEM (a), extended EFEM (b)	48
3.10	Different FE discretization of the specimen ($1\text{ m} \times 1\text{ m}$) and the expected crack orientations - two phase vertical and horizontal loading: 18 elements (a), 162 elements (b)	49
3.11	Force–displacement curves for different meshes: vertical loading (a), horizontal loading (b)	49
3.12	FE discretization of the specimen ($1\text{ m} \times 1\text{ m}$) and the expected crack orientations under Willam’s like loading (a) and the considered material parameters (b)	50
3.13	Time evolution of the applied displacement - Willam’s like loading	51
3.14	Time evolution of the components of stress - Willam’s like loading test using extended EFEM	52
3.15	Time evolution of the components of the displacement jump - Willam’s like loading test using extended EFEM	52
3.16	Time evolution of the rotation of the maximum principal stress and strain axes with respect to the vertical direction - Willam’s like loading test using extended EFEM	53
4.1	Representation of unit volume using the disk microplane system	57
4.2	FE discretization of the specimen ($1\text{ m} \times 1\text{ m}$) under vertical loading (a) and the material parameters of microplane microdamage model (b)	71
4.3	Force–displacement curve in vertical direction characterized by the softening response of the microplane microdamage model	73
4.4	Distribution profiles of ϵ_m^α (a) and ϵ_l^α (b) over the microplane system at various stages of uniaxial loading in vertical direction	73
4.5	Distribution profiles of $\tilde{\epsilon}^\alpha$ over the microplane system at various stages of uniaxial loading in vertical direction	74
4.6	Distribution profiles of σ_m^α (a) and σ_l^α (b) over the microplane system at various stages of uniaxial loading in vertical direction	75
4.7	Distribution profiles of ω^α (a) and ϕ_V^α (b) over the microplane system at various stages of uniaxial loading in vertical direction	75

4.8	Numerical localization analysis: distribution profiles of $\det \mathbf{Q}^*$ (a), time evolution of $\det \mathbf{Q}$ and $\det \mathbf{Q}^{\alpha=90^\circ}$ (b)	76
4.9	Influence of N^α : force–displacement curves in vertical direction for $\nu = 0$ (a) and $\nu = 0.2$ (b)	78
4.10	Influence of N^α on the peak of the global curve (a) and ϕ_V (b) of uniaxial tensile test	78
4.11	Influence of β on the global response of uniaxial tensile test: force–displacement curves in vertical direction (a) and corresponding peaks (b)	79
4.12	Influence of β on the evolution of ω^α : before vs. after the peak of the global response (a) and at the end of the vertical tensile loading (b)	79
4.13	Specimen for mesh dependency studies: a concrete bar under tensile loading	80
4.14	Mesh dependency studies: comparisons of force–displacement curves in horizontal direction for different meshes by considering $l_c = w_e$ (a) and $l_c = \sqrt{2A_e}$ (b)	81
4.15	Response of the isotropic damage model during the two phase loading experiment: force–displacement curves in vertical direction (a) and horizontal direction (b)	83
4.16	Response of the microplane microdamage model during the two phase loading experiment: force–displacement curves in vertical direction (a) and horizontal direction (b)	83
4.17	Distribution profiles of ϕ_V^α over the microplane system at various stages of two phase loading experiment	84
5.1	Strain localization in 1D bar: localization band and an equivalent cohesive crack	89
5.2	Equivalence between implicit and explicit description of cracking: area under the stress-strain curve (a) and the cohesive law (b) correspond to the energy dissipated during the strain localization process	89
5.3	Energy equivalence based coupled implicit-explicit description of cracking: the residual energy dissipation (b) and available energy at the crack surface (c)	90
5.4	Transition approach for a single crack: global force–displacement curve in vertical direction (a) and traction–separation law after transition (b) for uniaxial loading test	92
5.5	Distribution profiles of $\hat{\phi}_V^\alpha$ over the microplane system at various stages of uniaxial loading test using transition approach	92
5.6	Mesh objectivity of the transition criterion based on $\max(\bar{\epsilon}^\alpha)$: comparisons of force–displacement curves in horizontal direction (a) and local traction–separation laws (b) for different meshes by considering $l_c = w_e$	94
5.7	Mesh objectivity of the transition criterion based on $\max(\omega^\alpha)$: comparisons of force–displacement curves in horizontal direction (a) and local traction–separation laws (b) for different meshes by considering $l_c = w_e$	94
5.8	Mesh objectivity of the transition criterion based on $\max(\phi_V^\alpha)$: comparisons of force–displacement curves in horizontal direction (a) and local traction–separation laws (b) for different meshes by considering $l_c = w_e$	95
5.9	Time evolution of the components of stress - Willam’s like loading test using transition approach for the threshold at 20% of g_f^π	99
5.10	Distribution profiles of ω^α (a) and $\hat{\phi}_V^\alpha$ (b) over the microplane system at various stages of Willam’s like loading test using transition approach for the threshold at 20% of g_f^π	99

5.11	Time evolution of the components of displacement jump - Willam's like loading test using transition approach for the threshold at 20% g_f^T	100
5.12	Time evolution of the components of stress - Willam's like loading test using transition approach for the threshold at 40% of g_f^T	101
5.13	Time evolution of the components of stress - Willam's like loading test using transition approach for the threshold at 60% of g_f^T	101
5.14	Comparison of distribution profiles of ω^α (a) and $\hat{\phi}_V^\alpha$ (b) over the microplane system at various stages of Willam's like loading test using transition approach for different thresholds of transition criterion	102
6.1	Double notched specimen under tensile loading: geometry and loading conditions	108
6.2	Comparison of the global responses of the double notched specimen with eccentricity of 5 mm using the microplane microdamage model and the transition methodology: coarse unstructured mesh (a), fine structured mesh (b)	109
6.3	Comparison of the load-CMOD curves of the double notched specimen with eccentricity of 5 mm using the microplane microdamage model and the transition methodology: coarse mesh (a), fine mesh (b)	110
6.4	Distribution of $\max_\alpha \omega^\alpha$ for the double notched specimen with eccentricity of 5 mm in the case of coarse mesh before the initiation of crack at A_c	111
6.5	Distribution of $\max_\alpha \omega^\alpha$ for the double notched specimen with eccentricity of 5 mm in the case of fine mesh before the initiation of crack at A_f	112
6.6	Distribution of $flag_{cr}$ for the double notched specimen with eccentricity of 5 mm in the case of coarse mesh at B_c (a) and C_c (b)	112
6.7	Distribution of $flag_{cr}$ for the double notched specimen with eccentricity of 5 mm in the case of fine mesh at B_f (a) and C_f (b)	113
6.8	Distribution of $[[u]]_n$ (a) and $[[u]]_s$ (b) for the double notched specimen with eccentricity of 5 mm in the case of coarse mesh at the end of the numerical test C_c	114
6.9	Distribution of $[[u]]_n$ (a) and $[[u]]_s$ (b) for the double notched specimen with eccentricity of 5 mm in the case of fine mesh at the end of the numerical test C_f	115
6.10	Geometry and reinforcement details of the shear wall specimen [RIVILLON and GABS, 2011]	116
6.11	Finite element mesh of the shear wall, elastic beams and the reinforcement of the specimen (a) and the material parameters considered for the microplane microdamage model and the EFEM in the transition framework for the shear wall (b)	117
6.12	Comparison of the global responses of the shear wall specimen under monotonic loading using the microplane microdamage model and the transition methodology	118
6.13	Distribution of $\max_\alpha \omega^\alpha$ for the shear wall specimen under monotonic loading before the initiation of crack at A	119
6.14	Distribution of $\max_\alpha \omega^\alpha$ (a) and $flag_{cr}$ (b) for the shear wall specimen under monotonic loading after the initiation of crack at B	119
6.15	Distribution of $\max_\alpha \omega^\alpha$ (a) and $flag_{cr}$ (b) for the shear wall specimen under monotonic loading after the initiation of crack at C	120
6.16	Distribution of $\max_\alpha \omega^\alpha$ (a) and $flag_{cr}$ (b) for the shear wall specimen under monotonic loading at the end of the numerical test D	120

6.17	Distribution of $\llbracket u \rrbracket_n$ (a) and $\llbracket u \rrbracket_s$ (b) for the shear wall specimen under monotonic loading at the end of the numerical test D	121
6.18	Time evolution of the applied displacement – shear wall specimen under non–reverse cyclic loading	122
6.19	Comparison of the global responses of the shear wall specimen under non–reverse cyclic loading using the microplane microdamage model and the transition methodology	123
6.20	Distribution of $flag_{cr}$ for the shear wall specimen under alternate loading at start of the cycle A (a) and end of the cycle B (b)	123
6.21	Distribution of $\llbracket u \rrbracket_n$ for the shear wall specimen under alternate loading at the start of cycle A (a), end of unloading (b) and the end of cycle B (c)	124
6.22	Distribution of $\llbracket u \rrbracket_s$ for the shear wall specimen under alternate loading at the start of cycle A (a), end of unloading (b) and the end of cycle B (c)	125
7.1	Virtual testing: cubic specimen under biaxial loading	129
B1	Time evolution of the components of stress - Willam’s like loading test using transition approach for the threshold at 20% (a), 40% (b) and 60% (c) of g_f^T using modified traction–separation law	139

This page is intentionally empty

List of Tables

2.1	Comparison between various aspects of XFEM and EFEM [JIRÁSEK and BELYTSCJKO, 2002]	23
2.2	Various examples of transition framework	27
4.1	Different meshes adopted for the mesh dependency study	81
5.1	Transition quantities considered for mesh dependency studies and the corresponding threshold values	93
5.2	The material parameters considered for the microplane microdamage and strong discontinuity models in the transition framework – Willam’s like loading	98
6.1	The material parameters considered for the microplane microdamage model and the EFEM in the transition framework for the double notch specimen	109

This page is intentionally empty

List of Symbols

In this section we describe several symbols that are used within the body of the document. Here, variables related to vectors, second-order tensors, matrices, column vectors are denoted by a bold symbol. Rest of the variables can be found below.

Acronyms

AE	Acoustic Emissions
BVP	Boundary Value Problem
CMOD	Crack Mouth Opening Displacement
CNDI	Controlled Nodal Displacement Increment
COD	Crack Opening Displacement
CST	Constant Strain Triangle
DIC	Digital Image Correlation
DOF	Degree of Freedom
EFEM	Embedded Finite Element Method
FPZ	Fracture Process Zone
KOS	Kinematically Optimal Symmetric
LEFM	Linear Elastic Fracture Mechanics
NPP	Nuclear Power Plant
PVW	Principle of Virtual Work
SKON	Statically and Kinematically Optimal Nonsymmetric
SOS	Statically Optimal Symmetric
XFEM	eXtended Finite Element Method

Domain notations

$(\mathcal{B}_e^h)^+, (\mathcal{B}_e^h)^-$	Sub-domains of a finite element crossed by a discontinuity
\mathcal{B}	Domain of the material

$\mathcal{B}^+, \mathcal{B}^-$	Sub-domains of the body crossed by a discontinuity
\mathcal{B}_e^h	Finite element of the discretized body
Γ_d	Discontinuity surface
Γ_{d_k}	Band of discontinuity
$\Gamma_{d_{i=1,2}}$	Discontinuity surfaces of the first and the second crack
\mathcal{V}	Domain of nonlocal continuum
\mathcal{E}^h	Set of finite elements crossed by the discontinuity
$\mathcal{E}_{i=1,2}^h$	Set of finite elements crossed by the first and the second discontinuity
Ω	Domain of microplane system
Ω^α	A microplane in the disk microplane system
$\partial_t \mathcal{B}$	Boundary on which the traction is applied
$\partial_u \mathcal{B}$	Boundary on which the displacement is applied
$\mathbb{R}^{n_{dim} \times n_{dim}}$	Range of a tensor in the domain
$\mathbb{R}^{n_{dim}}$	Range of a vector in the domain
n_{dim}	Dimension of the continuum
n_{elem}	Number of finite elements in a discretized body
Vectors and matrices	
\mathbf{B}	Gradient matrix
\mathbf{d}	Discretized displacement vector
\mathbf{d}^*	Discretized virtual displacement vector
\mathbf{e}	Discretized enhanced displacement vector
\mathbf{e}^*	Discretized virtual enhanced displacement vector
$\mathbf{e}_{i=1,2}^*$	Discretized virtual enhanced displacement vectors associated with first and second crack
\mathbf{G}	Enhanced shape functions matrix
\mathbf{G}^*	Virtual enhanced shape functions matrix
$\mathbf{G}_{i=1,2}^*$	Virtual enhanced shape functions matrices associated with first and second crack
$\mathbf{G}_{i=1,2}$	Enhanced shape functions matrices associated with first and second crack
$\hat{\mathbf{d}}$	Direction of the indirectly controlled contribution to the imposed displacement
\mathbf{H}_{Γ_d}	Matrix formed using the Heaviside function
\mathbf{N}_a	Elementary shape functions matrix
\mathbf{N}_c	Shape functions matrix for the enhanced displacement field
$\mathbf{N}_{c_{i=1,2}}$	Shape functions matrix for the enhanced displacement fields associated with the first and second crack

\mathbf{P}	Projection matrix at the discontinuity
$\mathbf{P}_{i=1,2}$	Projection matrices at the first and the second discontinuity
\mathbf{a}^\top	Coefficients of the linear combination of the controlled degrees of Freedom
\mathbf{F}_{ext}	Column vector of external forces
\mathbf{F}_{int}	Column vector of internal forces
\mathbf{f}_{int}	Column vector of internal forces associated with the traction continuity condition
$\tilde{\mathbf{K}}$	Global stiffness matrix after static condensation
$\tilde{\mathbf{F}}_{int}$	Internal force vector after static condensation
Space notations	
\mathcal{L}^2	Set of square-integrable functions
\mathbf{E}	Admissible space of the enhanced strain field
$\mathbf{E}^{\perp S}$	Admissible space of enhanced strain field orthogonal to the stress field
\mathbf{S}	Admissible space of the stress field
\mathbf{U}	Admissible space of the displacement field
\mathbf{U}_0	Admissible space of the applied displacement field
Ω^1	Set of microplanes in loading
Ω^2	Set of microplanes in unloading
H^1	First-order Sobolev spaces
H_0^1	Homogeneous first-order Sobolev spaces
$R(\mathbf{x}_{i=1,2})$	Orthonormal basis
Functions and operators	
$(\bullet)_d$	Deviatoric part of (\bullet)
\mathbf{A}	Assembly operator
\cdot	Contraction operator
$:$	Double contraction operator
δ_{ij}	Kronecker delta
$\det(\bullet)$	Determinant of the second-order tensor (\bullet)
δ_{Γ_d}	Dirac delta function
∇^s	Symmetric part of the gradient
H_{Γ_d}	Heaviside function
$\langle\langle\bullet\rangle\rangle^+$	Positive part of (\bullet)
\mathbf{L}^α	Tangential projection operator of a microplane

\mathbf{M}^α	Normal projection operator of a microplane
\mathbb{P}^+	Positive projection operator
\mathbb{P}^-	Negative projection operator
$\delta_{\Gamma_{d_k}}$	Regularized Dirac delta function
\mathcal{F}	Constitutive relationship between stress and strain
div	Divergence operator
meas(\bullet)	Measure of (\bullet)
tr(\bullet)	Trace of (\bullet)
max(\bullet)	Maximum value of (\bullet)
$\mu_{\Gamma_{d_k}}$	Collocation function centered on a crack surface
$H_{\llbracket u \rrbracket_{n_{i=1,2}}}$	Heaviside functions associated with the first and second crack
g	Microdamage evolution function
h	Discrete constitutive law
$h_{i=1,2}$	Discrete constitutive laws for the first and second crack
P	Path-following constraint
q	Softening function of the microplane microdamage model
W^{nl}	Normalized nonlocal weight function
W_0^{nl}	Gaussian function
Scalar variables	
$(\sigma_I)_{tr}$	Maximum principal stress at transition
α	Angle of the normal to a microplane in the disk microplane system
α_c	Weights associated to the damage variables under compression condition
α_t	Weights associated to the damage variables under tensile condition
α_{crit}	Angle of a critical microplane
β	Parameter of the microplane microdamage model
β_{cr}	Model parameter of the traction–separation law
$\llbracket u \rrbracket_n$	Normal component of the displacement jump at a crack surface
$\llbracket u \rrbracket_s$	Tangential component of the displacement jump at a crack surface
ω^α	Microdamage variable
$\tilde{\epsilon}^\alpha$	Equivalent strain on a microplane
$\tilde{\epsilon}_{tr}^\alpha$	Equivalent strain on a microplane at transition pseudo-time
ϵ^e	Elastic part of the strain
ϵ^p	Plastic part of the strain

ϵ_d	Deviatoric component of strain on a microplane in the spherical microplane system
$\epsilon_l^{\alpha*}$	Virtual tangential component of strain on a microplane in the disk microplane system
ϵ_m	Normal component of strain on a microplane in the spherical microplane system
$\epsilon_m^{\alpha*}$	Virtual normal component of strain on a microplane in the disk microplane system
ϵ_v	Volumetric component of strain on a microplane in the spherical microplane system
ϵ_l^α	Tangential component of strain on a microplane in the disk microplane system
ϵ_m^α	Normal component of strain on a microplane in the disk microplane system
γ_ϵ^{asy}	Asymptotic value of the rotation of the maximum principal strain axis with respect to the vertical direction
γ_σ^{asy}	Asymptotic value of the rotation of the maximum principal stress axis with respect to the vertical direction
γ_ϵ	Rotation of the maximum principal strain axis with respect to the vertical direction
γ_σ	Rotation of the maximum principal stress axis with respect to the vertical direction
$\hat{\phi}_S$	Available energy for the crack
$\hat{\phi}_V$	Dissipated volumetric energy
$\hat{\phi}_V^\alpha$	Dissipated volumetric energy on a microplane
$\hat{\phi}_{S_{i=1,2}}$	Available energy for first and second crack
κ	Internal variable in a general thermodynamic framework
κ^α	History variable on a microplane
κ_{cr}	History variable associated to the traction–separation law
λ	Lame’s constant
$(\epsilon_l^{\alpha+})$	Positive tangential strain component on a microplane
$(\epsilon_m^{\alpha+})$	Positive normal strain component on a microplane
$(\phi_V^\alpha)_{tr}$	Volumetric energy dissipation on a microplane at transition pseudo-time
$\llbracket u \rrbracket_{n_{i=1,2}}$	Normal components of the displacement jump at the first and the second crack surface
$\llbracket u \rrbracket_{s_{i=1,2}}$	Tangential components of the displacement jump at the first and the second crack surface
\mathcal{E}	Total mechanical energy
μ	Lame’s constant

ν	Poisson's ratio
ω^α	Microdamage variable on a microplane
ω_{tr}^α	Microdamage variable on a microplane at transition pseudo-time
Φ	Energy dissipation of the whole material domain
ϕ_S	Energy dissipation at the crack
ϕ_V	Energy dissipation of a unit volume
ϕ_V^α	Volumetric energy dissipation on a microplane
Φ_{exp}	Energy dissipation of a model based on explicit description of cracking
$\Phi_{imp/exp}$	Energy dissipation of a model based on coupled implicit and explicit description of cracking
Φ_{imp}	Energy dissipation of a model based on implicit description of cracking
Ψ	Free energy of the whole material domain
ψ	Free energy of a unit volume
ψ_0^α	Elastic part of free energy on a microplane
ψ_S	Helmholtz free energy at a crack surface
ρ	Density of the material
σ_l^α	Tangential component of strain on a microplane in the disk microplane system
σ_m^α	Normal component of stress on a microplane in the disk microplane system
σ_d	Deviatoric component of stress on a microplane in the spherical microplane system
σ_I	Maximum principal stress
σ_m	Normal component of stress on a microplane in the spherical microplane system
σ_v	Volumetric component of stress on a microplane in the spherical microplane system
σ_{tr}	Stress in 1D at transition
τ	Path-step length parameter
d_a	Nodal displacement in 1D
e	Elemental displacement jump in 1D
u	Displacement in 1D
u_0	Applied displacement in 1D
x	Position of a point in 1D
θ_{th}	Threshold angle of the fixed multi-directional smeared crack model
$\tilde{\epsilon}_0^\pi$	Threshold equivalent strain on a microplane
ζ	Loading factor

A_e	Area of a finite element
B	Regularized parameter of microplane microdamage model
C_{pqrs}^t	Component of tangential stiffness tensor
C_d	Deviatoric constitutive law on a microplane in the spherical microplane system
C_l	Tangential constitutive law on a microplane in the spherical microplane system
C_m	Normal constitutive law on a microplane in the spherical microplane system
C_v	Volumetric constitutive law on a microplane in the spherical microplane system
d	Damage variable
d_c	Damage variable under compression condition
d_t	Damage variable under tensile condition
d_{cr}	Damage-like internal variable of the traction–separation law
E	Young’s modulus
E_l	Elastic stiffness component in tangential direction of a microplane
E_l^s	Secant stiffness component in tangential direction of a microplane
E_m	Elastic stiffness component in normal direction of a microplane
E_m^s	Secant stiffness component in normal direction of a microplane
f_t	Uniaxial tensile strength of the material
f_{cr}	Yield surface of the traction–separation law
$F_{i=1,2}$	Component of force in orthonormal basis
$flag$	Boolean variable to store information of crack activation
$flag_{i=1,2}$	Boolean variables to store information of activation of first and second crack
G_f	Fracture energy of the material
g_f	Energy dissipation density of a unit volume
g_f^π	Energy dissipation density of a microplane
h_e	Height of a finite element
K	Kinetic energy
l_c	Characterisitic length
l_c^{nl}	Nonlocal internal length
l_{FPZ}	Length of fracture process zone
N	Number of pseudo-time steps
N^α	Number of microplanes of a numerical integration scheme
t	Pseudo-time instant
t_n	Normal component of traction at the crack surface

t_s	Tangential component of traction at the crack surface
t_Ω	Pseudo-time corresponding to activation of microdamage
t_{tr}	Pseudo-time step at transition
$u_{i=1,2}$	Component of displacement in orthonormal basis
W^α	Weight corresponding to numerical integration on a microplane
w_e	Width of a finite element
Y	Conjugate variable associated with the internal variable
Y^α	Conjugate variable associated with the internal variable on a microplane

Tensor variables

ϵ_l	Tangential strain on a microplane in the spherical microplane system
σ_l	Tangential stress on a microplane in the spherical microplane system
\mathbb{C}^s	Secant stiffness tensor
\mathbb{C}^t	Tangential stiffness tensor
$\mathbb{C}^{\alpha,s}$	Secant stiffness tensor on a microplane
$\mathbb{C}^{\alpha,t}$	Tangent stiffness tensor on a microplane
$\Delta\mathbb{E}^+$	Reduction of the elastic stiffness tensor due to tension condition
$\Delta\mathbb{E}^-$	Reduction of the elastic stiffness tensor due to compression condition
\mathbb{E}	Hooke's elastic stiffness tensor
\mathbb{E}^α	Elastic stiffness tensor on a microplane
ϵ	Strain tensor
ϵ^*	Virtual strain field
ϵ^+	Positive strain tensor
ϵ^-	Negative strain tensor
\mathbb{I}	Fourth-order identity tensor
\mathbf{I}	Second-order identity tensor
\mathbf{D}	Second-order damage tensor
\mathbf{K}	Stiffness tensor of the traction–separation law
\mathbf{Q}	Acoustic tensor
\mathbf{Q}^α	Localization tensor on each microplane
$\nabla^s \bar{\mathbf{u}}$	Continuous part of the strain field
σ	Stress tensor
σ^α	Stress tensor on a microplane
σ^{eff}	Effective stress tensor

$\tilde{\mathbb{E}}$	Modified elastic tensor due to damage
$\tilde{\sigma}$	Actual stress field
$\tilde{\sigma}^*$	Virtual stress field
Vector variables	
$\bar{\mathbf{u}}$	Continuous part of the displacement field
θ^α	Vector of internal variables on a microplane
ξ	Source point in a nonlocal model
\mathbf{u}	Displacement field
\mathbf{u}^*	Virtual displacement field
\mathbf{u}_0	Applied displacement
$\llbracket \mathbf{u} \rrbracket$	Displacement jump field
\mathbf{l}^α	Tangent to a microplane in the disk microplane system
\mathbf{m}^α	Normal to a microplane in the disk microplane system
\mathbf{n}	Normal to a crack surface
\mathbf{n}^{cr}	Normal to a crack plane
$\mathbf{n}_{i=1,2}^{cr}$	Normal to the first and second crack plane
\mathbf{n}_{crit}	Critical plane of localization
$\mathbf{n}_{i=1,2}$	Normal to the first and the second crack
\mathbf{x}	Position of a point in the domain of the material
\mathbf{s}	Tangent to a crack surface
\mathbf{s}^{cr}	Tangent to a crack plane
$\mathbf{s}_{i=1,2}^{cr}$	Tangent to the first and second crack plane
$\mathbf{s}_{i=1,2}$	Tangent to the first and the second crack
$\mathbf{d}_{ext,0}$	Imposed contribution to the external displacement vector
$\mathbf{F}_{ext,0}$	Imposed contribution to the external force vector
$\mathbf{l}_{i=1,2}$	Tangent direction to a microplane in the spherical microplane system
\mathbf{m}	Normal to a microplane in the spherical microplane system
\mathbf{p}	Normal of the boundary
\mathbf{r}	Eigenvector of acoustic tensor
\mathbf{t}	Traction at the discontinuity
\mathbf{t}^{cr}	Traction vector on a crack plane
$\mathbf{t}_{i=1,2}^{cr}$	Traction vectors on the first and second crack plane
\mathbf{t}_0	Applied traction

This page is intentionally empty

Introduction

1.1 Context

Owing to the drastic increase in the computing power in recent decades, there is a surge in the flux of new developments in computational mechanics from research to the industry. Particularly, the development of numerical methods for the simulation of material failure is highly motivated by the necessity of the assessment of the performance of the structures. Especially in the case of crucial civil engineering structures like Nuclear Power Plants (NPP), periodic safety reviews are conducted to address the issues related to the durability and serviceability before they adversely affect the structural safety. Also, it is essential to avert any catastrophes in the case of extreme loading like earthquakes.

Massive concrete and reinforced concrete structural elements are used in the construction of different components of NPP that provides containment functionality like the fluid storage buildings [GRANGER et al., 2001a, GRANGER et al., 2001b, JASON and MASSON, 2014]. In these cases, the quantification of crack features like Crack Mouth Opening Displacement (CMOD), crack spacing and tortuosity plays a key role in estimating the leakage rates [AKHAVAN et al., 2012, RASTIELLO et al., 2014, RASTIELLO et al., 2018]. Also, predicting the information about cracking is important in devising the safety measures for large scale structures like concrete dams, bridges, multi-storey residential buildings, masonry structures, etc.

1.2 Motivation

Fracture process in quasi-brittle materials is a complex physical phenomenon with cracking process occurring in different zones fig. 1.1. It starts with the initiation of microcracks in the zone of distributed damage. This is followed by the formation of regions of highly localized microcracking, termed as 'localization band'. This phenomenon is known as 'strain localization'. In the localization band irreversible energy dissipation takes place while the material in the surrounding releases elastic energy. Finally, the microcracks coalesce to form the zone of stress free macrocracks. The zone of distributed damage and the localized strains is known as the Fracture Process Zone (FPZ) whose length is denoted by l_{FPZ} .

There are several efficient numerical methods that are dedicated for modeling crack initiation and propagation in solids. But simulation of the formation of multiple crack patterns, crack interactions and crack closure effects during cyclic loading is still a challenging issue. For example, in a shear wall under cyclic loading (fig. 1.2), the cracks formed during first phase of loading are crossed by the cracks formed during the second phase. Simulation of such complex multiple crack patterns is still an ongoing research work.

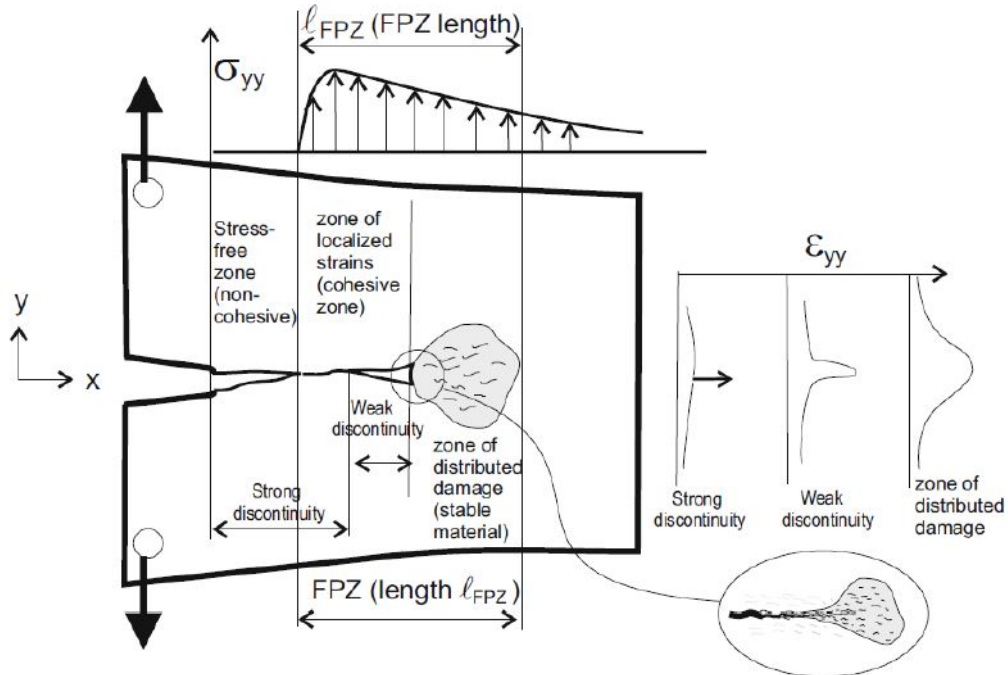


Figure 1.1: Schematic representation of the strain localization process [HUESPE and OLIVER, 2011]

The purpose of this work is to model the complex phenomenon of formation of multiple cracks in concrete and reinforced concrete structures submitted to complex loading.

Although it is customary to model concrete as an isotropic material prior to cracking, it is essential to tackle induced anisotropy due to cracking. In the literature, several models like elasto–plastic models [REYNOUARD, 1974, WILLAM and WARNKE, 1975, OTTOSEN and SCORDELIS, 1977], smeared crack models [NGO and SCORDELIS, 1967, BAŽANT and GAMBAROVA, 1980], damage models [MAZARS, 1984, LEMAITRE and MAZARS, 1982], microplane models [BAŽANT and OH, 1985, BAŽANT, 1984], etc., are developed for modeling cracking in concrete based on the phenomenological approach. Among these models, microplane models are able to describe the anisotropic damage in concrete by describing damage in several possible directions. Nevertheless, these models cannot provide the explicit information about cracking without extra computational effort. This motivates to explore further models that are dedicated for explicit modeling of cracks.

In the literature, several models like cohesive crack models, discontinuous kinematics models etc., are developed to model the cracks in an explicit manner. In the framework of discontinuous kinematics models, various numerical methods like Embedded Finite Element Method (EFEM) [ORTIZ et al., 1987, OLIVER, 1996a], eXtended Finite Element Method (XFEM) [BELYTSCHKO and BLACK, 1999, MOES et al., 1999], etc., are also developed. Among these numerical methods, EFEM has several computational advantages over the other methods.

On the other hand, transition methodologies are proposed in the literature [COMI et al., 2007, CAZES et al., 2009] to couple both the implicit and explicit description of cracking. In this manner, the complete strain localization process is captured in a single framework.

The purpose of this work is to model the anisotropic damage and multiple cracks in an explicit manner by coupling microplane model and EFEM in a transition framework. The main idea here is to take benefit of anisotropic damage description provided by microplane models in order to

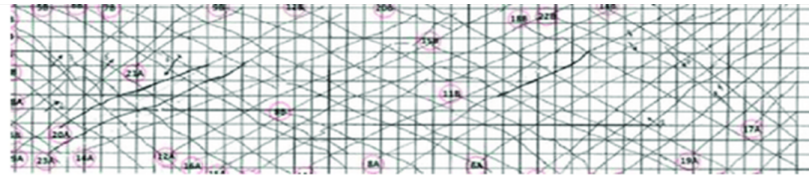


Figure 1.2: Shear wall [French research project, Ceos.fr] under cyclic loading

activate multiple cracks in a unit volume. Then an extended EFEM is used in order to tackle the activation and opening of multiple non-orthogonal cracks within a finite element.

1.3 Structure of the manuscript

The manuscript is structured as follows:

- (i) in the second chapter we perform the state-of-the-art literature review concerning the modeling of cracking in concrete. First, experimental observations of the behavior of concrete under different loading conditions are reviewed and the phenomenological features of modeling interest are described. Then, we present the thermodynamic framework for developing constitutive laws. Later, the formulations for modeling of cracking in quasi-brittle materials in implicit and explicit manner is presented. The pros and cons of several constitutive models and numerical formulations are discussed and the justifications for the appropriate choices are provided. This is followed by the experimental motivation for the transition models. Finally, the available numerical frameworks for the transition methodologies are presented;
- (ii) in the third chapter, we present the strong discontinuity formulation. First, different approaches for incorporating the strong discontinuity in the standard continuum are discussed. Later, EFEM to model a single strong discontinuity is presented in detail. We illustrate the proposed formulation using some numerical examples in the case of a single crack. After illustrating the cases in which the localization of multiple cracks is necessary, we extend the formulation of standard EFEM. Some numerical studies to study the interactions between multiple cracks are performed.
- (iii) in the fourth chapter, we present the microplane model. After discussing the underlying assumptions, the microplane formulation in a thermodynamic framework is presented. We study several aspects of the constitutive model. This is followed by some simple numerical tests to illustrate the main features of proposed formulations. We end this chapter by comparing the responses of a damage model, extended EFEM and microplane model to highlight the main features of the proposed model;

- (iv) in the fifth chapter, we present the general framework of transition models available in the literature and then propose a transition methodology from microplane model to a strong discontinuity model formulated in the EFEM. First, the formation of a single crack is considered and numerical aspects of the proposed methodologies are discussed. Later, the case of multiple orthogonal/non-orthogonal cracks is considered and both theoretical and numerical aspects are presented;
- (v) some structural test cases to show the applicability of the proposed transition methodology are performed in the last chapter. We simulate these examples using both the microplane model and the transition methodology. The obtained global, local responses and crack patterns are shown;
- (vi) finally, some conclusions of proposed methodologies are drawn and perspectives for the future work close the manuscript.

State-of-the-art literature review

Abstract. The main features of the mechanical behavior of quasi-brittle (e.g., concrete) materials are briefly illustrated in the first part of the chapter. Then, attention is focused on strategies and numerical formulations for modeling concrete and concrete-like materials. Representative continuum mechanics based (continuum displacement field, dissipation distributed over a volume of finite size) and strong discontinuity formulations (discontinuous displacement field, dissipation localized at a discontinuity surface) are discussed. Finally, some formulations allowing to explicitly model a progressive transition from one modeling approach to the other one are illustrated.

2.1 Mechanical phenomenology of concrete

Failure mechanisms observed under various types of loading suggests that plain concrete is a quasi-brittle material even though the composites of concrete behave like linear elastic perfectly brittle materials. Brittle materials exhibit a sudden and immediate loss of strength after the peak stress is reached but in quasi-brittle materials (as the nomenclature suggests) the strength of the material is reduced gradually and exhibits post-peak behavior before complete failure. In concrete, microcracking is the driving phenomenon for progressive loss of material strength. The complexity of the concrete behavior arises due to the fact that different physical mechanisms (depending on the interaction of microcracks with each other) dictates the macroscopic behavior for different types of loading. In the case of reinforced concrete, presence of steel limits the crack openings. Hence, the overall response of the composite material is ductile. However, at higher loading, steel bars yield and plastic hinges are formed in the structural members. Here, we summarize the main aspects of the response of concrete to various monotonic and cyclic loading conditions.

Uniaxial tension test During uniaxial tensile loading, the microcracks that initiate at the weaker zones coalesce without being intervened by the aggregate thus forming macrocracks perpendicular to the direction of the loading. Concrete undergoes through different stages [LEGENDRE, 1984] during loading from virgin intact material to the material failure. These physical mechanisms manifest the behavior of the concrete into two different regimes: (i) linear elastic regime up to the tensile strength; (ii) a softening response in the phase post-peak of load. In the later phase, if unloading-reloading cycles are performed (cyclic tensile loading) [TERRIEN, 1980, REINHARDT and CORNELISSEN, 1984, CORNELISSEN et al., 1986, NOUAILLETAS et al., 2015] then hysteresis loops with permanent strains are observed (fig. 2.1).

Uniaxial compression test During uniaxial compression loading, the formation of microcracks happens in the direction parallel to the loading due to lateral expansion (Poisson's effect). The

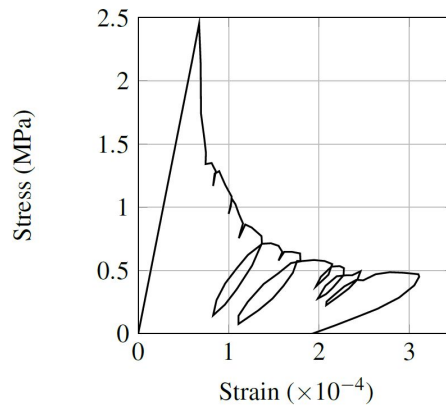


Figure 2.1: Uniaxial behavior of concrete in tension [TERRIEN, 1980]

traversing path of the microcracks is intervened by aggregate thus preventing the formation of macrocrack abruptly. Due to this mechanism, concrete becomes more ductile and exhibits a compressive strength much higher than the tensile strength. The compression behavior can be schematically divided into three regimes: (i) linear elastic regime with decreasing volume up to 30% of the compressive strength; (ii) non-linear irreversible regime with decreasing volume up to the compressive strength; (iii) softening regime with increasing volume (dilatancy) in the phase post-peak of load.

During the dilatancy phase, the Poisson's ratio increases abruptly. This can be explained on the basis of formation of macrocracks in the directions orthogonal to the external loading direction. As the material strength is lost in these directions, the lateral expansion (transversal strain in fig. 2.2a) is more dramatic than the longitudinal expansion (axial strain in fig. 2.2a) causing the increase in the Poisson's ratio (fig. 2.2b).

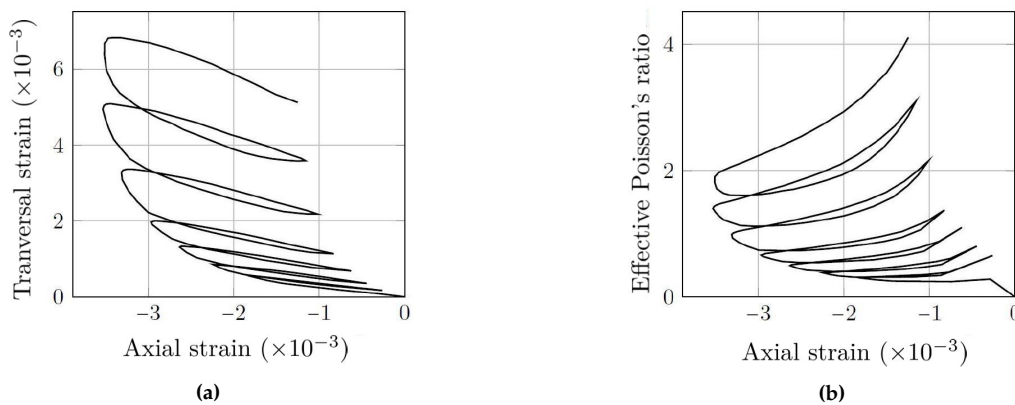


Figure 2.2: Dilatancy of concrete during uniaxial compression loading: evolution of the transversal deformation (a) and evolution of the effective Poisson's ratio (b) [RAMTANI, 1990]

Similar to tension, the uniaxial cyclic compressive behavior exhibits hysteresis loops with permanent strains [RAMTANI, 1990, SINHA et al., 1964, VASSAUX et al., 2014]. However, the contact between the microcrack surfaces increases as they are in crushing mode in compression (opposed to the opening mode in tension). Due to this, the internal friction between the macrocrack surfaces is more pronounced in compression causing larger hysteresis loops (fig. 2.3).

In addition to this, when material is subjected to compression after tensile damage, material stiffness is fully recovered due to the closure of microcracks (fig. 2.4). This is known as unilat-

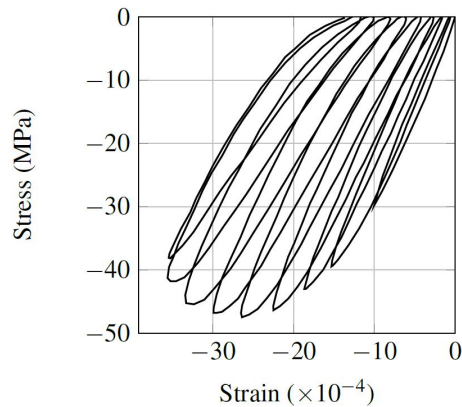


Figure 2.3: Uniaxial behavior of concrete under compression loading [RAMTANI, 1990]

eral effect [MAZARS et al., 1990, NOUAILLETAS et al., 2015, REINHARDT and CORNELISSEN, 1984, LA BORDERIE, 1991].

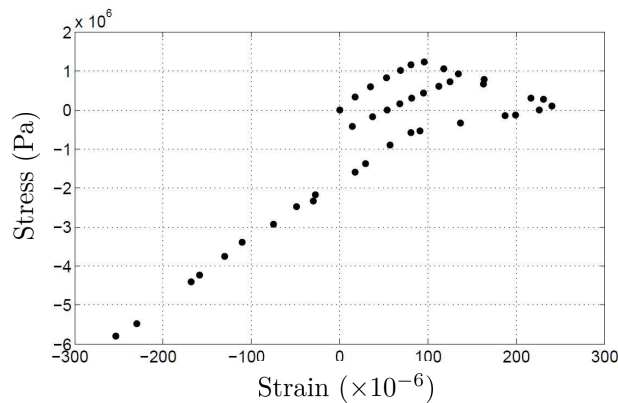


Figure 2.4: Unilateral effect in concrete [LA BORDERIE, 1991]

Biaxial tests Similar to the behavior during uniaxial tests, the biaxial compressive strength is much higher than the biaxial tensile strength [KUPFER et al., 1969, LEE et al., 2004]. Comparing uniaxial compressive strength and biaxial compressive strength, the later is about 25% higher than the former. A typical biaxial strength envelope curve is shown in fig. 2.5, where, σ_I , σ_{II} and f_c are the maximum and minimum principal stresses and strength of the concrete in compression respectively.

Remark. In the interest of describing the cracking in concrete when subjected to complex loading, we restrict ourselves to consider the following phenomenological features: (i) stiffness degradation due to cracking; (ii) unilateral effect; (iii) induced anisotropy due to cracking. The other aspects like hysteresis loops and permanent strains which are due to internal friction, strain rate effects (important in fatigue loading) are not considered in the present research work.

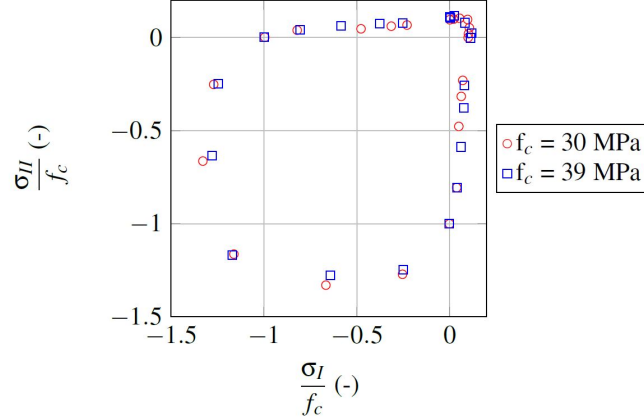


Figure 2.5: Normalised biaxial strength envelopes for concrete [LEE et al., 2004]

2.2 Thermodynamic framework

Here, we present a general formulation for developing constitutive models in thermodynamically consistent manner. In this framework, the method of local state [LEMAITRE and CHABOCHE, 1990] postulates that thermodynamic state at a given point and instant is defined by the state variables which comprises of the observable and the internal variables. The observable variables consists of measurable quantities like strain (ϵ) and temperature while the internal variables characterizes the dissipative phenomena like plastic strain or damage. Assuming an isothermal state, we drop here the dependence of temperature. Let us also assume that there exists a free energy density of Helmholtz type (ψ) which is a convex function of the state variables as given below:

$$\psi = \psi(\epsilon, \kappa) \quad (2.1)$$

where, κ is an internal variable. The stress tensor, σ and the associated variables (Y) are derived from ψ as given below:

$$\sigma = \rho \frac{\partial \psi}{\partial \epsilon} \quad (2.2)$$

$$Y = -\rho \frac{\partial \psi}{\partial \kappa} \quad (2.3)$$

The Clausius-Duhem-Truesdell inequality that restricts the rate of energy dissipation of a unit volume ($\dot{\phi}_V$) is written as:

$$\dot{\phi}_V = \sigma : \dot{\epsilon} - \rho \dot{\psi} \geq 0 \quad (2.4)$$

where, $' : '$ is the double contraction operator between two second-order tensors. From eqs. (2.1) and (2.3), we have $\rho \dot{\psi} = \sigma : \dot{\epsilon} - Y \dot{\kappa}$ and substituting this expression in eq. (2.4) gives the volumetric energy dissipation as:

$$\dot{\phi}_V = Y \dot{\kappa} \geq 0 \quad (2.5)$$

Now, by denoting the free energy and energy dissipation for whole material domain as Ψ and Φ respectively, we write the total mechanical energy (\mathcal{E}) using the work-energy theorem [CAZES et al., 2009] as:

$$\mathcal{E} = \Psi + K - W_{ext} + \Phi \quad (2.6)$$

where, W_{ext} is the work done by the external forces and K is the kinetic energy of the whole material.

In the next section, we present the constitutive and numerical models that attempt to describe the cracking in concrete.

2.3 Description of cracking in concrete

In the literature, various material and numerical models are developed to model dissipative phenomena like cracking in concrete. Some models take into account cracking in a diffused manner (e.g. through continuum constitutive laws) while some models take into account cracking in a discrete manner (e.g. as cohesive cracks). The modeling aspect of these types of description of cracking is the 'energy dissipation' during the strain localization process.

Based on the this aspect, the description of cracking can be classified as follows:

1. implicit description of cracking: energy dissipation associated with cracking processes is smeared over certain volume of the material. Accordingly, the displacement field is always assumed continuous. This kind of formulations are often used in applications due to their relative robustness and simplicity of implementation. Since discontinuous kinematics cannot be modeled explicitly, extracting fine information about cracking (e.g., crack opening displacements) need some additional steps (e.g. post-treatments) and assumptions;
2. explicit description of cracking: kinematic discontinuities associated with the formation of cracks are modeled explicitly. Accordingly, the energy dissipation occurring at the crack surface is directly taken into account. The resulting numerical implementations are however less straightforward than with the continuum models.

In the later sections, a brief description of the models based on the implicit and explicit descriptions of cracking is presented.

2.3.1 Implicit description of cracking

Following the phenomenological approach, the progressive loss of stiffness due to cracking is modeled using strain–softening relationship. In this work, we restrict ourselves to the models that are developed to describe the behavior of concrete, particularly during the cyclic loading. We present here a brief description of the chosen models before going into the chronological evolution of them in the later sections. In particular, we will first introduce continuum models based on elasto–plastic theory and damage mechanics. In these models, the progressive degradation due to the microcracking is achieved using constitutive laws written in terms of stress and strain tensors. Then, attention will be focused on smeared crack models, where the diffused microcracking is represented in a smeared manner on a crack plane. Finally, microplane models will be presented. In these models, the progressive degradation due to the microcracking is achieved using stress and strain vectors in several possible directions instead of tensorial constitutive relationships.

2.3.1.1 Elasto–plastic models

The classical theory of plasticity with a softening function is used to model concrete behavior in many works [REYNOUARD, 1974, WILLAM and WARNKE, 1975, OTTOSEN and SCORDELIS, 1977, IMRAN and PANTAZOPOULOU, 2001, GRASSL et al., 2002]. The key concept of this theory is the additive split of strain into elastic strain and plastic strain (ϵ^e and ϵ^p in fig. 2.6 respectively). The stresses are calculated using the elastic strain and the Hooke's law.

During unloading and reloading, these models exhibits permanent strains while the stiffness modulus remains elastic (fig. 2.6). This feature makes them more suitable to model the irreversible strains during cyclic loading [DRAGON and MROZ, 1979, FEENSTRA and de BORST, 1996]. However, in order to model other features of concrete behavior during cyclic loading like stiffness degradation, crack closure effects and hysteresis loops, more complex softening rules are required [MOHARRAMI and KOUTROMANOS, 2016, ORTIZ, 1985, FEENSTRA and de BORST, 1996]. Also, these models require a very high number of material parameters to fit the experimental curves.

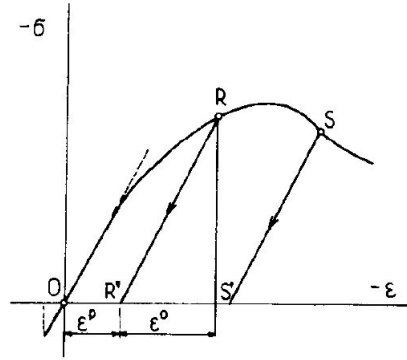


Figure 2.6: Elasto-plastic model for concrete: plastic strain and elastic unloading [DRAGON and MROZ, 1979]

2.3.1.2 Damage models

In the earlier work [KACHANOV, 1958], the concept of damage is introduced in the context of creep rupture of metals. Later it is used to describe the progressive degradation in concrete [MAZARS, 1984, LEMAITRE and MAZARS, 1982, MAZARS and PIJAUDIER-CABOT, 1989] that leads to the softening behavior. These models can be classified into isotropic and anisotropic damage models based on the description of stiffness degradation. We present below the development of these models in the perspective of cracking in concrete especially during cyclic loading.

Isotropic damage models In earlier damage models [LEMAITRE and MAZARS, 1982, MAZARS, 1984, MAZARS and PIJAUDIER-CABOT, 1989], the stiffness degradation is taken into account using a bounded internal variable termed as isotropic scalar damage variable (d) which varies from 0 in undamaged state to 1 in damaged state. In this framework, the thermodynamic potential and the stress tensor can be written as [MAZARS, 1984]:

$$\rho\psi = \frac{1}{2} (1 - d) \epsilon : \mathbb{E} : \epsilon \quad (2.7)$$

$$\sigma = (1 - d) \mathbb{E} : \epsilon \quad (2.8)$$

where, \mathbb{E} is the Hooke's elastic stiffness tensor. However, this model is well suitable for modeling uniaxial tensile behavior and other aspects like the concrete dissymmetry and unilateral effect when concrete is subjected to cyclic loading cannot be described easily using this framework. For modeling the behavior of concrete in both tension and compression, an earlier attempt was made in [MAZARS, 1986] by reformulating the damage variable as a weighted sum of two variables representing damage due to tension and compression (d_t and d_c respectively) as [MAZARS, 1986]:

$$d = \alpha_t d_t + \alpha_c d_c \quad (2.9)$$

where, α_t and α_c are the weights for the damage variables in tension and compression respectively. However, the unilateral effect is still not taken into account in this model. Later, a sophisticated approach using the concept of spectral decomposition of stress and strain is used to account for tensile and compressive damage mechanisms independently [LADEVÉZE and LEMAITRE, 1984, ORTIZ, 1985, MAZARS, 1985, SIMO and JU, 1987, STEVENS and LIU, 1992, LUBARDA et al., 1994].

Other approaches for modeling unilateral effect in this framework may include a bi-dissipative damage model [COMI and PEREGO, 2001, COMI, 2001, RASTIELLO et al., 2016] with separate flow surfaces as functions of two independent damage variables for tension and compression.

In another work [RICHARD et al., 2010], a partial unilateral effect, internal frictional effects like permanent strains and hysteresis loops are modeled using damage mechanics by splitting the free energy potential into hydrostatic and deviatoric parts. The unilateral effect is then handled by the hydrostatic part while the deviatoric part manages the frictional effects. Later, another model based on the previous one is proposed to take into account the full unilateral effect by using a closing function [RICHARD and RAGUENEAU, 2013, VASSAUX et al., 2015].

Anisotropic damage models While isotropic scalar damage models are successful to achieve isotropic stiffness degradation, anisotropic damage models are developed to tackle the crack induced anisotropy. In these models, the preferential microcrack orientations due to the type of loading are taken into account by using tensors rather than an isotropic damage variable. In some models [KRAJCINOVIC, 1985, LECKIE and ONATE, 1981, LEMAITRE and CHABOCHE, 1990, CHABOCHE, 1992], the damage is described using a fourth-order tensor while in another approach [MURAKAMI, 1988, HALM and DRAGON, 1998, MESCHKE et al., 1998], a second-order tensor is used.

In a general anisotropic damage framework [LEMAITRE, 2012], the Helmholtz free energy and the stress tensor can be defined using a modified elastic tensor due to damage, $\tilde{\mathbb{E}}$ as:

$$\rho\psi = \frac{1}{2} \boldsymbol{\epsilon} : \tilde{\mathbb{E}} : \boldsymbol{\epsilon} \quad (2.10)$$

$$\boldsymbol{\sigma} = \tilde{\mathbb{E}} : \boldsymbol{\epsilon} \quad (2.11)$$

Now, assuming that the inverse of $\tilde{\mathbb{E}}$ exists, a general fourth-order damage tensor can be obtained as:

$$\mathbb{C} = \mathbb{I} - \tilde{\mathbb{E}} : \mathbb{E}^{-1} \quad (2.12)$$

In order to take into account the unilateral and the microcrack closure-reopening effects, a spectral decomposition of the stress tensor [ORTIZ, 1985] or equivalently that of the strain tensor [CAROL and WILLAM, 1996] is considered as follows (here we focus on the strain based approach):

$$\boldsymbol{\epsilon}^+ = \langle \boldsymbol{\epsilon}_i \rangle \mathbf{x}'_i \otimes \mathbf{x}'_i \quad (2.13)$$

$$\boldsymbol{\epsilon}^- = \boldsymbol{\epsilon} - \boldsymbol{\epsilon}^+ = \langle -\boldsymbol{\epsilon}_i \rangle \mathbf{x}'_i \otimes \mathbf{x}'_i \quad (2.14)$$

where, $\boldsymbol{\epsilon}^+$ and $\boldsymbol{\epsilon}^-$ are the strains in tension and compression respectively, $\langle \bullet \rangle^+$ denotes the positive part of $\langle \bullet \rangle$ and \mathbf{x}'_i is the eigen basis of $\boldsymbol{\epsilon}$ for $i = \{1, 2\}$ in 2D and $i = \{1, 2, 3\}$ in 3D.

As introduced in [ORTIZ, 1985], the expressions of $\boldsymbol{\epsilon}^+$ and $\boldsymbol{\epsilon}^-$ can also be rewritten using the projection operators \mathbb{P}^+ and \mathbb{P}^- as $\boldsymbol{\epsilon}^+ = \mathbb{P}^+ : \boldsymbol{\epsilon}$ and $\boldsymbol{\epsilon}^- = \mathbb{P}^- : \boldsymbol{\epsilon}$. Using the above spectral decomposition, the secant (reduced) stiffness tensor can be obtained as:

$$\tilde{\mathbb{E}} = \mathbb{E} - \mathbb{P}^+ : \Delta\mathbb{E}^+ : \mathbb{P}^+ - \mathbb{P}^- : \Delta\mathbb{E}^- : \mathbb{P}^- \quad (2.15)$$

where, $\Delta\mathbb{E}^+$ and $\Delta\mathbb{E}^-$ are the reduction of the elastic tensor due to the microcracks active in tension and compression respectively.

However, the description of anisotropic damage by a fourth-order damage tensor would require to determine a high number of material parameters and complicated numerical implementation.

In [DESMORAT et al., 2007], a second-order tensor (\mathbf{D}) whose eigen values between 0 and 1 is used to obtain an effective stress tensor ($\boldsymbol{\sigma}^{eff}$) as follows:

$$\boldsymbol{\sigma}^{eff} = \left((\mathbf{I} - \mathbf{D})^{-\frac{1}{2}} \cdot \boldsymbol{\sigma}_d \cdot (\mathbf{I} - \mathbf{D})^{-\frac{1}{2}} \right)_d + \frac{1}{3} \left[\frac{\langle \text{tr} \boldsymbol{\sigma} \rangle}{\mathbf{I} - \text{tr} \mathbf{D}} \langle -\text{tr} \boldsymbol{\sigma} \rangle \right] \mathbf{I} \quad (2.16)$$

where, $\cdot\cdot$ denotes the simple contraction operator, $\text{tr}(\bullet)$ denotes the trace of a second-order tensor (\bullet) (it is defined as $\text{tr}(\bullet) = \mathbf{I} : (\bullet) = (\bullet)_{ii}$), and $(\bullet)_d$ denotes the deviatoric part of (\bullet) (for a second-order tensor it is defined as $(\bullet)_d = (\bullet) - \text{tr}(\bullet)\mathbf{I}/3$). Although this model is thermodynamically consistent and robust [RAGUENEAU et al., 2008], it is difficult to define the limits of the components of \mathbf{D} [DESMORAT et al., 2007]. Also, a second-order damage tensor would restrict the description of damage in orthotropic axes [MURAKAMI and OHNO, 1981].

Coupling elasto-plasticity and damage models The inadequacy of plasticity models to describe stiffness degradation due to cracking during unloading and reloading can be overcome by coupling plastic and damage models [ORTIZ, 1985, LUBLINER et al., 1989, YAZADANI and SCHREYER, 1990, GATUINGT and PIJAUDIER-CABOT, 2002]. The coupled plastic-damage models can also model the permanent strains during cyclic loading [LEE and FENVES, 1998, GRASSL and JIRÁSEK, 2006]. In [JASON et al., 2006], an isotropic damage model is coupled with a hardening yield plastic surface.

2.3.1.3 Smearred crack models

In smeared crack models [NGO and SCORDELIS, 1967, RASHID, 1968, ČERVENKA, 1971, BAŽANT and GAMBAROVA, 1980, de BORST, 1985], microcracks of different orientations which are not necessarily planar are represented in a smeared manner on a plane termed as 'crack plane'. This representation is then followed by the decomposition of total strain (ϵ) into elastic strain (ϵ^e) and crack strain (ϵ^{cr}) as shown below:

$$\epsilon = \epsilon^e + \epsilon^{cr} \quad (2.17)$$

The initial direction of the computational crack is specified by an initiation criterion. For example, following the Rankine criterion, let us postulate that the normal direction (\mathbf{n}^{cr}) to the initial crack is parallel to the direction of the maximum principal stress (\mathbf{x}'_I) (fig. 2.7). Let \mathbf{s}^{cr} ($\perp \mathbf{n}^{cr}$) denotes the tangent to the crack plane.

Next, the crack strain vector (\mathbf{e}^{cr}) is obtained by the projection of crack strain on the crack plane ($\mathbf{e}^{cr} = \epsilon^{cr} \cdot \mathbf{n}^{cr}$). Traction vector on the crack plane (\mathbf{t}^{cr}) is related to the stress tensor (σ) outside the cracking zone using Cauchy's stress principle ($\mathbf{t}^{cr} = \sigma \cdot \mathbf{n}^{cr}$) (fig. 2.7). Now, the crack strain is calculated by defining a constitutive relationship between the crack strain vector and crack traction.

Depending on the treatment of direction of the crack during the rotation of principal stress axes, three different models are developed in the literature as presented below.

Fixed crack model In this approach [de BORST, 1985, de BORST et al., 2004, JIRÁSEK, 2011], direction of the crack is fixed after its activation. This leads to the misalignment of crack plane

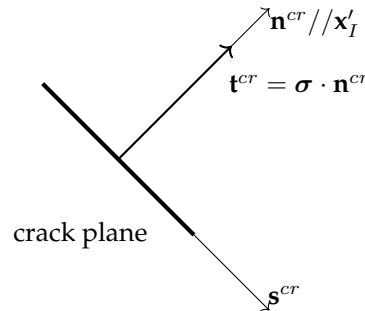


Figure 2.7: Smeared crack model: crack plane aligned with the maximum principal stress direction

with the maximum principal stress direction (fig. 2.8). In these models, a shear retention factor is used to transmit the shear traction across the crack [SUIDAN and SCHNOBRICH, 1973, ROTS and de BORST, 1987, ROTS et al., 1985]. This leads to the non-realistic generation of shear stresses [WILLAM et al., 1989]. Also, fixed crack approach leads to stress locking [WILLAM et al., 1989, JIRÁSEK, 2011] that is, in a finite element mesh which is not aligned with the crack orientation there is a spurious transfer of stress across the crack.

Rotating crack model Here [ROTS, 1991, GUPTA and AKBAR, 1984, JIRÁSEK, 2011], the idea is to rotate the crack as the maximum principal stress direction rotates by keeping the normal of the crack plane aligned (fig. 2.9) to the direction of the maximum principal stress. Let us assume that a first crack plane whose normal and tangent are denoted by \mathbf{n}_1^{cr} and \mathbf{s}_1^{cr} respectively is localized. Also, let $\mathbf{t}_1^{cr} = \boldsymbol{\sigma} \cdot \mathbf{n}_1^{cr}$ be the traction vector on this plane. Now, as the maximum principal stress direction rotates a second crack plane localizes such that its normal \mathbf{n}_2^{cr} (tangent \mathbf{s}_2^{cr}) is parallel to present \mathbf{x}'_I . Furthermore, the information regarding the previous crack is erased and a second traction vector $\mathbf{t}_2^{cr} = \boldsymbol{\sigma} \cdot \mathbf{n}_2^{cr}$ is defined. In rotating crack model, shear retention factor is avoided but stress locking still takes place [JIRÁSEK and ZIMMERMANN, 1998]. However, these models are thermodynamically inconsistent and also the unloading stiffness loses positive definiteness [ROTS, 1988, JIRÁSEK and ZIMMERMANN, 1998].

Fixed multi-directional crack model As proposed in [de BORST and NAUTA, 1998], in this approach a new crack is initiated after the angle between the previous crack and the present maximum principal stress direction exceeds a certain threshold value, θ_{th} (fig. 2.10). In this approach, all the cracks that are localized remains active and dissipate energy. In fixed multi-directional crack model, the threshold angle remains arbitrary and cannot be determined on a sound physical basis.

Also, these models inherits the problems of dependency on the mesh size and orientation. Later, in the section 2.3.2.3, we describe a method to embed the cracks inside the mesh to avoid these problems.

2.3.1.4 Microplane models

The phenomenological models presented above are based on the constitutive laws developed between stress and strain tensors. Thus the constitutive response remains invariant during the rigid body rotations. Although these models are capable of describing simple stress states it is very difficult to get a realistic description for more complex stress states and in particular cases where principal stress/strain axes rotate. Microplane models [BAŽANT and OH, 1985, BAŽANT, 1984, BAŽANT and PRAT, 1988a, BAŽANT, 1996] are developed with an aim to handle the directional dependent phenomena (e.g. microcracking in quasi-brittle materials) by describing the

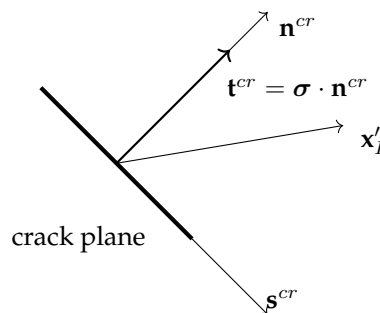


Figure 2.8: Fixed crack model: misalignment of crack plane with the maximum principal stress direction

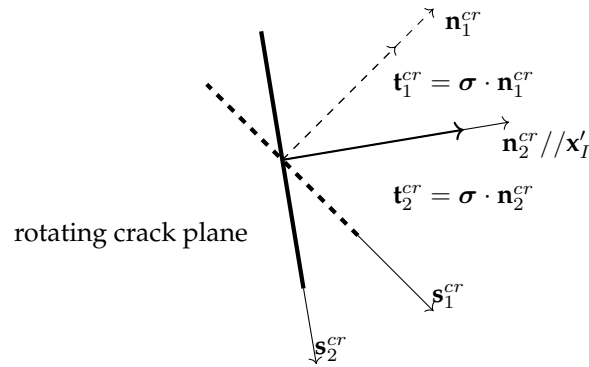


Figure 2.9: Rotating crack model: rotation of the crack plane along with the maximum principal stress direction

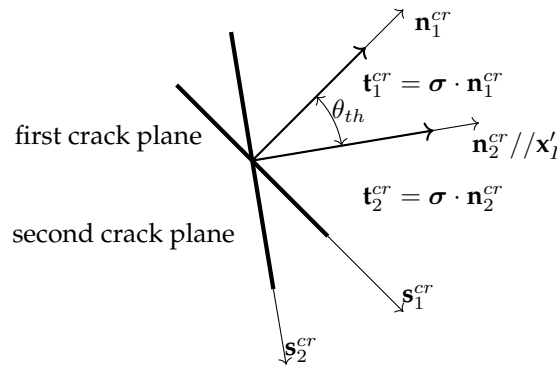


Figure 2.10: Fixed multi-directional crack model: opening of the second crack plane after certain rotation of the maximum principal stress direction

inelastic behavior in planes of all possible orientations known as ‘microplanes’. The key concept here is to develop constitutive relations between stress/strain vectors on each microplane instead of tensors and perform integration (spherical or circular) over all possible directions thus ensuring the tensorial invariance.

The concept of directional sampling of material behavior was introduced in [TAYLOR, 1938] which is later developed by [BATDORF and BUDIANSKY, 1949] as the slip theory of plasticity. In these models stresses on planes of all possible orientations are linked with the macroscopic stress by an assumed static constraint. However, in the case of softening behavior (e.g. in quasi-brittle materials) the static constraint leads to instabilities [BAŽANT, 1984]. Hence, it was realized [BAŽANT, 1984] that it is more appropriate to assume that strain components on the microplanes is linked with the strain at a unit volume by a ‘kinematic constraint’.

Here, following [BAŽANT and OH, 1985, BAŽANT, 1984], we present a general framework of the microplane system in 3D (fig. 2.11) using a discretized sphere. However, for planar problems [PARK and KIM, 2003] this representation can be simplified using a disk microplane system. Hence, we denote the closed surface of the microplane system (spherical or disk) by Ω . The framework consists of the projection operation of ϵ (kinematic constraint) on a microplane to obtain its components ϵ_m and ϵ_l in the normal (\mathbf{m}) and the tangential ($\mathbf{l}_1, \mathbf{l}_2$) directions (see [BAŽANT and OH, 1985] for expressions) respectively. The corresponding stress components, σ_m and σ_l are obtained by postulating constitutive laws on each microplane. Then the Principle of Virtual Work (PVW) is used to link the microplane stresses to that of the continuum one [BAŽANT, 1984] which is not the case in the slip theory of plasticity. Notice that in the case of classical framework for obtaining constitutive laws, we obtain a direct relationship between ϵ and σ .

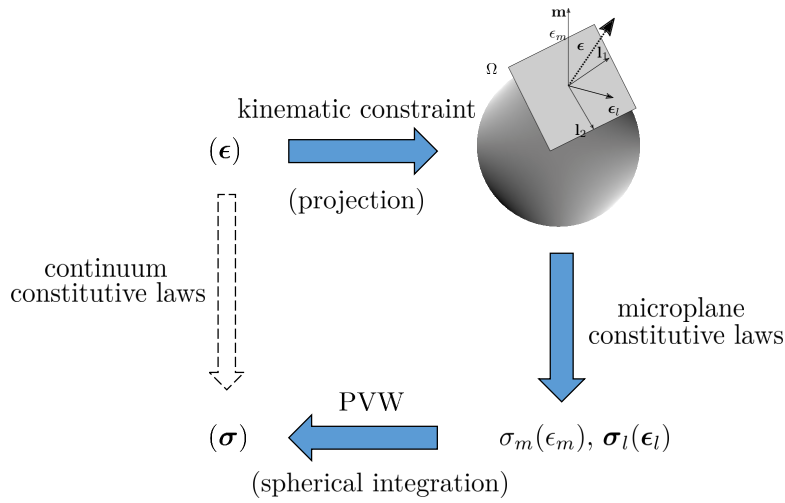


Figure 2.11: Framework of the microplane models: spherical microplane models

Since the initial conception various versions of the microplane models were developed. We present the chronological development of these models below.

M1-model In this version of the microplane models [BAŽANT and OH, 1985, BAŽANT, 1984], the primary emphasis is made to tackle the tension strain–softening. Failure in compression is achieved when the tensile limit is reached (due to Poisson’s effect) in the microplanes whose normal is perpendicular to the direction of compression. Also, it is assumed that only the normal component of the strain tensor on each microplane drives the cracking process. The constitutive relation at the microplane level is defined as [BAŽANT and OH, 1985], $\sigma_m = C_m(\epsilon_m)$. Then, the components of the tangent stiffness tensor (C_{pqrs}^t) are obtained by (using Einstein notation):

$$C_{pqrs}^t = \frac{3}{2\pi} \int_{\Omega} C'_m m_p m_q m_r m_s dS \quad (2.18)$$

where, m_p are the components of \mathbf{m} and C'_m is the derivative of the constitutive law at the microplane level.

As a consequence, the Poisson’s ratio is restricted to $\frac{1}{4}$. The possible remedies are either to add an elastic shear stiffness by including the tangential component of strain and stress (ϵ_l and σ_l respectively) on each microplane [BAŽANT, 1984] or to add an elastic strain to the total strain of the material [BAŽANT and OH, 1985].

M2-model In order to describe the biaxial and triaxial behavior of concrete, it is proposed in [BAŽANT and PRAT, 1988a, BAŽANT and PRAT, 1988b] to split the normal behavior into volumetric and deviatoric parts. The corresponding components of stress and strain on each microplane are denoted by $\sigma_v, \epsilon_v, \sigma_d$ and ϵ_d respectively. This enables to capture the compression failure due to the lateral expansion caused by inelastic deviatoric strains and slip on inclined microplanes. In addition to this, the tangential component of strain and stress are also considered. The relations between various components of stress and strain on each microplane are assumed as, $\sigma_v = C_v(\epsilon_v)$, $\sigma_d = C_d(\epsilon_d)$ and $\sigma_l = C_l(\epsilon_l, \sigma)$, where, C_v, C_d and C_l are the volumetric, deviatoric and tangential stiffness parameters respectively. The parameter C_l is dependent on σ to model the frictional phenomena. The components of tangent stiffness tensor in this case are

obtained as [BAŽANT and PRAT, 1988a]:

$$C_{pqrs}^t = \frac{3}{2\pi} \int_{\Omega} \left[(C'_d - C'_l) m_p m_q m_r m_s + \frac{1}{3} (C'_v - C'_d) m_p m_q \delta_{rs} \right] dS + \frac{3}{2\pi} \int_{\Omega} \left[\frac{1}{4} C'_l (m_p m_r \delta_{qs} + m_p m_s \delta_{qr} + m_q m_r \delta_{ps} + m_q m_s \delta_{pr}) \right] dS \quad (2.19)$$

where, C'_v , C'_d and C'_l are the derivatives of the volumetric, deviatoric and the tangential constitutive laws respectively and δ_{rs} is Kronecker delta defined as:

$$\delta_{rs} = \begin{cases} 0 & \text{if } r \neq s \\ 1 & \text{if } r = s \end{cases}$$

In this version, all Poisson's ratios between -1 to 0.5 are achievable. The major disadvantage of this model is that it lacks the work-conjugacy of volumetric stress. An explicit formulation of M2-model was proposed in [CAROL et al., 1992]. Also, a regularization scheme of nonlocal type is coupled with this model to avoid mesh sensitivity and the failure modes with zero energy dissipation in [BAŽANT, 1994].

M3-model To avoid any discrepancies during cyclic loading, the concept of stress-strain boundaries is introduced in [BAŽANT, 1996, BAŽANT et al., 1996]. These conditions limit the maximum value of the stress components that can be attained in tensile and compressive regimes. In [BAŽANT, 1996], stress-strain boundaries for normal, volumetric, positive and negative deviatoric and tangential components of stress (F_m , F_v , F_d^+ , F_d and F_l respectively) are defined as :

$$\begin{aligned} \sigma_m &= F_m(\epsilon_m, \sigma_v), & \sigma_v &= -F_v(-\epsilon_v), & \sigma_l &= F_l(\sigma_m) \\ \sigma_d &= -F_d(-\epsilon_d), & \sigma_d &= F_d^+(\epsilon_d) \end{aligned} \quad (2.20)$$

Here, the normal stress-strain boundary is also defined to ensure the continuity of transition from the elastic behavior. The shear response is modeled by a friction-cohesive yield surface (F_l) that relates the shear stress component to the normal stress component on the microplane instead of the shear strain component in M2-model.

M4-model In the M4-model [BAŽANT et al., 2000, CANER and BAŽANT, 2000], the normal stress boundaries are improved to tackle more efficiently tensile cracking with the fragment pull-out, aggregate bridging and crack closing. In M3-model [BAŽANT, 1996], a linear relationship is considered between the shear and normal stress components on the microplane which leads to an overestimation of stress. Hence, in M4-model this is replaced by a hyperbolic relationship between the shear and normal stress components on the microplane.

M5-model Even though M4-model is a refined version of the older microplane models, it is suffered from problems at the far post-peak tensile softening regime such as excessive lateral contraction and stress locking. As a remedy, a series coupling of kinematically constrained and statically constrained microplane systems is proposed in M5-model [BAŽANT and CANER, 2005a, BAŽANT and CANER, 2005b]. Using this model, the test data for far post-peak tensile softening and also the shear-compression failure envelope of concrete is well represented.

M6-model In M6-model model [CANER and BAŽANT, 2005], another idea is pursued to solve the problem of excessive lateral contraction in far post-peak tensile softening regime. It was realized that the volumetric-deviatoric split causes this problem due to the generation of large

compressive strains in directions parallel to the crack in far post-peak tensile softening regime. This problem is solved by a transition from an explicit volumetric–deviatoric split to no split when the maximum principal stress exceeds certain limit. In addition to this, loading/unloading rules for tension–compression load cycles are also introduced.

M7-model In M7-model [CANER and BAŽANT, 2013, CANER and BAŽANT, 2012], explicit volumetric–deviatoric split is abandoned for elastic part of microplane strains and for the tensile stress–strain boundaries. For compressive stress–strain boundaries, the volumetric–deviatoric split is retained and both the components are summed to obtain the normal component. In addition to this, multiple hysteresis loops in cyclic loading are also well represented.

Instead of using stress–strain boundaries, plasticity and damage based constitutive laws [CAROL and BAŽANT, 1997, OŽBOLT and BAŽANT, 1992, ZREID and KALISKE, 2018] are also introduced in the framework of microplane models. A thermodynamic consistent framework for microplane models is also developed in [CAROL et al., 2001a]. In this thermodynamic framework of microplane models, the inelastic constitutive modeling is described by considering plasticity and damage [KUHLE et al., 2001] at the microplane level.

Among various implicit models presented in this section, the microplane models are used to model the anisotropic damage due to their simplicity in the present work.

2.3.1.5 Regularization techniques

In softening regime, the governing equations of equilibrium become ill-posed and the numerical solutions suffer from lack of objectivity with respect to spatial discretization (mesh dependency). This leads to the prediction of zero energy dissipation at the failure surface which is not realistic. Several regularization methods are proposed to preserve the objectivity of the numerical solutions. In the literature, techniques known as localization limiters are developed by limiting the size of the localization zone based on the internal structure of the continuum [BELYTCHKO and LASRY, 1989].

Localization limiters that use the concept of nonlocal continua incorporate an internal length into the constitutive law by considering nonlocal interactions between the microcracks. In integral nonlocal models [PIJAUDIER-CABOT and BAŽANT, 1987, PIJAUDIER-CABOT et al., 2004], nonlocal variables ($\bar{f}(\mathbf{x})$) driving damage evolution are computed using an integral of the product of the local ($f(\mathbf{x})$) variable and a nonlocal weight function (W^{nl}) over a domain (\mathcal{V}) as:

$$\bar{f}(\mathbf{x}) = \int_{\mathcal{V}} W^{nl} f(\mathbf{x}, \boldsymbol{\xi}) d\xi \quad (2.21)$$

where, \mathbf{x} is the target point and $\boldsymbol{\xi}$ is the source point. Here, nonlocal weight function is normalized in order not to alter a uniform field as [JIRÁSEK, 2007]:

$$W^{nl} = \frac{W_0^{nl}(\mathbf{x}, \boldsymbol{\xi})}{\int_{\mathcal{V}} W_0^{nl}(\mathbf{x}, \boldsymbol{\xi}) d\xi} \quad (2.22)$$

where, $W_0^{nl}(\mathbf{x}, \boldsymbol{\xi})$ is monotonically decreasing non-negative function of the distance, $\|\mathbf{x} - \boldsymbol{\xi}\|$ which is usually considered as a Gaussian distribution function:

$$W_0^{nl}(\mathbf{x}, \boldsymbol{\xi}) = \exp\left(\frac{-4\|\mathbf{x} - \boldsymbol{\xi}\|^2}{(l_c^{nl})^2}\right) \quad (2.23)$$

and l_c^{nl} is an internal length of the nonlocal continuum. Enhancements to the original framework were also introduced by several authors in order to solve some well known drawbacks of standard formulations (e.g., damage diffusion across damaged bands), through considering nonlocal

interactions which evolve based on mechanical fields [NGUYEN, 2011, PIJAUDIER-CABOT and DUFOUR, 2010, KRAYANI et al., 2009, GIRY et al., 2011, DESMORAT et al., 2015, RASTIELLO et al., 2018].

In differential nonlocal or gradient enhanced models [PEERLINGS et al., 1996, SIMONE et al., 2003, SAROUKHANI et al., 2013], higher order gradients of the local variable are considered. Constitutive models based on the gradient of internal variables [de BORST and MÜHLHAUS, 1992, MÜHLHAUS and ALFANTIS, 1991, LORENTZ and GODARD, 2011] are also used as localization limiters.

In other class of localization limiters, continuum with microstructure is used to introduce the internal length. In [CHAMBON et al., 2001, FERNANDES et al., 2008, JOUAN et al., 2017] localization phenomenon in quasi-brittle materials is modeled using a local second gradient model where the standard kinematics of the continuum is enhanced with the gradients of strain.

The energetic regularization method proposed in [HILLERBORG et al., 1976] assumes that fracture energy depends on some length measure characteristic to the finite element. Nevertheless, it is very difficult to solve the issue of directional mesh bias [JIRÁSEK and GRASSL, 2008] induced by this method.

In the context of the microplane models, several of the above mentioned approaches are employed to avoid the pathological mesh sensitivity. In [ČERVENKA et al., 2005], the crack band approach in which the Crack Opening Displacement (COD) is calculated using the inelastic strain in a band of fixed width. This width is determined using the finite element size [JIRÁSEK and BAUER, 2012]. In [BAŽANT and di LUZIO, 2004, di LUZIO, 2007], the nonlocal approach for the microplane models (like M4 model) is formulated in which the softening yield limit is defined using a spatially averaged strains. In [ZREID and KALISKE, 2018], the implicit gradient approach is used to regularize a combined plasticity–damage microplane model. A high–order and micropolar microplane theories are also developed in [CUSATIS and ZHOU, 2013] and [ETSE et al., 2003, ETSE and NIETO, 2004] respectively.

In the present work, for the sake of computational effectiveness, we employ an energy regularization technique to obtain mesh independent results using the microplane models.

2.3.2 Explicit description of cracking

The extraction of fine information about cracking from continuum strain–softening models involves adaptation of a finer mesh or post-processing [MATALLAH et al., 2010, OLIVER-LEBLOND et al., 2013, DUFOUR et al., 2011]. In the context of finite element analysis of large structures, this increases the computational demand substantially. In order to avoid the use of additional tools to extract information related to cracking process (location, crack opening, etc.) and to describe more precisely the displacement discontinuity occurring at failure, numerical methods have been developed to describe cracking in an explicit manner.

2.3.2.1 Cohesive crack models

The cohesive crack models [NGO and SCORDELIS, 1967, RASHID, 1968, INGRAFFEA and SAUOMA, 1985, ALLIX and LADEVÈZE, 1992] were developed by treating the crack as geometrical discontinuity in continuous material (fig. 2.12). The basic idea of this approach is to form a crack as the stress level reaches its peak and consider that the crack can still transmit the stress across its width (hence the term cohesive crack). This is also termed as fictitious crack model [HILLERBORG et al., 1976] and can be a crude description of fracture process zone around the tip of the crack where strain localization phenomenon occurs.

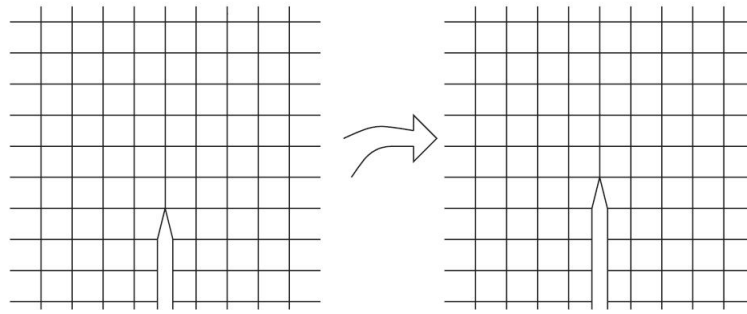


Figure 2.12: Cohesive crack approach [de BORST et al., 2004]

In numerical solutions using the finite element method, the strategy is to duplicate the node at which the nodal force reaches a limit into two nodes and to gradually release the stress until the separation of the two nodes reaches certain value. After that the crack tip is transferred to the next node and the process is repeated (fig. 2.12). The main disadvantage in this approach is that the crack is formed only along the inter element boundaries which introduces mesh bias. The possible remedy is re-meshing but it involves high computational demand in the finite element codes [CARPINTERI et al., 2003]. Meshless methods [BELYTSCHKO et al., 1994, HEGEN, 1996] were also coupled with this approach by modifying the nodal support for the node in front of the crack. But the difficulties like high computational demand and requirement of a better base mesh for accurate integration [BELYTSCHKO et al., 1996, de BORST et al., 2004] are inherited from the meshless methods. Nevertheless, these methods were limited for one and two dimensional applications.

2.3.2.2 Discontinuous kinematics models

The discontinuous kinematics models try to capture the failure in quasi-brittle materials by incorporating the strain/displacement discontinuities inside the continuum. From a physical stand point, the formulation for modeling strain localization in quasi-brittle materials can be classified based on the width of the localization band as follows:

1. localization into a band of finite thickness where the strain field is discontinuous which is termed as weak discontinuity,
2. localization into a line or a surface of zero thickness where the displacement field is discontinuous which is termed as strong discontinuity.

To demonstrate the characteristics of weak and strong discontinuities, let us consider a one dimensional bar of length L whose spatial coordinates are denoted by x and applied displacements by u_0 as shown in the fig. 2.13a.

Let us consider the possibility of two localized cases, one in which a band of thickness l_c is formed (fig. 2.13b) and one in which a crack of zero thickness is formed (fig. 2.13c). In the former case, $x_A = (L - l_c)/2$ and $x_B = (L + l_c)/2$ denotes the end points of the localization band while $x_C = L/2$ denotes the location of the discontinuity in the later case. For the case of weak discontinuity, displacement distribution is characterized by a smooth jump (fig. 2.13d) and strain distribution is characterized by a sharp jump (fig. 2.13f). For the case of strong discontinuity, displacement distribution is characterized by a sharp jump (fig. 2.13e) while the strain distribution is unbounded at the discontinuity (fig. 2.13g).

In the context of finite elements, these discontinuities are modeled by introducing additional Degrees of Freedom (DOFs) pertaining to the modes of localization. These additional DOFs are interpolated using enhanced shape functions. Depending on the technique of enhancement, different

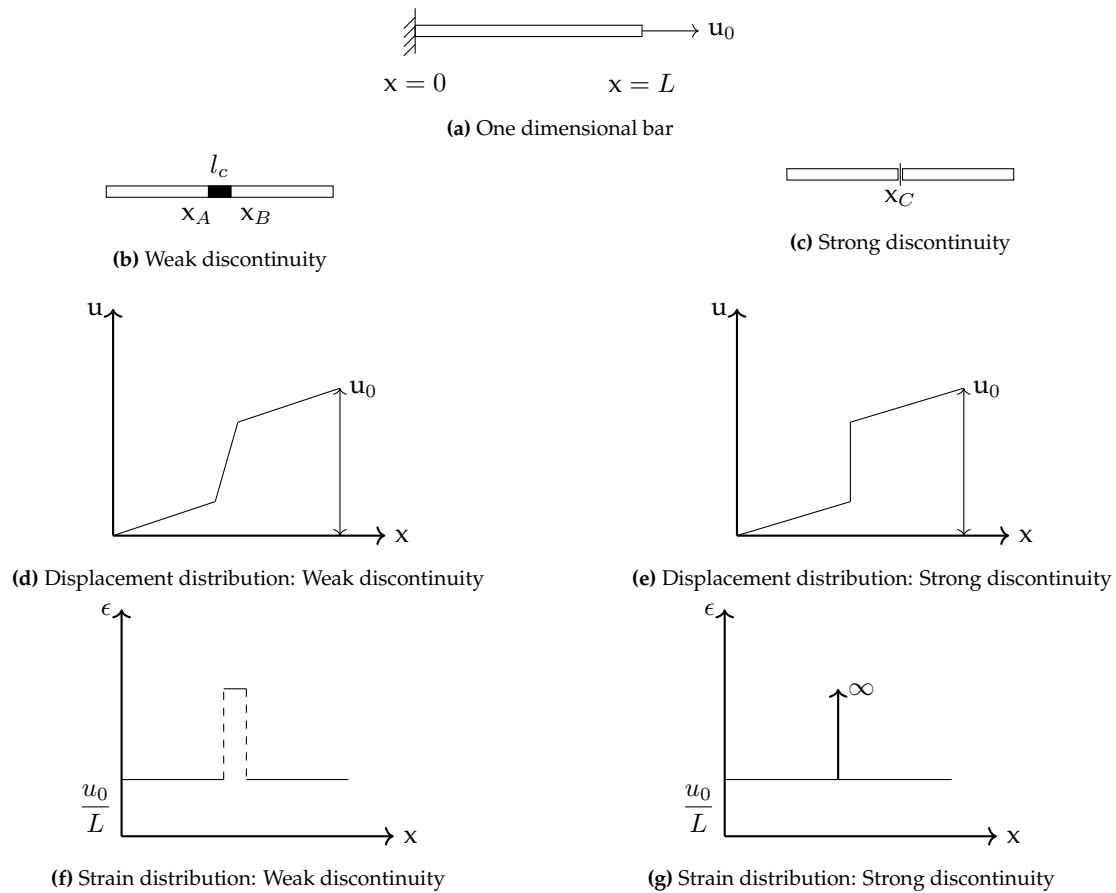


Figure 2.13: Illustration of weak and strong discontinuities

numerical methods developed to construct the discontinuous kinematics fields can be classified as:

1. embedded discontinuity method, where, the additional DOFs are embedded inside the localized finite elements and the global DOFs of the discretized finite element model remains unchanged.
2. nodal enrichment method, where, the additional DOFs are supported by the nodes of the localized finite elements. Hence, the global DOFs of the discretized finite element model are increased.

In the next sections, we present both the methods in detail and discuss the differences between them.

2.3.2.3 Embedded finite element method

The modeling features of EFEM can be illustrated by a bar discretized using 4 nodes as shown in the fig. 2.14a. Let us assume the presence of a discontinuity (e) at an arbitrary location between nodes 2 and 3. Due to this, the discretized displacement field (d_a , $a = 1, 2, 3, 4$) consists of a jump at the location of the discontinuity as shown in the fig. 2.14d. Also, a constant displacement jump distribution is assumed in the domain of influence (fig. 2.14b) which includes nodes 2 and 3 as shown in the fig. 2.14e. Now, the distribution of continuous displacements in the bulk portion of

the bar (fig. 2.14c) are obtained by removing the jump from the displacement field d as shown in the fig. 2.14f. Later this displacement distribution is used to compute the strain/stress in the bulk that satisfy the equilibrium.

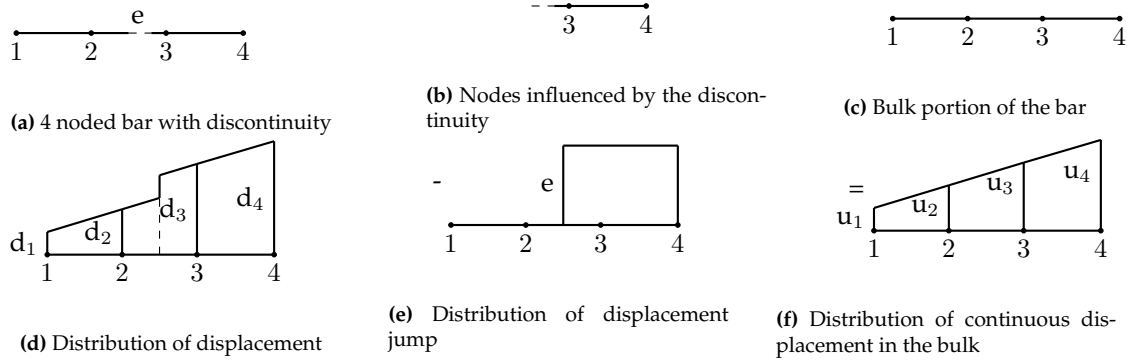


Figure 2.14: Illustration of embedded finite element method

In this method, both the weak and strong discontinuities can be embedded inside the finite element to capture the localization phenomenon.

Weak discontinuity approach The concept of embedding a weak discontinuity inside the finite element is introduced in [ORTIZ et al., 1987, BELYTSCHKO and BLACK, 1999]. After the onset of localization, certain additional DOFs are added which represent the magnitude of strain discontinuity associated with the given localization mode. These additional DOFs are statically condensed at the element level thus not effecting the global DOFs.

Strong discontinuity approach In strong discontinuity approach, a discontinuity is introduced in the displacement field. So the variable that drive the cracking process is the discontinuous displacement field itself. In the earlier works [DVORKIN et al., 1990, DVORKIN et al., 1991], the discontinuity line was introduced in the finite element. Extension of this approach to a standard bilinear quadrilateral is done in [KLISINSKI et al., 1991] and for Constant Strain Triangular element (CST) in [OHLSSON and OLOFSSON, 1997] using physical considerations. In [LOTFI, 1992] an Enhanced Assumed Strain (EAS) format starting from the Hu-Washizu variational principle [WASHIZU, 1955] is used to derive a symmetric formulation. A non-symmetric formulation is also developed in [SIMO and RIFAI, 1990, SIMO et al., 1993, WELLS and SLUYS, 2000] by using the same approach but with different interpolation functions for real and virtual quantities. It was shown in [OLIVER, 1996a, OLIVER, 1996b] that relationship between the cohesive traction and the displacement discontinuity can be derived from the continuum constitutive laws instead of using a cohesive law at the displacement discontinuity. This approach is used to propose a transition model from weak discontinuity to strong discontinuity for an elasto-plastic constitutive law in [OLIVER et al., 1999] and for a damage constitutive law in [OLIVER, 2000]. This method is also extended for treatment of crack branching problems in a dynamic setting [ALFAIATE et al., 2001, ARMERO and EHRLICH, 2006]. Recently, an anisotropic cracking model in the framework of strong discontinuity is also developed in [KISHTA, 2017]. In [JIRÁSEK, 2000] different formulations are classified into three major classes based on representation of the kinematics and the equilibrium at the crack surface.

2.3.2.4 Nodal enrichment method

The notion of enriching the nodes of a finite element with additional DOFs is an idea that is exploited in Partition of Unity based Finite Element Method (PUFEM) [MELENK and BABUSKA,

1996, BABUSKA and MELENK, 1997]. The general idea of this method is to introduce enrichment functions which are multiplied by the partition of unity functions to construct the approximation of the displacement field. Consequently, the resulting product has the approximation properties (say, modes of localization) inherited from enrichment functions and the limited support inherited from partition of unity functions. The choice of the enrichment functions is based on the analytical solution of the problem in the cases where one exists. So, in order to design PUM it is required to have a priori knowledge about the solution of the problem. Depending on the physical nature of the enriched field the choice of the enrichment functions can be polynomial or non-polynomial functions [DUARTE and ODEN, 1996, DUARTE et al., 2007, KIM et al., 2011]. However, except for low order polynomial functions, the computation of element stiffness is costly because of the requirement of higher number of integration points.

In the case of XFEM [BELYTSCHKO and BLACK, 1999, DOLBOW and BELYTSCHKO, 1999, MOES et al., 1999, SUKUMAR et al., 2001], two different types of enrichment functions are used. The asymptotic functions are used to enrich the nodes of the crack tip and the Heaviside function is used to enrich the nodes far from the crack tip (fig. 2.15). The asymptotic functions are constructed based on the Westergaard's analytical solution [WESTERGAARD, 1939].

EFEM vs. XFEM Comparative studies between EFEM and XFEM have been carried out in [JIRÁSEK and BELYTSCHKO, 2002] and [OLIVER et al., 2006]. The differences between the two methods lies in both the modeling and computational aspects. Following [JIRÁSEK and BELYTSCHKO, 2002], a one-dimensional example is chosen to demonstrate the differences between the two methods.

Let us consider a discontinuity Γ_d which divides the discretized 1D domain in to two parts (fig. 2.16). Let the part right of the discontinuity be influenced by it. The EFEM enhancement functions are constructed such that the value of the function is equal to 1 at the discontinuity and 0 at the all the other nodes in the right side of the discontinuity. Consequently, the enhancement is non-conforming and the obtained displacement jump is discontinuous along the elements. In contrast to this, the enrichment functions in XFEM are designed using the shape functions of nodes in the right side of the discontinuity such that the displacement jump is non-zero at the respective nodes. Consequently, the obtained displacement jump is continuous along the elements except at the discontinuity. Various aspects of EFEM and XFEM are compared in the table 2.1.

While the discontinuous kinematics models can provide the explicit description of cracking, they cannot capture the initial anisotropic damage during the strain localization process. Also, the crack directions for multiple cracks during complex loading are not accurate using the explicit models [JIRÁSEK and ZIMMERMANN, 2001].

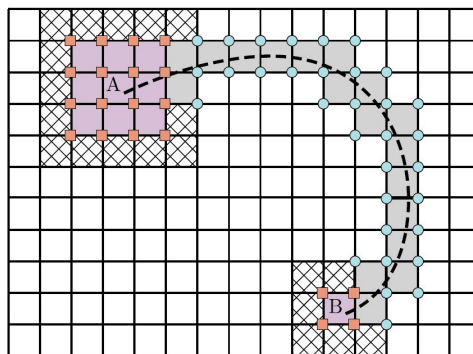


Figure 2.15: Enrichment in XFEM: nodes enriched using asymptotic function (red squares) and nodes enriched using Heaviside function (blue circles) [BELYTSCHKO et al., 2009]

	XFEM	EFEM	
modeling aspects	global	local	
	nodal	elemental	
	continuous	discontinuous	
computational aspects	not performed	performed	
	modified	standard	
	increases	remains the same	
	increases	remains the same	
	higher	lower	
	additional DOFs support crack path		
	static condensation integration scheme number of equations (relative to elastic computations) half band width of the stiffness matrix (relative to elastic computations) absolute computational time		

Table 2.1: Comparison between various aspects of XFEM and EFEM [JIRÁSEK and BELYTCHIKO, 2002]

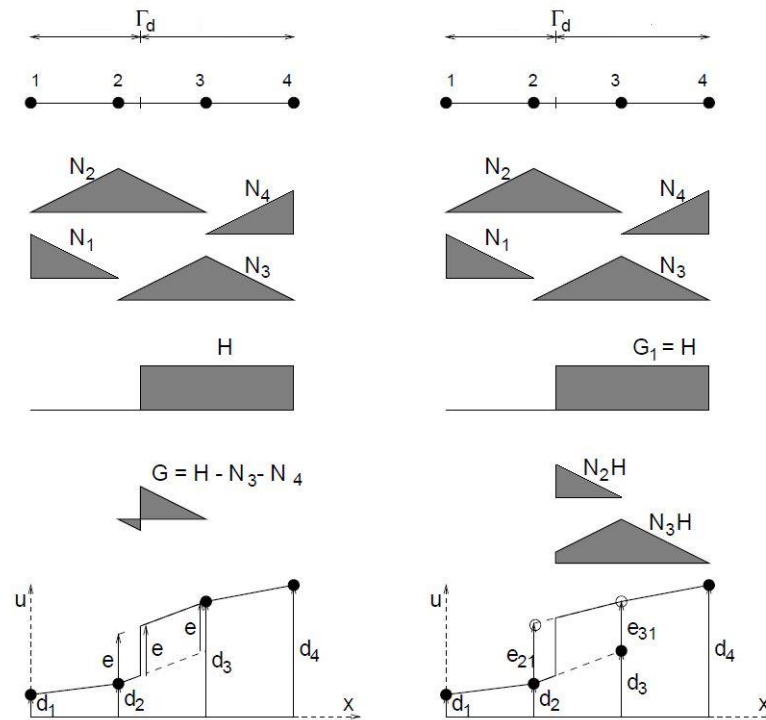


Figure 2.16: Enrichment function: EFEM (right) and XFEM (left) [JIRÁSEK and BELYTSCHKO, 2002]

In the literature, several models that performs a transition from implicit description of cracking to explicit description of cracking are proposed [MAZARS and PIJAUDIER-CABOT, 1996, JIRÁSEK and ZIMMERMANN, 2001, SIMONE et al., 2003, COMI et al., 2002, COMI et al., 2007, CUVILLIEZ et al., 2012, CAZES et al., 2009, ROTH et al., 2015, SAKSALA et al., 2015] to describe the entire strain localization process from localized damage to the initiation and propagation of cracks.

2.4 Transition from implicit to explicit descriptions of cracking

2.4.1 Experimental motivation

Experimental investigation to study the fracture growth from the localized damage to the crack opening is conducted in [ALAM and LOUKILI, 2017]. In this experimental campaign, three point bending tests are performed on single notched beams as shown in fig. 2.17a. The information regarding the energy dissipation in the localized damage zone is obtained using Acoustic Emission (AE) while Digital Image Correlation (DIC) technique is used to obtain the COD. The plot of AE energy rate for different relative crack lengths (distance from the bottom of the beam) is shown in fig. 2.17b.

According to [ALAM and LOUKILI, 2017], the following 3 phases can be identified during the failure process of the concrete: (i) the damage growth phase, where the AE energy rate increases due to the progressive increase in microcrack density; (ii) the transition phase, between 90% pre-peak load and 80% post-peak load, where the AE energy rate reaches a maximum value; (iii) the crack opening phase, where the AE energy rate decreases.

This gives a physical motivation for a modeling strategy of strain localization process with transition from localized damage zone to initiation and propagation of multiple cracks.

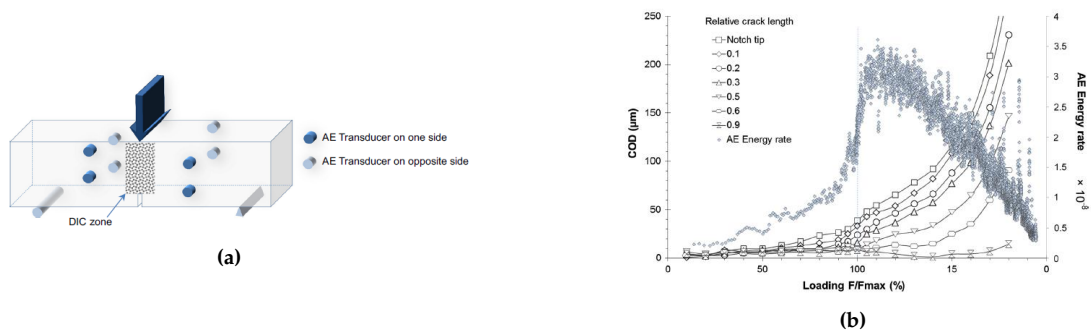


Figure 2.17: Experimental investigation of fracture growth (localized damage/crack opening) in a single notched beam: set up (a) and simultaneous behavior of crack openings and AE energy dissipation with loading steps (b) [ALAM and LOUKILI, 2017]

In literature, several transition methodologies are proposed to model the initial phase of damage using the implicit description of cracking and perform a transition to explicit description of cracking to model the crack opening which are presented in the next section.

2.4.2 Numerical transition methodologies

In [MAZARS and PIJAUDIER-CABOT, 1996], an equivalent crack is introduced in the given damage zone using the concept of ‘energetic equivalence’ within the framework of Linear Elastic Fracture Mechanics (LEFM). The main idea here is that the fracture energy required to create the equivalent crack is calculated using the energy dissipated during the formation of damage zone.

In later works [CAZES et al., 2009, COMI et al., 2007, ROTH et al., 2015, CAZES et al., 2009, CUVILLIEZ et al., 2012], the approach of energetic equivalence is followed to introduce a cohesive crack in the localized damage zone.

Even though the energetic equivalence is used in transition methodologies, different numerical strategies [WU et al., 2014] are developed to enforce it either strongly or in a weak manner. The main difference of these strategies lies in the way in which the corresponding cohesive law at the crack after transition is formulated.

2.4.2.1 Weak energetic equivalence enforcement

In this approach [COMI et al., 2007, ROTH et al., 2015, WU et al., 2014], the shape of the cohesive law at the crack surface is predefined and the unknowns to be determined are the parameters of cohesive law such as the fracture energy per unit area of the crack surface. These parameters are determined by enforcing the energetic equivalence over the entire pseudo-time, $t \in [0, \infty)$ domain either using 1D or multi-directional considerations. The relations between the total energy dissipated in the domain by the implicit (Φ_{imp}), explicit (Φ_{exp}) and coupled models ($\Phi_{imp/exp}$) obtained by using the energy equivalence are [WANG and WAISMAN, 2016]:

$$\Phi_{imp} = \Phi_{exp} = \Phi_{imp/exp} \quad (2.24)$$

Based on 1D considerations In [COMI et al., 2007], a nonlocal damage model is used for the description of diffused damage while a cohesive crack is introduced in the framework of XFEM. The energy available for the cohesive law is computed from the dissipated energy in the localization band in a 1D setting and the corresponding stored elastic energy. A similar approach is also followed in [ROTH et al., 2015] where a continuum damage model is used to model the

initial localized damage zone and the residual energy is computed analytically by equating the area under the uniaxial stress–strain curve to that of the cohesive law.

In another work [WU et al., 2014], a transition methodology coupling the nonlocal implicit discontinuous Galerkin model to cohesive crack approach using the interface elements is proposed. In this work, a relationship between the damage level and the available energy to be dissipated at the crack surface is established using 1D assumption.

Here, the cohesive law which is formulated in 1D setting is used for 2D problems where the cracks exhibit mode I behavior [COMI et al., 2007, ROTH et al., 2015, WU et al., 2014] and propagate in a straight manner. This may lead to a mismatch between the global response using the model based on implicit description of cracking and that of the transition methodology [WANG and WAISMAN, 2016].

Based on multi-directional considerations On the other hand, a more general transition methodology is proposed in [WANG and WAISMAN, 2016] to handle the cases involving propagation of curved cracks and mixed mode behavior. In [CAZES et al., 2016], a thermodynamically consistent approach is developed to couple the models based on implicit and explicit descriptions of cracking. In these works, both the energy dissipation in the localization band and the available energy at the crack are computed by considering a multi-directional stress/strain states.

2.4.2.2 Strong energetic equivalence enforcement

In another approach, as introduced in [CUVILLIEZ et al., 2012], the shape of the cohesive law at the crack surface is not predefined. But it is obtained by enforcing the energy equivalence at each pseudo-time step.

In the same work, a gradient damage model is used to describe the damage growth, and transition is performed after the regularized damage parameter reaches a certain limit. Also, the cohesive law is obtained using the relations in 1D setting and the framework is extended for 2D problems under mode I crack opening. Here, only parameters required are the ones of the model used to describe the implicit description of cracking. However, the main advantage of this approach is that global responses obtained using continuous and discontinuous (after transition) models has a perfect match [WU et al., 2014, CUVILLIEZ et al., 2012].

The continuous, discontinuous approaches and transition criteria used in several transition methodologies from literature are summarized in the table 2.2.

2.5 Summary

When concrete is subjected to cycling loading, stiffness degradation, unilateral effect and crack induced anisotropy are observed. In order to predict the response of a plain or reinforced concrete structures under cyclic loading, these behavioral features should be take into account.

Of various models based on implicit description of cracking, microplane models are particularly interesting because these models provide a simple way of developing constitutive laws between components of stress and strain vectors in several possible directions instead of tensors. This way of modeling material behavior is very promising to handle anisotropy due to cracking. Of various models based on explicit description of cracking, EFEM is computationally effective and requires low implementation effort.

Furthermore, the models based on implicit description of cracking are well suitable to model the initial phase of diffused microcracking and models based on explicit description are capable of modeling crack initiation and propagation. A detailed study on the transition models suggests

Table 2.2: Various examples of transition framework

	continuous approach	discontinuous approach	transition criterion
[JIRÁSEK and ZIMMERMANN, 2001]	smeared crack	EFEM	equivalent crack opening
[SIMONE et al., 2003]	gradient-enhanced continuum damage	XFEM	damage variable
[COMI et al., 2002, COMI et al., 2007]	integral nonlocal damage	XFEM	damage variable
[CUVILLIEZ et al., 2012]	gradient damage	cohesive zone	damage variable
[SAKSALA et al., 2015]	continuum viscodamage consistency	EFEM	damage strain
[ROTH et al., 2015]	anisotropic damage	XFEM	damage variable
[WU et al., 2014]	nonlocal implicit discontinuous Galerkin	cohesive zone	effective stress
[WANG and WAISMAN, 2016]	nonlocal	XFEM	damage

that both implicit and explicit descriptions of cracking can be coupled to model the complete strain localization process. Hence, in this work, microplane models are considered to model anisotropic damage and EFEM is considered to model multiple cracks by coupling them in a transition framework.

Strong discontinuity kinematics and embedded finite element method

Abstract. In this chapter, we describe in detail the modeling of media crossed by cracks using the strong discontinuity approach in the framework of the EFEM. In the standard EFEM, a single discontinuity per element is allowed to appear, which limits its applicability for the cases involving multiple cracks. So, the purpose of this chapter is to propose a possible extension of the standard EFEM into model multiple intersecting cracks within the same finite element.

3.1 Introduction

First, the kinematics of strong discontinuity is presented in section 3.2. This is followed by a discussion on strong discontinuity approaches available in the literature to derive the constitutive relationships for the crack. The Boundary Value Problem (BVP) taking into account the strong discontinuity framework is presented in section 3.4.

The numerical solution procedure of this BVP in the context of EFEM involves in writing the variational form of the governing equilibrium equations in a non-classical manner. This is obtained in the framework of enhanced assumed strain method. This is presented in section 3.5.1 along with the FE discretization. Numerical resolution scheme to solve the discretized equilibrium equations is presented in section 3.5.2. The representative example to illustrate the methodology of EFEM is presented in section 3.5.3.

The framework of multiple intersecting strong discontinuities is presented in section 3.6. First the assumptions involved in the extension of the standard framework is presented which is followed by the kinematics and the augmented BVP for continuum with multiple intersecting strong discontinuities. The EAS formulation and the EFEM are revisited, taking into account the multiple discontinuity jumps in section 3.6.3.

Numerical examples to show that the extended EFEM is able to tackle the localization of multiple cracks are presented in section 3.6.5. Finally, the conclusions of the proposed methodology for modeling multiple intersecting cracks are drawn in section 3.7.

3.2 Kinematics of strong discontinuity

Let us consider a body $\mathcal{B} \subset \mathbb{R}^{n_{dim}}$ which is in quasi-static equilibrium, and denote by \mathbf{x} the material points in \mathcal{B} . Here, $n_{dim} = 1, 2, 3$ for one, two and three dimensional continuum respectively. Let $\partial\mathcal{B} \subset \mathbb{R}^{n_{dim}}$ be the boundary of \mathcal{B} and denote with \mathbf{p} its outer normal vector.

The kinematic response at any material point $\mathbf{x} \in \mathcal{B}$ is characterized by an infinitesimal displacement field, $\mathbf{u} = \mathbf{u}(\mathbf{x}, t) : \mathcal{B} \times [0, \infty) \mapsto \mathbb{R}^{n_{dim}}$. We define the infinitesimal strain tensor $\epsilon = \epsilon(\mathbf{x}, t) : \mathcal{B} \times [0, \infty) \mapsto \mathbb{R}^{n_{dim} \times n_{dim}}$ (state variable introduced in section 2.2) as the symmetric part of the gradient of displacement ($\nabla^s \mathbf{u}$) at \mathbf{x} . Also, its conjugate variable (eq. (2.2)), is taken as the symmetric Cauchy stress tensor, $\sigma = \sigma(\mathbf{x}, t) : \mathcal{B} \times [0, \infty) \mapsto \mathbb{R}^{n_{dim} \times n_{dim}}$.

In the absence of the body forces, let us consider an applied traction $\mathbf{t}_0 = \mathbf{t}_0(\mathbf{x}, t) : \partial_t \mathcal{B} \times [0, \infty) \mapsto \mathbb{R}^{n_{dim}}$ and displacement $\mathbf{u}_0 = \mathbf{u}_0(\mathbf{x}, t) : \partial_u \mathcal{B} \times [0, \infty) \mapsto \mathbb{R}^{n_{dim}}$. Here, $\partial_t \mathcal{B} \subset \partial \mathcal{B}$ and $\partial_u \mathcal{B} \subset \partial \mathcal{B}$ are the parts of the boundary, where \mathbf{t}_0 and \mathbf{u}_0 are prescribed respectively. These subsets are defined such that $\partial_t \mathcal{B} \cup \partial_u \mathcal{B} = \mathcal{B}$ and $\partial_t \mathcal{B} \cap \partial_u \mathcal{B} = \emptyset$.

Now, let us suppose that \mathcal{B} is crossed by a crack surface/line $\Gamma_d \in \mathbb{R}^{n_{dim}}$ (fig. 3.1), whose normal is denoted by \mathbf{n} and tangent by \mathbf{s} (i.e., $\mathbf{s} \cdot \mathbf{n} = 0$). Here, Γ_d divides the domain into two sub-domains \mathcal{B}^+ and \mathcal{B}^- .

The inclusion of Γ_d introduces a jump in the displacement field, $[[\mathbf{u}]] = [[\mathbf{u}]](\mathbf{x}, t) : \mathcal{B} \times [0, \infty) \mapsto \mathbb{R}^{n_{dim}}$. The enhanced displacement, by taking into account the motion at the discontinuity, is thus given by:

$$\mathbf{u} = \bar{\mathbf{u}} + H_{\Gamma_d} [[\mathbf{u}]] \quad (3.1)$$

where, $\bar{\mathbf{u}} = \bar{\mathbf{u}}(\mathbf{x}, t) : \mathcal{B} \times [0, \infty) \mapsto \mathbb{R}^{n_{dim}}$ is the continuous part of the displacement field, and $H_{\Gamma_d} = H_{\Gamma_d}(\mathbf{x})$ is the Heaviside function centered on Γ_d :

$$H_{\Gamma_d} = \begin{cases} 0 & \forall \mathbf{x} \in \mathcal{B}^- \\ 1 & \forall \mathbf{x} \in \mathcal{B}^+ \end{cases} \quad (3.2)$$

Under the small perturbations assumption, the strain field compatible to the displacement field presented above is given by:

$$\epsilon = \underbrace{\nabla^s \bar{\mathbf{u}} + H_{\Gamma_d} \nabla^s [[\mathbf{u}]]}_{\text{regular part}} + \underbrace{\delta_{\Gamma_d} ([[\mathbf{u}]]) \otimes \mathbf{n}}_{\text{singular part}} \quad (3.3)$$

where, $\delta_{\Gamma_d} = \delta_{\Gamma_d}(\mathbf{x})$ is the Dirac's delta distribution appearing from the gradient of the Heaviside function, $(\bullet)^s$ denotes the symmetric part of tensor (\bullet) and symbol ' \otimes ' denotes the dyadic product between second order tensors. As it can be seen from eq. (3.3), the strain field has a regular part which is bounded and a singular part which is unbounded. Let us denote the bounded strains in the remaining of this work by:

$$\bar{\epsilon} = \nabla^s \bar{\mathbf{u}} + H_{\Gamma_d} \nabla^s [[\mathbf{u}]] \quad (3.4)$$

From now on, the implicit dependence on (\mathbf{x}, t) is considered by default and is not shown unless otherwise.

3.3 Strong discontinuity approach

Due to the singularity introduced by δ_{Γ_d} in the strain field, it is not straightforward to define constitutive relationships. This comes from the fact that σ has to be bounded to satisfy the equilibrium even though ϵ is unbounded. There are two approaches to define the constitutive relationships for both the bulk and the discontinuity. They are briefly described here.

Continuum Strong Discontinuity Approach (CSDA) The first approach consists in deriving the discrete constitutive equations at the discontinuity level using the continuum constitutive

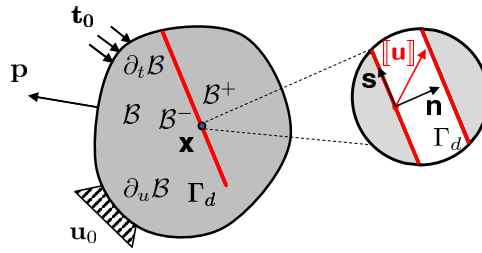


Figure 3.1: Strong discontinuity kinematics - a body (\mathcal{B}) crossed by discontinuity Γ_d

law [ARMERO and GARIKIPATI, 1995, OLIVER et al., 1999, OLIVER, 2000]. First, a collocation function, $\mu_{\Gamma_{d_k}} = \mu_{\Gamma_{d_k}}(\mathbf{x})$ is defined on a band (Γ_{d_k}) of width k and centered on Γ_d :

$$\mu_{\Gamma_{d_k}} = \begin{cases} 0 & \forall \mathbf{x} \in \mathcal{B} \setminus \Gamma_{d_k} \\ 1 & \forall \mathbf{x} \in \Gamma_{d_k} \end{cases} \quad (3.5)$$

This allows regularizing the Dirac's delta function using k as:¹

$$\delta_{\Gamma_{d_k}}(\mathbf{x}) = \lim_{k \rightarrow 0} \frac{1}{k} \mu_{\Gamma_{d_k}}(\mathbf{x}) \quad (3.6)$$

and to write the k -regularized strain field as:

$$\epsilon = \bar{\epsilon} + \frac{1}{k} \mu_{\Gamma_{d_k}}([\mathbf{u}] \otimes \mathbf{n}) \quad (3.7)$$

The continuum constitutive law is then defined in terms of the k -regularized strain (eq. (3.7)). The criterion for localization and the direction of the discontinuity are obtained from the bifurcation analysis. Finally, the 'strong discontinuity analysis' is performed to derive the discrete constitutive law at the discontinuity surface from the continuum one using the limit condition $k \rightarrow 0$ (localization of discontinuity). Thus, there is a consistency between the constitutive laws at the bulk and that of the discontinuity surface. It has to be noted that in this approach, the volumetric energy dissipation takes place before the surface energy dissipation begins.

Discrete Strong Discontinuity Approach (DSDA) In this approach, the discontinuity is treated as a discrete surface in the continuum [WELLS and SLUYS, 2001, BRANCHERIE, 2003]. The crack initiates when an assumed criterion is reached and the discrete constitutive law at the discontinuity is defined independently from the continuum constitutive law. As a consequence, the consistency between both the constitutive laws is not ensured as in the previous case of CSDA.

The equivalence between the two approaches can be shown [BRANCHERIE, 2003] if the continuum is assumed to be elastic (i.e., $\sigma = \mathbb{E} : \epsilon$ with \mathbb{E} the fourth-order elastic stiffness tensor) prior to the crack initiation. In this case, the energy dissipation takes place only at the discontinuity surface. Hence, the discrete constitutive law obtained either by performing strong discontinuity analysis or by following DSDA coincides.

In this chapter, DSDA is followed and the crack is initiated when the maximum principal stress reaches the tensile strength of the material (f_t).

3.4 Boundary value problem

In a general continuum mechanics context, the Boundary Value Problem (BVP) to be solved consists of finding the displacement field \mathbf{u} which satisfies the equilibrium equations, compatibility

¹The strong discontinuity regime is reached as $k \rightarrow 0$.

conditions and constitutive relationship along with the given displacement and traction boundary conditions.

In the presence of a strong discontinuity, the enhanced kinematics and the traction continuity condition across the crack have to be taken into account. Hence, an augmented BVP is written as follows:

$$\begin{cases} \operatorname{div} \boldsymbol{\sigma} = 0 & \text{on } \mathcal{B} & (3.8a) \\ \boldsymbol{\epsilon} = \nabla^s \mathbf{u} & \text{on } \mathcal{B} & (3.8b) \\ \boldsymbol{\sigma} = \mathcal{F}(\boldsymbol{\epsilon}) & \text{on } \mathcal{B} & (3.8c) \\ \mathbf{u} = \mathbf{u}_0 & \text{on } \partial_u \mathcal{B} & (3.8d) \\ \boldsymbol{\sigma} \cdot \mathbf{p} = \mathbf{t}_0 & \text{on } \partial_t \mathcal{B} & (3.8e) \\ \boldsymbol{\sigma} \cdot \mathbf{n} = \mathbf{t} & \text{on } \Gamma_d & (3.8f) \\ \mathbf{t} = h(\llbracket \mathbf{u} \rrbracket) & \text{on } \Gamma_d & (3.8g) \end{cases}$$

where, 'div' denotes the divergence operator, \mathcal{F} denotes a constitutive relation between $\boldsymbol{\sigma}$ and $\boldsymbol{\epsilon}$ (eventually expressed in the rate form), \mathbf{t} is the traction vector on the discontinuity surface, and h is the discrete constitutive law written in terms of \mathbf{t} and $\llbracket \mathbf{u} \rrbracket$. Other quantities are defined in fig. 3.1.

The augmentation comes from the fact that along with the global equilibrium eq. (3.8a), the traction continuity condition (3.8f) is to be fulfilled across the crack to ensure the local equilibrium. Finally, h is the traction–separation law (3.8g) that drives the evolution of the traction with respect to the displacement jump at the discontinuity.

Traction–separation law Following [ALFAIATE et al., 2001], a constitutive law at the discontinuity can be defined in the framework of thermodynamics of irreversible processes using an isotropic damage-like internal variable d_{cr} . The latter represents the degradation of the properties of the discontinuity, ranging between $-\infty$ (no crack) and 1 (fully opened cohesive crack).

The Helmholtz free energy at a surface, $\psi_S = \psi_S(\llbracket \mathbf{u} \rrbracket, d_{cr})$, available for the formation of crack is thus written as:

$$\psi_S = \frac{1}{2}(1 - d_{cr}) \llbracket \mathbf{u} \rrbracket \cdot \mathbf{K} \cdot \llbracket \mathbf{u} \rrbracket \quad (3.9)$$

where, \mathbf{K} is an elastic stiffness-like operator. Using standard continuum mechanics arguments, the traction vector at Γ_d depends on $\llbracket \mathbf{u} \rrbracket$ according to the following traction–separation law:

$$\mathbf{t} = \frac{\partial \psi_S}{\partial \llbracket \mathbf{u} \rrbracket} = (1 - d_{cr}) \mathbf{K} \cdot \llbracket \mathbf{u} \rrbracket \quad (3.10)$$

Now, if the principal stress axes are aligned with \mathbf{n} , then mode I crack opening takes place. Hence, only the normal component of the displacement jump ($\llbracket u \rrbracket_n = \mathbf{n} \cdot \llbracket \mathbf{u} \rrbracket$) and the traction ($\mathbf{n} \cdot \mathbf{t} = t_n(\llbracket u \rrbracket_n, d_{cr})$) evolves. In the cases in which the principal stress axes rotate after opening of the crack, mixed mode crack opening is evident. As a consequence, the tangential component of the displacement ($\llbracket u \rrbracket_s = \mathbf{s} \cdot \llbracket \mathbf{u} \rrbracket$) and the traction ($\mathbf{s} \cdot \mathbf{t} = t_s(\llbracket u \rrbracket_s, d_{cr})$) also evolves.

In order to handle these cases, a mixed mode traction–separation law is considered. The expression for the damage-like variable is given by [ALFAIATE et al., 2001]:

$$d_{cr} = 1 - \exp\left(-\frac{f_t}{G_f} \kappa_{cr}\right) \quad (3.11)$$

where, G_f is the fracture energy and κ_{cr} is an internal (history) variable. It is defined using the historical maxima of $\llbracket u \rrbracket_n$ and $\llbracket u \rrbracket_s$ as:

$$\kappa_{cr} = \max\langle \llbracket u \rrbracket_n \rangle^+ + \beta_{cr} \max |\llbracket u \rrbracket_s| \quad (3.12)$$

where, $\beta_{cr} \leq 1$ is a model parameter.

Finally, the Mohr–Coloumb like yield surface $f_{cr} = f_{cr}(\llbracket u \rrbracket_n, \llbracket u \rrbracket_s, \kappa_{cr})$ and the loading–unloading (Kuhn–Tucker) conditions are finally given as:

$$f_{cr} = \langle \llbracket u \rrbracket_n \rangle^+ + \beta_{cr} |\llbracket u \rrbracket_s| - \kappa_{cr} = 0 \quad (3.13)$$

$$\dot{\kappa}_{cr} \geq 0, \dot{f}_{cr} \leq 0, \dot{\kappa}_{cr} \dot{f}_{cr} = 0 \quad (3.14)$$

3.5 Embedded finite element method

In this section, the discretization procedure of the augmented BVP in the framework of embedded finite element method is presented. The variational form of the augmented BVP is derived using the Hu–Washizu variational principle [WASHIZU, 1955] in the framework of EAS method. Since the displacement jump is embedded inside a finite element in EFEM, the enhanced assumed strains are treated as local. Here, EAS method for one local enhancement corresponding to one crack is illustrated.

3.5.1 Enhanced assumed strain method

Variational form of the augmented BVP In EAS method, the enhanced kinematics of the continuum is taken into account by representing the discontinuous part of the strain field as enhanced strain ($\tilde{\epsilon}$) as follows:

$$\epsilon = \nabla^s \mathbf{u} + \tilde{\epsilon} \quad (3.15)$$

The Hu–Washizu variational principle consists in writing the variational forms of the equilibrium, kinematic and the constitutive equations individually. This is achieved by considering the virtual work done by the displacement field, actual stress field ($\tilde{\sigma}$) and the strain field independently.

Let us denote with $(\mathbf{u}^*, \epsilon^*, \tilde{\sigma}^*)$ the virtual variations corresponding to $(\mathbf{u}, \epsilon, \tilde{\sigma})$. The three-fields variational problem to be solved consist in finding $(\mathbf{u}, \epsilon, \tilde{\sigma}) \in (U, E, S)$ such that $\forall (\mathbf{u}^*, \epsilon^*, \tilde{\sigma}^*) \in (U_0, E, S)$,

$$\int_{\mathcal{B}} \nabla^s(\mathbf{u}^*) : \boldsymbol{\sigma}(\epsilon) dV - \int_{\partial_t \mathcal{B}} \mathbf{u}^* \cdot \mathbf{t}_0 dS = 0 \quad (3.16)$$

$$\int_{\mathcal{B}} \tilde{\sigma}^* : [\nabla^s \mathbf{u} - \epsilon] dV = 0 \quad (3.17)$$

$$\int_{\mathcal{B}} \epsilon^* : [-\tilde{\sigma} + \boldsymbol{\sigma}(\epsilon)] dV = 0 \quad (3.18)$$

where $\boldsymbol{\sigma}(\epsilon)$ is the stress in the continuum defined using the constitutive law (3.8c), and the admissibility spaces U, U_0, E and S are defined as:

$$U = \{ \mathbf{u} | \mathbf{u} \in H^1(\mathcal{B}), \mathbf{u} = \mathbf{u}_0 \text{ on } \partial_u \mathcal{B} \} \quad (3.19)$$

$$U_0 = \{ \mathbf{u} | \mathbf{u} \in H_0^1(\mathcal{B}), \mathbf{u} = 0 \text{ on } \partial_u \mathcal{B} \} \quad (3.20)$$

$$E = \{ \epsilon | \epsilon \in \mathcal{L}^2(\mathcal{B}) \} \quad (3.21)$$

$$S = \{ \tilde{\sigma} | \tilde{\sigma} \in \mathcal{L}^2(\mathcal{B}) \} \quad (3.22)$$

where $H^1(\mathcal{B})$ and $H_0^1(\mathcal{B})$ are first-order and homogeneous first-order Sobolev spaces of functions on \mathcal{B} respectively, and $\mathcal{L}^2(\mathcal{B})$ denotes the set of square-integrable functions on \mathcal{B} .

The virtual enhanced strain is given in terms of \mathbf{u}^* and $\tilde{\epsilon}^* \in E$ as:

$$\epsilon^* = \nabla^s(\mathbf{u}^*) + \tilde{\epsilon}^* \quad (3.23)$$

Substituting eqs. (3.15) and (3.23) in eqs. (3.17) and (3.18) we obtain:

$$\int_{\mathcal{B}} \tilde{\boldsymbol{\sigma}}^* : \tilde{\boldsymbol{\epsilon}} dV = 0 \quad (3.24)$$

$$\int_{\mathcal{B}} \nabla^s(\mathbf{u}^*) : [-\tilde{\boldsymbol{\sigma}} + \boldsymbol{\sigma}(\nabla^s \mathbf{u} + \tilde{\boldsymbol{\epsilon}})] dV + \int_{\mathcal{B}} \tilde{\boldsymbol{\epsilon}}^* : [-\tilde{\boldsymbol{\sigma}} + \boldsymbol{\sigma}(\nabla^s \mathbf{u} + \tilde{\boldsymbol{\epsilon}})] dV = 0 \quad (3.25)$$

We can eliminate eq. (3.24) by assuming that the enhanced strain field is orthogonal to the stress field [SIMO and RIFAI, 1990, WELLS and SLUYS, 2000], i.e., $\tilde{\boldsymbol{\epsilon}}$ belongs to space $E^{\perp S}$ such that $\tilde{\boldsymbol{\sigma}}^* : \tilde{\boldsymbol{\epsilon}} = 0 \forall \tilde{\boldsymbol{\sigma}}^* \in S$.

Finally, combining eqs. (3.16) and (3.25) the governing equations are:

$$\int_{\mathcal{B}} \nabla^s(\mathbf{u}^*) : \boldsymbol{\sigma}(\nabla^s \mathbf{u} + \tilde{\boldsymbol{\epsilon}}) dV - \int_{\partial_t \mathcal{B}} \mathbf{u}^* \cdot \mathbf{t}_0 dS = 0 \quad (3.26)$$

$$\int_{\mathcal{B}} \tilde{\boldsymbol{\epsilon}}^* : \boldsymbol{\sigma}(\nabla^s \mathbf{u} + \tilde{\boldsymbol{\epsilon}}) dV = 0 \quad (3.27)$$

Finite element approximation Now, let us consider the finite element discretization $\mathcal{B}^h \subset \mathcal{B}$, composed by n_{elem} non-overlapping finite elements \mathcal{B}_e^h such that:

$$\mathcal{B}^h = \cup_{e=1}^{n_{elem}} \mathcal{B}_e^h \quad (3.28)$$

In general, the inter element connectivity is not imposed on the stress and strain fields which allows to introduce the required enhancements locally in a finite element. Hence, the corresponding discretized displacement field consists of the nodal DOFs (\mathbf{d}) and the elemental enhanced displacement field (\mathbf{e}). Let \mathcal{E}^h denotes the set of finite elements that are crossed by the discontinuity.

Now, consider that Γ_d divides the finite element $\mathcal{B}_e^h \in \mathcal{E}^h$ into two sub-domains $(\mathcal{B}_e^h)^+$ and $(\mathcal{B}_e^h)^-$ such that \mathbf{n} is inward $(\mathcal{B}_e^h)^+$ (fig. 3.2). The finite element approximation of \mathbf{u} is constructed as:

$$\mathbf{u} = \sum_{a \in \mathcal{B}_e^h} \mathbf{N}_a \mathbf{d}_a + \mathbf{N}_c \mathbf{e} \quad (3.29)$$

where, \mathbf{N}_a denotes the elementary shape functions matrix and \mathbf{N}_c is the shape functions matrix for the enhanced displacement field. Following the standard EFEM [SIMO et al., 1993, OLIVER, 1996b], \mathbf{N}_c is chosen as:

$$\mathbf{N}_c = \mathbf{H}_{\Gamma_d} - \sum_{a \in (\mathcal{B}_e^h)^+} \mathbf{N}_a \quad (3.30)$$

where, \mathbf{H}_{Γ_d} is a matrix formed using the Heaviside function (3.2). For the sake of simplicity, we remove the subscript a for the nodal DOFs and interpolation functions.

The finite element approximation of $\boldsymbol{\epsilon}$ is obtained as:

$$\boldsymbol{\epsilon} = \mathbf{Bd} + \mathbf{Ge} \quad (3.31)$$

where, \mathbf{B} is the standard strain-displacement matrix (i.e., the gradient matrix of \mathbf{N}), and \mathbf{G} is the interpolation matrix of the enhanced strain. Using the orthogonality condition between spaces E and S , it can be shown [SIMO and RIFAI, 1990, JIRÁSEK, 2000] that \mathbf{G} is required to fulfill the zero mean condition over \mathcal{B}_e^h (i.e., to pass the so-called patch-test).

The approximations of the variational fields \mathbf{u}^* and $\boldsymbol{\epsilon}^*$ are accordingly given by:

$$\mathbf{u}^* = \mathbf{Nd}^* + \mathbf{N}_c \mathbf{e}^* \quad (3.32)$$

$$\boldsymbol{\epsilon}^* = \mathbf{Bd}^* + \underbrace{\mathbf{G}^* \mathbf{e}^*}_{\tilde{\boldsymbol{\epsilon}}^*} \quad (3.33)$$

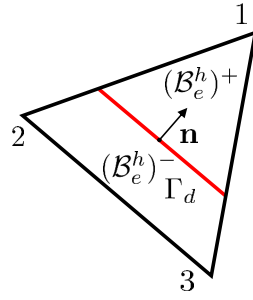


Figure 3.2: EFEM - a finite element $(\mathcal{B}_e^h \in \mathcal{E})$ with a discontinuity Γ_d

where, \mathbf{G}^* is the interpolation matrix of the virtual enhanced strain field.

Substituting eqs. (3.31) to (3.33) in eqs. (3.26) and (3.27), we obtain:

$$\mathbf{d}^* \left(\int_{\mathcal{B}} \mathbf{B}^\top \boldsymbol{\sigma}(\mathbf{B}\mathbf{d} + \mathbf{G}\mathbf{e}) dV - \int_{\partial_t \mathcal{B}} \mathbf{N}^\top \mathbf{t}_0 dS \right) + \mathbf{e}^* \left(\int_{\mathcal{B}} \mathbf{B}^\top \boldsymbol{\sigma}(\mathbf{B}\mathbf{d} + \mathbf{G}\mathbf{e}) dV - \int_{\partial_t \mathcal{B}} \mathbf{N}_c^\top \mathbf{t}_0 dS \right) = 0 \quad (3.34)$$

and

$$\mathbf{e}^* \left(\int_{\mathcal{B}} \mathbf{G}^* \boldsymbol{\sigma}(\mathbf{B}\mathbf{d} + \mathbf{G}\mathbf{e}) dV \right) = 0 \quad (3.35)$$

Here, we assume that the $\partial_t \mathcal{B} \cap \Gamma_d = \emptyset$, i.e., no traction is imposed on the Γ_d . For arbitrary variations, the governing equations are finally obtained as:

$$\left\{ \begin{array}{l} \int_{\mathcal{B}} \mathbf{B}^\top \boldsymbol{\sigma}(\mathbf{B}\mathbf{d} + \mathbf{G}\mathbf{e}) dV = \mathbf{F}_{ext} \\ \int_{\mathcal{B}} \mathbf{G}^* \boldsymbol{\sigma}(\mathbf{B}\mathbf{d} + \mathbf{G}\mathbf{e}) dV = 0 \end{array} \right. \quad (3.36a)$$

$$\left\{ \begin{array}{l} \int_{\mathcal{B}} \mathbf{B}^\top \boldsymbol{\sigma}(\mathbf{B}\mathbf{d} + \mathbf{G}\mathbf{e}) dV = \mathbf{F}_{ext} \\ \int_{\mathcal{B}} \mathbf{G}^* \boldsymbol{\sigma}(\mathbf{B}\mathbf{d} + \mathbf{G}\mathbf{e}) dV = 0 \end{array} \right. \quad (3.36b)$$

where, \mathbf{F}_{ext} is the standard external force vector given by:

$$\mathbf{F}_{ext} = \int_{\partial_t \mathcal{B}} \mathbf{N}^\top \mathbf{t}_0 dS \quad (3.37)$$

Interpolation operators Depending on the type of discontinuity and the chosen method for fulfillment of traction continuity condition, \mathbf{G} and \mathbf{G}^* matrices can be constructed in three different ways as described in [JIRÁSEK, 2000, CAZES et al., 2016]. In particular:

- (i) the case in which \mathbf{G} and \mathbf{G}^* are constructed such as the zero mean condition is satisfied without considering \mathbf{N}_c is known as, *Statically Optimal Symmetric* (SOS) formulation. In this case, even though the traction continuity condition is satisfied, the kinematics of strong discontinuity is not well represented;
- (ii) in order to represent the kinematics correctly, the gradient matrix \mathbf{B}_c can be chosen for both \mathbf{G} and \mathbf{G}^* matrices. But this results in the traction continuity condition expressed between the traction at Γ_d and the nodal forces of the nodes belonging to $(\mathcal{B}_e^h)^+$ which does not ensure equilibrium in complex deformation modes. This formulation is known as *Kinematically Optimal Symmetric* (KOS) formulation;

- (iii) alternatively, we can choose $\mathbf{G} = \mathbf{B}_c$ matrix and another matrix constructed from the functions that satisfies the zero mean over the finite element can be chosen for \mathbf{G}^* . This formulation is known as the *Statically and Kinematically Optimal Nonsymmetric* (SKON) formulation which takes into account both the kinematics of strong discontinuity and the traction continuity in a well manner.

In this work, the SKON approach is followed and the interpolation functions \mathbf{G} and \mathbf{G}^* are chosen as:

$$\mathbf{G} = \mathbf{P}\delta_{\Gamma_d} - \sum_{a \in (\mathcal{B}_e^h)^+} \mathbf{B}_a \quad (3.38)$$

$$\mathbf{G}^* = \left(\delta_{\Gamma_d} - \frac{\text{meas}(\Gamma_d)}{\text{meas}(\mathcal{B}_e^h)} \right) \mathbf{P} \quad (3.39)$$

where, \mathbf{P} is a projection operator given by:

$$\mathbf{P} = \begin{bmatrix} n_1 & 0 \\ 0 & n_2 \\ n_2 & n_1 \end{bmatrix} \quad (3.40)$$

with, $[n_1, n_2]$ denoting the components of vector \mathbf{n} in the orthonormal basis $R(\mathbf{x}_1, \mathbf{x}_2)$, and 'meas(\bullet)' representing the measure of (\bullet).

The following property holds true for a given function $z(\mathbf{x})$ defined on \mathcal{B} ,

$$\int_{\mathcal{B}} \delta_{\Gamma_d} z(\mathbf{x}) dV = \int_{\Gamma_d} z_{\Gamma_d} dS \quad (3.41)$$

where, z_{Γ_d} is the value of the function on the discontinuity.

Here, we assume that the traction is constant across the element. We then substitute eqs. (3.38) and (3.39) in eqs. (3.36a) and (3.36b), and use the relation (3.41), to obtain the final global and local equilibrium equations (using the assembly operator \mathbf{A}):

$$\begin{cases} \mathbf{A} \int_{\mathcal{B}_e} \mathbf{B}^T \boldsymbol{\sigma}(\mathbf{B}\mathbf{d} + \mathbf{G}\mathbf{e}) dV = \mathbf{F}_{ext} & (3.42a) \\ \mathbf{t}(\mathbf{e}) - \int_{\mathcal{B}_e^h} \frac{1}{\text{meas}(\mathcal{B}_e^h)} \mathbf{P}^T \boldsymbol{\sigma}(\mathbf{B}\mathbf{d} + \mathbf{G}\mathbf{e}) dV = 0 \quad \forall \mathcal{B}_e^h \in \mathcal{E} & (3.42b) \end{cases}$$

3.5.2 Numerical resolution

In this section the numerical resolution of the governing equilibrium equations is presented. First, the static condensation procedure to obtain the global solution is presented in the framework of the incremental iterative scheme. Later, the so called 'operator split method' for the solution of the local equilibrium equation is presented.

3.5.2.1 Incremental iterative scheme

The governing discretized equilibrium eqs. (3.42a) and (3.42b) are solved using an incremental iterative scheme. In this procedure, the pseudo-time domain is discretized according to a sequence of N pseudo-time instants $\{t^i\}_{i=1}^N$ such that $t^{n+1} = t^n + \Delta t$, with Δt being a pseudo-time step. The evolution of the external load is then applied in increments ($\Delta \mathbf{F}_{ext}^{n+1}$) with respect to the discretized pseudo-time t^{n+1} as:

$$\mathbf{F}_{ext}^{n+1} = \mathbf{F}_{ext}^n + \Delta \mathbf{F}_{ext}^{n+1} \quad (3.43)$$

Next, the unknown increments $\Delta \mathbf{d}^{n+1}$ and $\Delta \mathbf{e}^{n+1}$ obtained by solving the discrete system of eqs. (3.42a) and (3.42b), for the given $\Delta \mathbf{F}_{ext}^{n+1}$, and the solution at t^{n+1} is updated as:

$$\mathbf{d}^{n+1} = \mathbf{d}^n + \Delta \mathbf{d}^{n+1} \quad (3.44)$$

$$\mathbf{e}^{n+1} = \mathbf{e}^n + \Delta \mathbf{e}^{n+1} \quad (3.45)$$

In general, eqs. (3.42a) and (3.42b) are non-linear. Hence, the increments of the solution fields are obtained using an iterative procedure. Here, we adopt a modified Newton method for each pseudo-time step. The solution increments at iteration $i + 1$ and time increment t^{n+1} is given by:

$$\Delta \mathbf{d}^{n+1,i+1} = \Delta \mathbf{d}^{n+1,i} + \delta \mathbf{d}^{n+1,i+1} \quad (3.46)$$

$$\Delta \mathbf{e}^{n+1,i+1} = \Delta \mathbf{e}^{n+1,i} + \delta \mathbf{e}^{n+1,i+1} \quad (3.47)$$

where, $\delta \mathbf{d}^{n+1,i+1}$ and $\delta \mathbf{e}^{n+1,i+1}$ are the solution increments between iterations i and $i + 1$, whereas $\Delta \mathbf{d}^{n+1,i+1}$ and $\Delta \mathbf{e}^{n+1,i}$ are the solution increments at iteration i . From here-forth, the dependency on the time step is skipped for the sake of conciseness. As a consequence, every quantity without the upper-script $n + 1$ has to be intended as referred to t^{n+1} .

In order to obtain $(\delta \mathbf{d}^{n+1,i+1}, \delta \mathbf{e}^{n+1,i+1})$, we define the residuals of the global and local equilibrium equations at iteration $i + 1$ (for the sake of simplicity we remove the index $n + 1$) as follows:

$$\left\{ \begin{array}{l} \mathbf{R}(\mathbf{d}^{i+1}, \mathbf{e}^{i+1}) = \mathbf{A} \int_{e=1}^{n_{elem}} \mathbf{B}^\top \boldsymbol{\sigma}(\mathbf{d}^{i+1}, \mathbf{e}^{i+1}) dV - \mathbf{F}_{ext} \\ \mathbf{r}(\mathbf{d}^{i+1}, \mathbf{e}^{i+1}) = \mathbf{t}(\mathbf{e}^{i+1}) - \int_{\mathcal{B}_e^h} \frac{1}{\text{meas}(\mathcal{B}_e^h)} \mathbf{P}^\top \boldsymbol{\sigma}(\mathbf{d}^{i+1}, \mathbf{e}^{i+1}) dV \quad \forall \mathcal{B}_e^h \in \mathcal{E} \end{array} \right. \quad (3.48a)$$

$$\left\{ \begin{array}{l} \mathbf{R}(\mathbf{d}^{i+1}, \mathbf{e}^{i+1}) = \mathbf{R}(\mathbf{d}^i, \mathbf{e}^i) + \frac{\partial \mathbf{R}}{\partial \mathbf{d}} \Big|_{\mathbf{d}^i} \delta \mathbf{d}^{i+1} + \frac{\partial \mathbf{R}}{\partial \mathbf{e}} \Big|_{\mathbf{e}^i} \delta \mathbf{e}^{i+1} = 0 \\ \mathbf{r}(\mathbf{d}^{i+1}, \mathbf{e}^{i+1}) = \mathbf{r}(\mathbf{d}^i, \mathbf{e}^i) + \frac{\partial \mathbf{r}}{\partial \mathbf{d}} \Big|_{\mathbf{d}^i} \delta \mathbf{d}^{i+1} + \frac{\partial \mathbf{r}}{\partial \mathbf{e}} \Big|_{\mathbf{e}^i} \delta \mathbf{e}^{i+1} = 0 \end{array} \right. \quad (3.48b)$$

Now, we minimize the residuals at the iteration $i + 1$ using the solution $(\mathbf{d}^i, \mathbf{e}^i)$ at non-converged iteration i (i.e., corresponding to a non-equilibrium state) as follows:

$$\left\{ \begin{array}{l} \mathbf{R}(\mathbf{d}^{i+1}, \mathbf{e}^{i+1}) = \mathbf{R}(\mathbf{d}^i, \mathbf{e}^i) + \frac{\partial \mathbf{R}}{\partial \mathbf{d}} \Big|_{\mathbf{d}^i} \delta \mathbf{d}^{i+1} + \frac{\partial \mathbf{R}}{\partial \mathbf{e}} \Big|_{\mathbf{e}^i} \delta \mathbf{e}^{i+1} = 0 \\ \mathbf{r}(\mathbf{d}^{i+1}, \mathbf{e}^{i+1}) = \mathbf{r}(\mathbf{d}^i, \mathbf{e}^i) + \frac{\partial \mathbf{r}}{\partial \mathbf{d}} \Big|_{\mathbf{d}^i} \delta \mathbf{d}^{i+1} + \frac{\partial \mathbf{r}}{\partial \mathbf{e}} \Big|_{\mathbf{e}^i} \delta \mathbf{e}^{i+1} = 0 \end{array} \right. \quad (3.49a)$$

$$\left\{ \begin{array}{l} \mathbf{R}(\mathbf{d}^{i+1}, \mathbf{e}^{i+1}) = \mathbf{R}(\mathbf{d}^i, \mathbf{e}^i) + \frac{\partial \mathbf{R}}{\partial \mathbf{d}} \Big|_{\mathbf{d}^i} \delta \mathbf{d}^{i+1} + \frac{\partial \mathbf{R}}{\partial \mathbf{e}} \Big|_{\mathbf{e}^i} \delta \mathbf{e}^{i+1} = 0 \\ \mathbf{r}(\mathbf{d}^{i+1}, \mathbf{e}^{i+1}) = \mathbf{r}(\mathbf{d}^i, \mathbf{e}^i) + \frac{\partial \mathbf{r}}{\partial \mathbf{d}} \Big|_{\mathbf{d}^i} \delta \mathbf{d}^{i+1} + \frac{\partial \mathbf{r}}{\partial \mathbf{e}} \Big|_{\mathbf{e}^i} \delta \mathbf{e}^{i+1} = 0 \end{array} \right. \quad (3.49b)$$

Using the assembly operator, the linearized system of the global and local equilibrium equations is written as:

$$\left\{ \begin{array}{l} \mathbf{K}_{bb}^i \delta \mathbf{d}^{i+1} + \mathbf{K}_{bg}^i \delta \mathbf{e}^{i+1} = \mathbf{F}_{ext} - \mathbf{F}_{int}^i \\ \mathbf{K}_{gb}^i \delta \mathbf{d}^{i+1} + \mathbf{K}_{gg}^i \delta \mathbf{e}^{i+1} = \mathbf{f}_{int}^i \quad \forall \mathcal{B}_e^h \in \mathcal{E} \end{array} \right. \quad (3.50a)$$

$$\left\{ \begin{array}{l} \mathbf{K}_{bb}^i \delta \mathbf{d}^{i+1} + \mathbf{K}_{bg}^i \delta \mathbf{e}^{i+1} = \mathbf{F}_{ext} - \mathbf{F}_{int}^i \\ \mathbf{K}_{gb}^i \delta \mathbf{d}^{i+1} + \mathbf{K}_{gg}^i \delta \mathbf{e}^{i+1} = \mathbf{f}_{int}^i \quad \forall \mathcal{B}_e^h \in \mathcal{E} \end{array} \right. \quad (3.50b)$$

where,

$$\mathbf{K}_{bb}^i = \mathbf{A} \int_{e=1}^{n_{elem}} \mathbf{B}^\top \mathbf{C} \mathbf{B} dV \quad (3.51)$$

$$\mathbf{K}_{bg}^i = \int_{\mathcal{B}_e^h} \mathbf{B}^\top \mathbf{C} \mathbf{G} dV \quad (3.52)$$

$$\mathbf{F}_{int}^i = \mathbf{A} \int_{e=1}^{n_{elem}} \mathbf{B}^\top \boldsymbol{\sigma}(\mathbf{d}^i, \mathbf{e}^i) dV \quad (3.53)$$

$$\mathbf{K}_{gb}^i = - \int_{\mathcal{B}_e^h} \frac{1}{\text{meas}(\mathcal{B}_e^h)} \mathbf{P}^\top \mathbf{C} \mathbf{B} dV \quad (3.54)$$

$$\mathbf{K}_{gg}^i = \frac{\partial \mathbf{t}}{\partial \mathbf{e}} \Big|_{\mathbf{e}^i} - \int_{\mathcal{B}_e^h} \frac{1}{\text{meas}(\mathcal{B}_e^h)} \mathbf{P}^\top \mathbf{C} \mathbf{G} dV \quad (3.55)$$

$$\mathbf{f}_{int}^i = \mathbf{t}(\mathbf{e}^i) - \int_{\mathcal{B}_e^h} \frac{1}{\text{meas}(\mathcal{B}_e^h)} \mathbf{P}^\top \boldsymbol{\sigma}(\boldsymbol{\epsilon}^i) dV \quad (3.56)$$

also, in general, \mathbf{C} is the tangent stiffness matrix obtained from the constitutive law of the bulk. However, in this work, we chose a positive definite matrix defined using the Hooke's law to ensure the convergence in the softening regime.

Here, the static condensation can be performed at the element level to eliminate DOFs corresponding to the discretized displacement jump from the global DOFs. This allows obtaining the following modified system of equations:

$$\tilde{\mathbf{K}}^i \delta \mathbf{d}^{i+1} = \mathbf{F}_{ext} - \tilde{\mathbf{F}}_{int}^i \quad (3.57)$$

where,

$$\tilde{\mathbf{K}}^i = \mathbf{K}_{bb}^i - \mathbf{K}_{bg}^i [\mathbf{K}_{gg}^i]^{-1} \mathbf{K}_{gb}^i \quad (3.58)$$

$$\tilde{\mathbf{F}}_{int}^i = \mathbf{F}_{int}^i - \mathbf{K}_{bg}^i [\mathbf{K}_{gg}^i]^{-1} \mathbf{f}_{int}^i \quad (3.59)$$

However, as we do not use a tangent stiffness matrix in this work, the global stiffness matrix, $\tilde{\mathbf{K}}^i$ is assembled using the components of positive definite matrix chosen for \mathbf{C} .

3.5.2.2 Path-following technique

In general, the numerical solutions of non-linear analysis of structures constituted by the strain-softening materials may exhibit snap-back behavior at the global scale [de BORST, 1987, RASTIELLO et al., 2019]. In order to avoid this, we employ a path-following technique. The main idea is to make the intensity of the external loading to depend on a novel problem unknown, the loading factor $\zeta \in \mathbb{R}$. Accordingly, the external forces vector and the imposed displacements vector are written as:

$$\mathbf{F}_{ext} = \mathbf{F}_{ext,0} + \zeta \hat{\mathbf{F}} \quad (3.60)$$

$$\mathbf{d}_0 = \mathbf{d}_0 + \zeta \hat{\mathbf{d}} \quad (3.61)$$

where, $\mathbf{F}_{ext,0}$ is the imposed contribution to the external forces vector, $\hat{\mathbf{F}}$ is a normalized vector which determines the direction of the indirectly controlled part of the external force. Similarly, \mathbf{d}_0 is the vector of imposed displacements and $\hat{\mathbf{d}}$ gives the direction of the indirectly controlled contribution to the imposed displacement.

In order to compute ζ , the BVP is augmented through the path following constraint equation $P = P(\mathbf{d}, \mathbf{e}, \zeta; \tau) = 0$, with τ , a user-defined path-step length parameter. As shown in [RASTIELLO et al., 2019] discontinuity scale constraint equations can be written in order to control the loading based on quantities directly related to the response of elemental strong discontinuities (e.g., enhanced displacement variations, variation of d_{cr} , ...). In a more standard framework that is considered in this work, the dependency on the enhanced displacement field is skipped, i.e.,

$$P = P(\mathbf{d}, \zeta; \tau) = 0 \quad (3.62)$$

Moreover, we assume that function P can be differentiated with respect to all the unknowns.

The novel problem to solve consists of computing the increments of the solution $(\delta \mathbf{d}^{i+1}, \delta \mathbf{e}^{i+1}, \delta \zeta^{i+1})$, that solves the global and local equilibrium equations (now linearized with respect to the three unknowns), together with the linearized constraint equation. In the framework of the iterative process that is used, the loading factor is thus computed in an iterative manner. At iteration $i + 1$, ζ^{i+1} is written as:

$$\zeta^{i+1} = \zeta^i + \delta \zeta^{i+1} \quad (3.63)$$

with $\delta\zeta^{i+1}$ denoting the loading factor increment between iterations i and $i + 1$.

Now, the local equilibrium equation (3.48b) is independent of ζ and is not affected by the introduction of the novel unknown ζ . Conversely, from the linearization of the global equilibrium eq. (3.48a) with respect to $(\mathbf{d}, \mathbf{e}, \zeta)$, we obtain the displacement variation $\delta\mathbf{d}^{i+1}$ as:

$$\delta\mathbf{d}^{i+1} = \delta\zeta^{i+1}\delta\mathbf{d}_I^{i+1} + \delta\mathbf{d}_{II}^{i+1} \quad (3.64)$$

where $\delta\mathbf{d}_I^{i+1}$ and $\delta\mathbf{d}_{II}^{i+1}$ are computed by solving two independent systems of equations:

$$\tilde{\mathbf{K}}^i \delta\mathbf{d}_I^{i+1} = \hat{\mathbf{F}} \quad (3.65)$$

$$\tilde{\mathbf{K}}^i \delta\mathbf{d}_{II}^{i+1} = \mathbf{F}_{ext} - \mathbf{F}_{ext,0} - \zeta^i \hat{\mathbf{F}} \quad (3.66)$$

Substituting eq. (3.64) into the linearized constraint equation, one obtains a linear equation in $\delta\zeta^{i+1}$:

$$P(\mathbf{d}^i, \zeta^i) + \left(\frac{\partial P}{\partial \mathbf{d}}\right)^i \delta\mathbf{d}_{II}^{i+1} + \left[\left(\frac{\partial P}{\partial \mathbf{d}}\right)^i \delta\mathbf{d}_I^{i+1} + \left(\frac{\partial P}{\partial \zeta}\right)^i \right] \delta\zeta^{i+1} - \Delta\tau = 0 \quad (3.67)$$

Here, we chose a path following constraint first proposed in [de BORST, 1987] which is termed as ‘Controlled Nodal Displacement Increment’ (CNDI). It is given by:

$$P = \mathbf{a}^\top \Delta\mathbf{d}^{i+1} - \Delta\tau = \mathbf{a}^\top \left(\Delta\mathbf{d}^i + \delta\zeta^{i+1}\delta\mathbf{d}_I^{i+1} + \delta\mathbf{d}_{II}^{i+1} \right) - \Delta\tau = 0 \quad (3.68)$$

where, \mathbf{a}^\top is a column vector that provides the coefficients of the linear combination between the controlled degrees of freedom. Finally, $\delta\zeta^{i+1}$ is obtained by solving eq. (3.68) as:

$$\delta\zeta^{i+1} = \frac{\Delta\tau - \mathbf{a}^\top (\Delta\mathbf{d}^i + \delta\mathbf{d}_{II}^{i+1})}{\mathbf{a}^\top \delta\mathbf{d}_I^{i+1}} \quad (3.69)$$

3.5.2.3 Staggered solution scheme: operator split method

The solution of the linearized system of equations eqs. (3.50a) and (3.50b) is obtained in a staggered manner. That is to say, the solution of the global equilibrium at the iteration $i + 1$ is obtained first using the solution of the local equilibrium at previous iteration i and then the residual of the local equilibrium is redefined taking into account the global solution at the iteration $i + 1$. This procedure is known as ‘operator split method’ which is described in detail here.

Global equilibrium equation The residual of the global equilibrium eq. (3.49a) is redefined as, $\mathbf{R}(\mathbf{d}^{i+1}, \mathbf{e}^i) = 0$. Since \mathbf{e}^i are known, the static condensation can be performed and the solution $\delta\mathbf{d}^{i+1}$ of eq. (3.57) is obtained.

Local equilibrium equation The residuals of the traction continuity condition (3.49b) is redefined using $\delta\mathbf{d}^{i+1}$. Since these equations are also non-linear, an iterative procedure is used at the local level to compute $\delta\mathbf{e}^{i+1}$. At local iteration $j + 1$, one solves the following problem:

$$\mathbf{r}(\mathbf{d}^{i+1}, \mathbf{e}^{j+1}) = \mathbf{r}(\mathbf{d}^i, \delta\mathbf{d}^{i+1}, \mathbf{e}^j) + \mathbf{K}_{gg}^j \delta\mathbf{e}^{j+1} = 0 \quad (3.70)$$

The discretized displacement jump at $j + 1$ is then obtained as,

$$\mathbf{e}^{j+1} = \mathbf{e}^j + \delta\mathbf{e}^{j+1} \quad (3.71)$$

and once local convergence is achieved \mathbf{e}^{i+1} is set equal to \mathbf{e}^{j+1} . The residual at the iteration $i + 1$ is then updated as $\mathbf{R}(\mathbf{d}^{i+1}, \mathbf{e}^{i+1}(= \mathbf{e}^{j+1}))$, which is checked for a given tolerance (ϵ_{tol}).

As an advantage of the operator split method, the terms \mathbf{f}_{int}^i figuring in eq. (3.59) are null during the local solving. Thus, the internal force vector comprises alone of the global forces coming from the stress in the bulk i.e., $\tilde{\mathbf{F}}_{int}^i = \mathbf{F}_{int}^i$. The algorithm for resolution of global and local equilibrium equations is presented in algorithm 1. The above methodology is implemented in an in-house FE code in MATLAB® environment called CastLab [RICHARD et al., 2019].

When a path-following method as the one presented in the previous section is used, the solution process is only slightly different. In particular, increments $\delta \mathbf{d}_I^{i+1}$ and $\delta \mathbf{d}_{II}^{i+1}$ are first computed. Then the path-following constraint equation is solved for $\delta \zeta^{i+1}$, and the displacement correction is updated as defined in eq. (3.64). Finally, enhanced displacements are computed as explained previously. The solving process when using path-following constraints depending on the enhanced displacements is quite different, but this kind of algorithms is not treated in the present work. For more details, the interested reader can refer to [RASTIELLO et al., 2019].

3.5.3 Representative example: uniaxial tension-compression test

We show here a representative example to validate the numerical implementation and to illustrate the ability of the method to describe the initiation and evolution of the crack in the continuous media. The response in mode I crack opening is studied followed by crack closure and the unilateral effect.

Problem setting A unit concrete specimen which is discretized using 2 CST elements and the corresponding material parameters are shown in fig. 3.3. The specimen is simply supported at the bottom edge and vertical loading–unloading is applied on the top edge. The evolution of the applied displacement² in vertical direction (u_2) is shown in fig. 3.4. Here, plane strain conditions are assumed for the sake of illustration.

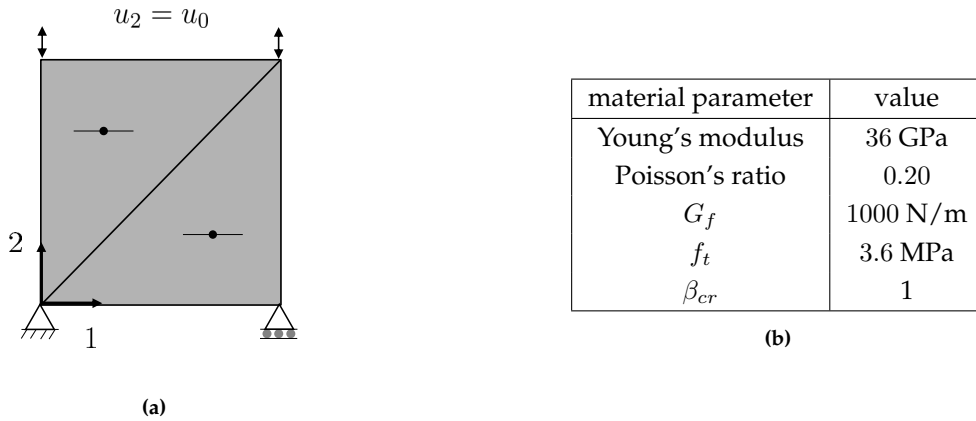


Figure 3.3: FE discretization of the specimen (1 m × 1 m) and the expected crack orientations under vertical loading–unloading (a) and the considered material parameters (b)

Results First, a tensile loading is applied till P_1 , followed by the unloading of the specimen. The components of the global force against the global displacement in vertical direction (F_2, u_2

²In the CastLab, double Lagrange multipliers technique is used to impose the applied displacement [VERPEAUX and CHARRAS, 2011, RICHARD et al., 2019].

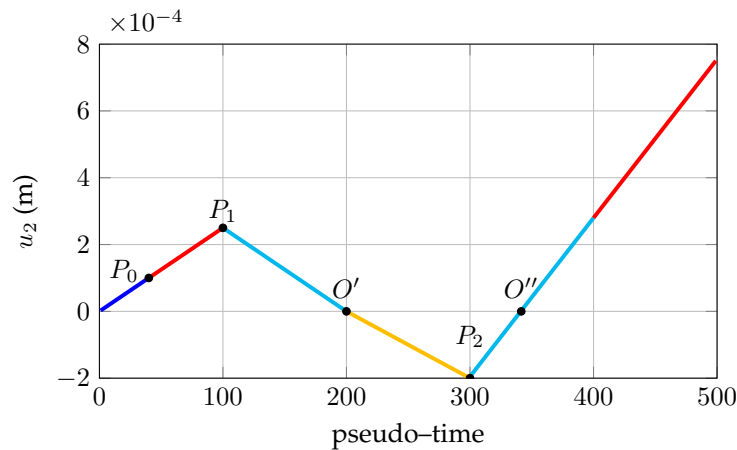


Figure 3.4: Time evolution of the applied loading - vertical loading-unloading

respectively) are plotted in fig. 3.5a. The material remains elastic until P_0 (figs. 3.5a and 3.5b), where the maximum principal stress reaches f_t .

At P_0 , the crack is initiated and the energy dissipation takes place. Since the uniaxial tensile loading is applied, the direction of the maximum principal stress is always aligned with the normal of the crack, hence only mode I is activated. The evolution of the normal components of the traction (t_n) and the displacement jump ($\llbracket u \rrbracket_n$) are plotted in fig. 3.5b.

The crack opens between stages P_0 and P_1 . This is followed by the elastic unloading of the specimen between stages P_1 and O' , during which the crack closes without dissipating energy. Due to the presence of the crack, the global unloading stiffness is reduced with respect to the initial stiffness of the specimen as shown in fig. 3.5a.

At O' , load reversal takes place and the compression loading is applied. On further loading into compression regime, the crack is completely closed as shown in fig. 3.5b, and the initial stiffness is fully recovered in the global response curve. The behavior of the material is assumed to be elastic in compression.

At P_2 in the compression regime, the direction of the loading is again reversed. After reentering the tension regime at O'' , the crack reopens (fig. 3.5b). The reopening of the crack is assumed to be elastic without energy dissipation until the previous unloading point P_1 is reached. As both closing and reopening of the crack are assumed to be elastic, the same path $P_1 - O'$ and $O'' - P_1$ is followed without any hysteresis loops in both the global response curve and the traction-separation law. Upon further loading in tension, the evolution of crack opening and the energy dissipation continues.

Remark. It is worth noting that in the numerical test case studied here, the direction of the principal stress axes does not rotate with respect to the loading. Hence the energy dissipation happens at a single localized crack, as stated by the chosen EFEM. However, in order to tackle the cases involving complex loading paths leading to the rotation of the principal stress axes, it is realized that multiple cracks needs to be localized [de BORST and NAUTA, 1998, MANZOLI and SHING, 2004]. Hence, we extend the standard EFEM for the case of multiple cracks in the next section.

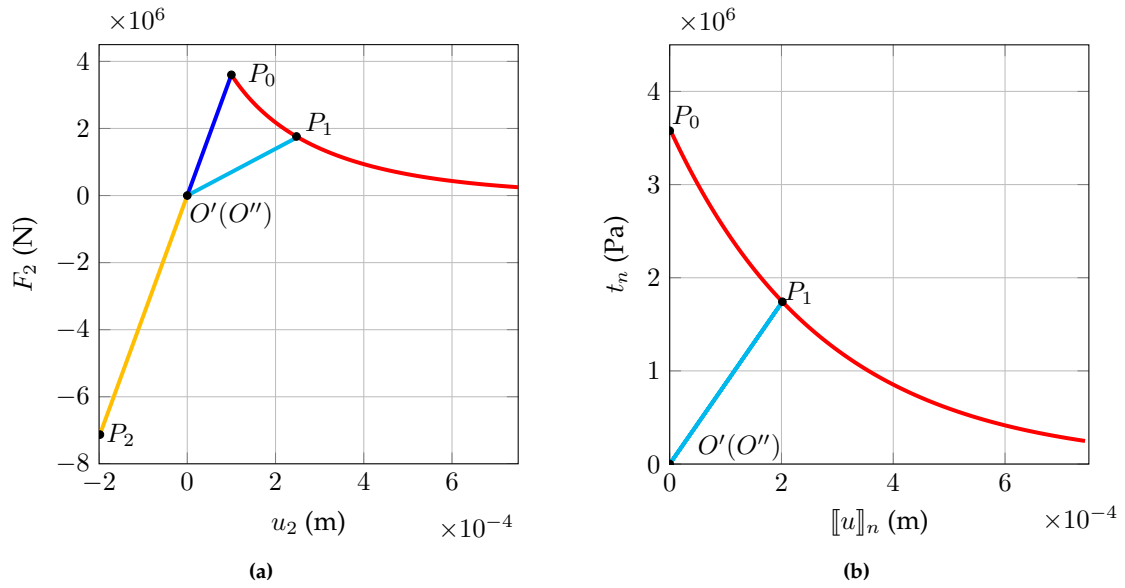


Figure 3.5: Global and local responses of the vertical loading–unloading test: force–displacement curve (a) and traction–separation law - opening of horizontal crack (b)

3.6 Multiple cracks in EFEM

The problem of a quasi–brittle media developing multiple intersecting discontinuities in quasi–static case is treated with in the framework of EFEM in [MANZOLI and SHING, 2004]. In this paper, the discontinuous part of the displacement is obtained as the sum of displacement jumps at the multiple discontinuities. Also, the local equilibrium is fulfilled by satisfying the traction continuity conditions at each discontinuity surface. Following a similar approach, we present here the kinematics and the augmented BVP of the continuum with multiple intersecting cracks.

3.6.1 Motivation

Let us present here the motivations for extension of the standard EFEM by considering a case in which the principal stress axes are rotated after the initiation of the first crack. For example, consider the vertical loading–unloading experiment performed in section 3.5.3 and let us apply a loading in the orthogonal direction to the initial one, after the crack closure at $O'(O'')$ in figs. 3.5a and 3.5b. As the loading progresses, the direction of the maximum principal stress rotates to the horizontal direction from the previous vertical direction. Hence, the evolution of the damage like variable associated with the horizontal crack does not take place anymore and it stays closed. Now, if the second crack (aligned in the vertical direction) is not localized, then the numerical response in the horizontal direction remains elastic because there is no energy dissipation during this phase of loading. Hence, in complex loading conditions, it is necessary to localize more than one crack to dissipate the energy in multiple directions.

3.6.2 Kinematics and boundary value problem

Let us revisit the case of a body \mathcal{B} crossed by a single discontinuity $\Gamma_{d_1} \in \mathbb{R}^{n_{dim} \times n_{dim}}$ whose normal is now denoted by \mathbf{n}_1 . Now, let us assume that during history of the loading, a second crack $\Gamma_{d_2} \in \mathbb{R}^{n_{dim} \times n_{dim}}$ with normal \mathbf{n}_2 is localized (fig. 3.6).

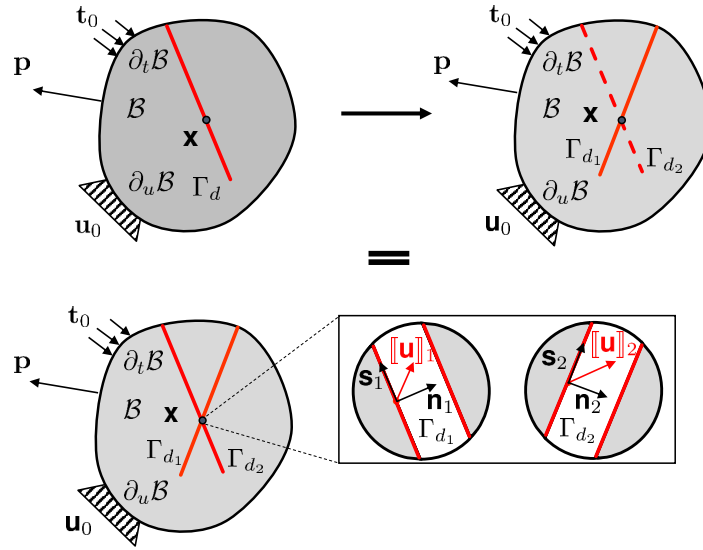


Figure 3.6: Extension of strong discontinuity kinematics - a body (\mathcal{B}) with multiple intersecting discontinuities Γ_{d_1} and Γ_{d_2}

Here, the main underlying assumption is that the state of the body with two discontinuities is obtained as the superposition of the states with each discontinuity. Interaction between discontinuities is then modeled through coupled traction continuity conditions. From now on, under-scripts 1 and 2 are used to denote quantities proper to the cracks Γ_{d_1} and Γ_{d_2} respectively.

Kinematics Let $[[\mathbf{u}]]_1 = [[\mathbf{u}]]_1(\mathbf{x}, t) : \mathcal{B} \times [0, \infty) \mapsto \mathbb{R}^{n_{dim}}$ and $[[\mathbf{u}]]_2 = [[\mathbf{u}]]_2(\mathbf{x}, t) : \mathcal{B} \times [0, +\infty) \mapsto \mathbb{R}^{n_{dim}}$ be the displacement jump functions associated with Γ_{d_1} and Γ_{d_2} respectively. Following this approach, the displacement and the strain fields of continuum with multiple discontinuities are given by:

$$\mathbf{u} = \bar{\mathbf{u}} + H_{\Gamma_{d_1}} [[\mathbf{u}]]_1 + H_{\Gamma_{d_2}} [[\mathbf{u}]]_2 \quad (3.72)$$

and

$$\boldsymbol{\epsilon} = \nabla^s \bar{\mathbf{u}} + H_{\Gamma_{d_1}} \nabla^s [[\mathbf{u}]]_1 + H_{\Gamma_{d_2}} \nabla^s [[\mathbf{u}]]_2 + \delta_{\Gamma_{d_1}} [[\mathbf{u}]]_1 \otimes \mathbf{n}_1 + \delta_{\Gamma_{d_2}} [[\mathbf{u}]]_2 \otimes \mathbf{n}_2 \quad (3.73)$$

where, $H_{\Gamma_{d_1}}$ and $H_{\Gamma_{d_2}}$ are the Heaviside functions at Γ_{d_1} and Γ_{d_2} respectively. In this context, the bounded part of the strain is defined as:

$$\bar{\boldsymbol{\epsilon}} = \nabla^s \bar{\mathbf{u}} + H_{\Gamma_{d_1}} \nabla^s [[\mathbf{u}]]_1 + H_{\Gamma_{d_2}} \nabla^s [[\mathbf{u}]]_2 \quad (3.74)$$

Augmented BVP Due to the principle of superposition, the individual traction continuity conditions for both the discontinuities are coupled to obtain the local equilibrium of the superposed state. The coupled traction continuity conditions are given by:

$$\boldsymbol{\sigma} \cdot \mathbf{n}_1 = \mathbf{t}_1 \quad \forall \mathbf{x} \in \Gamma_{d_1} \quad (3.75)$$

$$\boldsymbol{\sigma} \cdot \mathbf{n}_2 = \mathbf{t}_2 \quad \forall \mathbf{x} \in \Gamma_{d_2} \quad (3.76)$$

The augmented BVP in the case of multiple cracks reads exactly as in the one crack case, with the only difference that now eqs. (3.75) and (3.76) have to be fulfilled, together with two independent traction-separation laws defining the behaviors of cracks:

$$\mathbf{t}_1 = h_1([[\mathbf{u}]]_1) \quad \forall \mathbf{x} \in \Gamma_{d_1} \quad (3.77)$$

$$\mathbf{t}_2 = h_2([[\mathbf{u}]]_2) \quad \forall \mathbf{x} \in \Gamma_{d_2} \quad (3.78)$$

3.6.3 Enhanced assumed strain method – multiple local enhancements

The variational form of the augmented BVP with coupled traction continuity conditions is obtained in the framework of EAS method, following the same procedure as in section 3.5.1.

Variational form of the augmented BVP Let us assume that the enhanced strain field consists of contributions from two superposed local enhancements. In this case, the strain field and its variation are expressed as:

$$\boldsymbol{\epsilon} = \nabla^s \mathbf{u} + \tilde{\boldsymbol{\epsilon}}_1 + \tilde{\boldsymbol{\epsilon}}_2 \quad (3.79)$$

$$\boldsymbol{\epsilon}^* = \nabla^s \mathbf{u}^* + \tilde{\boldsymbol{\epsilon}}_1^* + \tilde{\boldsymbol{\epsilon}}_2^* \quad (3.80)$$

Here, $\tilde{\boldsymbol{\epsilon}}_1$ and $\tilde{\boldsymbol{\epsilon}}_2$ belong to E , $\tilde{\boldsymbol{\epsilon}}_1^*$ and $\tilde{\boldsymbol{\epsilon}}_2^*$ belong to $E^{\perp S}$. Substituting the above expressions in eqs. (3.26) and (3.27), the global and the local equilibrium equations become,

$$\int_{\mathcal{B}} \nabla^s(\mathbf{u}^*) : \boldsymbol{\sigma}(\nabla^s \mathbf{u} + \tilde{\boldsymbol{\epsilon}}_1 + \tilde{\boldsymbol{\epsilon}}_2) dV - \int_{\partial_t \mathcal{B}} \mathbf{u}^* \cdot \mathbf{t}_0 dS = 0 \quad (3.81)$$

$$\int_{\mathcal{B}} \tilde{\boldsymbol{\epsilon}}_1^* : \tilde{\boldsymbol{\sigma}}(\nabla^s \mathbf{u} + \tilde{\boldsymbol{\epsilon}}_1 + \tilde{\boldsymbol{\epsilon}}_2) dV + \int_{\mathcal{B}} \tilde{\boldsymbol{\epsilon}}_2^* : \tilde{\boldsymbol{\sigma}}(\nabla^s \mathbf{u} + \tilde{\boldsymbol{\epsilon}}_1 + \tilde{\boldsymbol{\epsilon}}_2) dV = 0 \quad (3.82)$$

Finite element discretization Now, let us consider a finite element that is crossed by two intersecting discontinuities Γ_{d_1} and Γ_{d_2} . The discretized displacement jumps across Γ_{d_1} and Γ_{d_2} are given by \mathbf{e}_1 and \mathbf{e}_2 . The finite element approximations for \mathbf{u} and \mathbf{u}^* are constructed using the enhanced displacement interpolation functions \mathbf{N}_{c_1} , \mathbf{N}_{c_2} as:

$$\mathbf{u} = \mathbf{N} \mathbf{d} + \mathbf{N}_{c_1} \mathbf{e}_1 + \mathbf{N}_{c_2} \mathbf{e}_2 \quad (3.83)$$

$$\mathbf{u}^* = \mathbf{N} \mathbf{d}^* + \mathbf{N}_{c_1} \mathbf{e}_1^* + \mathbf{N}_{c_2} \mathbf{e}_2^* \quad (3.84)$$

Following the SKON approach, the approximation of $\boldsymbol{\epsilon}$ and $\boldsymbol{\epsilon}^*$ are obtained using the strain interpolation functions \mathbf{G}_1 , \mathbf{G}_2 , \mathbf{G}_1^* and \mathbf{G}_2^* as:

$$\boldsymbol{\epsilon} = \mathbf{B} \mathbf{d} + \mathbf{G}_1 \mathbf{e}_1 + \mathbf{G}_2 \mathbf{e}_2 \quad (3.85)$$

$$\boldsymbol{\epsilon}^* = \mathbf{B} \mathbf{d}^* + \underbrace{\mathbf{G}_1^* \mathbf{e}_1^*}_{\tilde{\boldsymbol{\epsilon}}_1^*} + \underbrace{\mathbf{G}_2^* \mathbf{e}_2^*}_{\tilde{\boldsymbol{\epsilon}}_2^*} \quad (3.86)$$

Also, we assume that the enhanced fields do not interact with each other, hence the variations \mathbf{e}_1^* and \mathbf{e}_2^* are independent.

We substitute eqs. (3.84) to (3.86) in eqs. (3.81) and (3.82), and consider that the variations \mathbf{u}^* and $\boldsymbol{\epsilon}^*$ are arbitrary to obtain the following discretized equations:

$$\left\{ \begin{array}{l} \int_{\mathcal{B}} \mathbf{B}^T \boldsymbol{\sigma}(\mathbf{B} \mathbf{d} + \mathbf{G}_1 \mathbf{e}_1 + \mathbf{G}_2 \mathbf{e}_2) dV = \mathbf{F}_{ext} \quad (3.87a) \\ \int_{\mathcal{B}} \mathbf{G}_1^* \boldsymbol{\sigma}(\mathbf{B} \mathbf{d} + \mathbf{G}_1 \mathbf{e}_1 + \mathbf{G}_2 \mathbf{e}_2) dV = 0 \quad (3.87b) \\ \int_{\mathcal{B}} \mathbf{G}_2^* \boldsymbol{\sigma}(\mathbf{B} \mathbf{d} + \mathbf{G}_1 \mathbf{e}_1 + \mathbf{G}_2 \mathbf{e}_2) dV = 0 \quad (3.87c) \end{array} \right.$$

Following the EFEM, the interpolation functions are given by:

$$\mathbf{N}_{c_1} = \mathbf{H}_{\Gamma_{d_1}} - \sum_{a \in (\mathcal{B}_{e^1}^{h_1})^+} \mathbf{N}_a \quad (3.88)$$

$$\mathbf{N}_{c_2} = \mathbf{H}_{\Gamma_{d_2}} - \sum_{a \in (\mathcal{B}_{e^2}^{h_2})^+} \mathbf{N}_a \quad (3.89)$$

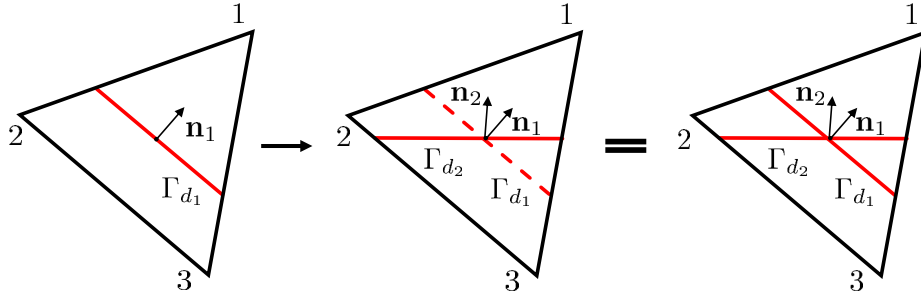


Figure 3.7: Extended EFEM - a finite element ($\mathcal{B}_e^h \in \mathcal{E}_1 \cap \mathcal{E}_2$) with multiple intersecting discontinuities Γ_{d_1} and Γ_{d_2}

$$\mathbf{G}_1 = \mathbf{P}_1 \delta_{\Gamma_{d_2}} - \sum_{a \in (\mathcal{B}_e^{h_2})^+} \mathbf{B}_a \quad (3.90)$$

$$\mathbf{G}_2 = \mathbf{P}_2 \delta_{\Gamma_{d_1}} - \sum_{a \in (\mathcal{B}_e^{h_1})^+} \mathbf{B}_a \quad (3.91)$$

$$\mathbf{G}_1^* = \left(\delta_{\Gamma_{d_1}} - \frac{\text{meas}(\Gamma_d)}{\text{meas}(\mathcal{B}_e^{h_1})} \right) \mathbf{P}_1 \quad (3.92)$$

$$\mathbf{G}_2^* = \left(\delta_{\Gamma_{d_2}} - \frac{\text{meas}(\Gamma_d)}{\text{meas}(\mathcal{B}_e^{h_2})} \right) \mathbf{P}_2 \quad (3.93)$$

where,

$$\mathbf{P}_1 = \begin{bmatrix} n_{1_1} & 0 \\ 0 & n_{1_2} \\ n_{1_2} & n_{1_1} \end{bmatrix} \quad (3.94)$$

$$\mathbf{P}_2 = \begin{bmatrix} n_{2_1} & 0 \\ 0 & n_{2_2} \\ n_{2_2} & n_{2_1} \end{bmatrix} \quad (3.95)$$

where, $[n_{1_1}, n_{1_2}]$, $[n_{2_1}, n_{2_2}]$ are the components of \mathbf{n}_1 and \mathbf{n}_2 respectively. Let \mathcal{E}_1^h , \mathcal{E}_2^h denote the set of finite elements that are crossed by the Γ_{d_1} and Γ_{d_2} respectively. In case of multiple intersecting cracks, $\mathcal{E}_1 \cap \mathcal{E}_2$ is not a null set.

Substituting the interpolation functions (eqs. (3.88) and (3.93)) in eqs. (3.87a) to (3.87c), the discretized global and local equilibrium equations to be solved in the case of multiple intersecting cracks are given by:

$$\begin{cases} \mathbf{A} \int_{e=1}^{n_{elem}} \int_{\mathcal{B}_e} \mathbf{B}^\top \boldsymbol{\sigma}(\mathbf{B}\mathbf{d} + \mathbf{G}_1 \mathbf{e}_1 + \mathbf{G}_2 \mathbf{e}_2) dV = \mathbf{F}_{ext} & (3.96a) \end{cases}$$

$$\begin{cases} \mathbf{t}_1(\mathbf{e}_1) - \int_{\mathcal{B}_e^{h_1}} \frac{1}{\text{meas}(\mathcal{B}_e^{h_1})} \mathbf{P}_1^\top \boldsymbol{\sigma}(\mathbf{B}\mathbf{d} + \mathbf{G}_1 \mathbf{e}_1 + \mathbf{G}_2 \mathbf{e}_2) dV = 0 \quad \forall \mathcal{B}_e^{h_1} \in \mathcal{E}_1 & (3.96b) \end{cases}$$

$$\begin{cases} \mathbf{t}_2(\mathbf{e}_2) - \int_{\mathcal{B}_e^{h_2}} \frac{1}{\text{meas}(\mathcal{B}_e^{h_2})} \mathbf{P}_2^\top \boldsymbol{\sigma}(\mathbf{B}\mathbf{d} + \mathbf{G}_1 \mathbf{e}_1 + \mathbf{G}_2 \mathbf{e}_2) dV = 0 \quad \forall \mathcal{B}_e^{h_2} \in \mathcal{E}_2 & (3.96c) \end{cases}$$

3.6.4 Numerical resolution - two embedded cracks

In the presence of two cracks, the residuals eqs. (3.49a) and (3.49b) are redefined by taking into account an additional unknown \mathbf{e}_2^{i+1} as follows:

$$\begin{cases} \mathbf{R}(\mathbf{d}^{i+1}, \mathbf{e}_1^{i+1}, \mathbf{e}_2^{i+1}) = \mathbf{R}(\mathbf{d}^i, \mathbf{e}_1^i, \mathbf{e}_2^i) + \frac{\partial \mathbf{R}}{\partial \mathbf{d}} \Big|_{\mathbf{d}^i} \delta \mathbf{d}^{i+1} + \frac{\partial \mathbf{R}}{\partial \mathbf{e}_1} \Big|_{\mathbf{e}_1^i} \delta \mathbf{e}_1^{i+1} + \frac{\partial \mathbf{R}}{\partial \mathbf{e}_2} \Big|_{\mathbf{e}_2^i} \delta \mathbf{e}_2^{i+1} & (3.97a) \\ \mathbf{r}_1(\mathbf{d}^{i+1}, \mathbf{e}_1^{i+1}, \mathbf{e}_2^{i+1}) = \mathbf{r}_1(\mathbf{d}^i, \mathbf{e}_1^i, \mathbf{e}_2^i) + \frac{\partial \mathbf{r}_1}{\partial \mathbf{d}} \Big|_{\mathbf{d}^i} \delta \mathbf{d}^{i+1} + \frac{\partial \mathbf{r}_1}{\partial \mathbf{e}_1} \Big|_{\mathbf{e}_1^i} \delta \mathbf{e}_1^{i+1} + \frac{\partial \mathbf{r}_1}{\partial \mathbf{e}_2} \Big|_{\mathbf{e}_2^i} \delta \mathbf{e}_2^{i+1} & (3.97b) \\ \mathbf{r}_2(\mathbf{d}^{i+1}, \mathbf{e}_1^{i+1}, \mathbf{e}_2^{i+1}) = \mathbf{r}_2(\mathbf{d}^i, \mathbf{e}_1^i, \mathbf{e}_2^i) + \frac{\partial \mathbf{r}_2}{\partial \mathbf{d}} \Big|_{\mathbf{d}^i} \delta \mathbf{d}^{i+1} + \frac{\partial \mathbf{r}_2}{\partial \mathbf{e}_1} \Big|_{\mathbf{e}_1^i} \delta \mathbf{e}_1^{i+1} + \frac{\partial \mathbf{r}_2}{\partial \mathbf{e}_2} \Big|_{\mathbf{e}_2^i} \delta \mathbf{e}_2^{i+1} & (3.97c) \end{cases}$$

The linearized system of the global and local equilibrium equations are rewritten by taking into account the coupled traction continuity conditions as:

$$\begin{cases} \mathbf{K}_{bb}^i \delta \mathbf{d}^{i+1} + \mathbf{K}_{bg_1}^i \delta \mathbf{e}_1^{i+1} + \mathbf{K}_{bg_2}^i \delta \mathbf{e}_2^{i+1} = \mathbf{F}_{ext} - \mathbf{F}_{int}^i & (3.98a) \\ \mathbf{K}_{g_1b}^i \delta \mathbf{d}^{i+1} + \mathbf{K}_{g_1g_1}^i \delta \mathbf{e}_1^{i+1} + \mathbf{K}_{g_1g_2}^i \delta \mathbf{e}_2^{i+1} = (\mathbf{f}_1)_{int}^i \quad \forall \mathcal{B}_e^{h_1} \in \mathcal{E}_1 & (3.98b) \\ \mathbf{K}_{g_2b}^i \delta \mathbf{d}^{i+1} + \mathbf{K}_{g_2g_1}^i \delta \mathbf{e}_1^{i+1} + \mathbf{K}_{g_2g_2}^i \delta \mathbf{e}_2^{i+1} = (\mathbf{f}_2)_{int}^i \quad \forall \mathcal{B}_e^{h_2} \in \mathcal{E}_2 & (3.98c) \end{cases}$$

where,

$$\mathbf{K}_{bg_1}^i = \int_{\mathcal{B}_e^{h_1}} \mathbf{B}^\top \mathbf{C} \mathbf{G}_1 dV \quad (3.99)$$

$$\mathbf{K}_{bg_2}^i = \int_{\mathcal{B}_e^{h_2}} \mathbf{B}^\top \mathbf{C} \mathbf{G}_2 dV \quad (3.100)$$

$$\mathbf{K}_{g_1b}^i = - \int_{\mathcal{B}_e^{h_1}} \frac{1}{\text{meas}(\mathcal{B}_e^{h_1})} \mathbf{P}_1^\top \mathbf{C} \mathbf{B} dV \quad (3.101)$$

$$\mathbf{K}_{g_1g_1}^i = \frac{\partial \mathbf{t}_1}{\partial \mathbf{e}_1} \Big|_{\mathbf{e}_1^i} - \int_{\mathcal{B}_e^{h_1}} \frac{1}{\text{meas}(\mathcal{B}_e^{h_1})} \mathbf{P}_1^\top \mathbf{C} \mathbf{G}_1 dV \quad (3.102)$$

$$\mathbf{K}_{g_1g_2}^i = - \int_{\mathcal{B}_e^{h_1}} \frac{1}{\text{meas}(\mathcal{B}_e^{h_1})} \mathbf{P}_1^\top \mathbf{C} \mathbf{G}_2 dV \quad (3.103)$$

$$(\mathbf{f}_1)_{int}^i = \mathbf{t}_1(\mathbf{e}_1^i) - \int_{\mathcal{B}_e^{h_1}} \frac{1}{\text{meas}(\mathcal{B}_e^{h_1})} \mathbf{P}_1^\top \boldsymbol{\sigma}(\boldsymbol{\epsilon}^i) dV \quad (3.104)$$

$$\mathbf{K}_{g_2b}^i = - \int_{\mathcal{B}_e^{h_2}} \frac{1}{\text{meas}(\mathcal{B}_e^{h_2})} \mathbf{P}_2^\top \mathbf{C} \mathbf{B} dV \quad (3.105)$$

$$\mathbf{K}_{g_2g_2}^i = \frac{\partial \mathbf{t}_2}{\partial \mathbf{e}_2} \Big|_{\mathbf{e}_2^i} - \int_{\mathcal{B}_e^{h_2}} \frac{1}{\text{meas}(\mathcal{B}_e^{h_2})} \mathbf{P}_2^\top \mathbf{C} \mathbf{G}_2 dV \quad (3.106)$$

$$\mathbf{K}_{g_2g_1}^i = - \int_{\mathcal{B}_e^{h_2}} \frac{1}{\text{meas}(\mathcal{B}_e^{h_2})} \mathbf{P}_2^\top \mathbf{C} \mathbf{G}_1 dV \quad (3.107)$$

$$(\mathbf{f}_2)_{int}^i = \mathbf{t}_2(\mathbf{e}_2^i) - \int_{\mathcal{B}_e^{h_2}} \frac{1}{\text{meas}(\mathcal{B}_e^{h_2})} \mathbf{P}_2^\top \boldsymbol{\sigma}(\boldsymbol{\epsilon}^i) dV \quad (3.108)$$

The stiffness matrices $\mathbf{K}_{g_1g_2}^i$ and $\mathbf{K}_{g_2g_1}^i$ have non-zero stiffness terms only if both $\mathcal{B}_e^{h_1}$ and $\mathcal{B}_e^{h_2}$ belong to $\mathcal{E}_1 \cap \mathcal{E}_2$. That is to say, for the elements in which the two cracks intersect, the coupled traction–separation laws are solved. In the elements that contain only the first crack, we solve the system of equations concerning only a single crack eqs. (3.50a) and (3.50b).

Now, both \mathbf{e}_1^i and \mathbf{e}_2^i are eliminated from the global unknowns by performing static condensation. The final system of the equations is given by:

$$\tilde{\mathbf{K}}^i \delta \mathbf{d}^{i+1} = \mathbf{F}_{ext} - \tilde{\mathbf{F}}_{int}^i \quad (3.109)$$

where,

$$\tilde{\mathbf{K}}^i = \mathbf{K}_{bb}^i - \mathbf{K}_{bg_1}^i [\mathbf{K}_{g_1g_1}^i]^{-1} \mathbf{K}_{g_1b}^i - \mathbf{K}_{bg_2}^i [\mathbf{K}_{g_2g_2}^i]^{-1} \mathbf{K}_{g_2b}^i \quad (3.110)$$

$$\tilde{\mathbf{F}}_{int}^i = \mathbf{F}_{int}^i - \mathbf{K}_{bg_1}^i [\mathbf{K}_{g_1g_1}^i]^{-1} (\mathbf{f}_1)_{int}^i - \mathbf{K}_{bg_2}^i [\mathbf{K}_{g_2g_2}^i]^{-1} (\mathbf{f}_2)_{int}^i \quad (3.111)$$

As in the previous case of a single crack, $\tilde{\mathbf{K}}^i$ is defined using the components of positive definite stiffness matrix \mathbf{C} .

Operator split method - coupled traction continuity conditions Following the operator split method, the local residuals eqs. (3.97b) and (3.97c) are solved in a coupled manner. After freezing the displacement increment $\delta \mathbf{d}^{i+1}$, the displacement jump increments at the local iteration $j + 1$ ($\delta \mathbf{e}_1^{j+1}$ and $\delta \mathbf{e}_2^{j+1}$) are obtained by solving the following simultaneous system of the equations:

$$\mathbf{r}_1(\mathbf{d}^{i+1}, \mathbf{e}_1^{j+1}, \mathbf{e}_2^{j+1}) = \mathbf{r}_1(\mathbf{d}^i, \delta \mathbf{d}^{i+1}, \mathbf{e}_1^j, \mathbf{e}_2^j) + \mathbf{K}_{g_1g_1}^j \delta \mathbf{e}_1^{j+1} + \mathbf{K}_{g_1g_2}^j \delta \mathbf{e}_2^{j+1} = 0 \quad (3.112)$$

$$\mathbf{r}_2(\mathbf{d}^{i+1}, \mathbf{e}_1^{j+1}, \mathbf{e}_2^{j+1}) = \mathbf{r}_2(\mathbf{d}^i, \delta \mathbf{d}^{i+1}, \mathbf{e}_1^j, \mathbf{e}_2^j) + \mathbf{K}_{g_2g_1}^j \delta \mathbf{e}_1^{j+1} + \mathbf{K}_{g_2g_2}^j \delta \mathbf{e}_2^{j+1} = 0 \quad (3.113)$$

The algorithm 2 presents the resolution process of global and local equilibrium equations in the extended EFEM, by considering the coupled traction continuity conditions for multiple intersecting cracks.

3.6.5 Numerical examples: multiple cracks

To illustrate the main features of the proposed extended EFEM, in this section, we show two simple examples. We first focus on the case of two orthogonal intersecting cracks such that, given the BVP formulation, no interaction occurs between them. Then we study a more complicated situation in which two non-orthogonal cracks localize in the medium.

3.6.5.1 Two phase tensile test: orthogonal cracks

Problem setting Let us perform a two phase loading experiment using the framework of the extended EFEM where a first phase vertical loading-unloading is applied which is followed by the horizontal loading.

In the first phase, we open a horizontal crack by applying a vertical loading (fig. 3.3) and after certain energy is dissipated at the crack, the crack is closed. The corresponding global curve and the traction–separation law are represented by $O' - P_0 - P_1 - O''$ in figs. 3.5a and 3.5b respectively.

Later, the boundary conditions are changed and a horizontal loading (u_1) is applied on the specimen (fig. 3.8). In this phase, both the global and the local fields are initiated using the corresponding fields at the end of the first phase. Thus, the presence of the first crack is taken into account during the application of the horizontal loading.

Results The components of the global force and displacement in the horizontal direction (F_1 and u_1 respectively) are plotted against each other in figs. 3.9a and 3.9b for the standard EFEM and the extended EFEM respectively. It can be observed that the response remains elastic in the former case, since the localization of an additional crack is not possible. However, owing to the coupled traction continuity conditions governing the local equilibrium of multiple cracks in the extended EFEM, the second crack in the direction orthogonal to the first crack is localized.

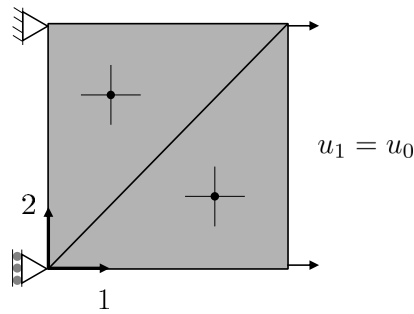


Figure 3.8: FE discretization of the specimen (1 m \times 1 m) and the expected crack orientations - horizontal loading after vertical loading-unloading

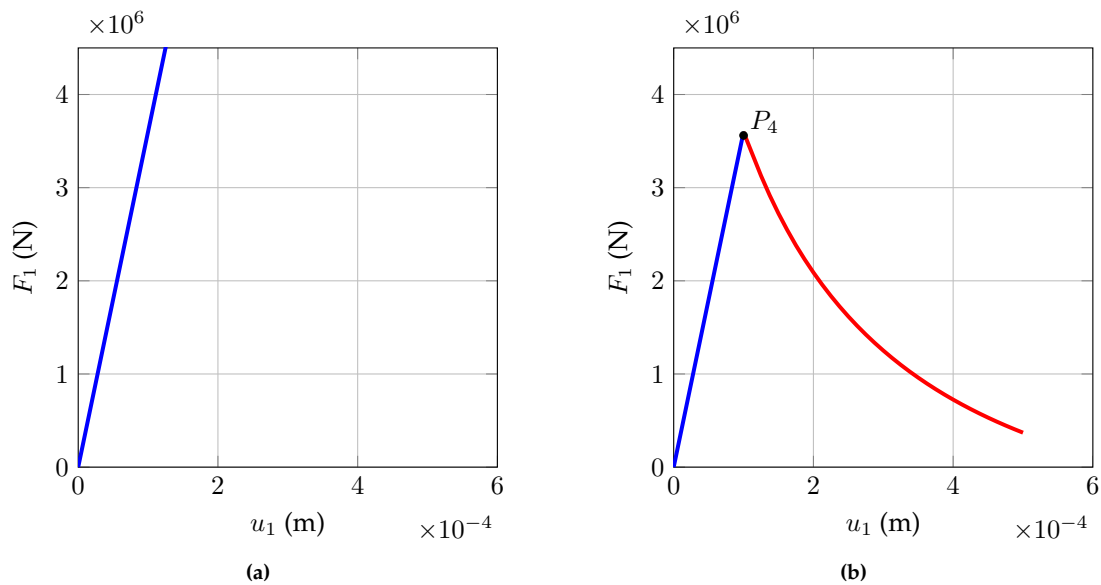


Figure 3.9: Force–displacement curve - horizontal loading: standard EFEM (a), extended EFEM (b)

Notice that, the crack initiation criterion and the material parameters for the second crack are assumed to be the same as for the first crack. This is justified as the bulk is assumed to be an isotropic elastic material. The maximum principal stress reaches the tensile strength of the material at P_4 in the force–displacement curve fig. 3.9a.

Mesh dependency study Given that the energy dissipation is at the surface of the crack, the numerical results are expected to be independent on the spatial discretization. This is studied by comparing the global response of the same specimen discretized with different meshes. Two additional meshes with 18 and 162 elements (fig. 3.10) are considered. The global curve for different meshes during horizontal and vertical loading is shown in fig. 3.11.

Remark. An important point to note is that the traction–separation laws of both the cracks are identical because the material parameters of the cracks are assumed to be the same. Also, since the cracks are orthogonal, the coupled traction continuity conditions evolve independently to each other. Hence, the first crack stays closed while the opening of second crack takes place, that is to say, the cracks do not interact with each other. It will be shown in the next section that it is not the case for the non-orthogonal cracks. The interaction between the cracks depends on the angle between them.

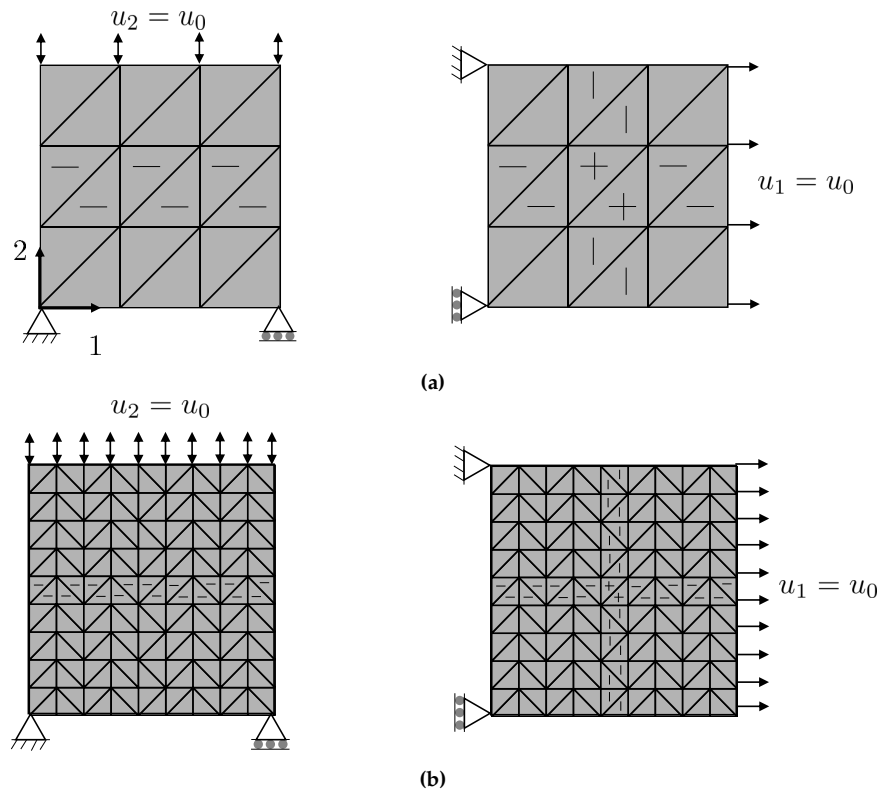


Figure 3.10: Different FE discretization of the specimen (1 m × 1 m) and the expected crack orientations - two phase vertical and horizontal loading: 18 elements (a), 162 elements (b)

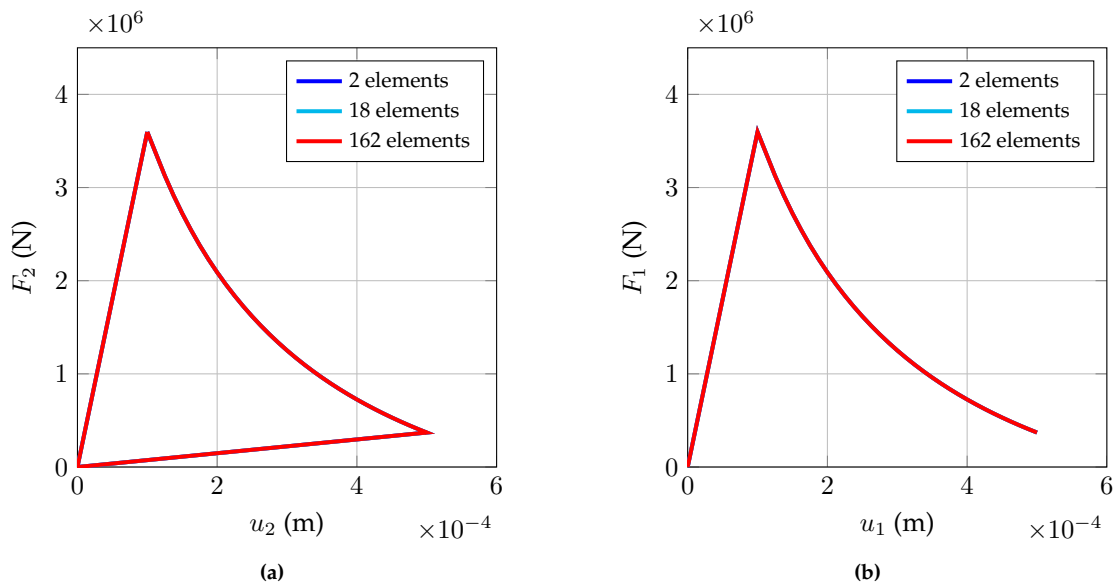


Figure 3.11: Force–displacement curves for different meshes: vertical loading (a), horizontal loading (b)

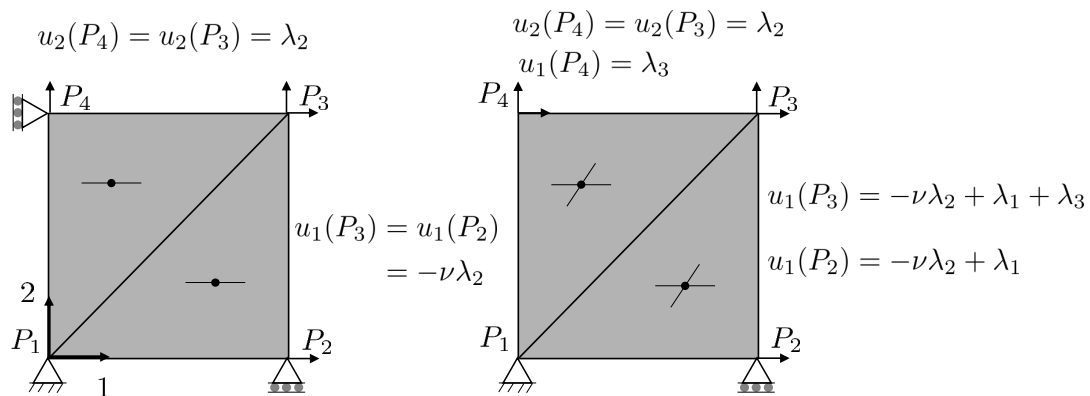
3.6.5.2 Willam’s test: non-orthogonal cracks

In this section, we demonstrate the capability of the proposed methodology to tackle the localization of non-orthogonal cracks. Let us consider a multi axial test with Willam’s test like loading

[WILLAM et al., 1989]. In this test, the loading is applied in a non-proportional manner in the horizontal and vertical directions that leads to a progressive rotation of principal stress axes. This changes the behavior of the cracks from mode I to mixed mode. The test is successful if the model is able to handle the mixed mode cracking and dissipate the available energy in multiple directions.

Problem setting The considered geometry, loading, boundary conditions and material properties are given in fig. 3.12. Loading is applied (imposed displacements) in two phases. In the first phase, a tensile loading in the vertical direction is applied along with the compression loading in the horizontal direction as shown in fig. 3.13. The horizontal loading is applied to negate the Poisson's effect.

Just after the opening of the first crack at A , the second phase of the loading starts at B . In this phase, a combined horizontal tensile loading and shear loading along with the vertical tensile loading is applied in a non-proportional manner.



(a)

material parameter	value
Young's modulus	10 GPa
Poisson's ratio	0.20
G_f	500 N/m
f_t	1.0 MPa
β_{cr}	1

(b)

Figure 3.12: FE discretization of the specimen (1 m \times 1 m) and the expected crack orientations under Willam's like loading (a) and the considered material parameters (b)

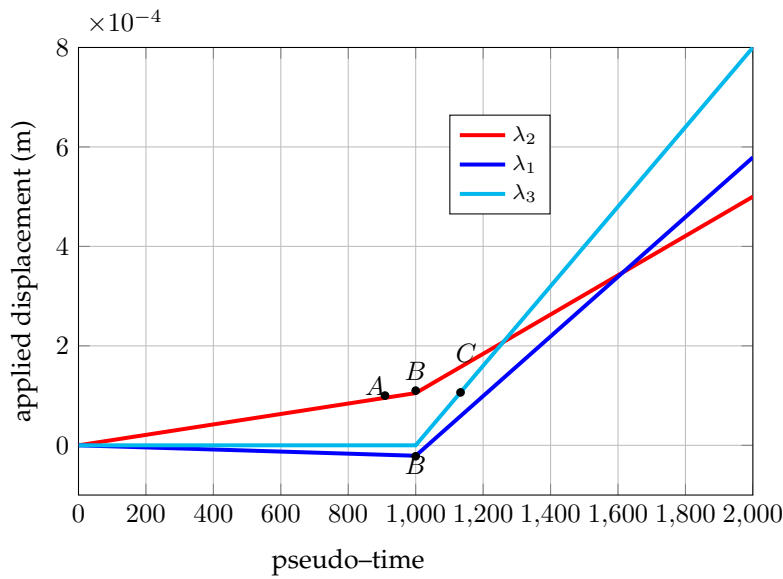


Figure 3.13: Time evolution of the applied displacement - Willam's like loading

Global results The time evolution of the components of the stress tensor is shown in fig. 3.14. The first crack is initiated when σ_{22} reaches the tensile strength at *A*. Due to the application of the non-proportional loading at *B*, the normal of the first crack is no longer aligned with the direction of principal stress axes. As loading increases, the principal stress axes rotate further, and the tensile strength limit reaches in the direction of the present maximum principal stress axes which is at 48° to the normal of the first crack at *C* in fig. 3.14. Now, both the cracks continue to dissipate energy leading to the simultaneous decrease of the stress components σ_{11} , σ_{12} and σ_{22} from *C*.

Local results During the first phase, the crack behaves in mode I and only the normal displacement of the first crack ($\llbracket u \rrbracket_{n_1}$) evolves from *A* to *B* in fig. 3.15. During the second phase, the first crack begins to slide due to the rotation of the principal stress axes as soon as the non-proportional loading is applied. This leads to the evolution of ($\llbracket u \rrbracket_{s_1}$) from *B* in fig. 3.15. Furthermore, the constant rotation of the principal stress axes compel the cracks to behave in mixed mode condition to satisfy the local equilibrium. This leads to the evolution of both $\llbracket u \rrbracket_{n_2}$ and $\llbracket u \rrbracket_{s_2}$ from the onset of second crack at *C*.

Characterization of anisotropy Before the initiation of the crack, the principal stress and strain axes stay parallel with each other as we assumed an isotropic elastic response prior to the cracking. However, due to induced anisotropy, the principal stress and strain axes rotates at different rate with respect to a fixed direction. Using Willam's test, rate of anisotropy can be quantified by computing the difference between the asymptotic values of the rotation of the principal stress and strain axes during the loading history.

Let γ_σ and γ_ϵ be the rotation of the maximum principal stress and strain axes respectively with respect to the vertical direction. Here, we consider two cases; the first one is the case in which we allow only one crack to initiate, whereas in the second case (which is the present case) two non-orthogonal cracks are initiated. The evolution of γ_ϵ remains the same in both cases as it is related to the applied loading while the evolution of γ_σ is compared for both the cases in fig. 3.16.

It can be observed from this figure that γ_σ becomes non-zero at the beginning of the second phase and if the second crack is not initiated then it keeps on increasing before reaching an asymptotic

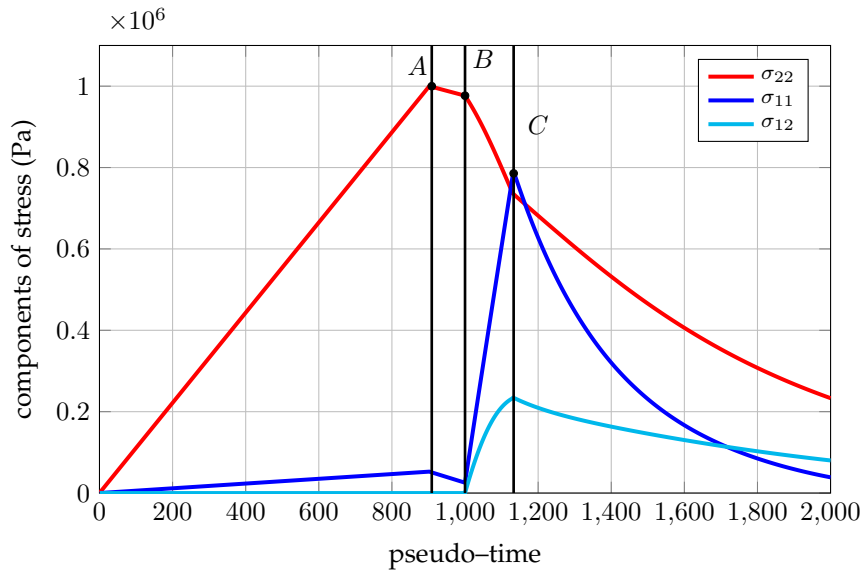


Figure 3.14: Time evolution of the components of stress - Willam's like loading test using extended EFEM

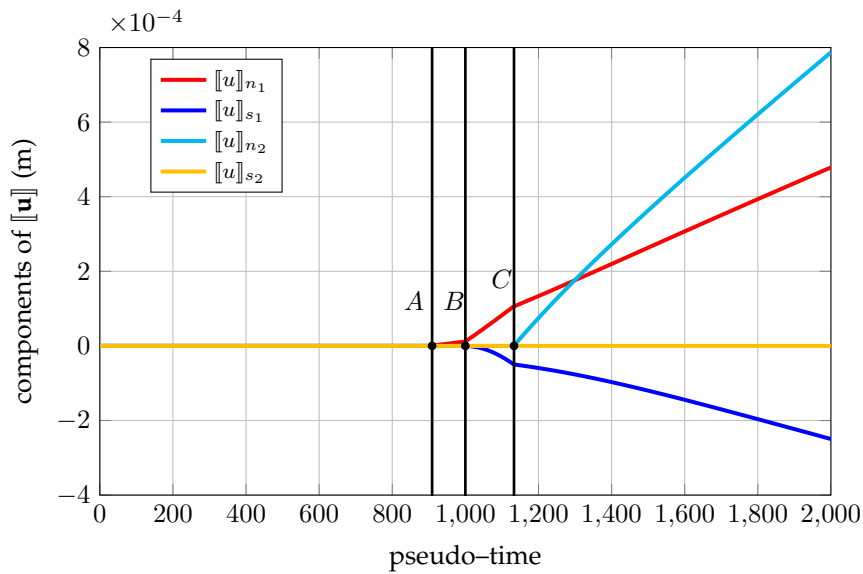


Figure 3.15: Time evolution of the components of the displacement jump - Willam's like loading test using extended EFEM

value of 90° . That is to say, the maximum principal direction is aligned with the horizontal direction. This is because, if the second crack is not localized, then the local response in the horizontal direction (σ_{11}) stays elastic. However, as the second crack localizes, reduction takes place for all the stress components. Hence, γ_σ starts decreasing before reaching an asymptotic value (γ_σ^{asy}) of 19.73° . The asymptotic value of the rotation of the maximum principal strain axis (γ_ϵ^{asy}) is obtained as 47.82° . Finally, the rate of anisotropy is computed as, $\frac{\gamma_\epsilon^{asy} - \gamma_\sigma^{asy}}{\gamma_\epsilon^{asy}} \times 100 = 58.74\%$.

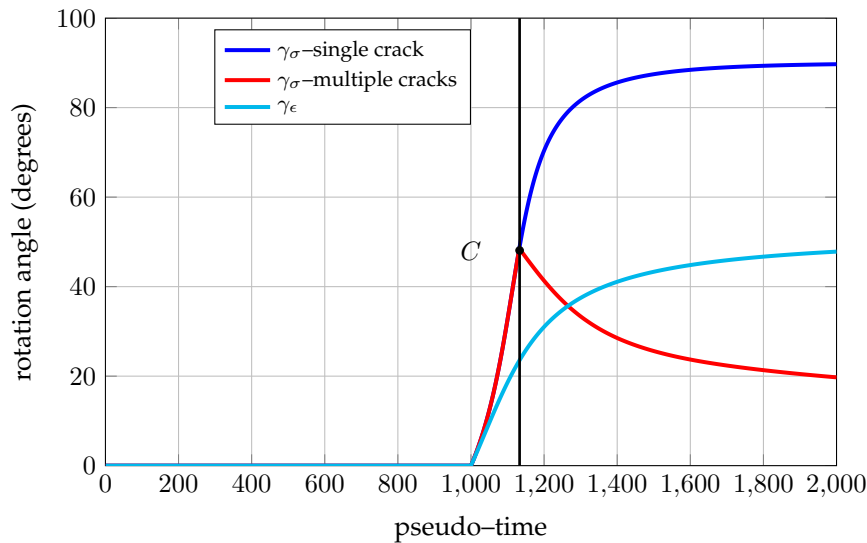


Figure 3.16: Time evolution of the rotation of the maximum principal stress and strain axes with respect to the vertical direction - Willam's like loading test using extended EFEM

3.7 Conclusions

In this chapter, the modeling of cracks using a strong discontinuity approach in the framework of EFEM is elaborated. Following a DSDA, crack is initiated using a criterion based on maximum principal stress. An isotropic damage like traction–separation law is then followed. The unilateral conditions that describe the full stiffness recovery upon the crack closure are taken into account.

The standard EFEM with a single discontinuity has limited scope in the context of multiple cracks. Modeling of the formation of multiple intersecting cracks in complex loading conditions is achieved by extending the strong discontinuity approach for multiple crack cases. The kinematics of the continuum, as well as the coupled traction continuity conditions expressing local equilibrium at the cracks, are obtained by assuming that the cracks are superposed. The proposed methodology is applied in the loading cases that result in orthogonal and non–orthogonal cracks. The energy dissipated at the first crack influence the orientation of the second crack. Also, the assumption of initial isotropy leads to the assignment of the same material parameters to both the cracks.

In the proposed model, the bulk is assumed to be elastic, and the energy dissipation occurs only at the crack. But the assumption of no energy dissipation before initiation of cracks is far from reality. To model the complete process of strain localization, the phase of damage growth needs to be taken into account.

We propose an anisotropic damage model to describe the initial phase of strain localization in chapter 4. This is followed by a transition approach to initiate a crack inside the localization zone in chapter 5. Owing to the anisotropic description of the bulk, a method to compute the material parameters of the cracks, depending on their orientations, is also proposed the chapter 5.

```

Fextn+1 = Fextn + ΔFextn+1;
i = 0;
convglobal = 0;
while convglobal = 0 do
    δdn+1,i+1 = - { Ki }-1 R(di);
    dn+1,i+1 = dn+1,i + δdn+1,i+1;
    for loop over Gauss points do
        j = 0;
        convlocal = 0;
        while convlocal = 0 do
            if j = 0 then
                δen+1,i+1,0 = - [Kggi]-1 r(dn+1,i+1, en+1,i);
                en+1,i+1,0 = en+1,i + δen+1,i+1,0;
            else
                compute Kggi+1,j using eq. (3.55);
                δen+1,i+1,j+1 = - [Kggi+1,j]-1 r(dn+1,i+1, en+1,i+1,j);
                en+1,i+1,j+1 = en+1,i+1,j + δen+1,i+1,j+1;
            end
            en+1,i+1,j+1 → t(dn+1,i+1, en+1,i+1,j+1);
            dn+1,i+1, en+1,i+1,j+1 → σ(dn+1,i+1, en+1,i+1,j+1);
            dn+1,i+1, en+1,i+1,j+1 → r(dn+1,i+1, en+1,i+1,j+1);
            if ||rn+1,i+1,j+1|| < εtol then
                | j = j + 1;
            else
                | convlocal = 1;
            end
        end
    end
    σ(dn+1,i+1, en+1,i+1) → Fintn+1,i+1;
    Fextn+1, Fintn+1,i+1 → R(dn+1,i+1, en+1,i+1);
    if ||Rn+1,i+1|| < εtol then
        | i = i + 1;
    else
        | convglobal = 1;
    end
end

```

Algorithm 1: Algorithm for resolution of global and local equilibrium equations in EFEM

```

Fextn+1 = Fexts + ΔFextn+1;
i = 0;
convglobal = 0;
while convglobal = 0 do
  ...;
  computation of dn+1,i+1 algorithm 1;
  ...;
  for loop over Gauss points do
    j = 0;
    convlocal = 0;
    while convlocal = 0 do
      if j = 0 then
        
$$\begin{cases} \delta \mathbf{e}_1^{n+1,i+1,0} \\ \delta \mathbf{e}_2^{n+1,i+1,0} \end{cases} = \begin{bmatrix} \mathbf{K}_{g_1 g_1}^i & \mathbf{K}_{g_1 g_2}^i \\ \mathbf{K}_{g_2 g_1}^i & \mathbf{K}_{g_2 g_2}^i \end{bmatrix}^{-1} \begin{cases} \mathbf{r}_1(\mathbf{d}^{n+1,i+1}, \mathbf{e}_1^{n+1,i}, \mathbf{e}_2^{n+1,i}) \\ \mathbf{r}_2(\mathbf{d}^{n+1,i+1}, \mathbf{e}_1^{n+1,i}, \mathbf{e}_2^{n+1,i}) \end{cases}$$


$$\begin{cases} \mathbf{e}_1^{n+1,i+1,0} \\ \mathbf{e}_2^{n+1,i+1,0} \end{cases} = \begin{cases} \mathbf{e}_1^{n+1,i} \\ \mathbf{e}_2^{n+1,i} \end{cases} + \begin{cases} \delta \mathbf{e}_1^{n+1,i+1,0} \\ \delta \mathbf{e}_2^{n+1,i+1,0} \end{cases}$$

      else
        compute  $\begin{bmatrix} \mathbf{K}_{g_1 g_1}^{i+1,j} & \mathbf{K}_{g_1 g_2}^{i+1,j} \\ \mathbf{K}_{g_2 g_1}^{i+1,j} & \mathbf{K}_{g_2 g_2}^{i+1,j} \end{bmatrix}$  using eqs. (3.102), (3.103), (3.106) and (3.107);

$$\begin{cases} \delta \mathbf{e}_1^{n+1,i+1,j+1} \\ \delta \mathbf{e}_2^{n+1,i+1,j+1} \end{cases} = \begin{bmatrix} \mathbf{K}_{g_1 g_1}^{i+1,j} & \mathbf{K}_{g_1 g_2}^{i+1,j} \\ \mathbf{K}_{g_2 g_1}^{i+1,j} & \mathbf{K}_{g_2 g_2}^{i+1,j} \end{bmatrix}^{-1} \begin{cases} \mathbf{r}_1(\mathbf{d}^{n+1,i+1}, \mathbf{e}_1^{n+1,i+1,j+1}, \mathbf{e}_2^{n+1,i+1,j}) \\ \mathbf{r}_2(\mathbf{d}^{n+1,i+1}, \mathbf{e}_1^{n+1,i+1,j+1}, \mathbf{e}_2^{n+1,i+1,j}) \end{cases}$$


$$\begin{cases} \mathbf{e}_1^{n+1,i+1,j+1} \\ \mathbf{e}_2^{n+1,i+1,j+1} \end{cases} = \begin{cases} \mathbf{e}_1^{n+1,i+1,j} \\ \mathbf{e}_2^{n+1,i+1,j} \end{cases} + \begin{cases} \delta \mathbf{e}_1^{n+1,i+1,j+1} \\ \delta \mathbf{e}_2^{n+1,i+1,j+1} \end{cases}$$

      end

$$\begin{cases} \mathbf{e}_1^{n+1,i+1,j+1} \\ \mathbf{e}_2^{n+1,i+1,j+1} \end{cases} \rightarrow \begin{cases} \mathbf{t}_1(\mathbf{d}^{n+1,i+1}, \mathbf{e}_1^{n+1,i+1,j+1}, \mathbf{e}_2^{n+1,i+1,j+1}) \\ \mathbf{t}_2(\mathbf{d}^{n+1,i+1}, \mathbf{e}_1^{n+1,i+1,j+1}, \mathbf{e}_2^{n+1,i+1,j+1}) \end{cases}$$


$$\mathbf{d}^{n+1,i+1}, \mathbf{e}_1^{n+1,i+1,j+1}, \mathbf{e}_2^{n+1,i+1,j+1} \rightarrow \sigma(\mathbf{d}^{n+1,i+1}, \mathbf{e}_1^{n+1,i+1,j+1}, \mathbf{e}_2^{n+1,i+1,j+1});$$


$$\mathbf{d}^{n+1,i+1}, \mathbf{e}_1^{n+1,i+1,j+1}, \mathbf{e}_2^{n+1,i+1,j+1} \rightarrow \mathbf{r}_1(\mathbf{d}^{n+1,i+1}, \mathbf{e}_1^{n+1,i+1,j+1}, \mathbf{e}_2^{n+1,i+1,j+1});$$


$$\mathbf{d}^{n+1,i+1}, \mathbf{e}_1^{n+1,i+1,j+1}, \mathbf{e}_2^{n+1,i+1,j+1} \rightarrow \mathbf{r}_2(\mathbf{d}^{n+1,i+1}, \mathbf{e}_1^{n+1,i+1,j+1}, \mathbf{e}_2^{n+1,i+1,j+1});$$

      if ||r1, r2|| < εtol then
        | j = j + 1;
      else
        | convlocal = 1;
      end
    end
  end
  σ(dn+1,i+1, e1n+1,i+1, e2n+1,i+1) → Fintn+1,i+1;
  Fextn+1, Fintn+1,i+1 → R(dn+1,i+1, e1n+1,i+1, e2n+1,i+1);
  if ||R|| < εtol then
    | i = i + 1;
  else
    | convglobal = 1;
  end
end

```

Algorithm 2: Algorithm for resolution of global and local equilibrium equations in extended EFEM using coupled traction continuity conditions for multiple intersecting cracks

This page is intentionally empty

Microplane microdamage model

Abstract. An approach for describing anisotropic damage growth in the initial stage of strain localization using microplane constitutive model [BAŽANT and OH, 1985, BAŽANT, 1984] is presented. In this approach, the constitutive model of the continuum is developed using the simple constitutive laws defined on planes of generic orientation known as ‘microplanes’. After illustrating the mathematical formulation of the simple proposed model, the secant and tangent stiffness tensors are derived and the localization properties in the case of the uniaxial tension (of main interest in this work) are analyzed. Finally, some numerical examples are presented in order to show the main features of the model both in terms of the obtained global response and of the induced anisotropy.

4.1 Introduction

According to microplane models, the anisotropic damage is modeled by sampling the material behavior in several possible directions. In earlier microplane models [BAŽANT and PRAT, 1988a, BAŽANT, 1996], the unit volume is represented by a spherical microplane system. Even though the triaxial experimental results are well reproduced using this representation, it is realized in [PARK and KIM, 2003] that a simplification can be achieved for the analysis of planar members. In these cases, we can idealize the spherical microplane system (section 2.3.1.4) by the disk microplane system (Ω in fig. 4.1) to represent the unit volume.

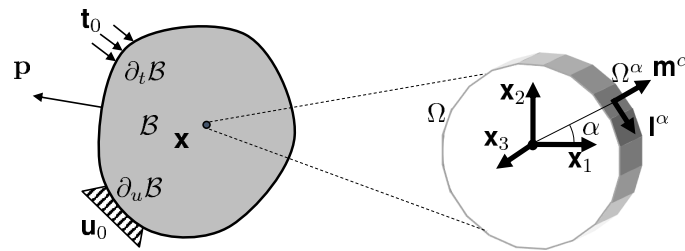


Figure 4.1: Representation of unit volume using the disk microplane system

Starting from this idea, simple microplane models can be derived leading to 2D formulations that are easier to implement and less time consuming than full three-dimensional modeling (integration is no more performed over a sphere but over a circle).

First, the general framework of the microplane models is presented. The microplane system used to represent the unit volume is detailed in the section 4.2. Second, the assumptions involved in developing a relationship between the unit volume and the microplane system are described

in the section 4.2.1. This is followed by different approaches for deriving the continuum tensor quantities from the microplane scalar/vector quantities in the section 4.2.2.

In section 4.3, a specific constitutive law ‘microplane microdamage model’ is formulated in thermodynamic framework. This is followed by the derivation of secant and the tangent material stiffness tensors. After this, the conditions under which the loss of ellipticity of the rate equilibrium problem occurs for the proposed model are investigated in the section 4.3.4. In section 4.4.2, a simple energetic regularization technique to solve the mesh dependency issues (typically associated with constitutive models exhibiting softening) is presented.

Numerical studies are performed in the section 4.5 to understand several aspects of the proposed model. Finally some conclusions are drawn in the section 4.7 based on the ability of the proposed constitutive model in handling the anisotropic damage.

4.2 Framework of microplane models

In the simplified microplane representation that is considered in this work, microplanes are located on the circumference of the unit disk¹ Ω (fig. 4.1). In this chapter, the disk microplane system under the plane strain assumptions is used to represent the unit volume². A kinematic constraint is assumed between the microplane system and the unit volume. According to this, the components of the strain vector (normal strain and tangential strain) on each microplane are obtained as the projection of the continuum strain tensor in the normal and tangential directions. The components of stress vector (normal stress and tangential stress) on each microplane are defined using the constitutive laws on the each microplane. The continuum stress tensor is then obtained as an integral of the components of stress vector on each microplane. Finally, the stress and strain components in the direction of x_3 (fig. 4.1) are assumed to be independent of the microplane system.

4.2.1 Projection of strain tensor

Let us consider a microplane Ω^α whose normal vector (denoted by \mathbf{m}^α) makes an angle α with reference axis x_1 (fig. 4.1). The tangent vector to Ω^α is denoted by \mathbf{I}^α ($\mathbf{I}^\alpha \cdot \mathbf{m}^\alpha = 0$). From now on, we distinguish the quantities of the disk microplane system from that of the spherical one by using a superscript α .

Following the kinematic constraint, the normal component of strain (ϵ_m^α) and the tangential component of strain (ϵ_t^α) at microplane Ω^α are obtained as the projection of the strain tensor:

$$\epsilon_m^\alpha = \mathbf{m}^\alpha \cdot \boldsymbol{\epsilon} \cdot \mathbf{m}^\alpha = \mathbf{M}^\alpha : \boldsymbol{\epsilon} \quad (4.1)$$

$$\epsilon_t^\alpha = \mathbf{I}^\alpha \cdot \boldsymbol{\epsilon} \cdot \mathbf{m}^\alpha = \mathbf{L}^\alpha : \boldsymbol{\epsilon} \quad (4.2)$$

where the second-order tensors \mathbf{M}^α and \mathbf{L}^α are the projection operators given by:

$$\mathbf{M}^\alpha = \mathbf{m}^\alpha \otimes \mathbf{m}^\alpha \quad (4.3)$$

$$\mathbf{L}^\alpha = \frac{1}{2} (\mathbf{I}^\alpha \otimes \mathbf{m}^\alpha + \mathbf{m}^\alpha \otimes \mathbf{I}^\alpha) \quad (4.4)$$

Notice that the projection tensor $\mathbf{I}^\alpha \otimes \mathbf{m}^\alpha$ could have been alternatively used for computing ϵ_t^α . However, exploiting the orthogonality condition between the vectors \mathbf{m}^α and \mathbf{I}^α and given the symmetry of $\boldsymbol{\epsilon}$, one can easily show that $\epsilon_t^\alpha = \mathbf{L}^\alpha : \boldsymbol{\epsilon} = (\mathbf{I}^\alpha \otimes \mathbf{m}^\alpha) : \boldsymbol{\epsilon}$. Here, the symmetric part of the \mathbf{L}^α tensor was considered since this will also be used to obtain a symmetric stress tensor.

¹The planar surfaces with outward normal parallel to x_3 (fig. 4.1) are not included in the system.

²In the introductory paper [PARK and KIM, 2003], the thickness of the unit disk is assumed to be equal to that of the planar member which corresponds to a state of plane stress.

Considering the assumption of disk microplane system, the expressions of the projection operators can be derived by writing the vectors \mathbf{m}^α and \mathbf{l}^α in an orthogonal basis $R(\mathbf{x}_1, \mathbf{x}_2)$ as given below:

$$\mathbf{m}^\alpha = \cos \alpha \mathbf{x}_1 + \sin \alpha \mathbf{x}_2 \quad (4.5)$$

$$\mathbf{l}^\alpha = -\sin \alpha \mathbf{x}_1 + \cos \alpha \mathbf{x}_2 \quad (4.6)$$

As a consequence:

$$\mathbf{M}^\alpha = \cos^2 \alpha (\mathbf{x}_1 \otimes \mathbf{x}_1) + \frac{1}{2} \sin 2\alpha (\mathbf{x}_1 \otimes \mathbf{x}_2 + \mathbf{x}_2 \otimes \mathbf{x}_1) + \sin^2 \alpha (\mathbf{x}_2 \otimes \mathbf{x}_2) \quad (4.7)$$

$$\mathbf{L}^\alpha = \frac{1}{2} [\sin 2\alpha (\mathbf{x}_2 \otimes \mathbf{x}_2 - \mathbf{x}_1 \otimes \mathbf{x}_1) + \cos 2\alpha (\mathbf{x}_1 \otimes \mathbf{x}_2 + \mathbf{x}_2 \otimes \mathbf{x}_1)] \quad (4.8)$$

Now, the symmetric 2D strain tensor ($\epsilon_{12} = \epsilon_{21}$) can be expressed as:

$$\epsilon = \epsilon_{11} (\mathbf{x}_1 \otimes \mathbf{x}_1) + \epsilon_{12} (\mathbf{x}_1 \otimes \mathbf{x}_2 + \mathbf{x}_2 \otimes \mathbf{x}_1) + \epsilon_{22} (\mathbf{x}_2 \otimes \mathbf{x}_2) \quad (4.9)$$

By considering the expressions of projection operators and the 2D strain tensor (eqs. (4.7) to (4.9) respectively), ϵ_m^α and ϵ_l^α thus read:

$$\epsilon_m^\alpha = \cos^2 \alpha \epsilon_{11} + \sin(2\alpha) \epsilon_{12} + \sin^2 \alpha \epsilon_{22} \quad (4.10)$$

$$\epsilon_l^\alpha = \frac{1}{2} \sin(2\alpha) (\epsilon_{11} + \epsilon_{22}) + \cos(2\alpha) \epsilon_{12} \quad (4.11)$$

4.2.2 Derivation of stress tensor

In this section, we derive the continuum stress tensor of the unit volume from the normal and tangential stress components on each microplane. In microplane models, tensor σ is obtained either using the principle of virtual work [BAŽANT and OH, 1985] or a thermodynamic framework [CAROL et al., 2001b, KUHL et al., 2001]. In the first case, the equivalence of the virtual works computed using macroscopic quantities and their microplane counterparts is imposed. In contrast, in the second case, thermodynamically consistent constitutive laws are written at the microplane level. The stress tensor is obtained from the spherical/circular integration of the microplane stresses.

It has to be noted that in the case of spherical microplane system with deviatoric/volumetric split, both the approaches may not lead to the same expression for the stress tensor [CAROL et al., 2001b]. However, in the following, we show that in the case of ‘disk microplane system’ without any volumetric/deviatoric split of the normal component, both the PVW and thermodynamic framework will give the same expression for σ .

4.2.2.1 Using principle of virtual work

Let us denote the normal and tangential stress components on Ω^α as σ_m^α and σ_l^α respectively. Furthermore, let $\epsilon_m^{\alpha*}$ and $\epsilon_l^{\alpha*}$ be the virtual quantities of the normal and tangential strain components on Ω^α . Here, the dissipative processes are assumed to be uniform on Ω (i.e., the same dissipation mechanism is assumed for each microplane), and the stress components are computed at the centroid of each microplane. Hence, the contour of the microplanes can be idealized as a circle, and the work done by the stress and strain components is expressed as an integral over the contour of a circle.

In this context, the PVW states that the total work (in an integral sense) done by the components of stress and strain on the microplane system is equal to the work done by the stress and strain tensors in a unit volume, i.e.,

$$\sigma : \epsilon^* = \frac{1}{\pi} \int_{\Omega} (\sigma_m^\alpha \epsilon_m^{\alpha*} + \sigma_l^\alpha \epsilon_l^{\alpha*}) dS \quad (4.12)$$

where, ϵ^* is the virtual strain tensor at the continuum level.

Now, using the projection operators introduced above for expressing $\epsilon_m^{\alpha*}$ and $\epsilon_l^{\alpha*}$ as functions of an arbitrary strain variation ϵ^* , one can easily obtain the following expression of the stress tensor:

$$\boldsymbol{\sigma} = \frac{1}{\pi} \int_{\Omega} \boldsymbol{\sigma}^{\alpha} dS = \frac{1}{\pi} \int_{\Omega} (\sigma_m^{\alpha} \mathbf{M}^{\alpha} + \sigma_l^{\alpha} \mathbf{L}^{\alpha}) dS \quad (4.13)$$

where, $\boldsymbol{\sigma}^{\alpha} = (\sigma_m^{\alpha} \mathbf{M}^{\alpha} + \sigma_l^{\alpha} \mathbf{L}^{\alpha})$ is the microplane stress tensor. It can be easily verified that the tensor, $\boldsymbol{\sigma}$ is symmetric since \mathbf{M}^{α} and \mathbf{L}^{α} are both symmetric.

4.2.2.2 Using thermodynamic framework

Alternatively, stress tensor can be derived using thermodynamic framework. For this purpose, one defines the free energy potential on each microplane as:

$$\psi^{\alpha} = \psi^{\alpha}(\epsilon_m^{\alpha}, \epsilon_l^{\alpha}, \boldsymbol{\theta}^{\alpha}) \quad (4.14)$$

where, $\boldsymbol{\theta}^{\alpha}$ denotes a vector of internal variables defined on each microplane. Then, the normal and tangential stresses on Ω^{α} are obtained as the first partial derivatives of ψ^{α} with respect to the normal and tangential strain respectively:

$$\sigma_m^{\alpha} = \rho \frac{\partial \psi^{\alpha}}{\partial \epsilon_m^{\alpha}} \quad (4.15)$$

$$\sigma_l^{\alpha} = \rho \frac{\partial \psi^{\alpha}}{\partial \epsilon_l^{\alpha}} \quad (4.16)$$

Now, the free energy potential at the unit volume (ψ) is defined using the following integral relationship:

$$\rho \psi = \frac{1}{\pi} \int_{\Omega} \rho \psi^{\alpha} dS \quad (4.17)$$

By substituting eq. (4.17) in the relation between ψ and $\boldsymbol{\sigma}$ eq. (2.2), we obtain:

$$\boldsymbol{\sigma} = \rho \frac{\partial \psi}{\partial \boldsymbol{\epsilon}} = \frac{1}{\pi} \int_{\Omega} \frac{\partial (\rho \psi^{\alpha})}{\partial \boldsymbol{\epsilon}} dS = \frac{1}{\pi} \int_{\Omega} \rho \left(\frac{\partial \psi^{\alpha}}{\partial \epsilon_m^{\alpha}} \frac{\partial \epsilon_m^{\alpha}}{\partial \boldsymbol{\epsilon}} + \frac{\partial \psi^{\alpha}}{\partial \epsilon_l^{\alpha}} \frac{\partial \epsilon_l^{\alpha}}{\partial \boldsymbol{\epsilon}} \right) dS \quad (4.18)$$

Finally, using kinematic constraints eqs. (4.1) and (4.2), and the definitions of the normal and tangential stresses eqs. (4.15) and (4.16) respectively, we obtain the stress tensor as the same in the previous case (i.e., using PVW):

$$\boldsymbol{\sigma} = \frac{1}{\pi} \int_{\Omega} \boldsymbol{\sigma}^{\alpha} dS = \frac{1}{\pi} \int_{\Omega} (\sigma_m^{\alpha} \mathbf{M}^{\alpha} + \sigma_l^{\alpha} \mathbf{L}^{\alpha}) dS \quad (4.19)$$

4.3 Microplane microdamage model

In this section, we define a scalar isotropic damage constitutive law on each microplane and derive the constitutive model of the unit volume. Damage is considered as the only dissipative mechanism on a given microplane for the sake of simplicity.

We recall that several approaches like plasticity and damage [CAROL and BAŽANT, 1997, KUHL et al., 2001] are available in literature for this purpose. In the original formulation [KUHL and

RAMM, 1998], more than one microdamage variable is used to describe dissipation in each direction in a decoupled manner. It is shown in [OŽBOLT and BAŽANT, 1992] that the decoupled description of microdamage is, however, not suitable for cohesive frictional materials like concrete.

For that reason, we adopt the microplane microdamage model that employ a single microdamage variable [KUHL and RAMM, 2000, FICHANT, 1996]. From a numerical viewpoint, such a choice also leads to a more computationally efficient formulation.

4.3.1 Thermodynamic framework

Free energy The following particular form of the free energy on each microplane can be assumed using the state variables on the microplane (ϵ_m^α and ϵ_l^α) and the microdamage scalar variable ($\omega^\alpha \in [0, 1]$):

$$\rho\psi^\alpha = (1 - \omega^\alpha) \rho\psi_0^\alpha \quad (4.20)$$

where $\rho\psi_0^\alpha$ is the stored elastic energy on each microplane:

$$\rho\psi_0^\alpha = \frac{1}{2} \left[E_m (\epsilon_m^\alpha)^2 + E_l (\epsilon_l^\alpha)^2 \right] \quad (4.21)$$

Here, E_m and E_l are the elastic constants for each microplane in normal and tangential directions respectively.

Conjugate variables Now, substituting eq. (4.20) in eqs. (4.15) and (4.16), the normal and tangential stresses on each microplane are obtained as:

$$\sigma_m^\alpha = \rho \frac{\partial \psi^\alpha}{\partial \epsilon_m^\alpha} = (1 - \omega^\alpha) E_m \epsilon_m^\alpha \quad (4.22)$$

$$\sigma_l^\alpha = \rho \frac{\partial \psi^\alpha}{\partial \epsilon_l^\alpha} = (1 - \omega^\alpha) E_l \epsilon_l^\alpha \quad (4.23)$$

Furthermore, the energy release rate (Y^α) on each microplane is obtained as a conjugate of the internal variable as:

$$Y^\alpha = -\rho \frac{\partial \psi^\alpha}{\partial \omega^\alpha} = \frac{1}{2} \left[E_m (\epsilon_m^\alpha)^2 + E_l (\epsilon_l^\alpha)^2 \right] \quad (4.24)$$

Rate of energy dissipation Using the Clausius–Duhem–Truesdell inequality for a unit volume (2.5), and the integral relations (4.17) and (4.19), we obtain the following relation for the rate of volumetric energy dissipation, $\dot{\phi}_V$ as:

$$\dot{\phi}_V = \frac{1}{\pi} \int_{\Omega} -Y^\alpha \dot{\omega}^\alpha dS = \frac{1}{\pi} \int_{\Omega} \dot{\phi}_V^\alpha dS \geq 0 \quad (4.25)$$

where, $\dot{\phi}_V^\alpha = -Y^\alpha \dot{\omega}^\alpha$ is the rate of energy dissipation on each microplane.

Remark. It is worth noting that a relationship equivalent to Clausius–Duhem–Truesdell inequality on each microplane, that is, $\dot{\phi}_V^\alpha \geq 0$ is not straight forward because of the complex integral eq. (4.25). In fact it is mentioned in the recent M7–model [CANER and BAŽANT, 2013] that: ‘The dissipation rate on each microplane being non–negative is only a sufficient condition, not a necessary one; only the combined dissipation rate on the microplane system must be non–negative, which means that the dissipation can be negative on some microplanes.’

From this discussion, we can consider the following two cases: (i) $\dot{\phi}_V^\alpha \geq 0 \forall \Omega^\alpha$ which directly verifies $\dot{\phi}_V \geq 0$; (ii) $\exists \Omega^\alpha$ such that $\dot{\phi}_V^\alpha \leq 0$, however, $\dot{\phi}_V \geq 0$ is satisfied at the unit volume (eq. (4.25)).

In [CAROL et al., 2001a], the negative dissipation on some microplanes is demonstrated using examples that involve complex loading–unloading behavior laws at the microplane level. However, in the present context of microplane microdamage model, since we use simple constitutive laws at the microplane level, we follow a different approach and derive a threshold on the Poisson’s ratio such that the energy dissipation is non–negative both at the unit volume and the microplane level for any loading–unloading path in section 4.3.2.2.

Internal variable Let us now define ω^α as a function of an internal (history) variable, κ^α as:

$$\omega^\alpha = g(\kappa^\alpha) = 1 - \frac{q(\kappa^\alpha)}{\kappa^\alpha} \quad (4.26)$$

where, $g(\kappa^\alpha)$ is the microdamage evolution function and $q(\kappa^\alpha)$ is the softening function. Here, κ^α is defined as the historical maxima of an equivalent strain measure ($\tilde{\epsilon}^\alpha$) on each microplane as:

$$\kappa^\alpha = \max_t(\tilde{\epsilon}_0^\pi, \tilde{\epsilon}^\alpha(t)) \quad (4.27)$$

where, $\tilde{\epsilon}_0^\pi$ is a threshold equivalent strain corresponding to microdamage activation, t is the present pseudo–time. Notice that in the following, upper-script π will always be used to denote microplane quantities that are independent of the chosen Ω^α .

In the simple formulation proposed in this work, κ^α is defined as:

$$\tilde{\epsilon}^\alpha = \sqrt{(\epsilon_m^{\alpha+})^2 + \beta (\epsilon_l^{\alpha+})^2} \quad (4.28)$$

where, $\epsilon_m^{\alpha+}$ and $\epsilon_l^{\alpha+}$ are defined as the projections of the positive part of the continuum strain tensor (eq. (2.13)) in the respective directions as:

$$\epsilon_m^{\alpha+} = \mathbf{M}^\alpha : \langle \epsilon \rangle^+ \quad (4.29)$$

$$\epsilon_l^{\alpha+} = \mathbf{L}^\alpha : \langle \epsilon \rangle^+ \quad (4.30)$$

and $\beta \geq 0$ is a parameter that takes into account the contribution of the tangential strain to the growth of microdamage. Since cracking in quasi–brittle materials is mainly controlled by extensions [MAZARS, 1984], such a choice seems quite consistent from a physical viewpoint.

Remark. In microplane models with more than one microdamage variable [CAROL and BAŽANT, 1997, KUHLE and RAMM, 1998], the corresponding internal variables are defined using the respective strain components in a decoupled manner. In the case of the proposed microplane microdamage model, the coupling between different components of strain is necessary since we use a single microdamage variable to drive the dissipation in both the normal and tangential directions. This is taken into account by the parameter β appearing in eq. (4.28).

Yield function The yield function (denoted by f^α) is expressed in terms of $\tilde{\epsilon}^\alpha$ on each microplane as:

$$f^\alpha = f^\alpha(\tilde{\epsilon}^\alpha) = \tilde{\epsilon}^\alpha - \kappa^\alpha \quad (4.31)$$

Finally, the Kuhn–Tucker loading–unloading conditions are written for each microplane as:

$$\dot{\omega}^\alpha \geq 0, f^\alpha \leq 0, \dot{\omega}^\alpha f^\alpha = 0 \quad (4.32)$$

Damage evolution law In the present work, we define the softening function as an exponential function of κ^α as:

$$q^\alpha = q(\kappa^\alpha) = \tilde{\epsilon}_0^\pi \exp(-B(\kappa^\alpha - \tilde{\epsilon}_0^\pi)) \quad (4.33)$$

where, B is a material parameter controlling the shape of the damage evolution function.

According to this choice, microdamage growth starts when $\tilde{\epsilon}^\alpha$ reaches the threshold value $\tilde{\epsilon}_0^\pi$ and then evolves exponentially to achieve unity when κ^α tends to infinity. Notice that alternative (linear, bilinear ...) damage evolution models could have been used without major changes to the theoretical framework.

Density of energy dissipation Let g_f be the energy available for unit volume which is dissipated at the end of the fracture process. This can be expressed using the expended power for a unit volume as:

$$g_f = \int_0^\infty \boldsymbol{\sigma} : \dot{\boldsymbol{\epsilon}} dt \quad (4.34)$$

Owing to the representation of the unit volume using microplane system, the relation between the energy dissipation in a unit volume and that of on each microplane is given by:

$$g_f = \int_0^\infty \left[\frac{1}{\pi} \int_\Omega (\sigma_m^\alpha \dot{\epsilon}_m^\alpha + \sigma_l^\alpha \dot{\epsilon}_l^\alpha) dS \right] dt \quad (4.35)$$

where, $\dot{\epsilon}_m^\alpha = \mathbf{M}^\alpha : \dot{\boldsymbol{\epsilon}}$ and $\dot{\epsilon}_l^\alpha = \mathbf{L}^\alpha : \dot{\boldsymbol{\epsilon}}$.

Since microplanes do not interact with each other, eq. (4.35) can be rewritten using the expended power on each microplane (g_f^α) as:

$$g_f = \frac{1}{\pi} \int_\Omega g_f^\alpha dS \quad (4.36)$$

where:

$$g_f^\alpha \equiv \int_0^\infty (\sigma_m^\alpha \dot{\epsilon}_m^\alpha + \sigma_l^\alpha \dot{\epsilon}_l^\alpha) dt \quad (4.37)$$

It has to be noted that the power expended on the microplanes depends on the loading cycle. Now, let us consider a load cycle in which all the available energy in a unit volume is dissipated. This is possible only if all the microplanes dissipate the corresponding available energy at the end of the load cycle (see eqs. (4.36) and (4.37)).

Hence, due to the assumed initial material isotropy, the time integral of the stress power on each microplane is the equal for all the microplane, even though the evolution depends on the phase of the load cycle (importantly, the direction of loading). According to this consideration, g_f^α is the same on all the microplanes (i.e., $g_f^\alpha = g_f^\pi$).

The energy dissipation on each microplane (i.e., the fracture energy density at microplane level) such that energy g_f is dissipated at the continuum level, can now be easily computed from analytical integration of eq. (4.36):

$$g_f^\pi = \frac{g_f}{2} \quad (4.38)$$

4.3.2 Secant stiffness

Secant stiffness tensor can be derived by substituting the constitutive relations on microplanes (eqs. (4.22) and (4.23)) in the stress tensor (4.19) as given below:

$$\begin{aligned}
 \boldsymbol{\sigma} &= \frac{1}{\pi} \int_{\Omega} (\sigma_m^\alpha \mathbf{M}^\alpha + \sigma_l^\alpha \mathbf{L}^\alpha) dS \\
 &= \frac{1}{\pi} \int_{\Omega} [(1 - \omega^\alpha) (E_m \epsilon_m^\alpha \mathbf{M}^\alpha + E_l \epsilon_l^\alpha \mathbf{L}^\alpha)] dS \\
 &= \frac{1}{\pi} \int_{\Omega} (E_m^s \epsilon_m^\alpha \mathbf{M}^\alpha + E_l^s \epsilon_l^\alpha \mathbf{L}^\alpha) dS
 \end{aligned} \tag{4.39}$$

where, E_m^s and E_l^s are the reduced secant stiffness parameters in normal and tangential directions of each microplane:

$$E_m^s = (1 - \omega^\alpha) E_m \tag{4.40}$$

$$E_l^s = (1 - \omega^\alpha) E_l \tag{4.41}$$

Now using the definitions of ϵ_m^α and ϵ_l^α (see eq. (4.1) and eq. (4.2) respectively), eq. (4.39) is rewritten as³:

$$\boldsymbol{\sigma} = \mathbb{C}^s : \boldsymbol{\epsilon} \tag{4.42}$$

where, \mathbb{C}^s is the fourth-order secant damage stiffness tensor:

$$\mathbb{C}^s = \frac{1}{\pi} \int_{\Omega} \mathbb{C}^{\alpha,s} dS \tag{4.43}$$

with:

$$\mathbb{C}^{\alpha,s} = E_m^s (\mathbf{M}^\alpha \otimes \mathbf{M}^\alpha) + E_l^s (\mathbf{L}^\alpha \otimes \mathbf{L}^\alpha) \tag{4.44}$$

Alternatively, this can be written as the reduction of the Hooke's elastic stiffness matrix (\mathbb{E}), due to the evolution of microdamage on the localized microplane as:

$$\mathbb{C}^s = \frac{1}{\pi} \int_{\Omega} (1 - \omega^\alpha) \mathbb{E}^\alpha dS \tag{4.45}$$

$$= \mathbb{E} - \frac{1}{\pi} \int_{\Omega} \omega^\alpha \mathbb{E}^\alpha dS \tag{4.46}$$

where, \mathbb{E} is retrieved using the microplane elastic constants (E_m and E_l) as:

$$\mathbb{E} = \frac{1}{\pi} \int_{\Omega} \mathbb{E}^\alpha dS \tag{4.47}$$

with \mathbb{E}^α denoting the symmetric fourth order tensor defined on each microplane as:

$$\mathbb{E}^\alpha = E_m^\alpha (\mathbf{M}^\alpha \otimes \mathbf{M}^\alpha) + E_l^\alpha (\mathbf{L}^\alpha \otimes \mathbf{L}^\alpha) \tag{4.48}$$

4.3.2.1 Microplane elastic constants

Now, using the plane strain assumption and the relation (4.47), we derive the elastic constants in normal and the tangential directions of the microplane.

³We use the definition of the dyadic product \otimes between second order tensors. Given three second order tensors \mathbf{A} , \mathbf{B} and \mathbf{D} , one has: $(\mathbf{A} \otimes \mathbf{B}) : \mathbf{D} = (\mathbf{B} : \mathbf{D})\mathbf{A}$.

By performing the analytical integration over the surface of a semi-circle, the stress–strain relation is obtained as:⁴

$$\begin{Bmatrix} \sigma_{11} \\ \sigma_{22} \\ \sigma_{21} \end{Bmatrix} = \frac{1}{4} \begin{bmatrix} 3E_m + E_l & E_m - E_l & 0 \\ E_m - E_l & 3E_m + E_l & 0 \\ 0 & 0 & 2(E_m + E_l) \end{bmatrix} \begin{Bmatrix} \epsilon_{11} \\ \epsilon_{22} \\ \epsilon_{21} \end{Bmatrix} \quad (4.50)$$

The stress–strain relation using the Hooke's law in a plane strain condition is given by:

$$\begin{Bmatrix} \sigma_{11} \\ \sigma_{22} \\ \sigma_{21} \end{Bmatrix} = \begin{bmatrix} \lambda + 2\mu & \lambda & 0 \\ \lambda & \lambda + 2\mu & 0 \\ 0 & 0 & 2\mu \end{bmatrix} \begin{Bmatrix} \epsilon_{11} \\ \epsilon_{22} \\ \epsilon_{21} \end{Bmatrix} \quad (4.51)$$

where, λ and μ are Lamé's constants given in terms of the Young's modulus E and the Poisson's ratio ν . Now, using the equivalence between eqs. (4.50) and (4.51), we obtain the following microplane elastic constants after some algebraic manipulations:

$$E_m = 2(\lambda + \mu) \quad (4.52)$$

$$E_l = 2(\mu - \lambda) \quad (4.53)$$

More details about the analytical derivation of microplane elastic constants are given in appendix 7.2.

4.3.2.2 Effect of ν on $\dot{\phi}_V^\alpha$

Here, we obtain the range of Poisson's ratio for which the energy dissipation on each microplane (section 4.3.1) stays non-negative. By substituting the elastic constants (4.52), (4.53) in the eq. (4.24) we get the following expression for $\dot{\phi}_V^\alpha$:

$$\dot{\phi}_V^\alpha = -Y^\alpha \dot{\omega}^\alpha = \frac{1}{2} \left[2(\lambda + \mu) (\epsilon_m^\alpha)^2 + 2(\mu - \lambda) (\epsilon_l^\alpha)^2 \right] \dot{\omega}^\alpha \quad (4.54)$$

Now, in the present context of microplane microdamage model, given that the Kuhn–Tucker loading–unloading conditions (4.32) are satisfied, the rate of microdamage growth is always non-negative, that is, $\dot{\omega}^\alpha \geq 0$. Hence, from eq. (4.54), non-negative energy dissipation at the microplane level is possible only if the energy release rate is negative. That is,

$$Y^\alpha < 0 \implies \frac{1}{2} \left[2(\lambda + \mu) (\epsilon_m^\alpha)^2 + 2(\mu - \lambda) (\epsilon_l^\alpha)^2 \right] > 0 \implies \left(\frac{\epsilon_m^\alpha}{\epsilon_l^\alpha} \right)^2 > \frac{-(\mu - \lambda)}{(\lambda + \mu)} \quad (4.55)$$

Now, the expressions $(\epsilon_m^\alpha/\epsilon_l^\alpha)^2$ and $(\lambda + \mu)$ are always non-negative for any loading–unloading path and all values of μ and λ . Hence, the condition (4.55) is satisfied for all loading–unloading paths if $\mu - \lambda > 0$, that is $\nu < 0.25$. Since this is the case for concrete, the non-negative energy dissipation both at the unit volume and on each microplane is ensured in this work.

⁴Components $\sigma_{ij} = \mathbf{x}_i \cdot \boldsymbol{\sigma} \cdot \mathbf{x}_j$ of the stress tensor can be easily computed as:

$$\sigma_{ij} = \frac{1}{\pi} \int_{\Omega} (E_m \epsilon_m^\alpha M_{ij}^\alpha + E_l \epsilon_l^\alpha L_{ij}^\alpha) dS \quad (4.49)$$

4.3.3 Tangent stiffness

Tangent stiffness tensor can be derived by rewriting the constitutive relations on microplanes in the rate form as:

$$\dot{\sigma}_m^\alpha = (1 - \omega^\alpha) E_m \dot{\epsilon}_m^\alpha - \dot{\omega}^\alpha E_m \epsilon_m^\alpha = E_m^s \dot{\epsilon}_m^\alpha - \dot{\omega}^\alpha E_m \epsilon_m^\alpha \quad (4.56)$$

$$\dot{\sigma}_l^\alpha = (1 - \omega^\alpha) E_l \dot{\epsilon}_l^\alpha - \dot{\omega}^\alpha E_l \epsilon_l^\alpha = E_l^s \dot{\epsilon}_l^\alpha - \dot{\omega}^\alpha E_l \epsilon_l^\alpha \quad (4.57)$$

The rate of variation of the damage variable ($\dot{\omega}^\alpha$) is given by:

$$\dot{\omega}^\alpha(\kappa^\alpha) = (g^\alpha)' \dot{\kappa}^\alpha \quad (4.58)$$

where, $(g^\alpha)' = dg^\alpha/d\kappa^\alpha$ is the derivative of the damage function with respect to κ^α , which is obtained using eqs. (4.26) and (4.33) as:

$$(g^\alpha)' = \left[\frac{B}{\kappa^\alpha} + \left(\frac{1}{\kappa^\alpha} \right)^2 \right] \tilde{\epsilon}_0 \exp(-B(\kappa^\alpha - \epsilon_0^\pi)) \quad (4.59)$$

and

$$\dot{\kappa}^\alpha = \eta_m^\alpha \dot{\epsilon}_m^\alpha + \eta_l^\alpha \dot{\epsilon}_l^\alpha \quad (4.60)$$

where, η_m^α and η_l^α are the derivatives of κ^α with respect to ϵ_m^α and ϵ_l^α respectively:

$$\frac{d\kappa^\alpha}{d\epsilon_m^\alpha} = \frac{\epsilon_m^{\alpha+}}{\tilde{\epsilon}^\alpha} = \eta_m^\alpha \quad (4.61)$$

$$\frac{d\kappa^\alpha}{d\epsilon_l^\alpha} = \beta \frac{\epsilon_l^{\alpha+}}{\tilde{\epsilon}^\alpha} = \eta_l^\alpha \quad (4.62)$$

Now, the stress tensor can be rewritten in rate form as:

$$\dot{\sigma} = \frac{1}{\pi} \int_{\Omega} (\dot{\sigma}_m^\alpha \mathbf{M}^\alpha + \dot{\sigma}_l^\alpha \mathbf{L}^\alpha) dS \quad (4.63)$$

By substituting the constitutive relations eqs. (4.23) and (4.56) in eq. (4.63), and using the rate of microdamage evolution eq. (4.58), we obtain the following relation:

$$\begin{aligned} \dot{\sigma} = \frac{1}{\pi} \int_{\Omega} \{ [1 - \omega^\alpha - (g^\alpha)'(\eta_m^\alpha \dot{\epsilon}_m^\alpha + \eta_l^\alpha \dot{\epsilon}_l^\alpha) \epsilon_m^\alpha] E_m \epsilon_m^\alpha \mathbf{M}^\alpha \\ + [1 - \omega^\alpha - (g^\alpha)'(\eta_m^\alpha \dot{\epsilon}_m^\alpha + \eta_l^\alpha \dot{\epsilon}_l^\alpha) \epsilon_l^\alpha] E_l \epsilon_l^\alpha \mathbf{L}^\alpha \} dS \end{aligned} \quad (4.64)$$

Now, using the kinematic relations (eqs. (4.1) and (4.2)) in rate form, and after some mathematical manipulations, we obtain the constitutive relation at the unit volume in the rate form as:

$$\dot{\sigma} = \mathbb{C}^t : \dot{\epsilon} \quad (4.65)$$

where, \mathbb{C}^t is fourth order tangent stiffness tensor given by:

$$\begin{aligned} \mathbb{C}^t = \frac{1}{\pi} \int_{\Omega} \{ [1 - \omega^\alpha - (g^\alpha)' \eta_m^\alpha \epsilon_m^\alpha] E_m (\mathbf{M}^\alpha \otimes \mathbf{M}^\alpha) + [1 - \omega^\alpha - (g^\alpha)' \eta_l^\alpha \epsilon_l^\alpha] \\ E_l (\mathbf{L}^\alpha \otimes \mathbf{L}^\alpha) - (g^\alpha)' \eta_m^\alpha E_l \epsilon_l^\alpha (\mathbf{L}^\alpha \otimes \mathbf{M}^\alpha) - (g^\alpha)' \eta_l^\alpha E_m \epsilon_m^\alpha (\mathbf{M}^\alpha \otimes \mathbf{L}^\alpha) \} dS \end{aligned} \quad (4.66)$$

or equivalently by:

$$\begin{aligned} \mathbb{C}^t = \mathbb{C}^s - \frac{1}{\pi} \int_{\Omega} (g^\alpha)' [\eta_m^\alpha \epsilon_m^\alpha E_m (\mathbf{M}^\alpha \otimes \mathbf{M}^\alpha) + \eta_l^\alpha \epsilon_l^\alpha E_l (\mathbf{L}^\alpha \otimes \mathbf{L}^\alpha) \\ + \eta_m^\alpha E_l \epsilon_l^\alpha (\mathbf{L}^\alpha \otimes \mathbf{M}^\alpha) + \eta_l^\alpha E_m \epsilon_m^\alpha (\mathbf{M}^\alpha \otimes \mathbf{L}^\alpha)] dS \end{aligned} \quad (4.67)$$

From eq. (4.67), it can be easily noted that in the case of unloading (i.e., $\dot{\omega}^\alpha = 0$ for all microplanes) the tangent and secant stiffness tensors are identical.

In addition to that, the tangent stiffness tensor can also be written in more concise form as:

$$\mathbb{C}^t = \frac{1}{\pi} \int_S [\mathbb{C}^{\alpha,s} - (g^\alpha)' (\tilde{\sigma}^\alpha \otimes \boldsymbol{\eta}^\alpha)] \quad (4.68)$$

or equivalently as:

$$\mathbb{C}^t = \mathbb{C}^s - \frac{1}{\pi} \int_\Omega (g^\alpha)' (\tilde{\sigma}^\alpha \otimes \boldsymbol{\eta}^\alpha) dS \quad (4.69)$$

where $\tilde{\sigma}^\alpha$ is the effective (elastic) microplane stress tensor:

$$\tilde{\sigma}^\alpha = E_m \epsilon_m^\alpha \mathbf{M}^\alpha + E_l \epsilon_l^\alpha \mathbf{L}^\alpha \quad (4.70)$$

and tensor $\boldsymbol{\eta}^\alpha$ is the derivative of the internal variable with respect to the total strain tensor:

$$\boldsymbol{\eta}^\alpha = \frac{d\kappa^\alpha}{d\boldsymbol{\epsilon}} = \eta_m^\alpha \mathbf{M}^\alpha + \eta_l^\alpha \mathbf{L}^\alpha \quad (4.71)$$

Remark. It can be easily identified that the tangent damage stiffness tensor (4.68) of the microplane microdamage model has the same form as the corresponding ones of other continuum isotropic/anisotropic damage models [JIRÁSEK, 2016].

4.3.4 Loss of ellipticity of the rate equilibrium problem

In this section, we derive the conditions for which strain localization occurs when the material behavior is modeled using microplane microdamage model. Mathematically, the localization of strain into a band (whose outward normal is \mathbf{n}) is understood as the discontinuous bifurcation solution of the rate equilibrium problem due to the loss of ellipticity [HILL, 1958, HILL, 1962, RICE, 1976]. The later is associated with the so called acoustic tensor (\mathbf{Q}), which is defined in terms of the material tangent stiffness tensor as:

$$\mathbf{Q} = \mathbf{n} \cdot \mathbb{C}^t \cdot \mathbf{n} \quad (4.72)$$

Now, the localization analysis consists in finding the unit vector \mathbf{n} for which the acoustic tensor \mathbf{Q} becomes singular, that is:

$$\det \mathbf{Q} = 0 \quad (4.73)$$

where, ' $\det(\bullet)$ ' denotes the determinant of second-order tensor (\bullet).

By substituting the expression of \mathbb{C}^t , (4.66) in eq. (4.72), we obtain the acoustic tensor in the case of microplane microdamage model as:

$$\begin{aligned} \mathbf{Q} &= \mathbf{n} \cdot \left[\frac{1}{\pi} \int_\Omega [\mathbb{C}^{\alpha,s} - (g^\alpha)' (\tilde{\sigma}^\alpha \otimes \boldsymbol{\eta}^\alpha)] dS \right] \cdot \mathbf{n} \\ &= \frac{1}{\pi} \int_\Omega \mathbf{Q}^\alpha dS \end{aligned} \quad (4.74)$$

where:

$$\begin{aligned} \mathbf{Q}^\alpha &= \mathbf{n} \cdot [\mathbb{C}^{\alpha,s} - (g^\alpha)' (\tilde{\sigma}^\alpha \otimes \boldsymbol{\eta}^\alpha)] \cdot \mathbf{n} \\ &= \mathbf{n} \cdot \mathbb{C}^{\alpha,s} \cdot \mathbf{n} - (g^\alpha)' \tilde{\sigma}_n^\alpha \otimes \boldsymbol{\eta}_n^\alpha \end{aligned} \quad (4.75)$$

with $\tilde{\sigma}_n^\alpha = \mathbf{n} \cdot \tilde{\sigma}^\alpha$ and $\boldsymbol{\eta}_n^\alpha = \boldsymbol{\eta}^\alpha \cdot \mathbf{n}$, is the localization tensor defined on each microplane that gives the contribution of each microplane to the strain localization in the direction of \mathbf{n} .

Remark. It has to be noted that the loss of ellipticity of the rate equilibrium problem is associated to the acoustic tensor (\mathbf{Q}) which in turn is only associated to the integral of localization tensors from all the microplanes and not the individual contributions (\mathbf{Q}^α).

In general, several solutions of \mathbf{n} that satisfy the localization condition (4.73) are possible. In the standard localization analysis, a complementary condition is defined on an internal variable ($\tilde{\epsilon}^\alpha$ in this case) to find the potential discontinuity plane, \mathbf{n}_{crit} . But in the present context, this would require to perform an analytical integration which is not possible in general loading cases.

However, the localization analysis of the microplane model can be performed numerically [KUHL and RAMM, 1998] by choosing \mathbf{n} as the normal (\mathbf{m}^α) of each microplane. Then, a set containing the determinant of the acoustic tensors that satisfies the localization condition (denoted by L) is obtained as:

$$L = \{ \det \mathbf{Q}_{\mathbf{n}=\mathbf{m}^\alpha} \mid \det \mathbf{Q}_{\mathbf{n}=\mathbf{m}^\alpha} = \mathbf{m}^\alpha \cdot \mathbb{C}^t \cdot \mathbf{m}^\alpha \forall \mathbf{m}^\alpha \in \Omega; \det \mathbf{Q}_{\mathbf{n}=\mathbf{m}^\alpha} \leq 0 \} \quad (4.76)$$

Finally, \mathbf{n}_{crit} is chosen as normal of the microplane that corresponds to the critical determinant of the acoustic tensor (denoted by $\det \mathbf{Q}_{\mathbf{n}=\mathbf{n}_{crit}}$) which is defined as the minimum in L as:

$$\mathbf{n}_{crit} = \min_{\mathbf{m}^\alpha} [\det \mathbf{m}^\alpha \cdot \mathbb{C}^t \cdot \mathbf{m}^\alpha] \quad (4.77)$$

$$\det \mathbf{Q}_{\mathbf{n}=\mathbf{n}_{crit}} = \det(\mathbf{n}_{crit} \cdot \mathbb{C}^t \cdot \mathbf{n}_{crit}) \quad (4.78)$$

Now, if the condition for loss of ellipticity (4.73) is satisfied, then there exists a non-trivial vector \mathbf{r} such that:

$$\mathbf{Q}_{\mathbf{n}=\mathbf{n}_{crit}} \cdot \mathbf{r} = \frac{1}{\pi} \int_{\Omega} \mathbf{Q}_{\mathbf{n}=\mathbf{n}_{crit}}^\alpha dS \cdot \mathbf{r} = \mathbf{0} \quad (4.79)$$

Here, \mathbf{r} is the eigenvector of \mathbf{Q} corresponding to the direction of discontinuity in the strain field. Also, the mode of opening depends on inclination of \mathbf{r} with respect to \mathbf{n} . If \mathbf{r} is parallel to \mathbf{n} then the localization band opens in mode I without sliding while for other cases, a mixed mode opening occurs.

Remark. As for other microplane models, loss of ellipticity condition for the proposed model cannot be studied in an analytic way as in standard damage models (except for some simple loading path and simplified model). However, this study can be done numerically by computing microplane acoustic tensors \mathbf{Q}^α and finding the vector \mathbf{n}_{crit} given by eq. (4.77). Then one can identify vector \mathbf{r} . Furthermore, a criterion on each microplane equivalent to localization criterion (4.73) such as $\det \mathbf{Q}^\alpha = 0$ cannot be established because of the integral relation (4.74). In other words, localization has to be studied at the material point, since it concerns the rate equilibrium problem.

Further investigations on the implications of the integral relation (4.74) on the loss of ellipticity for uniaxial tension are carried out in the section 4.5.1 using a numerical example.

4.4 Numerical implementation of the microplane microdamage model

In a nonlinear finite element context, the microplane micro damage model is used at each Gauss integration point in order to evaluate the stress tensor and elementary stiffness matrices. From a computational viewpoint, this can be achieved easily by projecting the strain tensor on microplanes and then use relationships introduced above for computing the stress tensor and material stiffness at the continuum level from integration of the corresponding microplane quantities.

4.4.1 Integration of microplane quantities

A huge literature exist concerning spherical integration techniques for microplane models based on spherical representation of the microplane system. These schemes are developed based on either theory of orthogonal polynomials, for example, Stroud's integration scheme [STROUD, 1971] and Lebedev's integration scheme [LEBEDEV and LAIKOV, 1999] or the Taylor's series expansion of the function on the surface of the sphere (bazant's integration scheme [BAŽANT and OH, 1986]). The efficiency of the integration schemes depends on the invariance of the stress-strain response with respect to an arbitrary rigid body rotations of the set of integration points. All the developed integration formulae possess symmetry with respect to the center of the sphere. Due to this, the integration is performed over an hemisphere instead of a full sphere.

In this work, given the symmetry of the domain and because function σ^α is periodic with period π (i.e., $\sigma^\alpha = \sigma^{\alpha+\pi}$) the integration in eq. (4.19) is restricted to the contour of a unit semi-circle. The half microplane system Ω is then discretized as the set of N^α microplanes of normal \mathbf{m}^α , such that one microplane is always orthogonal to \mathbf{x}_1 (i.e., $\alpha = 0^\circ$). As a consequence, the inclination of the i -th microplane with respect to the horizontal axis is $(i - 1)180^\circ/N^\alpha$. Alternatively, if both microplanes whose normal corresponds to $\alpha = 0^\circ$ and $\alpha = 180^\circ$, the inclination of the i -th microplane with respect to the horizontal axis can be obtained as $(i - 1)180^\circ/(N^\alpha - 1)$. Note that for $N^\alpha = 2$, we can include either the microplane whose normal corresponds to $\alpha = 0^\circ$ or $\alpha = 180^\circ$ but not both.⁵

The stress tensor σ is finally obtained as:

$$\sigma = \frac{2}{\pi} \sum_{N^\alpha} (\sigma_m^\alpha \mathbf{M}^\alpha + \sigma_l^\alpha \mathbf{L}^\alpha) W^\alpha \quad (4.80)$$

where, $W^\alpha = \pi/N^\alpha$ is the weight associated to each microplane (equal in all directions in the present case). The same integration formula is used for other quantities (stiffness tensor, dissipated energy...) which are defined through circular integration on microplanes.

As it will be shown later, the chosen method is well suited for the purpose of the present work despite its relative simplicity.

4.4.2 Energetic regularization

Since the volumetric energy density of the microplane microdamage model is not an objective quantity, a characteristic length (l_c) is required to obtain mesh independent solutions in the context of FEM. In literature, microplane models are regularized using crack band [ČERVENKA et al., 2005], nonlocal [BAŽANT and di LUZIO, 2004] and gradient enhanced [ZREID and KALISKE, 2018] approaches, among others. In a finite element context, these formulation leads to restore mesh independence of the obtained results. They impose, however, additional computational costs due to the need of computing averaged quantities that drive the damage evolution (e.g., in nonlocal models) or to solve an additional diffusion-like equation (e.g., in gradient formulations).

An alternative approach that is commonly used in the literature [JIRÁSEK and BAUER, 2012, XENOS and GRASSL, 2014] in order to reduce mesh sensitivity, with a moderate computational cost, is based upon the so-called 'energetic regularization' technique [PIETRUSZCZAK and MROZ, 1981, BAŽANT and OH, 1983]. According to this approach, a length l_c is introduced into the constitutive equations using a direct relationship between the volumetric and the surface energy densities as follows:

$$g_f = \frac{G_f}{l_c} \quad (4.81)$$

⁵As an example of this, for $N^\alpha = 2$, the two considered microplanes are such that α is equal to 0° and 90° respectively. For $N^\alpha = 3$ one considers three microplanes with normal vectors inclined of 0° , 60° and 120° respectively with respect to the horizontal axis. Following the second approach, for $N^\alpha = 21$, microplanes are inclined at 0° , $9^\circ \dots 180^\circ$.

The relation (4.81) says that the volumetric energy dissipated in an unit l_c is taken equal to the energy required to create an unit crack surface which can be considered as a material property, in other words, an objective quantity. Length, l_c is defined using the characteristics of the mesh [OLIVER, 1989, JIRÁSEK and BAUER, 2012], e.g., the type of finite element and its size⁶. For example, in the case of 1D finite elements, l_c can be defined as the size of the element. In the case of higher dimensional finite elements, l_c is defined as a certain measure of the element.

Volumetric energy density Now, substituting eq. (4.81) in the relationship (4.38) between energy dissipation density on each microplane and that of a unit volume, we obtain the following relationship:

$$g_f^\pi = \frac{G_f}{2l_c} \quad (4.82)$$

By substituting the expression for the power expended on each microplane (4.37) in eq. (4.82), we get:

$$\frac{G_f}{2l_c} = \int_0^\infty (\sigma_m^\alpha \dot{\epsilon}_m^\alpha + \sigma_l^\alpha \dot{\epsilon}_l^\alpha) dt \quad (4.83)$$

Substituting eqs. (4.22) and (4.23) in eq. (4.83) we obtain:

$$\frac{G_f}{2l_c} = \int_0^\infty (1 - \omega^\alpha) (E_m \epsilon_m^\alpha \dot{\epsilon}_m^\alpha + E_l \epsilon_l^\alpha \dot{\epsilon}_l^\alpha) dt \quad (4.84)$$

Regularized damage evolution model Given the exponential damage evolution law (4.26), the energetic regularization problem comes into finding the scalar parameter $B = B(l_c)$ such that:

$$\frac{G_f}{2l_c} = \int_0^{t_0} (E_m \epsilon_m^\alpha \dot{\epsilon}_m^\alpha + E_l \epsilon_l^\alpha \dot{\epsilon}_l^\alpha) dt + \int_{t_0}^\infty \frac{\tilde{\epsilon}_0^\pi}{\kappa^\alpha} \exp(-B(\kappa^\alpha - \tilde{\epsilon}_0^\pi)) (E_m \epsilon_m^\alpha \dot{\epsilon}_m^\alpha + E_l \epsilon_l^\alpha \dot{\epsilon}_l^\alpha) dt \quad (4.85)$$

where, t_0 is the time instant at which the microplane equivalent strain reaches the strain level corresponding to damage activation.

This requires analytically integrating previous equation, which is possible only for the hypothetical case of $\nu = 0$ (i.e., $E_m = E_l = E$) and $\beta = 1$. Consider a uniaxial tensile loading in the direction of axis 2 (or equivalently 1), i.e., $\epsilon = \epsilon_{22} \mathbf{x}_2 \otimes \mathbf{x}_2$. Since in this case $\epsilon_m^{\alpha+} = \epsilon_m = \sin^2 \alpha \epsilon_{22}$ and $\epsilon_l^{\alpha+} = \epsilon_l = \sin \alpha \cos \alpha \epsilon_{22}$, the first term of previous equation reads:

$$E \int_0^t (\epsilon_m^\alpha \dot{\epsilon}_m^\alpha + \epsilon_l^\alpha \dot{\epsilon}_l^\alpha) dt = E \sin^2 \alpha \int_0^t \epsilon_{22} d\epsilon_{22} = E \int_0^{\tilde{\epsilon}_0^\pi} \tilde{\epsilon}^\alpha d\tilde{\epsilon}^\alpha = \frac{1}{2} E (\tilde{\epsilon}^\alpha)^2 \quad (4.86)$$

where, we used the relationship $\tilde{\epsilon}^\alpha = \epsilon_{22} \sin \alpha$. Furthermore, during the damaging phase, the history variable and its rate of variation (4.60) read:

$$\kappa^\alpha = \tilde{\epsilon}^\alpha \quad \text{and} \quad \dot{\kappa}^\alpha = \frac{\epsilon_m^\alpha \dot{\epsilon}_m^\alpha + \epsilon_l^\alpha \dot{\epsilon}_l^\alpha}{\tilde{\epsilon}^\alpha}. \quad (4.87)$$

So, we can rewrite the second contribution figuring in eq. (4.85) in terms of the sole variable κ^α . As a consequence, eq. (4.85) can be rewritten as:

$$\frac{G_f - E (\tilde{\epsilon}^\alpha)^2 l_c}{2l_c} = E \tilde{\epsilon}_0^\pi \int_{\tilde{\epsilon}_0^\pi}^\infty \exp(-B(\kappa^\alpha - \tilde{\epsilon}_0^\pi)) d\kappa^\alpha \quad (4.88)$$

⁶We recall that in other regularization methods like the nonlocal methods, l_c has a physical meaning in that it measures the fracture process zone.

for each microplane, except the one with \mathbf{m}^α orthogonal to the loading direction.

Finally, after performing the analytical integration, the material parameter B is obtained in terms of l_c as:

$$B = \frac{2E\tilde{\epsilon}_0^\pi l_c}{G_f - E(\tilde{\epsilon}_0^\pi)^2 l_c} \quad (4.89)$$

Even though we consider here the case of $\nu = 0$ (and $\beta = 1$) for the sake of analytical integration, we study the influence of non-zero Poisson's ratio, $\nu = 0.2$ (and $\beta = 1$) using a numerical example in the section 4.5.2.

4.5 Numerical case studies

In this section, we present the numerical test cases to study different aspects of the microplane microdamage model. First, we illustrate the projection operation and the thermodynamic consistency of the microplane microdamage model. This is followed by the study on the influence of the parameters of the constitutive model and the numerical integration. Later, the mesh dependency studies of the proposed model are performed. Finally, the advantages of the microplane model in handling the anisotropic damage growth are highlighted.

4.5.1 Uniaxial tensile loading

In order to illustrate the characteristic behavior of the microplane microdamage model, a numerical experiment with a uniaxial tensile loading is performed.

4.5.1.1 Problem setting

We consider a unit concrete specimen which is discretized using 2 CST elements (fig. 4.2) and apply the loading (vertical imposed displacements) on the upper boundary whereas the bottom boundary is constrained. Here, the only dissipation mechanism considered is the damage growth and no cracks are initiated. The material parameters of the microplane microdamage model are also shown in fig. 4.2.

Here, we chose the value of the parameter β as 1 in order to completely take into account the contribution of ϵ_t^α for $\tilde{\epsilon}^\alpha$. Also, $N^\alpha = 361$ which gives a microplane for each 0.5° is chosen to

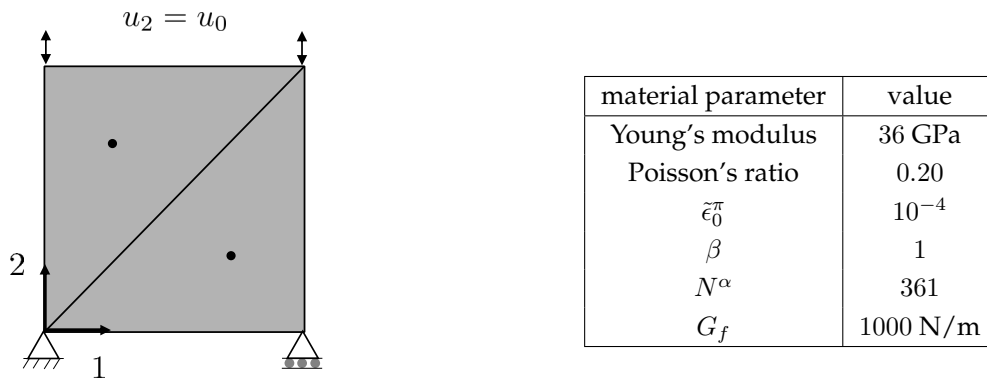


Figure 4.2: FE discretization of the specimen (1 m × 1 m) under vertical loading (a) and the material parameters of microplane microdamage model (b)

ensure a sufficient accuracy for the numerical integration. A detailed analysis of the response of the microplane microdamage model for other values of these parameters is studied later in the section 4.5.2. Finally, the reference axis to compute the angle α of the normal \mathbf{m}^α of a given microplane is chosen as the axis 1 aligned in the horizontal direction (fig. 4.2).

Preliminary considerations Given the simple geometrical and loading conditions, the expressions of ϵ_m^α and ϵ_l^α can be derived analytically by considering the state of strain at the Gauss point given by:

$$\boldsymbol{\epsilon} = \epsilon_{22}(-\nu \mathbf{x}_1 \otimes \mathbf{x}_1 + \mathbf{x}_2 \otimes \mathbf{x}_2) \quad (4.90)$$

where $\epsilon_{22} = u_2$ because of unit specimen. Using eqs. (4.10) and (4.11), the normal and tangential microplane strains can therefore be expressed as:

$$\epsilon_m^\alpha = \epsilon_{22}(-\nu \cos^2 \alpha + \sin^2 \alpha), \quad \epsilon_l^\alpha = \epsilon_{22}(1 - \nu) \cos \alpha \sin \alpha \quad (4.91)$$

Furthermore, since:

$$\langle \boldsymbol{\epsilon} \rangle^+ = \epsilon_{22} \mathbf{x}_2 \otimes \mathbf{x}_2 \quad (4.92)$$

one has that:

$$\epsilon_m^{\alpha+} = \sin^2 \alpha \epsilon_{22}, \quad \epsilon_l^{\alpha+} = \sin \alpha \cos \alpha \epsilon_{22} \quad (4.93)$$

So:

$$\tilde{\epsilon}^\alpha = \epsilon_{22} \sin \alpha \quad (4.94)$$

From previous equations, it can be noted that the microplanes corresponding to $\alpha = 0^\circ$ and $\alpha = 180^\circ$ stay in the compression regime (i.e., $\epsilon_m^\alpha = -\nu \epsilon_{22}$ and $\epsilon_l^\alpha = 0$) through out the loading history, whereas microplane corresponding to $\alpha = 90^\circ$ is under pure tension.

Moreover, damage evolution is driven by ϵ_{22} through the internal variable $\tilde{\epsilon}^\alpha = \epsilon_{22} \sin \alpha$. In other words, for the microplanes corresponding to $\alpha = 0^\circ$ and $\alpha = 180^\circ$ the history variable κ^α stay at ϵ_0^π throughout the loading process (i.e., no damage occurs), whereas $\kappa^\alpha = \max_t(\tilde{\epsilon}_0^\pi, \epsilon_{22}(t))$ for the microplane corresponding to $\alpha = 90^\circ$.

4.5.1.2 Global and local responses

Global response The global response of the specimen is shown in fig. 4.3. As expected, the reaction force first increases linearly (elastic phase). Then a softening phase, corresponding to the progressive evolution of microdamage at microplanes level is obtained.

Distribution profiles of strain components Here, we study the evolution of the local quantities (at Gauss point level) by plotting the corresponding distribution profiles over the microplanes.

The evolution of the distribution profiles of ϵ_m^α and ϵ_l^α computed at different points along the global curve (fig. 4.3) are given in figs. 4.4a and 4.4b respectively. It can be easily noticed that the distribution of ϵ_m^α is symmetric with respect to the direction of loading, while the distribution of ϵ_l^α is anti-symmetric with respect to the direction of loading.

The maximum value of ϵ_m^α occurs on the microplane corresponding to $\alpha = 90^\circ$ (fig. 4.4a) which is aligned with the direction of the loading. In the case of ϵ_l^α , the absolute maximum value occurs on the microplanes corresponding to $\alpha = 45^\circ$ and $\alpha = 135^\circ$ (fig. 4.4b), whose inclination with the direction of the loading is 45° in clockwise and anti-clockwise sense respectively.

These numerical results are in accordance with the analytical expressions obtained by the projection operation in the case of uniaxial loading. It can also be verified numerically that the microplanes whose normal ($\alpha = 0^\circ$ and $\alpha = 180^\circ$ in fig. 4.4a) is orthogonal to the direction of loading

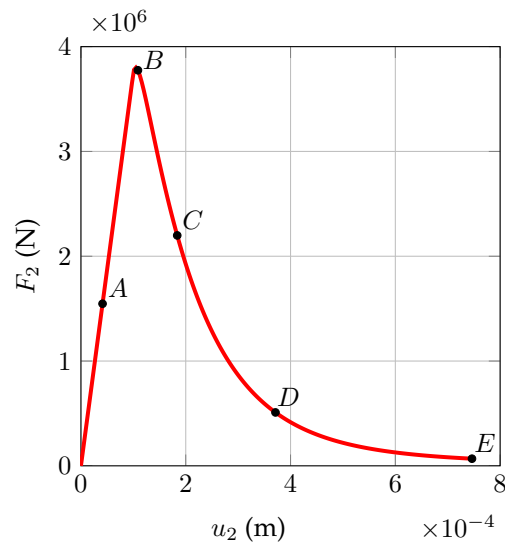


Figure 4.3: Force–displacement curve in vertical direction characterized by the softening response of the microplane microdamage model

are in the compression regime in normal direction due to the Poisson’s effect. It can also be observed from fig. 4.4a that as the loading progress there is a regime change for some microplanes from compression to tension in the normal direction.

The evolution of the distribution profiles of $\tilde{\epsilon}^\alpha$ is shown in fig. 4.5. Owing to the projection of the positive part of the strain tensor, the contribution of the microplanes in the compression regime to $\tilde{\epsilon}^\alpha$ is not taken into account. Given the definition of $\tilde{\epsilon}^\alpha$ (eq. (4.28)), it is expected to stay positive throughout the loading history which is observed.

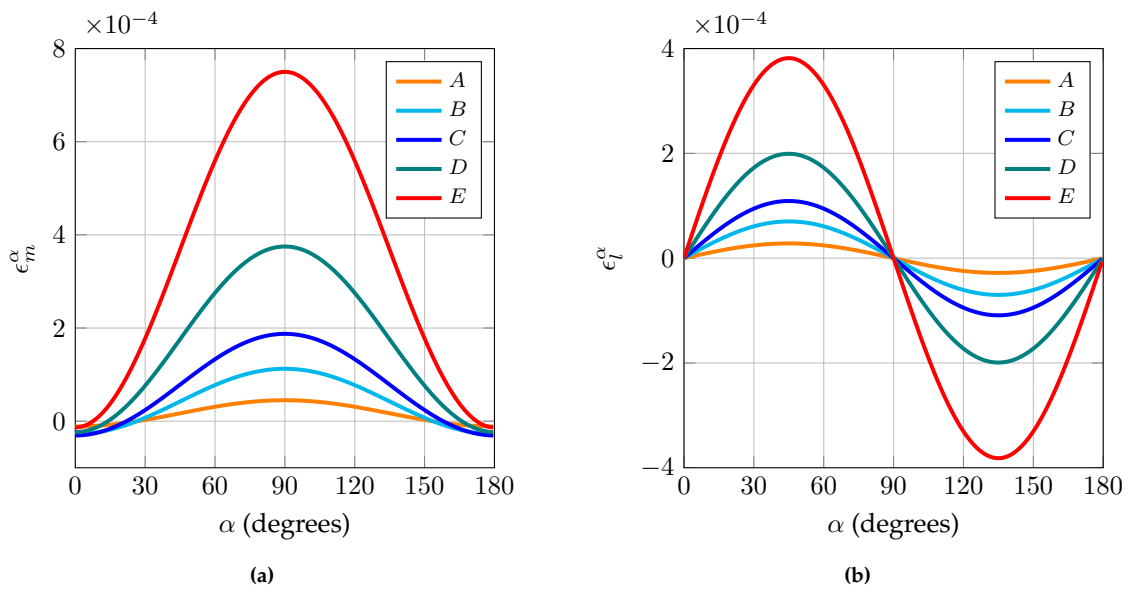


Figure 4.4: Distribution profiles of ϵ_m^α (a) and ϵ_l^α (b) over the microplane system at various stages of uniaxial loading in vertical direction

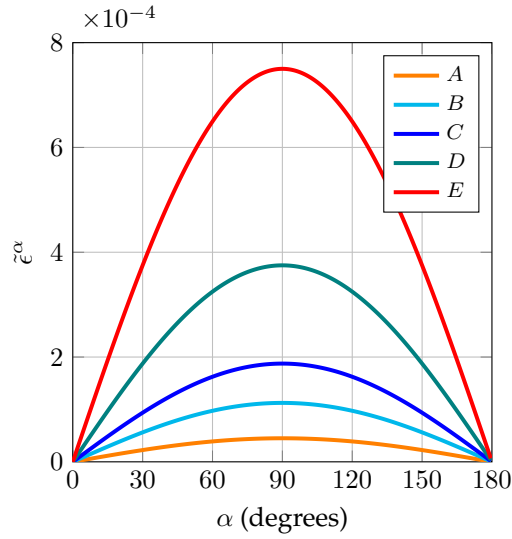


Figure 4.5: Distribution profiles of $\tilde{\epsilon}^\alpha$ over the microplane system at various stages of uniaxial loading in vertical direction

Distribution profiles of stress components The distributions of σ_m^α and σ_l^α before the peak follow the same trend as ϵ_m^α and ϵ_l^α , as shown in figs. 4.6a and 4.6b respectively. Before the load peak, the maximum value of σ_m^α occurs on the microplane $\alpha = 90^\circ$ while the absolute maximum value of σ_l^α occurs on the microplanes corresponding to $\alpha = 45^\circ$ and $\alpha = 135^\circ$.

Now, the elastic limits of σ_m^α and σ_l^α just before the initiation of microdamage can be computed as $E_m(\epsilon_m^\alpha)_{\tilde{\epsilon}^\alpha = \tilde{\epsilon}_0^\alpha} = 5 \times 10^6$ Pa and $E_l(\epsilon_l^\alpha)_{\tilde{\epsilon}^\alpha = \tilde{\epsilon}_0^\alpha} = 6.25 \times 10^5$ Pa. But the maximum values of the distributions of σ_m^α and σ_l^α at the peak (B in the figs. 4.6a and 4.6b respectively) does not correspond to the respective elastic limits, because the microdamage is initiated before the peak is reached. This will be explained later in the section 4.5.1.3 using the numerical localization analysis.

As the microdamage progresses, the stress level on the corresponding microplane decreases. The reduction in the stress level is more on the microplanes with maximum microdamage.

Distribution profiles of microdamage and energy dissipation The evolution of the microdamage distribution profiles over the microplane system is shown in fig. 4.7a. Due to the loading induced anisotropy, the evolution of the microdamage is maximum on the microplane whose normal is aligned with the loading direction ($\alpha = 90^\circ$ in fig. 4.7a). There is no microdamage evolution on the microplanes aligned in the orthogonal direction of the loading ($\alpha = 0^\circ$ and $\alpha = 180^\circ$ in fig. 4.7a) which are in compression regime.

The same trend is followed by the energy dissipation profile as shown in fig. 4.7b. The maximum energy dissipation occurs on the microplane on which the rate of microdamage is maximum. In the case of microplanes on which there is no evolution of microdamage, the energy dissipation is zero.

4.5.1.3 Numerical localization analysis

As discussed in the section 4.3.4, we perform the localization analysis of the microplane microdamage model numerically due to the presence of the complex integral in the definition of the acoustic tensor, eq. (4.74). First, we present the identification of critical normal of the localization band in the case of uniaxial tensile test. Then, the implications of the integral relation, eq. (4.74) on

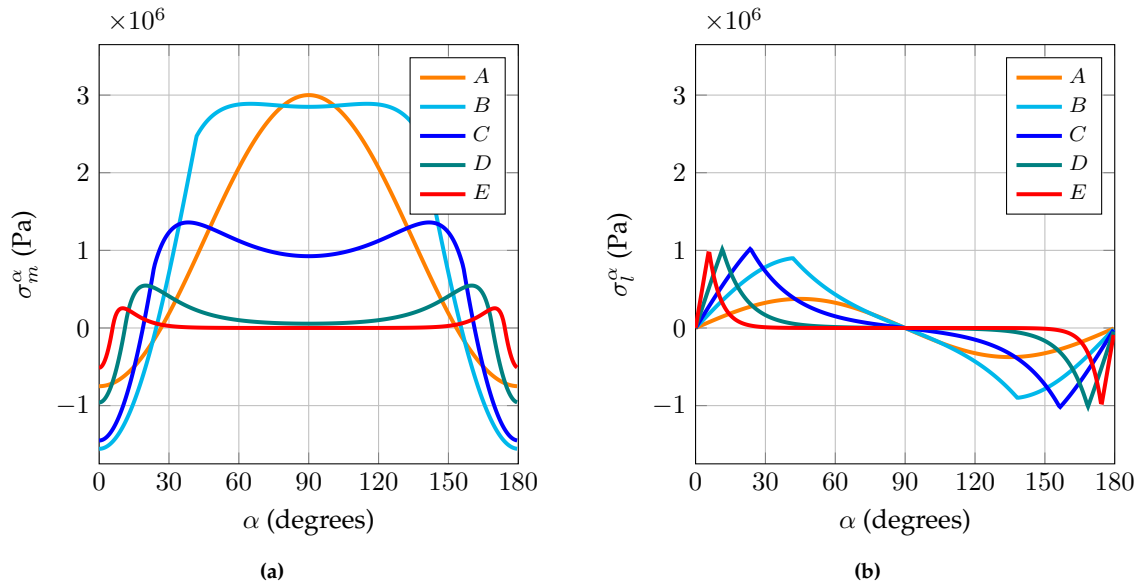


Figure 4.6: Distribution profiles of σ_m^α (a) and σ_l^α (b) over the microplane system at various stages of uniaxial loading in vertical direction

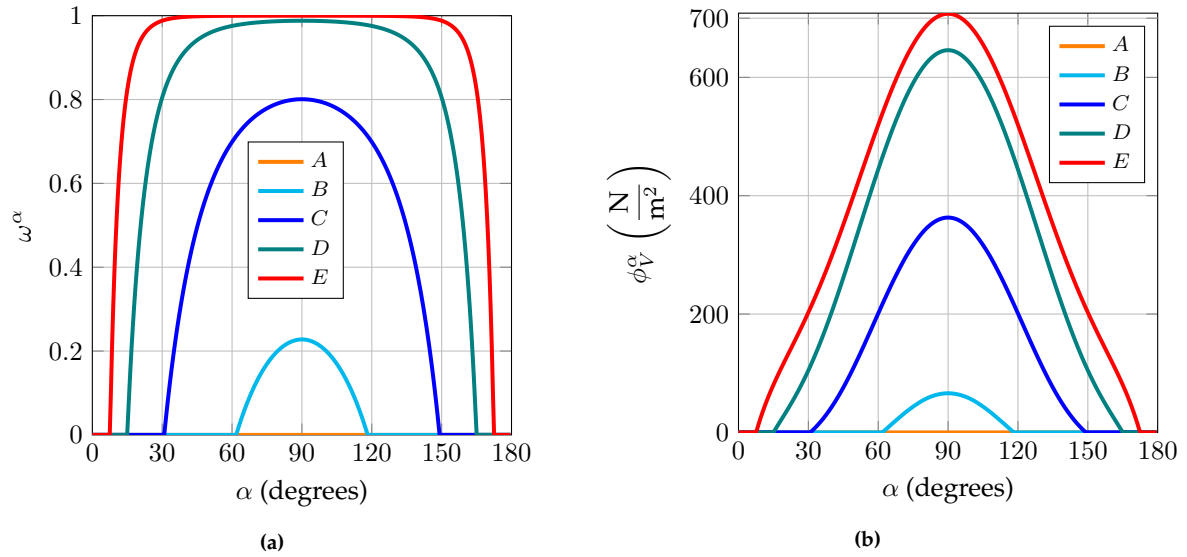


Figure 4.7: Distribution profiles of ω^α (a) and ϕ_V^α (b) over the microplane system at various stages of uniaxial loading in vertical direction

the critical internal variable at which the loss of ellipticity of the rate equilibrium problem occurs will be studied.

Critical normal to localization plane In order to identify the critical normal to the localization band, we first calculate $\mathbf{Q}_{\mathbf{n}=\mathbf{m}^\alpha}$ by choosing \mathbf{n} as the normal to each microplane:

$$\mathbf{Q}_{\mathbf{n}=\mathbf{m}^\alpha} = \mathbf{m}^\alpha \cdot \mathbb{C}^t \cdot \mathbf{m}^\alpha \quad \forall \mathbf{m}^\alpha \quad (4.95)$$

and compute its determinant, $\det \mathbf{Q}_{\mathbf{n}=\mathbf{m}^\alpha}$. Then, the critical normal of the localization band is identified according to the criterion (4.77).

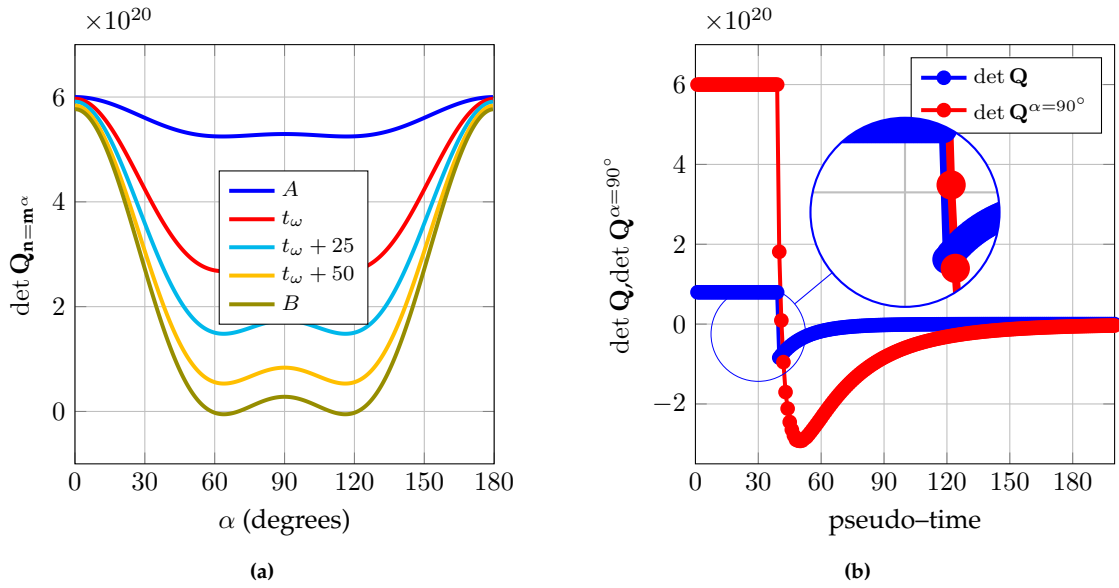


Figure 4.8: Numerical localization analysis: distribution profiles of $\det \mathbf{Q}^*$ (a), time evolution of $\det \mathbf{Q}$ and $\det \mathbf{Q}^{\alpha=90^\circ}$ (b)

fig. 4.8a depicts the evolution of distribution of $\det \mathbf{Q}_{n=m^\alpha}$. First, the distribution at the time step which corresponds to no microdamage (A in fig. 4.8a) which is followed by the distribution at the initiation of the microdamage (t_ω in fig. 4.8a). Later the distributions of $\det \mathbf{Q}_{n=m^\alpha}$ are plotted at an increment of 25 time steps from the initiation of the microdamage ($t_\omega + 25$ and $t_\omega + 50$ in the fig. 4.8a) to the time step at the peak (B in fig. 4.8a).

At the initiation of microdamage the determinant of the acoustic tensor is positive for the normals of all the microplanes. But the determinant of the acoustic tensor becomes negative on some microplanes at the peak. However, the time step at which it becomes zero is difficult to capture. In the present case, the minimum of $\det \mathbf{Q}_{n=m^\alpha}$ occurs in the direction of the microplane corresponding to $\alpha_{crit} = 63.82^\circ$.

From these observations, the deviation of the critical normal from the direction of the loading in the case of uniaxial tension is obtained as 26.7° for $\nu = 0.2$. This value can be compared with the deviation angle obtained in the same case using an isotropic damage model with Mazars equivalent strain [RIZZI et al., 1995] for which it is 27° and Desmorat's anisotropic damage model [JIRÁSEK, 2016] for which it is 23° .

In [KUHL and RAMM, 1998], the localization analysis is performed for the microplane model in which 3 independent microdamage variables are used for volumetric, deviatoric and the tangential components. In this case, it is identified that the localization occurs in the direction of the microplane corresponding to the direction of the loading. This is because the rate of evolution of the tangential microdamage variable is significantly less than that of the corresponding normal ones. As a consequence, the localization plane corresponds to the pure tension failure without any effect of the shear failure mechanism. However, in the present work, since a single microdamage variable is used for both the normal (no split) and the tangential directions of a given microplane, the shear mechanism has a significant impact on the orientation of the failure plane.

Critical internal variable The next step is to find the critical internal variable at the onset of localization. In order to do so, we first compute $\det \mathbf{Q}$ by substituting identified \mathbf{n}_{crit} in eq. (4.72). Here, we note that the important contribution to \mathbf{Q} comes from the microplane on which microdamage is initiated first, which in this case, corresponds to $\alpha = 90^\circ$. The corresponding contribu-

tion $\det \mathbf{Q}^{\alpha=90^\circ}$ is computed from eq. (4.75). Of course, comparison is established for illustrative purposes only, since loss of ellipticity of the rate equilibrium problem is only related to \mathbf{Q} .

The time evolution of $\det \mathbf{Q}^{\alpha=90^\circ}$ and $\det \mathbf{Q}$ are plotted in fig. 4.8b. Here, $\det \mathbf{Q}^{\alpha=90^\circ}$ becomes negative as soon as the evolution of the microdamage begins. But $\det \mathbf{Q}$ becomes negative only when sufficient number of microplanes are localized. In the present case, both the microdamage initiation occurs for the maximum value of $\kappa^\alpha = 10^{-4}$ while the loss of ellipticity occurs for the maximum value of $\kappa^\alpha = 1.047 \times 10^{-4}$.

4.5.2 Parametric studies

In this section, the influence of the parameters N^α and β on the response of the microplane microdamage model is studied. For this purpose, we repeat the the uniaxial tensile loading experiment as in the previous section 4.5.1 to study the global response for different values of these parameters.

4.5.2.1 Influence of the number of microplanes

One of the advantages of the disk microplane system [PARK and KIM, 2003] compared to the spherical microplane system is that the numerical integration over the surface of the circle is less complex than numerical integration over the surface of the sphere. But for the sake of accuracy of the numerical integration scheme, an optimum number of microplanes has to be selected. In order to achieve that, we study here the influence of the number of microplanes on the global response of the uniaxial tensile test.

We compare the force–displacement curve in vertical direction for different number of microplanes and two values of Poisson’s ratio in fig. 4.9a ($\nu = 0$) and fig. 4.9b ($\nu = 0.2$). For $\nu = 0$, the elastic stiffness is well captured for all the values of N^α . In the case of $\nu = 0.2$ (a more general case for $\nu > 0$), $N^\alpha = 2$ is no more enough, but at least $N^\alpha = 3$ microplanes are necessary for recovering the elastic properties.

Obtaining a microplane discretization independent response in the non-linear regime requires using more microplanes. In order to understand the convergence of the response, we plot the peak of the global curves $(F_2)_{\text{peak}}$ and the amount of dissipated energy during the uniaxial loading in vertical direction for different values of N^α and ν in figs. 4.10a and 4.10b respectively. For both the cases of $\nu = 0$ and $\nu = 0.2$, $(F_2)_{\text{peak}}$ can be considered as converged for $N^\alpha \geq 21$ (fig. 4.10a). Concerning the dissipated energy, convergence is achieved for $N^\alpha \geq 9$ (if $\nu = 0$) and for $N^\alpha \geq 21$ (if $\nu = 0.2$) (fig. 4.10b).

Remark. Notice that this result is fully consistent with results presented in the original work on disk microplane model [PARK and KIM, 2003], in which the same number of microplanes (21) are considered for numerical integration. As a result of this analysis, we consider $N^\alpha = 21$ for the rest of the numerical studies in this work.

4.5.2.2 Influence of parameter β

The parameter β influences the equivalent strain computed on each microplane which in turn affects the rate of microdamage growth on the localized microplanes. In the case of $\beta = 0$, the microdamage is driven by only the normal component of the positive strain tensor. For $\beta = 1$, the contribution of the tangential strain is completely taken into account and the definition of the equivalent strain becomes the norm of $\langle \epsilon \rangle^+ \cdot \mathbf{m}^\alpha$ on each microplane.

In fig. 4.11a the force–displacement curves in the case of uniaxial tension for different values of β are depicted. We observe that for higher the values of β , $(F_2)_{\text{peak}}$ is lowered (figs. 4.11a

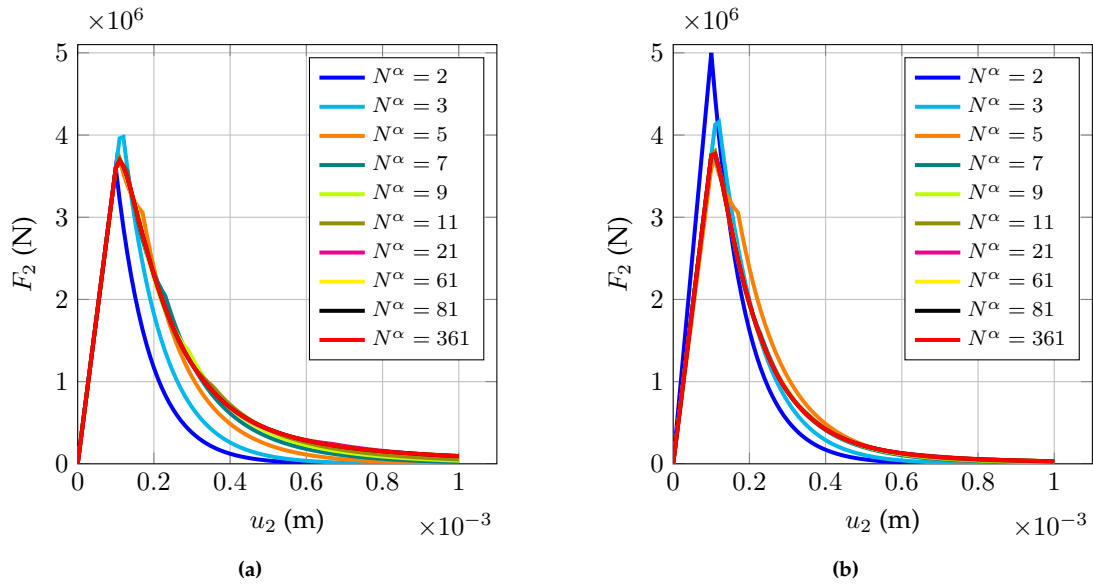


Figure 4.9: Influence of N^α : force–displacement curves in vertical direction for $\nu = 0$ (a) and $\nu = 0.2$ (b)

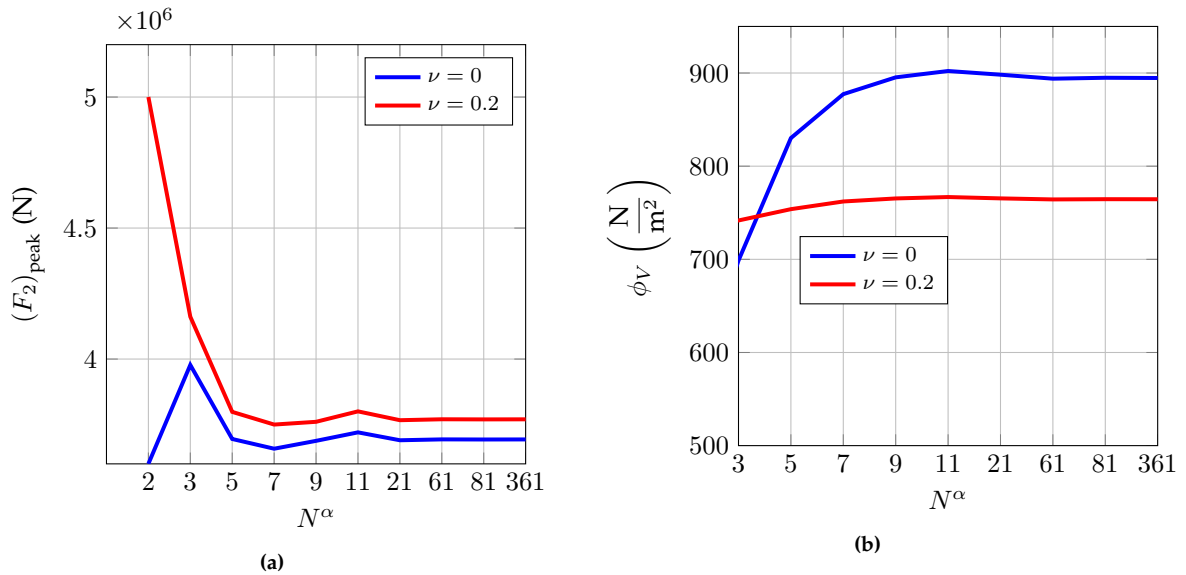


Figure 4.10: Influence of N^α on the peak of the global curve (a) and ϕ_V (b) of uniaxial tensile test

and 4.11b). Conversely, for lower values of β , non-zero residual forces, that is stress locking is observed (fig. 4.11a).

In order to explain the influence of β on the peak, we plot the distributions of microdamage on the microplanes at the peak and a time step after the peak in fig. 4.12a. We observe that the number of microplanes that enter into the damage regime are more for the case of $\beta = 1$ than for the case of $\beta = 0$. As the dissipation between these two steps is more for the higher values of β , the peak is lowered.

The stress locking can be explained by plotting the microdamage distribution on the microplanes at the end of the loading as shown in fig. 4.12b. The number of microplanes on which the damage is not initiated is higher in the case of $\beta = 0$ than in the case of $\beta = 1$. This is because for $\beta = 1$, even though ϵ_m^α is non-negative the microdamage is driven by ϵ_l^α (definition of $\tilde{\epsilon}^\alpha$). But this is not

the case for $\beta = 0$. Thus, the microplanes on which ϵ_m^α is negative does not dissipate any energy throughout the loading history for $\beta = 0$ leading to stress locking.

In order to avoid the stress locking, we chose $\beta = 1$ in all the numerical tests in the rest of this work.

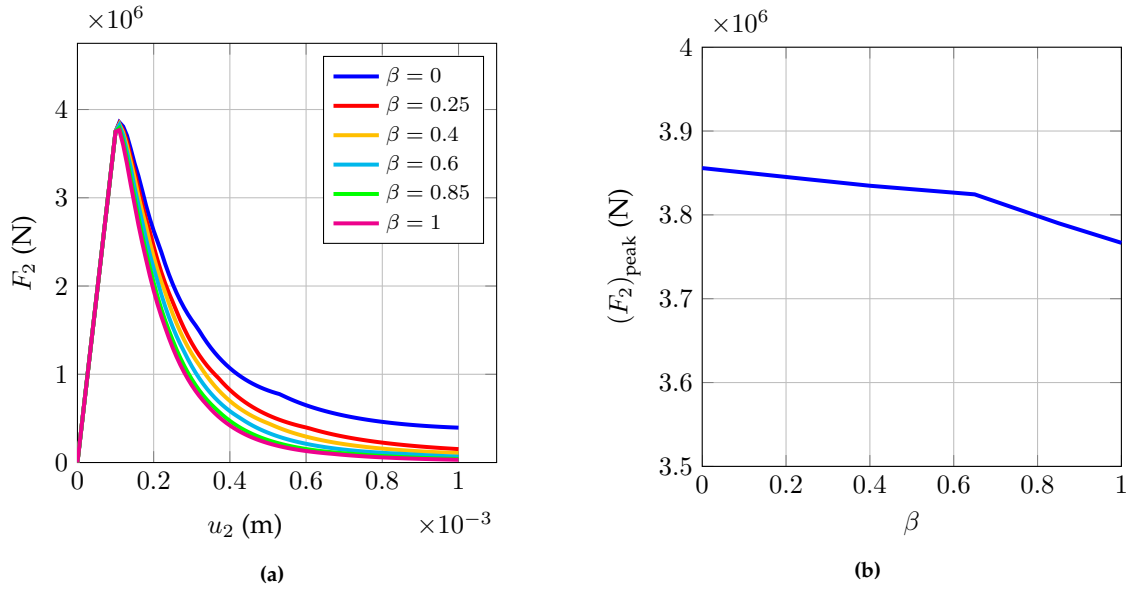


Figure 4.11: Influence of β on the global response of uniaxial tensile test: force–displacement curves in vertical direction (a) and corresponding peaks (b)

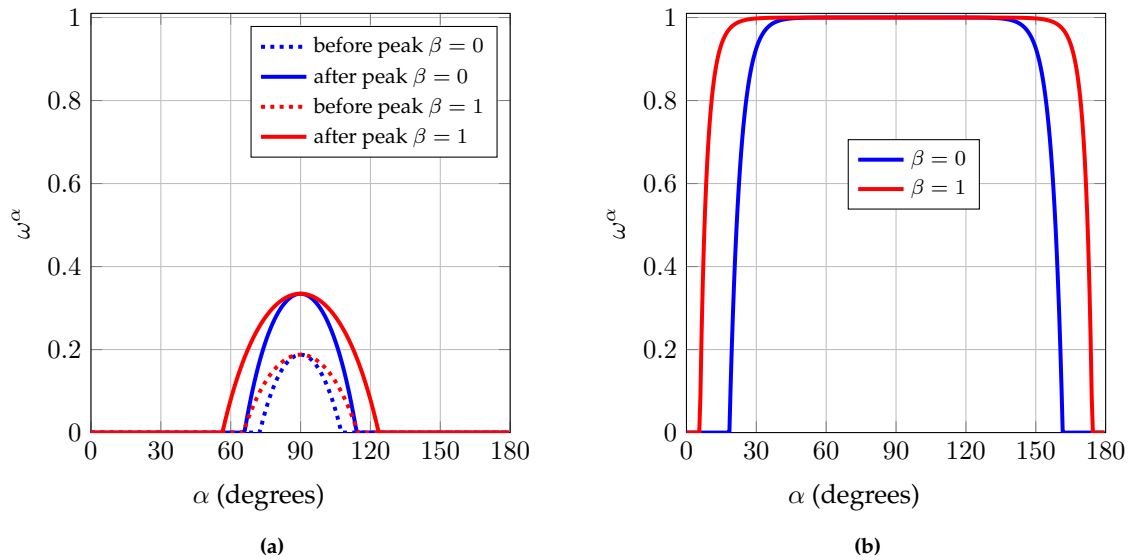


Figure 4.12: Influence of β on the evolution of ω^α : before vs. after the peak of the global response (a) and at the end of the vertical tensile loading (b)

4.5.3 Mesh dependency studies

In this section, the ability of the energy regularization technique to obtain mesh independent results for different combinations of mesh discretizations and definitions of l_c is studied.

4.5.3.1 Problem setting

A concrete bar with dimensions as shown in fig. 4.13 is considered and an uniaxial loading in the horizontal direction is applied. We allow the localization band of width w to form only in the central part of the bar by considering the microplane model in this part. The rest of the bar is assumed to behave in elasticity. Here, the indirect load control technique, CNDI (section 3.5.2.2) is used to apply the loading. The following path-following constraint is written:

$$P = \frac{1}{2} [(\Delta d_1^B - \Delta d_1^A) + (\Delta d_1^C - \Delta d_1^D)] - \Delta\tau = 0 \quad (4.96)$$

where, Δd_1^A , Δd_1^B , Δd_1^C and Δd_1^D are the nodal displacements at points A , B , C and D respectively (fig. 4.13) and $\Delta\tau$ is taken as 3.75×10^{-6} m.

Now, we consider different mesh discretizations of the given specimen using CST elements by parameterizing the width (w_e) and height (h_e) of the weakened element (or elements) as shown in the table 4.1. We obtain mesh-1, mesh-2 and mesh-3 by varying w_e while h_e is kept constant. For these meshes, the aspect ratio $a_e = w_e/h_e$ also varies. Finally, mesh-4 is obtained by keeping the same aspect ratio as in the case of mesh-1, that is, both w_e and h_e are different for the two meshes.

Here, we study the global response of the specimen for two definitions of l_c . Since, the width of the localization band is known in the present example, the first choice is $l_c = w_e$. Next, we consider another definition, $l_c = \sqrt{2A_e}$ which is widely used in the literature. This definition gives the width of the localization band formed in a square which is divided diagonally by 2 triangular elements.

4.5.3.2 Results

The global responses of the considered meshes (table 4.1) are shown in figs. 4.14a and 4.14b for $l_c = w_e$ and $l_c = \sqrt{2A_e}$ respectively. For the definition $l_c = w_e$, the global responses of all the meshes are independent with respect to each other. For the definition $l_c = \sqrt{2A_e}$, only the global responses of mesh-1 and mesh-4 are independent with respect to each other. That is, the mesh independent results are obtained only when the aspect ratio is kept constant for this definition. This can be explained by the fact that $l_c = \sqrt{2A_e}$ does not give a direct measure of the localization band (unlike $l_c = w_e$) because the central part of the specimen is a rectangle and not a square.

One can avoid this ambiguity by resorting to projection methods [OLIVER, 1989, JIRÁSEK and BAUER, 2012] for evaluating l_c . In the rest of this work, we keep the aspect ratio constant for different meshes (whenever possible) and use the definition $l_c = \sqrt{2A_e}$.

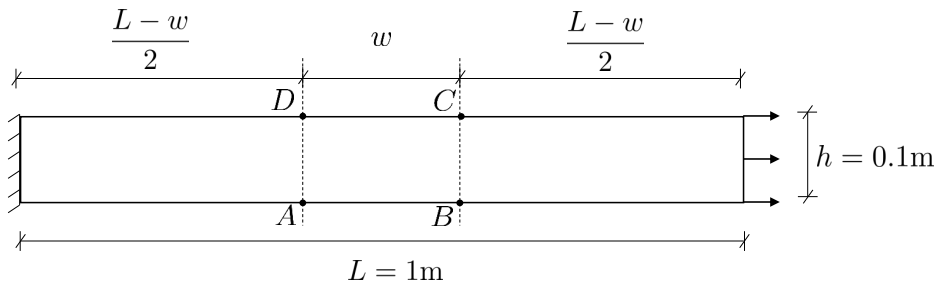
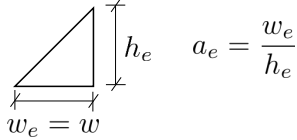
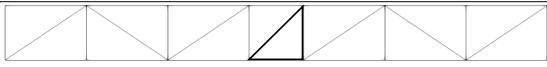
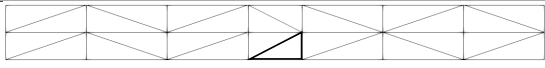


Figure 4.13: Specimen for mesh dependency studies: a concrete bar under tensile loading

Table 4.1: Different meshes adopted for the mesh dependency study

meshes	
	$w_e = 0.2\text{m}, h_e = 0.1\text{m}, a_e = 2$
	$w_e = 0.1\text{m}, h_e = 0.1\text{m}, a_e = 1$
	$w_e = 0.05\text{m}, h_e = 0.1\text{m}, a_e = 0.5$
	$w_e = 0.1\text{m}, h_e = 0.05\text{m}, a_e = 2$

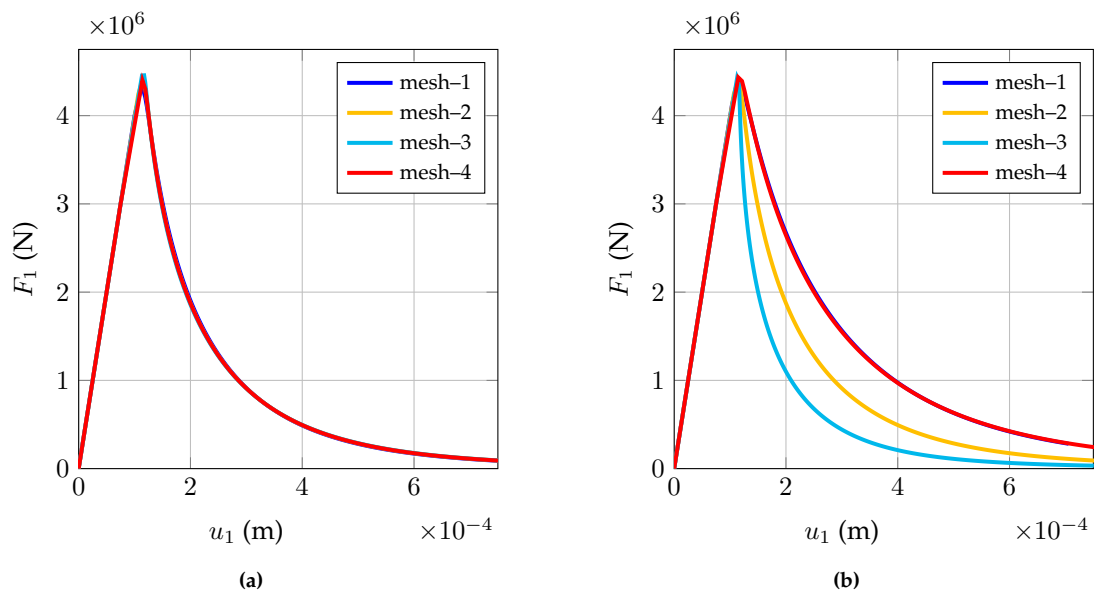


Figure 4.14: Mesh dependency studies: comparisons of force–displacement curves in horizontal direction for different meshes by considering $l_c = w_e$ (a) and $l_c = \sqrt{2}A_e$ (b)

4.6 Discussion on advantages of the microplane microdamage model

In this section, the anisotropic characteristics of the microplane microdamage model are highlighted. We compare the response of the microplane microdamage model in two phase loading case (detailed in the section 3.6.5.1) with that of the isotropic damage model [MAZARS, 1984] and the extended EFEM (section 3.6). We recall that during this experiment, we apply a vertical loading followed by unloading of the specimen and application of horizontal loading.

Isotropic damage model The global responses in vertical and horizontal loading phases using isotropic damage model are shown in figs. 4.15a and 4.15b respectively. During the vertical loading in the first phase, a peak is observed (stage *A*) followed by the softening behavior due to the damage growth. After dissipating certain amount of energy, unloading of the specimen begins (at stage *B*). During unloading phase, the stiffness of the material is reduced due to the irreversible nature of the damage. It has to be noted that the reduction of stiffness is the same in all the directions in this case because the damage is modelled in an isotropic manner. Hence, the response to the loading in horizontal direction is characterised by the reduced elastic stiffness. As the force level reaches the unloading point *B*, the softening occurs due to the further isotropic damage growth.

Extended EFEM In this case, we recall that the response to the two phase loading is characterized by the same initial elastic stiffness and the peak of the global responses in both the phases of loading. Further, two orthogonal cracks are initiated as the principal stress component exceeds the strength of the material in both directions (section 3.6). As the initial phase of anisotropic damage is not taken into account, the complete strain localization process is not captured. Moreover, the parameters of the cohesive laws (G_f and f_t) of the two cracks are considered the same.

Microplane microdamage model The global responses in vertical and horizontal directions using microplane microdamage model are presented in figs. 4.16a and 4.16b respectively. Owing to the anisotropic damage growth, the response in the second phase of the loading is characterized by the reduction of stiffness (*OF* in fig. 4.16b) which is different from both the initial elastic modulus (*OC* in fig. 4.16a) and the unloading modulus (*OD* in fig. 4.16a). Also, the peak force level reached in the second phase of loading (*F* in fig. 4.16b) is between the peak force level and the unloading force level (*C* and *D* in fig. 4.16a respectively) reached during the first phase of loading.

Comparisons in perspective of the energy dissipation This behavior can be easily explained by the evolution of the energy dissipation profiles on the microplane system during both the phases. During the first phase of uniaxial loading (in vertical direction), we recall that the maximum energy dissipation (fig. 4.7b) is in the direction of the loading ($\alpha = 90^\circ$) while there is no energy dissipation in the orthogonal direction ($\alpha = 0^\circ$ and $\alpha = 180^\circ$). Furthermore, as already mentioned, energy dissipation at other microplanes is in between these extreme values (fig. 4.7b). This explains the observed elastic stiffness and the peak during the second phase of the loading in the case of microplane microdamage model. It has to be noted that both the isotropic damage model and the extended EFEM lack the description of directional energy dissipation.

In the second phase of the loading, due to the change in the loading direction, the microplanes that are aligned in the horizontal direction ($\alpha = 0^\circ$ and $\alpha = 180^\circ$) starts dissipating energy (*F*, *G* and *H* in fig. 4.17). Also, we note that there is no further energy dissipation on the microplane corresponding to $\alpha = 0^\circ$. The residual energy at the end of the second phase of loading is shown in the shaded area of fig. 4.17.

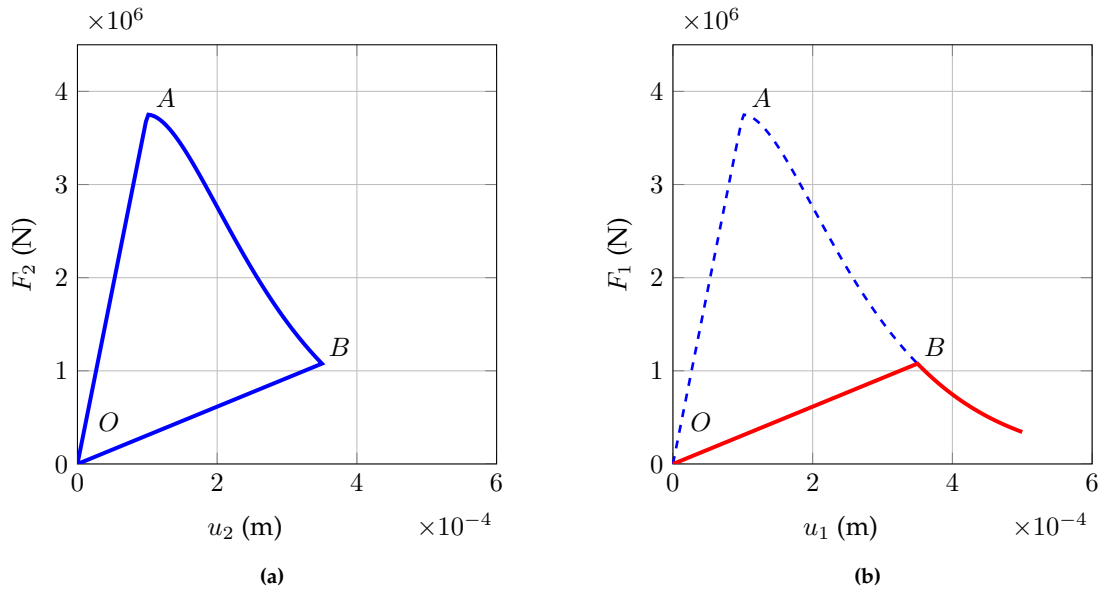


Figure 4.15: Response of the isotropic damage model during the two phase loading experiment: force–displacement curves in vertical direction (a) and horizontal direction (b)

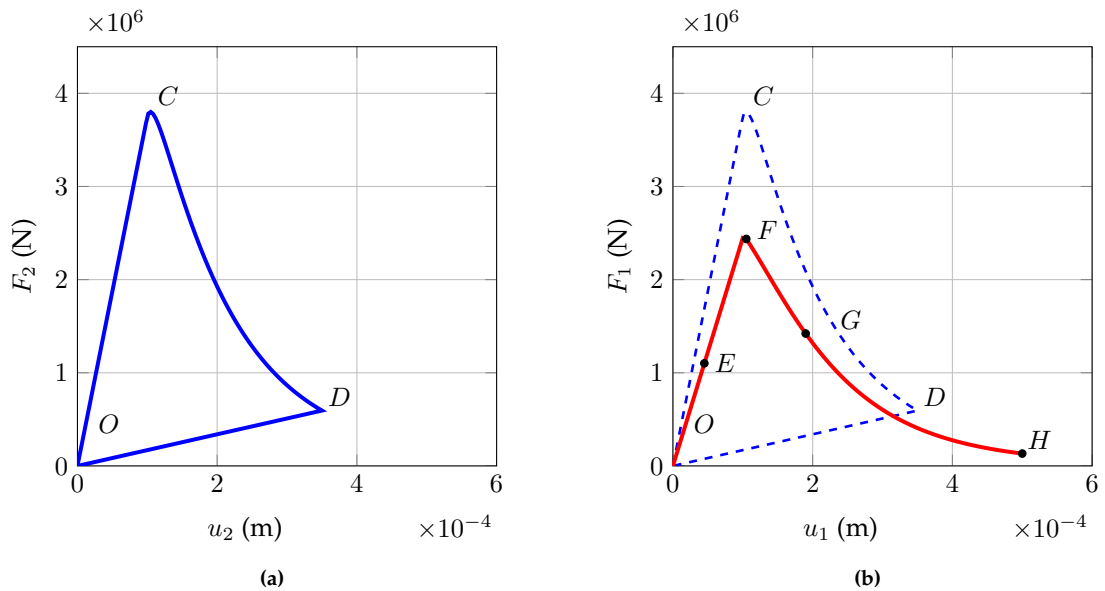


Figure 4.16: Response of the microplane microdamage model during the two phase loading experiment: force–displacement curves in vertical direction (a) and horizontal direction (b)

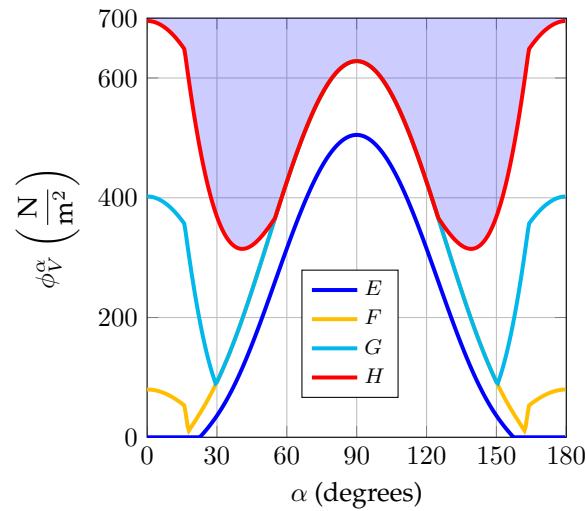


Figure 4.17: Distribution profiles of ϕ_V^α over the microplane system at various stages of two phase loading experiment

4.7 Conclusions

The microplane microdamage model is formulated in the framework of disk microplane system under plane strain assumption. In this framework, the projection operation of strain and the numerical integration of stress are carried out over the surface of a semi-circle. In thermodynamic framework, an integral relationship between the free energy potential at the unit volume and each microplane is assumed. This leads to a relationship between the density of the energy dissipation in the unit volume and that of on each microplane. Using this relationship, an expression for the residual energy on each microplane is derived. Using the energy regularization technique, an expression for the model material parameter (B) is derived in terms of the characteristic length. From numerical case study of the uniaxial tensile test, it can be concluded that the modeling strategy to use a single microdamage variable seems to be effective and simple. The evolution of the strain components, microdamage and the energy dissipation shows the anisotropic character of the proposed microplane microdamage model. Numerical localization analysis shows that there is a delay between the initiation of the microdamage and the loss of ellipticity of the rate equilibrium problem.

From the parametric studies, $N^\alpha = 21$ and $\beta = 1$ are selected for the rest of the numerical cases in this work. It is verified from global responses for several mesh discretizations that the proposed model gives mesh independent results.

Finally, it can be concluded that owing to the anisotropic behavior of the microplane microdamage model, the elastic stiffness, the peak of the global responses and the energy dissipation during the complex loading paths are well captured.

Indeed, the main advantage of the microplane microdamage model is the ability to calculate the residual energy at each stage of the loading cycle on each microplane using the energy dissipation profiles over the microplane system.

Microplane microdamage model to strong discontinuity model transition approach

Abstract. In this chapter, a strategy to couple the microplane microdamage model with the extended EFEM is presented. This coupling is a way to achieve a complete description of the strain localization process from diffused and anisotropic damage (representing the microcracking phase) to the formation of multiple cracks. To achieve this objective, a damage-to-fracture transition formulation based on the energetic equivalence between the two modeling approaches is presented. Exploiting the anisotropic damage description provided by the microplane model, directional transition criteria are formulated for modeling the successive localization of two non-orthogonal cracks at the same material point.

5.1 Introduction

In general, the coupling between the implicit and explicit descriptions of cracking can be established either in a framework of thermodynamics [CAZES et al., 2009] or using the kinematics of strong discontinuity [OLIVER et al., 1999, OLIVER, 2000]. In the first approach, we perform a transition from the implicit to explicit description of cracking based on energy equivalence of the two models. In the second approach, the strong discontinuity analysis is performed to introduce a crack in the media with induced anisotropy.

According to the strong discontinuity analysis introduced in section 3.3, the traction–separation law defining the response of the discontinuity is derived using the constitutive laws of the continuum. Now, performing a strong discontinuity analysis for the microplane model would require to derive the traction–separation laws on each microplane because constitutive laws are defined at the microplane level. However, it is not straight forward to describe the behavior of a discrete discontinuity using the traction–separation laws on each the microplane which represents a discretized unit volume. Hence, in this work we follow the energy equivalence based transition approach for a coupling between microplane microdamage model and a strong discontinuity formulation (implemented according to the EFEM).

First, a general transition approach is presented (section 5.2) using the framework of thermodynamics. This is followed by the formulation of the transition approach from microplane microdamage model to a strong discontinuity formulation (section 5.3). The traction-separation law is calibrated such that the global dissipation obtained using the damage-to-fracture model is the same as the one provided by the microplane formulation. Next, we extend the proposed methodology to the case of the formation of multiple cracks in extended EFEM (section 5.5). This is followed by presenting the numerical examples to illustrate the proposed model for transition from anisotropic damage growth to multiple orthogonal/non-orthogonal strong discontinuities.

5.2 Energy equivalence based transition approach

5.2.1 General framework

Description of energy dissipation in implicit and explicit manner In energy equivalence approach, we use the fact that the total mechanical energy of the body is the same for any modeling strategy [CAZES et al., 2009]. Hence, the total energy dissipated by the models based on both implicit and explicit description cracking are equivalent with each other [COMI et al., 2002, COMI et al., 2007, CUVILLIEZ et al., 2012].

By assuming zero kinetic energy (quasi–static conditions), \mathcal{E} (eq. (2.6)) is rewritten as:

$$\mathcal{E} = \Psi - W_{ext} + \Phi \quad (5.1)$$

The expression of the total dissipation, Φ for the models based on implicit description of cracking is given by the integration of the volumetric energy dissipation (ϕ_V) over \mathcal{B} (entire volume) as:

$$\Phi = \int_{\mathcal{B}} \phi_V dV \quad \text{with} \quad \phi_V = \int_0^\infty \dot{\phi}_V dt \quad (5.2)$$

Also, by considering a modeling strategy for dissipation based on the explicit description of cracking the total energy dissipation is obtained as the integral of the energy dissipation over the discontinuity surface as:

$$\Phi = \int_{\Gamma_d} \phi_S d\Gamma \quad \text{with} \quad \phi_S = \int_0^\infty \dot{\phi}_S dt \quad (5.3)$$

Transition approach Now, the purpose of the transition models is to describe the energy dissipation in a coupled implicit–explicit manner. From phenomenological point of view, the crack is formed inside a given localization zone. Hence, the energy dissipated during the strain localization process can be divided into two parts: (i) the volumetric part that accounts for energy dissipation during the formation and growth of a damaged/localization band (described though a continuum model, a microplane model in the present case); (ii) the surface part that accounts for the energy dissipation during the initiation and propagation of the crack (described through a strong discontinuity model, in the present case).

A transition framework is achieved such that the energy which is to be dissipated by the coupled model (sum of the volumetric and surface parts) is equivalent to the energy which is to be dissipated by the model based on implicit description of cracking without transition.

Following this, the total energy dissipation is split into the volumetric part ($\hat{\phi}_V$) before the transition and the surface part after the transition ($\hat{\phi}_S$) as:

$$\int_{\mathcal{B}} \phi_V dV = \int_{\mathcal{B}} \hat{\phi}_V dV + \int_{\Gamma_d} \hat{\phi}_S d\Gamma \quad (5.4)$$

where,

$$\hat{\phi}_V = \int_0^{t_{tr}} \dot{\phi}_V dt, \quad \hat{\phi}_S = \int_{t_{tr}}^\infty \dot{\phi}_S dt \quad (5.5)$$

and t_{tr} is the pseudo–time at which the transition is performed. This gives the energy dissipation at the crack surface as the difference between the energy which is to be dissipated by the model based on implicit description of cracking without transition and the energy already dissipated in the localization band before transition. This is written as:

$$\int_{\Gamma_d} \hat{\phi}_S d\Gamma = \int_{\mathcal{B}} (\phi_V - \hat{\phi}_V) dV \quad (5.6)$$

Owing to this coupling, the cohesive traction-separation law is constructed by taking into account the energy that is already dissipated at the localization band. Now, considering that the total energy dissipation in a unit volume is given by its density, g_f , eq. (5.6) is rewritten as:

$$\int_{\Gamma_d} \hat{\phi}_S d\Gamma = \int_{\mathcal{B}} (g_f - \hat{\phi}_V) dV \quad (5.7)$$

In previous equations we supposed that energy dissipation in the bulk materials stops once a crack is localized, due to progressive unloading in the neighborhood of the crack. According to this approach, before transition, the rate of the surface energy dissipation is equal to zero, (a crack does not exist) and the increment of the volumetric energy dissipation in the bulk material ($\dot{\hat{\phi}}_V$) is equal to the increment of the energy dissipation of the model based on implicit description of cracking as:

$$\int_{\mathcal{B}} \dot{\hat{\phi}}_V dV = \int_{\mathcal{B}} \dot{\phi}_V dV \implies \dot{\hat{\phi}}_V = \dot{\phi}_V \quad (5.8)$$

After transition, the rate of the volumetric energy dissipation is equal to zero due to unloading in the band and the increment of the surface energy dissipation ($\dot{\hat{\phi}}_S$) at the crack surface is given by:

$$\int_{\Gamma_d} \dot{\hat{\phi}}_S d\Gamma = \int_{\mathcal{B}} \dot{\phi}_V dV \quad (5.9)$$

Remark. Here, the transition approach is presented by enforcing the energy equivalence in a weak form [WANG and WAISMAN, 2016], that is to say, by considering the energy dissipation of the implicit and explicit models over entire pseudo-time domain (loading history). The terms in the eq. (2.24) can be identified with the notations introduced in this chapter as:

- $\Phi_{imp} = \int_{\mathcal{B}} \phi_V dV$
- $\Phi_{exp} = \int_{\Gamma_d} \phi_S d\Gamma$
- $\Phi_{imp/exp} = \int_{\mathcal{B}} \hat{\phi}_V dV + \int_{\Gamma_d} \hat{\phi}_S d\Gamma$

Following the same approach as in [COMI et al., 2002, CAZES et al., 2009], the available energy computed from eq. (5.6) is then used to identify the parameters of the cohesive law with a predefined shape.

In the next section, we use an example of 1D bar in tension to illustrate the transition methodology to activate a crack in the localization band and define a cohesive law at the crack surface.

5.2.2 Example in 1D setting: bar in tension

In order to illustrate the transition framework, let us consider a 1D bar of unit area and length L with spatial coordinates along the length of the bar denoted by x and let \mathbf{u}_0 be the applied displacement (fig. 5.1).

Energy dissipation in a localization band Following the implicit description of cracking, strain localization process is modeled in a band of width b (from $x = x_b$ to $x = x_b + b$ in fig. 5.1). Let us consider a representative uniaxial stress-strain curve as shown in fig. 5.2a which is characterized by the softening behavior as the elastic limit reaches at B . After localization, the material inside the band (point P_2 in fig. 5.1) follows the softening curve (path BC in the fig. 5.2a) while the material in the bulk (material point P_1 in the fig. 5.1) follows the elastic unloading curve (path BA in fig. 5.2a). In this case, the volumetric energy dissipation (ϕ_V) can be obtained as the area under the stress-strain curve (shaded region in fig. 5.2a).

Energy dissipation at cohesive crack Using the model based on explicit description of cracking, the strain localization can also be described as a cohesive crack formed at the center of the bar ($x = x_d$ in fig. 5.1) which is ‘energetically equivalent’ to the localization band. Let $(\sigma, \llbracket u \rrbracket)$ be the traction (equal to the stress σ in 1D to fulfill the traction continuity condition) and displacement discontinuity at the crack surface. The corresponding cohesive law is shown in fig. 5.2b with the area under it equal to ϕ_S .

Transition framework Using the model based on coupled implicit–explicit description of cracking, a transition is performed by introducing a cohesive crack as a displacement discontinuity after a defined criterion is fulfilled. After transition, the material in the band (point P_2 is considered in fig. 5.3a) starts unloading elastically with reduced unloading stiffness (path CA in fig. 5.3b) corresponding to the transition point (C in fig. 5.3b) by expending the stored volumetric energy.

The energy dissipation at the crack surface ($\hat{\phi}_S$) is equal to the residual energy available, which is the difference between the energy that is to be dissipated in the localization band (ϕ_V) if transition is not performed and the energy dissipated in the localization band before transition ($\hat{\phi}_V$). At transition, the traction at the crack surface is equal to stress in the bar corresponding to the transition point (σ_{tr}) to satisfy the equilibrium. Using $\hat{\phi}_S$ and σ_{tr} , the cohesive law at the discontinuity is constructed (fig. 5.3c) by assuming the same shape but different area, that is to say, different available energy as in the case of explicit description of cracking fig. 5.2b.

5.3 Microplane microdamage model to strong discontinuity transition approach

The transition approach presented in the previous section can be easily extended for coupling the microplane microdamage model and a standard strong discontinuity model in the case of single crack formation. So, the implicit description of cracking is provided by the microplane microdamage model and the cohesive crack is modeled using the EFEM.

5.3.1 Formulation

Now, starting from the general transition framework, we replace the energy dissipation at a unit volume, ϕ_V with that of the microplane model. The latter is obtained as an integral relationship of the dissipation on each microplane (see eq. (4.25)). Substituting this relation in eq. (5.5), the volumetric energy dissipation of the microplane model before the transition is given by:

$$\hat{\phi}_V = \frac{1}{\pi} \int_0^{t_{tr}} \int_{\Omega} \dot{\phi}_V^{\alpha} dS dt \quad (5.10)$$

with $\dot{\phi}_V^{\alpha}$ denoting the microplane energy dissipation as defined in eq. (4.25).

Also, we recall that the energy dissipation density of a unit volume is related to its microplane counterpart by eq. (4.36). Now, following eq. (5.7), the energy available for the crack formation which is equal to the residual energy of the microplane microdamage model at t_{tr} is given by:

$$\int_{\Gamma_d} \hat{\phi}_S d\Gamma = \frac{1}{\pi} \int_{\mathcal{B}} \int_{\Omega} (g_f^{\pi} - \hat{\phi}_V^{\alpha}) dS dV \quad (5.11)$$

where, $\hat{\phi}_V^{\alpha}$ is the volumetric energy dissipated on the given microplane before the transition. Thus, the term $(g_f^{\pi} - \hat{\phi}_V^{\alpha})$ gives the residual energy on each microplane at the moment of transition. That is, owing to the anisotropic nature of the microplane microdamage model, the residual energy is calculated as a directional dependent quantity.

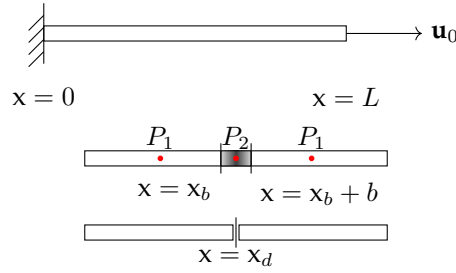


Figure 5.1: Strain localization in 1D bar: localization band and an equivalent cohesive crack

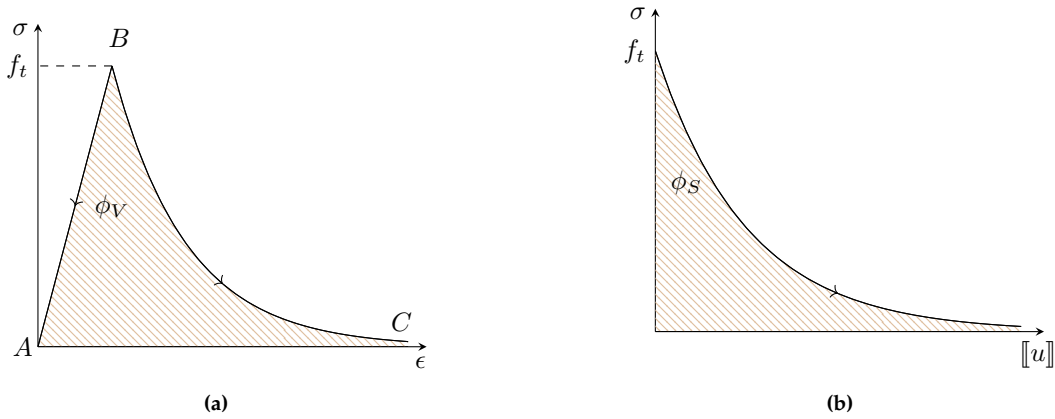


Figure 5.2: Equivalence between implicit and explicit description of cracking: area under the stress-strain curve (a) and the cohesive law (b) correspond to the energy dissipated during the strain localization process

After a defined criterion is fulfilled, the cohesive crack is introduced as a strong discontinuity in the direction of the maximum principal stress at the transition. Notice that, in transition models [SAKSALA et al., 2015, SIMONE et al., 2003, ROTH et al., 2015], the criterion for crack initiation is formulated based on the quantities at the unit volume or the internal variables (see table 2.2). In the present case, transition criteria can be formulated based on the quantities on the microplanes, such as $\tilde{\epsilon}^\alpha$, ω^α and $\hat{\phi}_V^\alpha$, to exploit the anisotropic damage description provided by the microplane model. In later section, we propose several transition criteria and use some numerical case studies to identify the most efficient one for the present framework.

Now, following the transition framework, the parameters (G_f, f_t) of the exponential traction-separation law (eq. (3.10) and eq. (3.11)), are taken proportional to the available energy (i.e., $G_f \propto \hat{\phi}_S$), and the value of the maximum principal stress (σ_I) at the transition (i.e., $f_t = (\sigma_I)_{tr}$) respectively.

5.3.2 Algorithm for microplane microdamage model to EFEM transition approach

Here, we focus on the formation of a single crack. This algorithm is presented for a given iteration $i+1$ at the present time step t^{n+1} (we drop the super-script $n+1$ for conciseness). A Boolean variable *flag* which is initiated with 0, is used to store the information of the crack opening activation. As soon as the crack is activated, *flag* is set to 1.

The steps involved the initiation of crack are described below:

1. at a given Gauss point, compute the microplane quantities using the discretized displacement at the present iteration \mathbf{d}^{i+1} and the displacement jump at the previous iteration \mathbf{e}^i

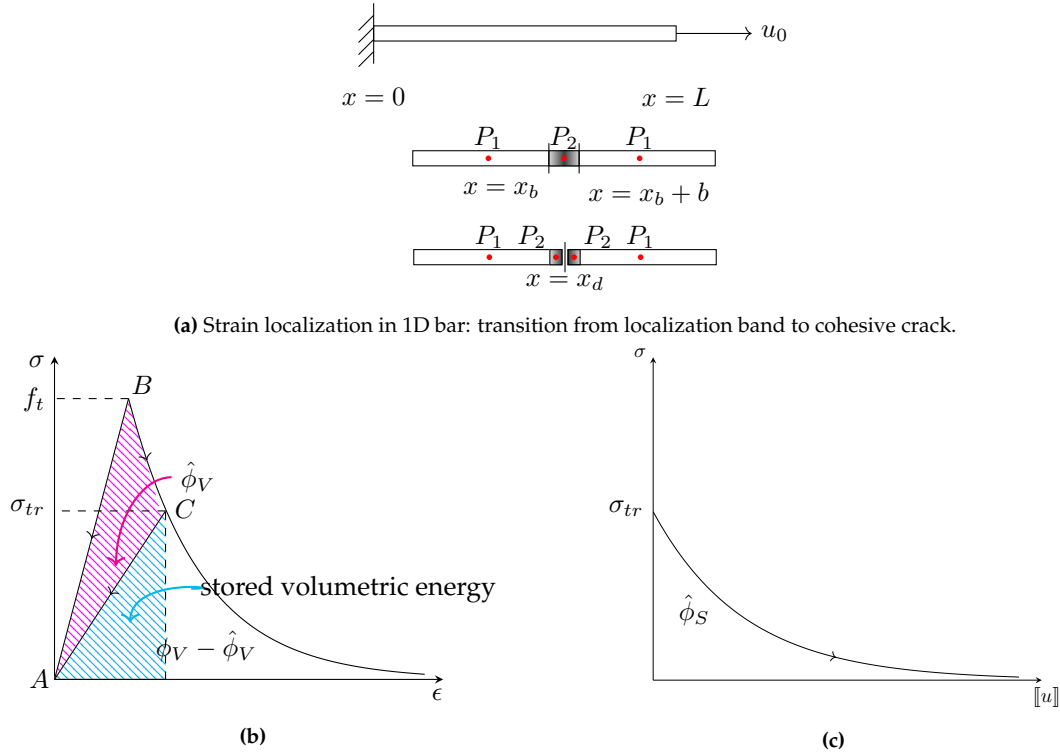


Figure 5.3: Energy equivalence based coupled implicit-explicit description of cracking: the residual energy dissipation (b) and available energy at the crack surface (c)

(initiated with $\mathbf{0}$). So, using projection operators defined in chapter 4, microplane strains are first computed as:

$$\epsilon_m^\alpha = (\mathbf{m}^\alpha)^\top (\mathbf{Bd} + \mathbf{Ge}) (\mathbf{m}^\alpha) \quad \text{and} \quad \epsilon_t^\alpha = (\mathbf{l}^\alpha)^\top (\mathbf{Bd} + \mathbf{Ge}) (\mathbf{m}^\alpha) \quad (5.12)$$

where, (\mathbf{m}^α) and (\mathbf{l}^α) are the column vectors which contains the components of the normal and the tangent of the given microplane respectively.

2. the transition criterion is then checked if the crack is not activated in the previous time step (i.e., $flag = 0$). Two cases can be distinguished:
 - (a) if the transition criterion is not fulfilled, the microdamage variable and the volumetric energy dissipation are updated.
 - (b) if the transition criterion is fulfilled on at least one microplane, then the crack is activated. Using the energy regularization technique introduced in section 4.4.2, the energy available for the crack is obtained as¹:

$$G_f = \hat{\phi}_S = \left(\frac{1}{\pi} \sum_{\Omega^\alpha} (g_f^\pi - \hat{\phi}_V^\alpha) W^\alpha \right) l_c \quad (5.13)$$

The traction continuity condition is then solved according to the algorithm 4.

Note that, while solving the local equilibrium equation using the operator split method, the stress tensor in the bulk needs to be updated during the iterations (algorithm 4). In order to avoid any instabilities at the local level, due to the concurrent correction of the microdamage distribution and crack-opening at the strong discontinuity level, the microdamage variables are frozen during the solution procedure of the local traction continuity condition.

¹Notice that similar expression is obtained in [WANG and WAISMAN, 2016] using a continuum damage model.

5.4 Numerical aspects of microplane microdamage to strong discontinuity formulation transition approach

In this section, we present some numerical aspects of the proposed transition approach. First, we verify the numerical implementation by performing a transition based on the equivalent strain defined on each microplane. We emphasize the behavior of the microplane microdamage and strong discontinuity models. Later, we present the mesh dependency studies based on different transition criteria. This study will allow us to select the less mesh sensitive transition criterion to be used in further computations.

5.4.1 Numerical validation of the transition approach in the case of a single crack

The proposed transition approach is validated using the same uniaxial tensile loading experiment (with two CST elements) that is performed in the previous chapters. Following the algorithms 3 and 4, the microplane microdamage model describes the dissipative process at the Gauss point in the standard FEM before the transition, while the EFEM is followed after the transition.

Problem setting A square unity domain, discretized using two CST elements, is submitted to a uniaxial tensile loading in the vertical direction (fig. 3.3). The material parameters of the microplane microdamage model and strong discontinuity models are considered the same as in the previous chapters (figs. 3.3 and 4.2). For the sake of illustration, we perform the transition when the equivalent microplane strain $\tilde{\epsilon}^\alpha$ on at least one microplane reaches a critical value of $\tilde{\epsilon}_{tr}^\alpha = 1.5\tilde{\epsilon}_0^\pi = 1.5 \times 10^{-4}$, but similar results can be obtained considering different transition criteria and threshold values.

Results The global force–displacement response in the vertical direction is shown in fig. 5.4a. The curve $O-A-B-C$ shows the elastic and the damage phases, while the curve $C-D$ (figs. 5.4a and 5.4b) represents the crack opening phase. Upon unloading at D , the crack closes (figs. 5.4a and 5.4b).

Microplane dissipation profiles at the different stages of the test are depicted in fig. 5.5. Based on these observations, the evolution of the volumetric and surface energy dissipation during the test can be summarized as follows:

1. the volumetric energy dissipation takes place during the microdamage growth phase before the transition, i.e.,

$$\dot{\hat{\phi}}_V \neq 0 \implies \dot{\hat{\phi}}_V^\alpha \geq 0 \forall \Omega^\alpha \in \Omega \quad \text{and} \quad \dot{\hat{\phi}}_S = 0 \quad (5.14)$$

where, $\dot{\hat{\phi}}_V^\alpha$ is the increment of volumetric energy dissipation on a given microplane.

2. as soon as the crack opening phase begins, there is no more volumetric energy dissipation and the residual energy (shaded area in fig. 5.5) is dissipated at the crack. In this phase, microplanes experience unloading (strain is reduced), the corresponding internal variables no more evolve and damage is naturally frozen. In other words:

$$\dot{\hat{\phi}}_V = 0 \implies \dot{\hat{\phi}}_V^\alpha = 0 \forall \Omega^\alpha \in \Omega \quad \text{and} \quad \dot{\hat{\phi}}_S \neq 0 \quad (5.15)$$

Remark. Here, the smoothness of the global curve fig. 5.4a obtained using the transition methodology is an attribute of the exponential softening (eq. (4.33) and eq. (4.26)) and traction–separation laws (eq. (3.10) and eq. (3.11)) of the microplane microdamage model and the EFEM respectively. Note that C^0 continuity is not enforced at the point of transition.

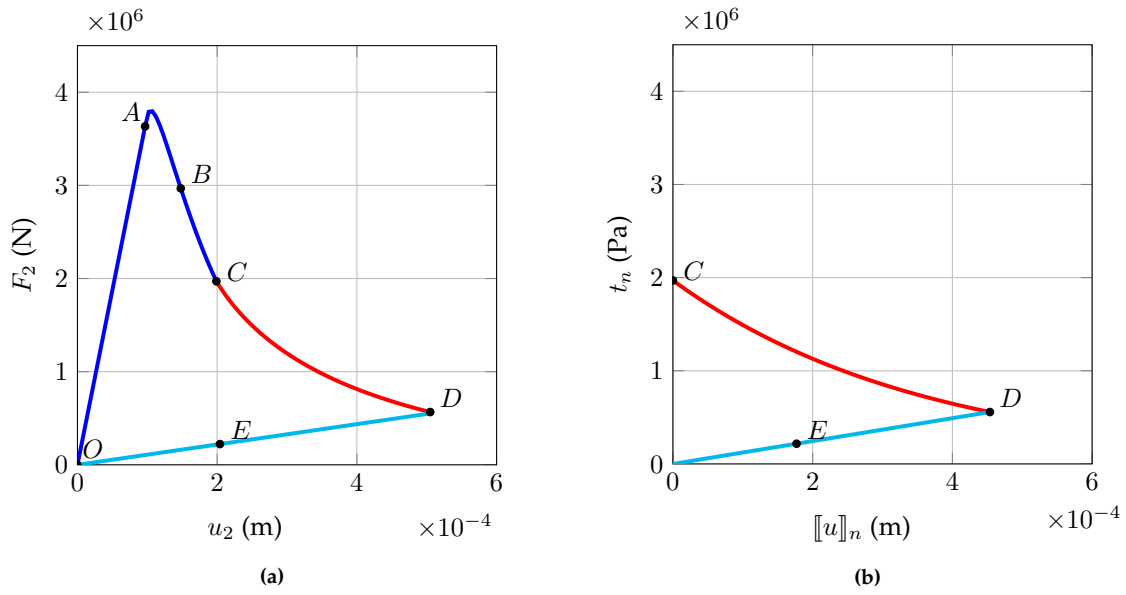


Figure 5.4: Transition approach for a single crack: global force–displacement curve in vertical direction (a) and traction–separation law after transition (b) for uniaxial loading test

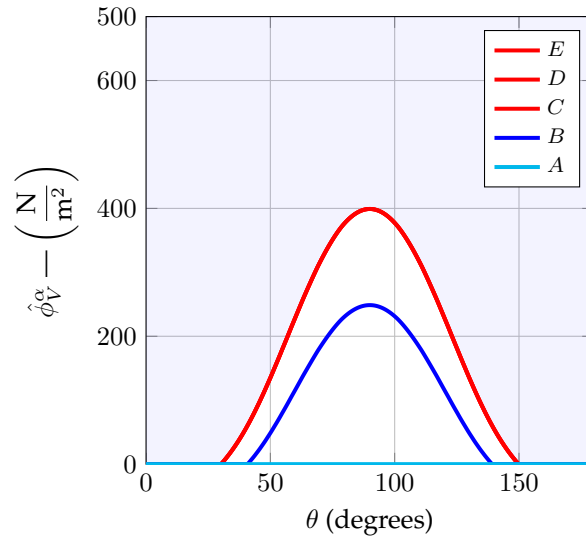


Figure 5.5: Distribution profiles of $\hat{\phi}_V^\alpha$ over the microplane system at various stages of uniaxial loading test using transition approach

5.4.2 Mesh dependency of various transition criteria

Transition criteria are to be formulated such that the crack initiation, as well as the obtained global (force-displacement) and local (crack opening evolution) responses, are not (or as less as possible) mesh dependent. In this section, we study the mesh dependency induced by various transition criteria, through repeating the same kind of analyses we performed in section 4.5.3. For the sake of simplicity, we restrict ourselves to the cases of mesh-1, mesh-2 and mesh-3 (see section 4.5.3 for more details). Moreover, the characteristic length to be used for energetic regularization of the microplane model is chosen equal to $l_c = w_e$. This is because these combinations of the mesh discretizations and the definition of l_c are proven to give mesh independent results in the case of

microplane microdamage model without transition for the considered meshes.

Transition criteria Here, we consider 3 different formulations for the transition criterion based on: (i) the maximum of the equivalent strain variables on all microplanes, $\max_{\alpha}(\tilde{\epsilon}^{\alpha})$; (ii) the maximum of the microdamage variables on all microplanes, $\max_{\alpha}(\omega^{\alpha})$; (iii) the maximum energy dissipation on the all microplanes, $\max_{\alpha}(\phi_V^{\alpha})$. The corresponding thresholds at the transition are denoted by, $\tilde{\epsilon}_{tr}^{\alpha}$, ω_{tr}^{α} and $(\phi_V^{\alpha})_{tr}$ respectively.

Results Global responses obtained using different transition criteria are given in figs. 5.6a, 5.7a and 5.8a. The corresponding calibrated traction-separation laws are given in figs. 5.4b, 5.7b and 5.8b. The corresponding threshold values at transition of the different parameters considered are given in table 5.1.

From fig. 5.6a, it can be seen that when performing the transition based on the equivalent strain on microplane, the global response is mesh independent before transition due to energetic regularization of the microplane microdamage model, but mesh sensitivity comes into the picture after the opening of the crack. The reason is that the crack is activated at different traction levels (fig. 5.4b) for the considered meshes, since $\tilde{\epsilon}^{\alpha}$ is not a regularized quantity. Similar considerations hold, when transition is performed based on a criterion defined on the maximum damage value at microplanes (figs. 5.7a and 5.7b). This is because ω^{α} despite a function of the regularized parameter B , also depends on $\tilde{\epsilon}^{\alpha}$.

As shown in figs. 5.8a and 5.8b, mesh independent results can be achieved considering a transition based on microplane dissipation. This is explained by the fact that we regularized the energy dissipation of the microplane microdamage model (see section 4.4.2).

Remark. According to these observations, we adopt a transition criterion based on the regularized maximum energy dissipation for the rest of the numerical tests.

5.5 Microplane microdamage model to strong discontinuity model transition approach for the case of multiple cracks

In this section, we extend the proposed transition framework for describing the formation of multiple intersecting orthogonal and non-orthogonal cracks. In particular, we capture the anisotropic damage growth due to the rotation of the principal stress/strain axes during loading, and take benefit of information provided by the microplane formulation in order to initiate multiple cracks.

5.5.1 Formulation

Let us consider a unit volume submitted to a complex loading conditions such that principal stress/strain axes rotate during loading. Now, as the condition $\max_{\alpha}(\phi_V^{\alpha}) \geq (\phi_V^{\alpha})_{tr}$ is attained,

Table 5.1: Transition quantities considered for mesh dependency studies and the corresponding threshold values

transition quantity	threshold value
$\tilde{\epsilon}_{tr}^{\alpha}$	$2.5 \times \tilde{\epsilon}_0^{\pi} = 2.5 \times 10^{-4}$
ω_{tr}^{α}	0.75
$(\phi_V^{\alpha})_{tr}$	$\frac{2g_f^{\pi}}{3} \approx 333 \text{ N/m}^2$

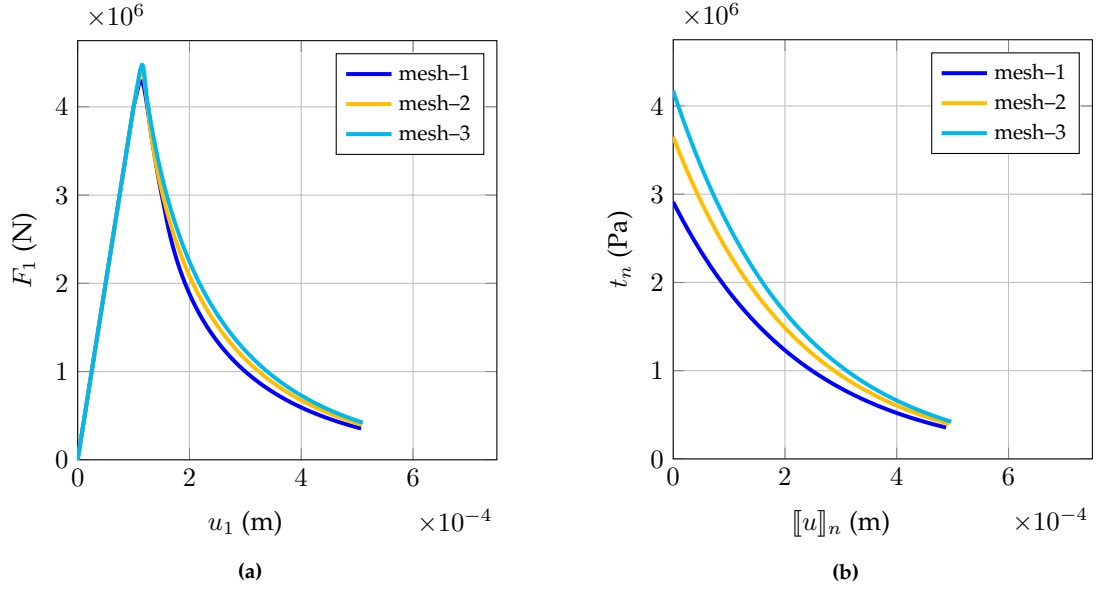


Figure 5.6: Mesh objectivity of the transition criterion based on $\max(\tilde{\epsilon}^\alpha)$: comparisons of force-displacement curves in horizontal direction (a) and local traction-separation laws (b) for different meshes by considering $l_c = w_e$

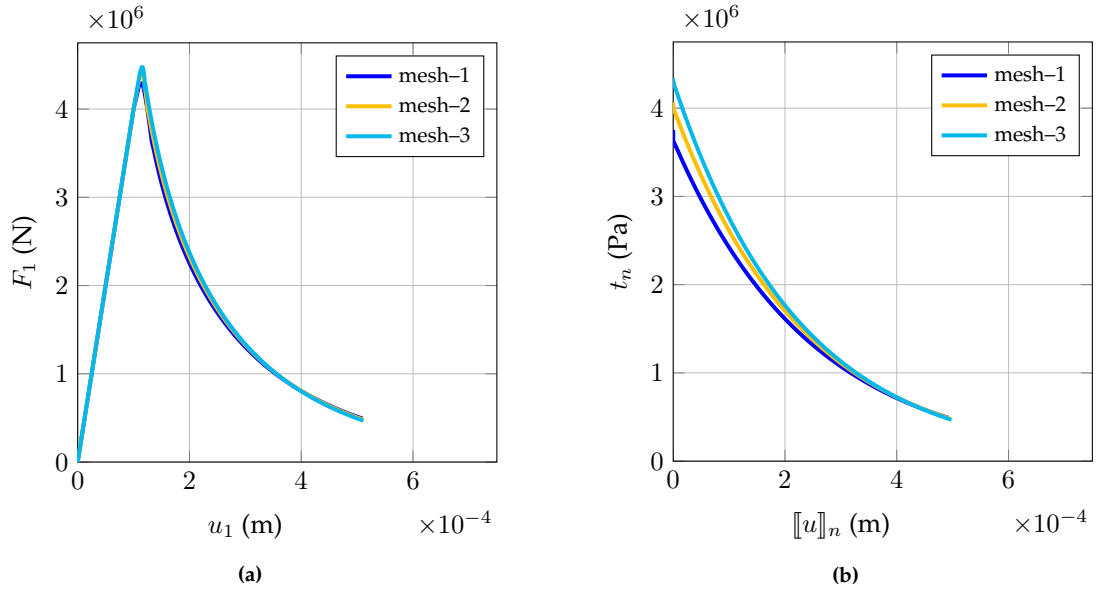


Figure 5.7: Mesh objectivity of the transition criterion based on $\max(\omega^\alpha)$: comparisons of force-displacement curves in horizontal direction (a) and local traction-separation laws (b) for different meshes by considering $l_c = w_e$

the first crack is initiated as discussed in previous section. Due to the evolution of the stress and strain state in the medium, however, a second crack can be localized in another direction.

In order to account for this situation in a damage-to-fracture transition approach, at each time, we identify the microplane system Ω into two non intersecting subsets:

$$\Omega = \Omega^1 \cup \Omega^2 \quad \emptyset = \Omega^1 \cap \Omega^2 \quad (5.16)$$

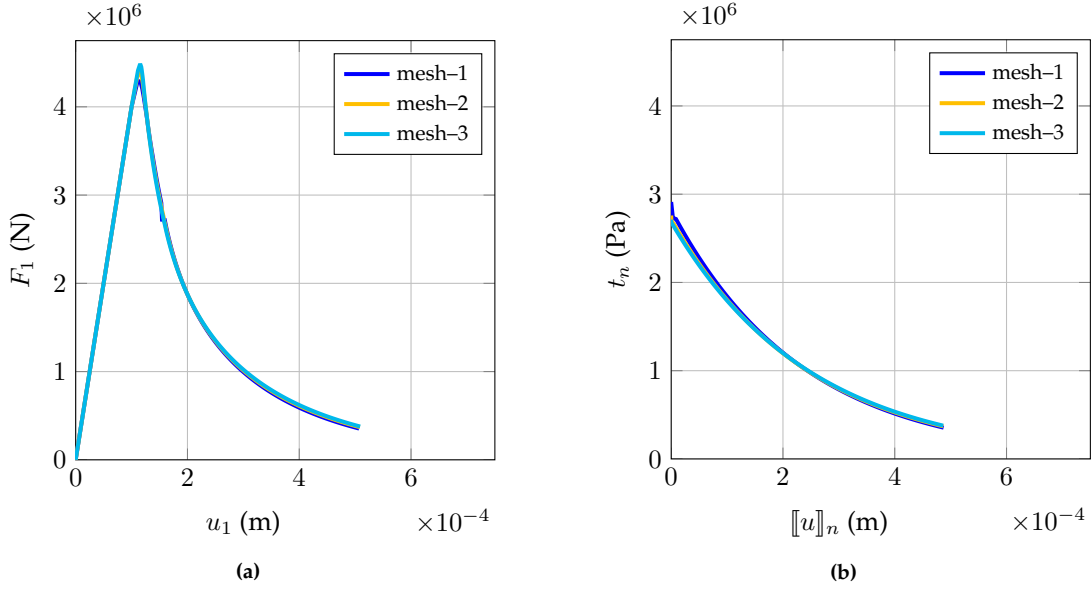


Figure 5.8: Mesh objectivity of the transition criterion based on $\max(\phi_V^\alpha)$: comparisons of force-displacement curves in horizontal direction (a) and local traction-separation laws (b) for different meshes by considering $l_c = w_e$

such that Ω^1 contains microplanes that are in unloading condition (eq. (4.32)):

$$\Omega^1 = \{\Omega^\alpha \in \Omega : \dot{\omega}^\alpha = 0, f^\alpha < 0\} \quad (5.17)$$

and Ω^2 is contains microplanes in loading condition (eq. (4.32)):

$$\Omega^2 = \{\Omega^\alpha \in \Omega : \dot{\omega}^\alpha > 0, f^\alpha = 0\} \quad (5.18)$$

Now, using the analogy between microplanes and microcracks, one can assume that microplanes belonging to Ω^1 correspond to the family of microcracks that coalesced to form the first crack, whereas microplanes belonging to Ω^2 represent still active (opening or dissipating) microcracks.

If the transition criterion for the second crack is reached on at least one microplane in Ω^2 then a second crack orthogonal/non-orthogonal to the first one is initiated in the direction of the maximum principal stress at the transition. The available energy for the crack (ϕ_{S_2}) is then obtained through eq. (5.11), but the integration for the calculation of the energy dissipation is now performed over Ω^2 only:

$$\int_{\Gamma_{d_2}} \hat{\phi}_{S_2} d\Gamma = \frac{1}{\pi} \int_{\mathcal{B}} \int_{\Omega} (g_f^\pi - \hat{\phi}_V^\alpha) dS dV = \int_{\Gamma_{d_1}} \hat{\phi}_{S_1} d\Gamma - \frac{1}{\pi} \int_{\mathcal{B}} \int_{\Omega^2} \hat{\phi}_V^\alpha dS dV \quad (5.19)$$

Notice that the same transition criterion is adopted for activation of both the cracks. This is justified because the material is isotropic before the initiation of the microdamage. More studies are needed, however, in order to better define transition criteria for multiple cracks as well as the more realistic way for calibrating traction-separation laws, in particular for the second crack.

5.5.2 Algorithm

The algorithm for performing the transition from the growth of microdamage (after the initiation of first crack) to the initiation of second crack is presented in algorithms 5 and 6. Two Boolean

variables $flag_1$ and $flag_2$ are used to store the information about the first and second crack respectively. Similar to the case of a single crack, these variables are initiated with 0 and set to 1 after the initiation of the respective cracks. Again, the variables related to the discretized displacement jump at both cracks, \mathbf{e}_1^i and \mathbf{e}_2^i respectively, are initiated with $\mathbf{0}$. From now on, down-scripts S_1 and S_2 are used to denote quantities referred to the first and second crack respectively.

Here, we focus on the steps involved in the initiation of the second crack assuming that the first crack is already initiated as described below:

1. after solving the traction–separation law at the first crack (i.e., computing the enhanced displacement corresponding to the first crack opening), project the updated strain on each microplane, i.e.,

$$\epsilon_m^\alpha = (\mathbf{m}^\alpha)^\top (\mathbf{B}\mathbf{d} + \mathbf{G}_1\mathbf{e}_1) (\mathbf{m}^\alpha) \quad \epsilon_l^\alpha = (\mathbf{l}^\alpha)^\top (\mathbf{B}\mathbf{d} + \mathbf{G}_1\mathbf{e}_1) (\mathbf{m}^\alpha) \quad (5.20)$$

2. recalculate ω^α and $\hat{\phi}_V^\alpha$ using the components of updated strain on each microplane.
3. check the transition criterion on the microplanes belonging to Ω^2 , on which microdamage growth takes place after updating the strain:

- (a) if the transition criterion is fulfilled then the second crack is initiated. Now the coupled traction–continuity conditions are solved using the algorithm 2. Following the same approach for the case of single crack (see eq. (5.13)), we obtain the energy available for the second crack as:

$$G_{f,S_2} = \hat{\phi}_{S_2} = \frac{1}{\pi} \sum_{\Omega} (g_f^\pi - \hat{\phi}_V^\alpha) W^\alpha l_c = \hat{\phi}_{S_1} - \frac{1}{\pi} \left(\sum_{\Omega^2} \hat{\phi}_V^\alpha W^\alpha \right) l_c \quad (5.21)$$

It has to be noted that we should avoid checking the transition criterion on the microplane on which it is fulfilled during the initiation of the first crack. That's why, we restrict the check of the transition criterion to the microplanes that enter into the loading phase due to the rotation of the principal strains;

- (b) if the transition criterion is not fulfilled that enter into the loading phase due to the rotation of the principal strains then we solve traction continuity condition for the first crack only and continue the solving process.

5.5.3 Numerical studies involving multiple crack formation

Here, we first describe the anisotropic microdamage growth followed by the initiation of two orthogonal cracks in the transition framework. Then, the attention is focused on the successive localization of two non-orthogonal cracks. In both cases, we use the results of the two-phase loading experiments performed in the cases of extended EFEM and microplane microdamage model as the references to better explain the main features of the proposed transition framework.

5.5.3.1 Orthogonal cracks case

We reproduce the two-phase loading experiment performed in the cases of extended EFEM and microplane microdamage model (sections 3.6.5 and 4.5.1). We recall that, in the case of extended EFEM, two orthogonal cracks with exactly the same behavior (i.e., same traction-separation laws) are opened in mode I. Conversely, in the case of microplane model, the microdamage growth occurs in both the phases, however, its distribution on the microplane system depends on the direction of the loading (fig. 4.7b and fig. 4.17).

Problem setting The opening of the first crack during the vertical loading in the transition framework is already tackled in sections 5.3 and 5.3.2. So, let us consider that the first crack already exist in the medium due to previous loading phases, and that stress/strain states in the system evolve due to the application of loading in the horizontal direction.

The influence of anisotropic damage on the global structural response becomes clear in that case. Indeed, due to the coupling between the microplane and strong discontinuity models, the material no longer exhibits pre-peak elastic response in the horizontal direction.

During this phase, microdamage growth occurs on a microplanes belonging to Ω^2 , whereas microplanes belonging to Ω^1 stay in unloading condition:

$$\dot{\hat{\phi}}_V \neq 0 \implies \dot{\hat{\phi}}_V^\alpha = 0 \forall \Omega^\alpha \in \Omega^1, \dot{\hat{\phi}}_V^\alpha \neq 0 \forall \Omega^\alpha \in \Omega^2 \quad (5.22)$$

At the same time, no more crack dissipation occurs at the first crack, since loading is in the orthogonal direction to its normal:²

$$\dot{\hat{\phi}}_{S_1} = 0 \quad (5.23)$$

where, $\dot{\hat{\phi}}_{S_1}$ is the dissipated energy at the first crack.

Now, the second horizontal crack is initiated when the transition criterion is fulfilled on at least one microplane in Ω^2 . After the activation of the second crack, no more energy dissipation occurs at the microplane level, i.e.,

$$\dot{\hat{\phi}}_V = 0 \implies \dot{\hat{\phi}}_V^\alpha = 0 \forall \Omega^\alpha \in \Omega^1 \cup \Omega^2 (\equiv \Omega) \quad (5.24)$$

The volumetric energy dissipation due to the microdamage growth during horizontal phase is taken into account while calculating the available energy at the second crack surface using eq. (5.21). This is one of the main differences between the proposed damage-to-fracture transition formulation and the extended EFEM for modeling the formation of multiple cracks, since in that case both the cracks dissipate the same amount of energy (anisotropic damage growth is not taken into account).

5.5.3.2 Non-orthogonal cracks case

In order to analyze the model response under a complex loading condition inducing the formation of two non-orthogonal cracks, here we simulate the William's like test performed in chapter 3.

Problem setting We recall that the loading is applied in two phases during this test. In the first phase, vertical loading is applied along with the compression loading in the horizontal direction which is followed by a combined shear and horizontal tensile loading. The applied loading is according to fig. 3.12 and the considered material parameters are shown in table 5.2.

In order to illustrate the role of the chosen transition threshold on obtained results (and in particular on the deviation angle between the two cracks), we first perform the transition at a small energy dissipation level. Hence, the transition is performed after 20% of g_f^π on at least one microplane is dissipated. Later, higher transition energy thresholds are considered to show the influence of this parameter on the angle between the two cracks and on the energy available at the second crack level.

²As it will be shown later, the first crack may continue to open during the second phase of loading for a more complex case.

Table 5.2: The material parameters considered for the microplane microdamage and strong discontinuity models in the transition framework – Willam’s like loading

material parameter	value
Young’s modulus	10 GPa
Poisson’s ratio	0.20
$\tilde{\epsilon}^\alpha$	10^{-4}
β	1
N^α	21
G_f	500 N/m
β_{cr}	1

Results - first phase In the first phase of the loading, we follow the algorithms 3 and 4 for initiation of the single crack in transition framework. In fig. 5.9, the evolution of different components of stress is shown. Here, the microdamage evolution starts at A and the crack opening starts at B which is the transition point.

From the microdamage profiles in fig. 5.10a, we can observe that the microplanes close to the orthogonal direction of the loading ($\alpha = 0^\circ$) are still in the elastic regime. As expected, all the microplanes enter into the unloading phase after the crack opening and there is no more volumetric energy dissipation on the microplanes (fig. 5.10b).

Results - second phase Now, a combined vertical, shear and horizontal loading is applied at C leading to the continuous rotation of principal strain axes. Consequently, the microdamage evolution first takes place on the microplanes which remained elastic during the first phase of loading (fig. 5.10a). Then, microdamage evolves on the microplanes that are in unloading regime after the first crack is opened. The corresponding energy dissipation profiles are shown in the fig. 5.10b.

Now, the second crack is initiated when the transition criterion is fulfilled on at least one of the microplanes on which the microdamage growth takes place during the second phase of loading. This crack is opened at 78.81° to the first crack. The energy dissipation profiles at the opening of the second crack are shown in fig. 5.10b.

The evolution of the components of the displacement jump (fig. 5.11) follow the same trend as in the extended EFEM case. That is, mode I opening in the first phase and mixed mode opening in the second phase of loading.

Although a direct comparison with the response obtained cannot be done, let us recall that the deviation angle between the two cracks was 48° in the case of extended EFEM. Differences between the two numerical formulations regarding this aspect can be explained by the fact that the criterion for the initiation of crack in the two cases is different. Also, in the transition case, the principal stress axes is rotated further during the damage growth phase before the transition criterion is fulfilled which is not modeled in extended EFEM. Moreover, the angle between the two non-orthogonal cracks also depends on the level of energy dissipation at which the transition is performed.

Sensitivity of the traction–separation law As it can be seen from fig. 5.9, the time evolution of the stress components is not smooth. There are several instabilities, particularly the stress component σ_{22} exhibits a jump at D . This could be due to the sensitivity of the traction–separation law. In order to understand the effect of the stiffness matrix used to solve the traction–separation law, we repeat the same test by using a penalized stiffness matrix with coefficients whose magnitude

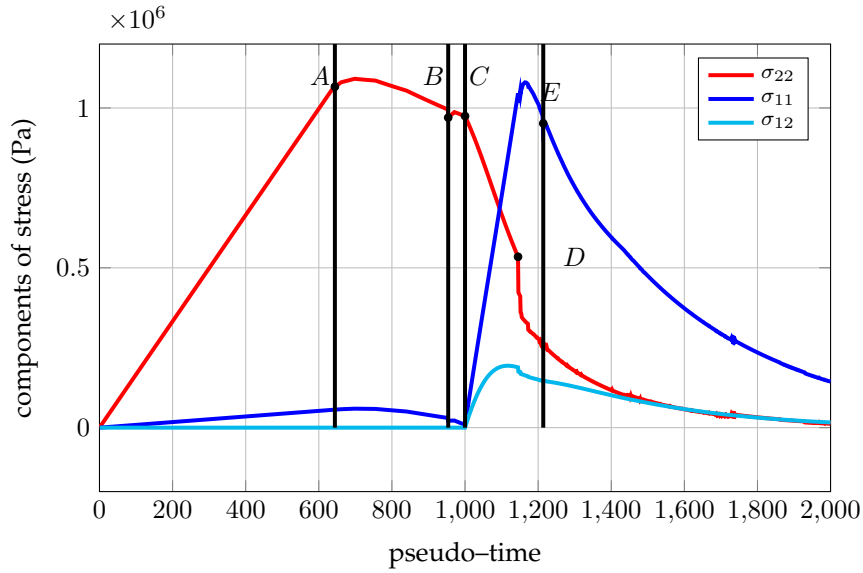


Figure 5.9: Time evolution of the components of stress - Willam's like loading test using transition approach for the threshold at 20% of g_f^π

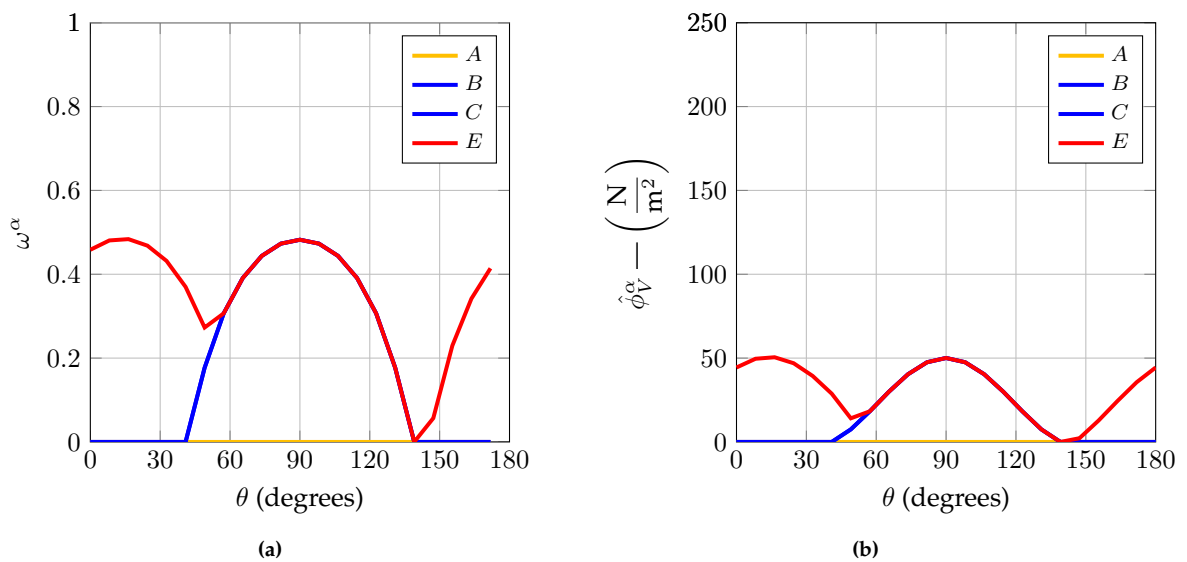


Figure 5.10: Distribution profiles of ω^α (a) and $\hat{\phi}_V^\alpha$ (b) over the microplane system at various stages of Willam's like loading test using transition approach for the threshold at 20% of g_f^π

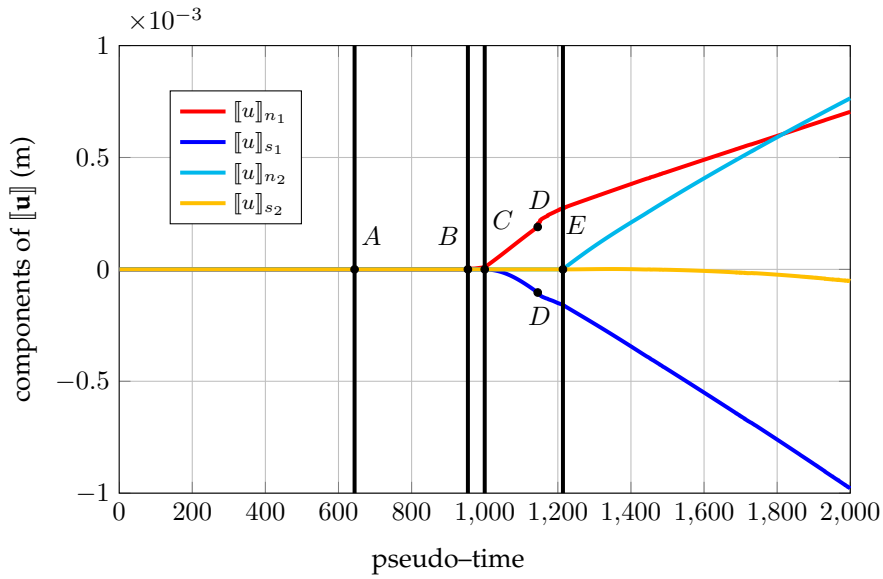


Figure 5.11: Time evolution of the components of displacement jump - Willam’s like loading test using transition approach for the threshold at 20% g_f^π

is 100 times the ones used for the previous computation. The obtained global response is different from the previously obtained one. In the evolution of σ_{22} , there is a stabilization effect at D where the jumps are observed previously. However, at the onset of the second crack E , there is a jump. Further sensitivity studies are required to understand the effect of the penalization of the stiffness matrix of the traction–separation law on the global response. In the later section, we carry out the studies without any penalization.

However, the global response is stabilized by introducing a non-zero value of the internal variable at the crack initiation (appendix 7.2). The global results of the numerical studies performed in this and the next section with the modified traction-separation law are presented in appendix 7.2.

Influence of the threshold of transition criterion To show the role of transitional damage threshold in the obtained response, we repeat the same test for different levels of energy dissipation at transition. For the sake of illustration, we now perform the transition after the dissipation reaches 40% and 60% of g_f^π on at least one microplane.

Similar to the previous case, jumps are also observed in the global responses, fig. 5.12 and fig. 5.13 at D . It is observed from the the evolution of the components of stress tensor (fig. 5.9 fig. 5.12 and fig. 5.13) that the peaks of the stress components, σ_{11} and σ_{12} are reduced as the threshold of the transition criterion increases. This is explained using the corresponding microdamage and energy dissipation profiles (figs. 5.14a and 5.14b) before the activation of the first and second crack (B and E respectively in figs. 5.12 and 5.13). It can be concluded from figs. 5.14a and 5.14b that as the threshold of transition criterion increases, higher is the level of microdamage before the activation of the second crack and also lower is the available energy. Moreover, as the level of energy dissipation at transition increases, the second crack is rotated farther from the first crack. It is observed that the angle between the two cracks is 81° and 97° in the cases for which the level of energy dissipation at transition is 40% and 60% of g_f^π respectively.

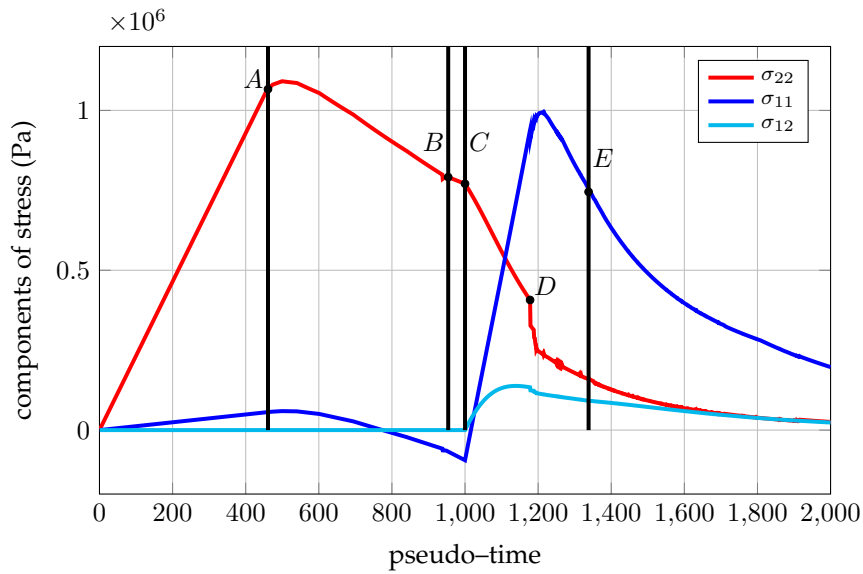


Figure 5.12: Time evolution of the components of stress - Willam's like loading test using transition approach for the threshold at 40% of g_f^π

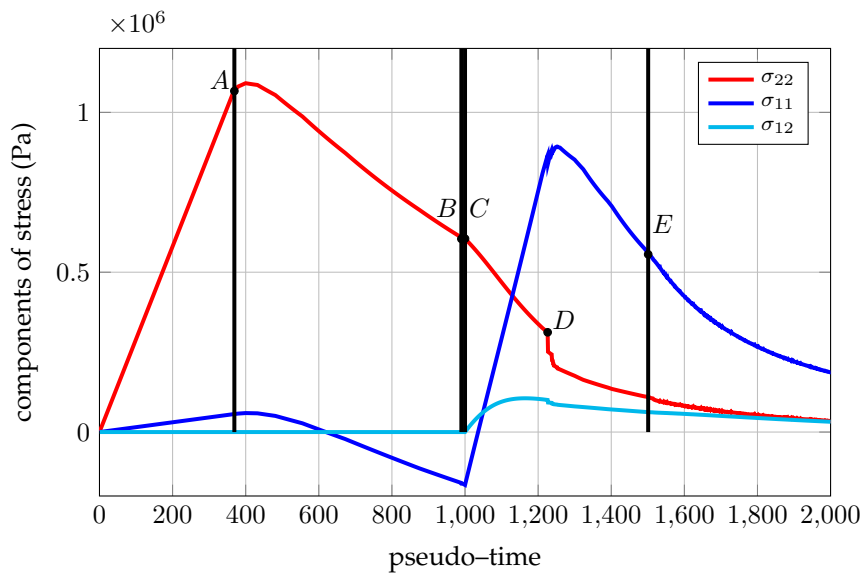


Figure 5.13: Time evolution of the components of stress - Willam's like loading test using transition approach for the threshold at 60% of g_f^π

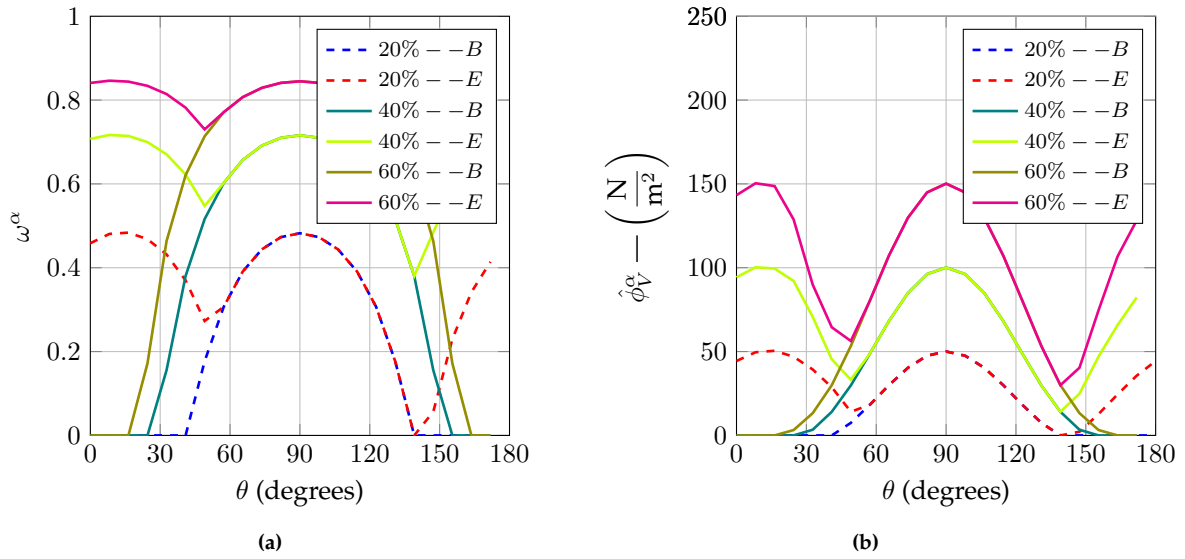


Figure 5.14: Comparison of distribution profiles of ω^α (a) and $\hat{\phi}_V^\alpha$ (b) over the microplane system at various stages of Willam's like loading test using transition approach for different thresholds of transition criterion

5.6 Conclusions

Microplane microdamage model and the strong discontinuity formulation are efficiently coupled using a transition approach. The anisotropic damage growth prior to the initiation of multiple cracks is well captured in the proposed transition framework. The implications of opening a crack in an induced anisotropic media are studied. The transition criterion is selected on the basis of a condition of mesh independent responses at both the global and the local level. Among other quantities studied for the transition criteria, the one based on the energy dissipation on each microplane gives the mesh independent results. The proposed transition methodology and algorithm are then extended to allow the formation of multiple cracks. The main novelty of the proposed approach is that the parameters of the traction–separation laws of each crack are computed using the anisotropic properties of the microplane microdamage model. The proposed algorithms and methodologies are validated using a simple numerical experiments. Some numerical instabilities encountered could be due to the sensitivity of the traction–separation law. Preliminary sensitivity analysis show that using a penalized stiffness matrix some instabilities disappear but still the global response is not stabilized.

```

Fextn+1 = Fextt + ΔFextn+1;
i = 0;
convglobal = 0;
while convglobal = 0 do
  ...;
  computation of dn+1,i+1 (see algorithm 1);
  ...;
  for loop over Gauss points do
    εn+1,i+1 = Bdn+1,i+1 + Gen+1,i;
    εn+1,i+1 → {εmα, εlα}n+1,i+1;
    if flag = 0 and the transition criterion on any Ωα ∈ Ω is not fulfilled then
      // update ωα
      {εmα, εlα}n+1,i+1 → {ωα}n+1,i+1;
      {ωα}n+1,i+1, {εmα, εlα}n+1,i+1 → {σmα, σlα}n+1,i+1;
      {σmα, σlα}n+1,i+1 → {φVα}n+1,i+1;
      {φVα}n+1,i+1 → {φSα}n+1,i+1 eq. (5.13);
      {σmα, σlα}n+1,i+1 → σ(dn+1,i+1, en+1,i+1,j+1);
    else
      compute en+1,i+1 using algorithm 4;
      εn+1,i+1 = Bdn+1,i+1 + Gen+1,i+1;
      εn+1,i+1 → {εmα, εlα}n+1,i+1, {ωα}n+1,i+1, {σmα, σlα}n+1,i+1;
      {σmα, σlα}n+1,i+1 → σ(dn+1,i+1, en+1,i+1);
    end
  end
  σ(dn+1,i+1, en+1,i+1,j+1) → Fintn+1,i+1;
  Fextn+1, Fintn+1,i+1 → R(dn+1,i+1, en+1,i+1);
  if ||Rn+1,i+1|| < εtol then
    | i = i + 1;
  else
    | convglobal = 1;
  end
end

```

Algorithm 3: Global algorithm for initiation of a single crack in microplane damage-to-fracture transition framework

```

for loop over Gauss points do
   $j = 0;$ 
   $conv_{local} = 0;$ 
  while  $conv_{local} = 0$  do
    if  $j = 0$  then
      // no update of  $\omega^\alpha$ 
       $\{\omega^\alpha\}^{n+1,i}, \{\epsilon_m^\alpha, \epsilon_l^\alpha\}^{n+1,i+1} \rightarrow \{\sigma_m^\alpha, \sigma_l^\alpha\}^{n+1,i+1,0};$ 
       $\{\sigma_m^\alpha, \sigma_l^\alpha\}^{n+1,i+1,0} \rightarrow \sigma(\mathbf{d}^{n+1,i+1}, \mathbf{e}^{n+1,i});$ 
      // compute the residual of the local traction continuity condition
       $\sigma(\mathbf{d}^{n+1,i+1}, \mathbf{e}^{n+1,i}) \rightarrow \mathbf{r}(\mathbf{d}^{n+1,i+1}, \mathbf{e}^{n+1,i});$ 
       $\mathbf{r}(\mathbf{d}^{n+1,i+1}, \mathbf{e}^{n+1,i}) \rightarrow \mathbf{e}^{n+1,i+1,0}$  eq. (3.48b);
    else
       $\epsilon^{n+1,i+1,j} = \mathbf{B}\mathbf{d}^{n+1,i+1} + \mathbf{G}\mathbf{e}^{n+1,i+1,j};$ 
       $\epsilon^{n+1,i+1,j} \rightarrow \{\epsilon_m^\alpha, \epsilon_l^\alpha\}^{n+1,i+1,j};$ 
      // no update of  $\omega^\alpha$ 
       $\{\omega^\alpha\}^{n+1,i}, \{\epsilon_m^\alpha, \epsilon_l^\alpha\}^{n+1,i+1,j} \rightarrow \{\sigma_m^\alpha, \sigma_l^\alpha\}^{n+1,i+1,j};$ 
       $\{\sigma_m^\alpha, \sigma_l^\alpha\}^{n+1,i+1,j} \rightarrow \sigma(\mathbf{d}^{n+1,i+1}, \mathbf{e}^{n+1,i+1,j});$ 
      // compute the residual of the local traction continuity condition
       $\sigma(\mathbf{d}^{n+1,i+1}, \mathbf{e}^{n+1,i+1,j}) \rightarrow \mathbf{r}(\mathbf{d}^{n+1,i+1}, \mathbf{e}^{n+1,i+1,j})$  eq. (3.48b);
       $\mathbf{r}(\mathbf{d}^{n+1,i+1}, \mathbf{e}^{n+1,i+1,j}) \rightarrow \mathbf{e}^{n+1,i+1,j+1};$ 
    end
    if  $\|\mathbf{r}\| < \epsilon_{tol}$  then
      |  $j = j + 1;$ 
    else
      |  $conv_{local} = 1;$ 
    end
  end
end

```

Algorithm 4: Local algorithm for initiation of a single crack in microplane damage-to-fracture transition framework

```

Fextn+1 = Fextt + ΔFextn+1;
i = 0;
convglobal = 0;
while convglobal = 0 do
  ...;
  computation of dn+1,i+1 (see algorithm 1);
  ...;
  for loop over Gauss points do
    εn+1,i+1 = Bdn+1,i+1 + G1e1n+1,i + G2e2n+1,i;
    εn+1,i+1 → {εmα, εlα}n+1,i+1;
    if flag1 = 0, flag2 = 0 and the transition criterion on any Ωα ∈ Ω is not fulfilled then
      // update ωα
      {εmα, εlα}n+1,i+1 → {ωα}n+1,i+1;
      {ωα}n+1,i+1, {εmα, εlα}n+1,i+1 → {σmα, σlα}n+1,i+1;
      {σmα, σlα}n+1,i+1 → {φVα}n+1,i+1;
      {φVα}n+1,i+1 → {φS1α}n+1,i+1;
      {σmα, σlα}n+1,i+1 → σ(dn+1,i+1, en+1,i+1,j+1);
    else
      if flag1 = 0, flag2 = 0 then
        compute e1n+1,i+1 using algorithm 4;
        εn+1,i+1 = Bdn+1,i+1 + G1e1n+1,i+1;
        εn+1,i+1 → {εmα, εlα}n+1,i+1, {ωα}n+1,i+1, {σmα, σlα}n+1,i+1;
        {σmα, σlα}n+1,i+1 → σ(dn+1,i+1, en+1,i+1,j+1);
        {σmα, σlα}n+1,i+1 → {φVα}n+1,i+1;
        if {ωα}n+1,i+1 > 0 and the transition criterion on at least one Ωα ∈ Ωl is fulfilled
          then
            {φVα}n+1,i+1 → {φS2α}n+1,i+1 eq. (5.21);
          end
        end
      else
        compute e1n+1,i+1, e2n+1,i+1 using algorithm 6;
        εn+1,i+1 = Bdn+1,i+1 + G1e1n+1,i+1 + G2e2n+1,i+1;
        εn+1,i+1 → {εmα, εlα}n+1,i+1, {ωα}n+1,i+1, {σmα, σlα}n+1,i+1;
        {σmα, σlα}n+1,i+1 → σ(dn+1,i+1, en+1,i+1,j+1);
      end
    end
  end
  σ(dn+1,i+1, e1n+1,i+1, e2n+1,i+1) → Fintn+1,i+1;
  Fextn+1, Fintn+1,i+1 → R(dn+1,i+1, e1n+1,i+1, e2n+1,i+1);
  if ||R|| < εtol then
    | i = i + 1;
  else
    | convglobal = 1;
  end
end

```

Algorithm 5: Global algorithm for initiation of two cracks in microplane damage-to-fracture transition framework

```

for loop over Gauss points do
   $j = 0$ ;
   $conv_{local} = 0$ ;
  while  $conv_{local} = 0$  do
    if  $j = 0$  then
      // no update of  $\omega^\alpha$ 
       $\{\omega^\alpha\}^{n+1,i}, \{\epsilon_m^\alpha, \epsilon_l^\alpha\}^{n+1,i+1} \rightarrow \{\sigma_m^\alpha, \sigma_l^\alpha\}^{n+1,i+1,0}$ ;
       $\{\sigma_m^\alpha, \sigma_l^\alpha\}^{n+1,i+1,0} \rightarrow \sigma(\mathbf{d}^{n+1,i+1}, \mathbf{e}_1^{n+1,i}, \mathbf{e}_2^{n+1,i})$ ;
      // compute the residuals of the local coupled traction continuity conditions
       $\sigma(\mathbf{d}^{n+1,i+1}, \mathbf{e}_1^{n+1,i}, \mathbf{e}_2^{n+1,i}) \rightarrow$ 
       $\mathbf{r}_1(\mathbf{d}^{n+1,i+1}, \mathbf{e}_1^{n+1,i}, \mathbf{e}_2^{n+1,i}), \mathbf{r}_2(\mathbf{d}^{n+1,i+1}, \mathbf{e}_1^{n+1,i}, \mathbf{e}_2^{n+1,i})$  eqs. (3.96b)
      and (3.96c);
       $\mathbf{r}_1(\mathbf{d}^{n+1,i+1}, \mathbf{e}_1^{n+1,i}, \mathbf{e}_2^{n+1,i}), \mathbf{r}_2(\mathbf{d}^{n+1,i+1}, \mathbf{e}_1^{n+1,i}, \mathbf{e}_2^{n+1,i}) \rightarrow$ 
       $\mathbf{e}_1^{n+1,i+1,0}, \mathbf{e}_2^{n+1,i+1,0}$ ;
    else
       $\epsilon^{n+1,i+1,j} = \mathbf{B}\mathbf{d}^{n+1,i+1} + \mathbf{G}_1\mathbf{e}_1^{n+1,i+1,j} + \mathbf{G}_2\mathbf{e}_2^{n+1,i+1,j}$ ;
       $\epsilon^{n+1,i+1,j} \rightarrow \{\epsilon_m^\alpha, \epsilon_l^\alpha\}^{n+1,i+1,j}$ ;
      // no update of  $\omega^\alpha$ 
       $\{\omega^\alpha\}^{n+1,i}, \{\epsilon_m^\alpha, \epsilon_l^\alpha\}^{n+1,i+1,j} \rightarrow \{\sigma_m^\alpha, \sigma_l^\alpha\}^{n+1,i+1,j}$ ;
       $\{\sigma_m^\alpha, \sigma_l^\alpha\}^{n+1,i+1,j} \rightarrow \sigma(\mathbf{d}^{n+1,i+1}, \mathbf{e}_1^{n+1,i+1,j}, \mathbf{e}_2^{n+1,i+1,j})$ ;
      // compute the residuals of the local coupled traction continuity conditions
       $\sigma(\mathbf{d}^{n+1,i+1}, \mathbf{e}_1^{n+1,i+1,j}, \mathbf{e}_2^{n+1,i+1,j}) \rightarrow$ 
       $\mathbf{r}_1(\mathbf{d}^{n+1,i+1}, \mathbf{e}_1^{n+1,i+1,j}, \mathbf{e}_2^{n+1,i+1,j}), \mathbf{r}_2(\mathbf{d}^{n+1,i+1}, \mathbf{e}_1^{n+1,i+1,j}, \mathbf{e}_2^{n+1,i+1,j})$ 
      eqs. (3.96b) and (3.96c);
       $\mathbf{r}_1(\mathbf{d}^{n+1,i+1}, \mathbf{e}_1^{n+1,i+1,j}, \mathbf{e}_2^{n+1,i+1,j}), \mathbf{r}_2(\mathbf{d}^{n+1,i+1}, \mathbf{e}_1^{n+1,i+1,j}, \mathbf{e}_2^{n+1,i+1,j}) \rightarrow$ 
       $\mathbf{e}_1^{n+1,i+1,j+1}, \mathbf{e}_2^{n+1,i+1,j+1}$ ;
    end
    if  $\|\mathbf{r}_1, \mathbf{r}_2\| < \epsilon_{tol}$  then
      |  $j = j + 1$ ;
    else
      |  $conv_{local} = 1$ ;
    end
  end
end

```

Algorithm 6: Local algorithm for initiation of a two cracks in microplane damage-to-fracture transition framework

Structural case studies

In this chapter, we perform numerical simulations of structural test cases using the microplane microdamage model coupled with strong discontinuity formulation. For this purpose, we choose (i) a double notched plain concrete specimen submitted to a rather simple tensile loading [SHI et al., 2000] and (ii) a reinforced concrete shear wall [RIVILLON and GABS, 2011] under complex loading conditions. The objective of the first test is to examine the capacity of the proposed transition methodology for the initiation and propagation of cracks in the highly localized damage zones at the structural level. The second test is performed to examine the capacity of the proposed transition methodology for not only the initiation and propagation of cracks but also the crack closure. We emphasize here that the purpose of these studies is not to reproduce the experimental results but to check if the proposed numerical formulations are able to capture the characteristic cracking patterns of these test cases.

6.1 Double notched specimen under tensile loading

6.1.1 Description of the test

In the experimental campaign [SHI et al., 2000], double notched concrete specimens with different eccentricities between the notches are tested by applying a tensile loading. The geometry and the loading of the specimen are shown in fig. 6.1. Here, two notches of 2 mm width and 10 mm length are considered on the opposite notches of the specimen. The experimental cracking pattern consists of two single cracks propagating through the specimen.

For the sake of illustration, we focus here on the configuration in which the eccentricity between the notches is 5 mm. This case is more interesting because in this configuration cracking pattern consists of two cracks approaching each other at the center of the specimen which is more difficult to capture than the other cases where they propagate by avoiding each other at the center. Nevertheless, from the point of view of the application of the proposed methodology, the aspects under study such as the effect of the energy regularization technique and threshold of transition criterion remain the same for all the configurations even though the cracking patterns changes.

6.1.2 Numerical simulations

The finite element discretization of the specimen is performed by considering unstructured coarse and structured fine meshes using CST elements. In the case of the later, right angled triangular elements with height and breadth equal to the width of the notch are considered. Hence, the characteristic length of the element, $l_c = \sqrt{2A_e}$ is equal to the width of the notch which is 2 mm.

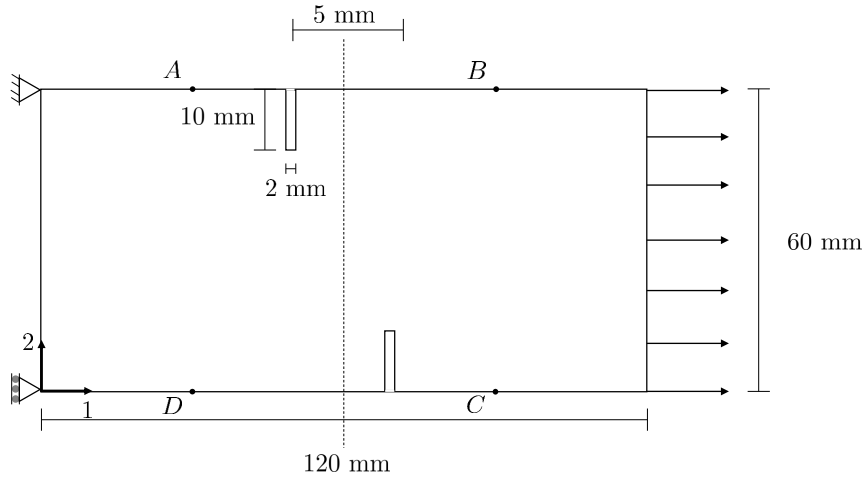


Figure 6.1: Double notched specimen under tensile loading: geometry and loading conditions

The microplane microdamage model is considered only for the central 60 mm portion of the specimen. The rest of the specimen is assumed as elastic. The considered material parameters are given in the table 6.1.

The horizontal tensile loading is applied on the right edge of the specimen as shown in fig. 6.1. The loading is applied using the CNDI technique (section 3.5.2.2) and the following path-following constraint is written:

$$P = \frac{1}{2} [(\Delta d_1^B - \Delta d_1^A) + (\Delta d_1^C - \Delta d_1^D)] - \Delta\tau = 0 \quad (6.1)$$

where, Δd_1^A , Δd_1^B , Δd_1^C and Δd_1^D are the nodal displacements in the horizontal direction (i.e., the direction of the loading) at points A, B, C and D respectively (fig. 6.1) and $\Delta\tau$ is taken as 2.5×10^{-7} m.

Damage-to-fracture transition is modeled through the formulation introduced in previous section considering a criterion based on the energy dissipation at the microplane level. Regarding threshold energy value for the transition criterion, the transition is performed when $\max_\alpha(\phi_V^\alpha)$ reaches 85% of g_f^τ . Notice that this does not mean that 85% of energy available at the unit volume is consumed before transition, given the circular integration (also relation (4.38)), at least 42.5% G_f is still available for the crack.

Preliminary analyses showed that a lower threshold value leads to abrupt opening and closing of the cracks during this test. On the other hand, if more volumetric energy is allowed to dissipate before crack localization (i.e., a higher threshold for the transition criterion is chosen), then the crack opens in a gradual manner. However, these sensitivity issues are not investigated in this work but we present here the case where there is a smooth evolution of the traction–separation law.

Global results The force–displacement curves in the vertical direction for the coarse and the fine meshes using both the microplane microdamage model and the transition framework are compared in figs. 6.2a and 6.2b respectively. Moreover, the load–CMOD curves for both models are given in figs. 6.3a and 6.3b.

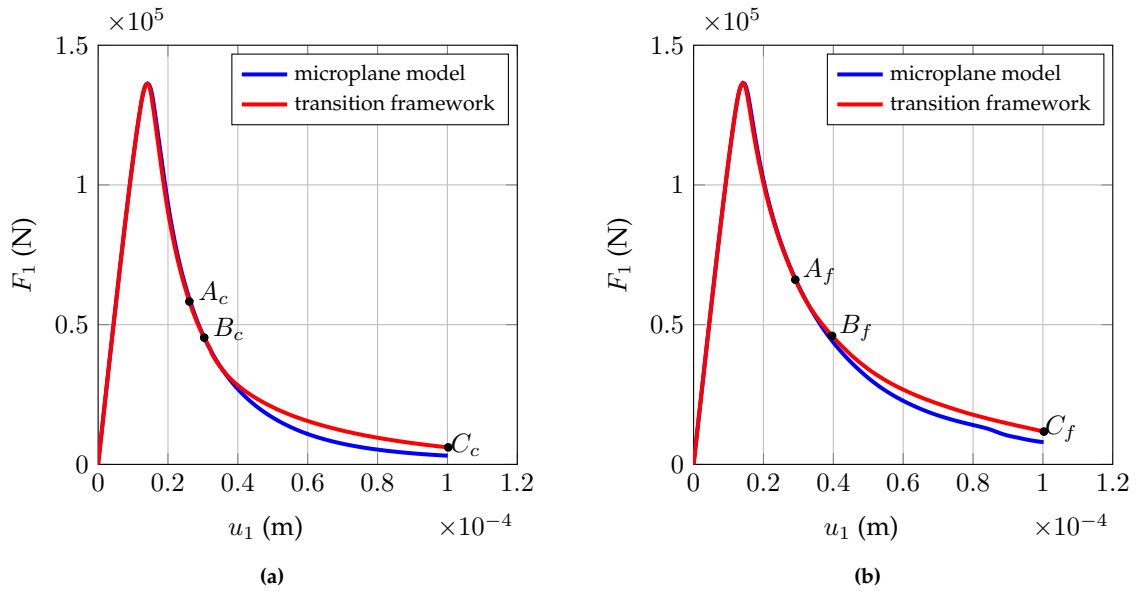
As energy regularization technique depends on the characteristic length of the mesh, the global responses using the two meshes (for a given model) are different. The aspect of effectiveness of the energy regularization technique as a dependant on the definition of the characteristic length is also demonstrated using 1D bar in section 4.5.3 for mode I cracking. Moreover, in the present

Table 6.1: The material parameters considered for the microplane microdamage model and the EFEM in the transition framework for the double notch specimen

material parameter	value
Young's modulus	24 GPa
Poisson's ratio	0.2
$\tilde{\epsilon}_0^\pi$	1.2×10^{-4}
β	1
N^α	21
G_f	100 N/m
β_{cr}	1

case, as the cracking process is more complex, it is difficult to define the characteristic length in order to obtain the mesh independent solutions.

It can be observed that the energy dissipation (area under the global curves figs. 6.2a and 6.2b) of the double notched specimen using the transition methodology is more than that of the microplane microdamage model. This is explained by the fact that the volumetric energy dissipation, g_f is defined in terms of G_f (eq. (4.81)) by assuming a mode I crack opening. So, we have on one hand the global response characterized by the microplane microdamage constitutive law whose energy dissipation is obtained under the mode I assumption and on the other hand the global response using EFEM which takes into account the mixed mode opening of cracks. Since the mixed mode is activated here, there is a difference between the energy dissipation obtained from the microplane microdamage model and that of the EFEM after transition.

**Figure 6.2:** Comparison of the global responses of the double notched specimen with eccentricity of 5 mm using the microplane microdamage model and the transition methodology: coarse unstructured mesh (a), fine structured mesh (b)

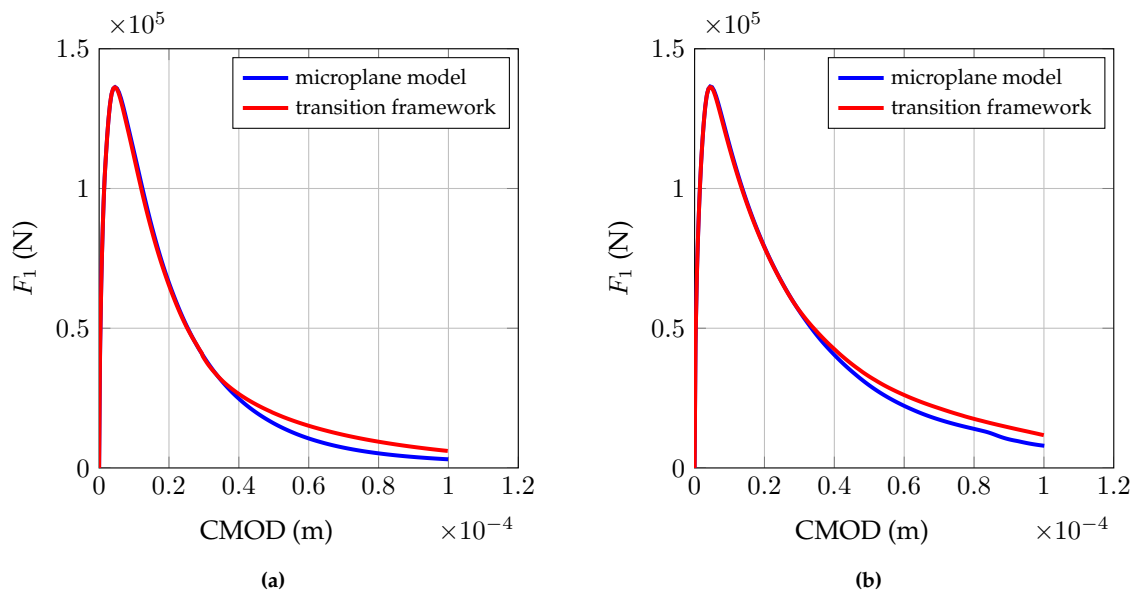


Figure 6.3: Comparison of the load–CMOD curves of the double notched specimen with eccentricity of 5 mm using the microplane microdamage model and the transition methodology: coarse mesh (a), fine mesh (b)

Local results In order to analyze the damage growth, we plot here the distribution of the local quantity $\max_{\alpha} \omega^{\alpha}$, which is the maximum of ω^{α} on the microplane system. The cracking pattern is analyzed by plotting the Boolean variable, $flag_{cr}$ whose non-zero value represents the initiation of the crack.

The local results are obtained by plotting the interested quantities at the Gauss point of each finite element. Since in this case we have only one Gauss point per element (CST), the value of a given local quantity is represented using a single color smeared over the finite element.

The points on the global curve after which the transition takes place are denoted by A_c and A_f (figs. 6.2a and 6.2b) for the coarse and the fine meshes respectively. The corresponding distributions of $\max_{\alpha} \omega^{\alpha}$ at these points are shown in figs. 6.4 and 6.5. Since the transition is performed after a higher percentage of the energy density at the microplane level ($85\%g_f^{\pi}$) is dissipated, the microdamage variable also reaches a high level before transition.

The cracking patterns of the coarse mesh at two different load levels, B_c and C_c (fig. 6.2a) are depicted in figs. 6.6a and 6.6b respectively. It can be observed that the cracks originated at the two notches approach each other at the center of the specimen. Similarly, the cracking patterns for a fine mesh are depicted in figs. 6.7a and 6.7b at B_f and C_f (fig. 6.2b) respectively. In this case, only the crack originated at the upper notch tends towards the lower notch.

From these two results, it can be clearly seen that there is an induced bias with respect to the orientation of the mesh. This is a known disadvantage of the energy regularization [OLIVER, 1989, JIRÁSEK and BAUER, 2012]. This can be alleviated by adopting other regularization techniques, for instance, the nonlocal approaches [BAŽANT and di LUZIO, 2004, GIRY et al., 2011] which is to be tested in the future work. The crack opening and sliding at the end of test are shown in the fig. 6.8a-figs. 6.8b and 6.9a-fig. 6.9b for coarse and fine mesh respectively. As expected, both the crack opening and sliding is more pronounced near the notch.

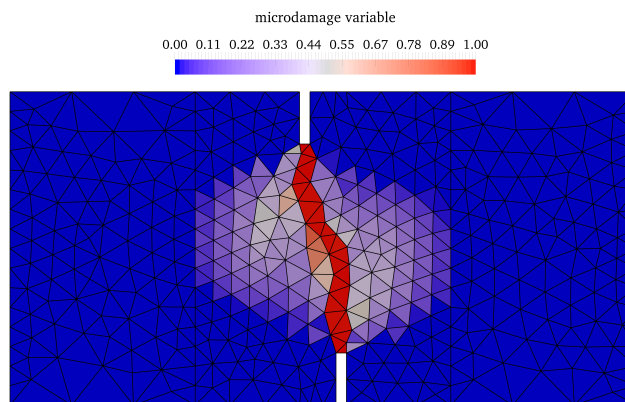


Figure 6.4: Distribution of $\max_{\alpha} \omega^{\alpha}$ for the double notched specimen with eccentricity of 5 mm in the case of coarse mesh before the initiation of crack at A_c

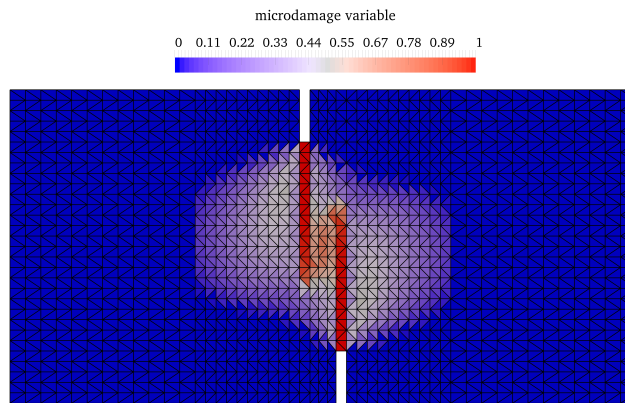
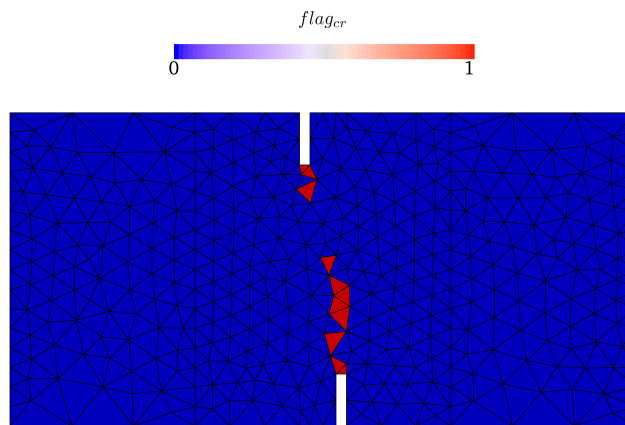
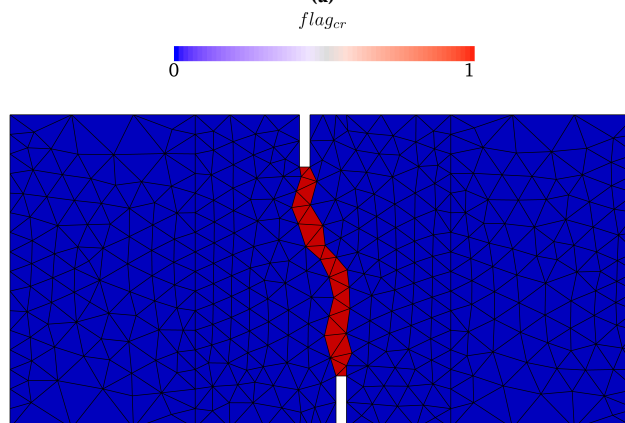


Figure 6.5: Distribution of $\max_{\alpha} \omega^{\alpha}$ for the double notched specimen with eccentricity of 5 mm in the case of fine mesh before the initiation of crack at A_f



(a)



(b)

Figure 6.6: Distribution of $flag_{cr}$ for the double notched specimen with eccentricity of 5 mm in the case of coarse mesh at B_c (a) and C_c (b)

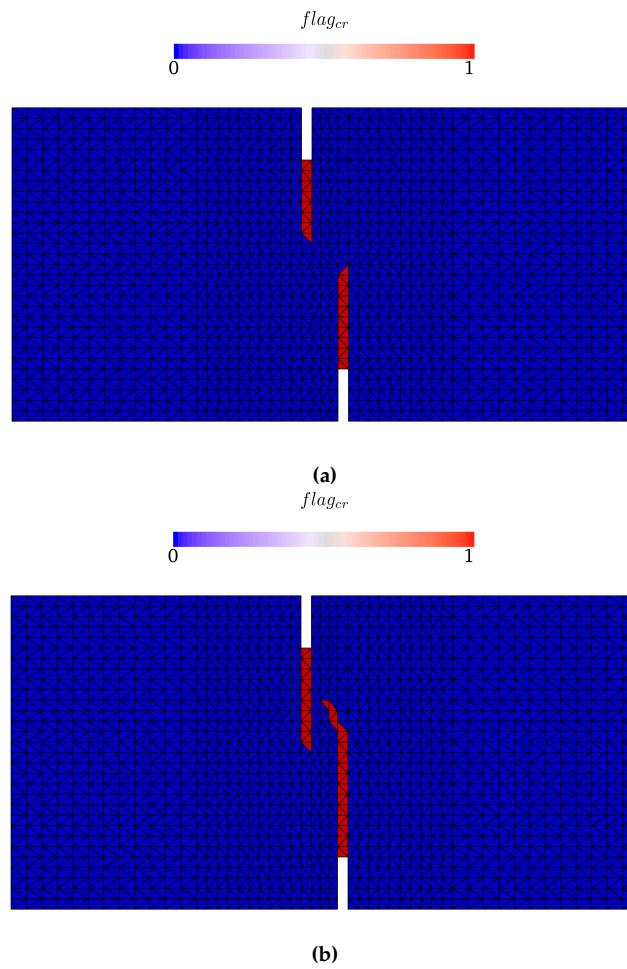


Figure 6.7: Distribution of $flag_{cr}$ for the double notched specimen with eccentricity of 5 mm in the case of fine mesh at B_f (a) and C_f (b)

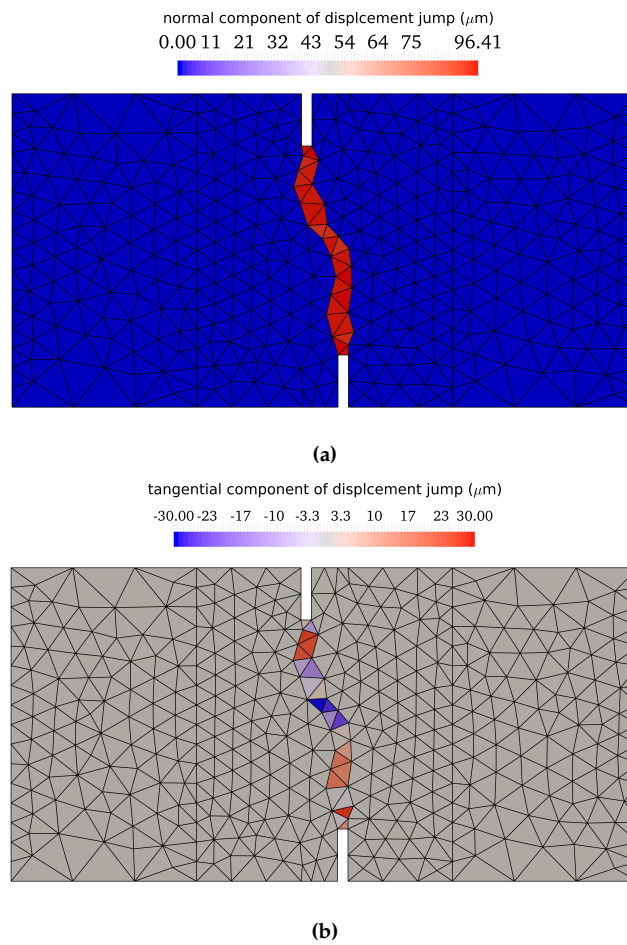


Figure 6.8: Distribution of $[[u]]_n$ (a) and $[[u]]_s$ (b) for the double notched specimen with eccentricity of 5 mm in the case of coarse mesh at the end of the numerical test C_c

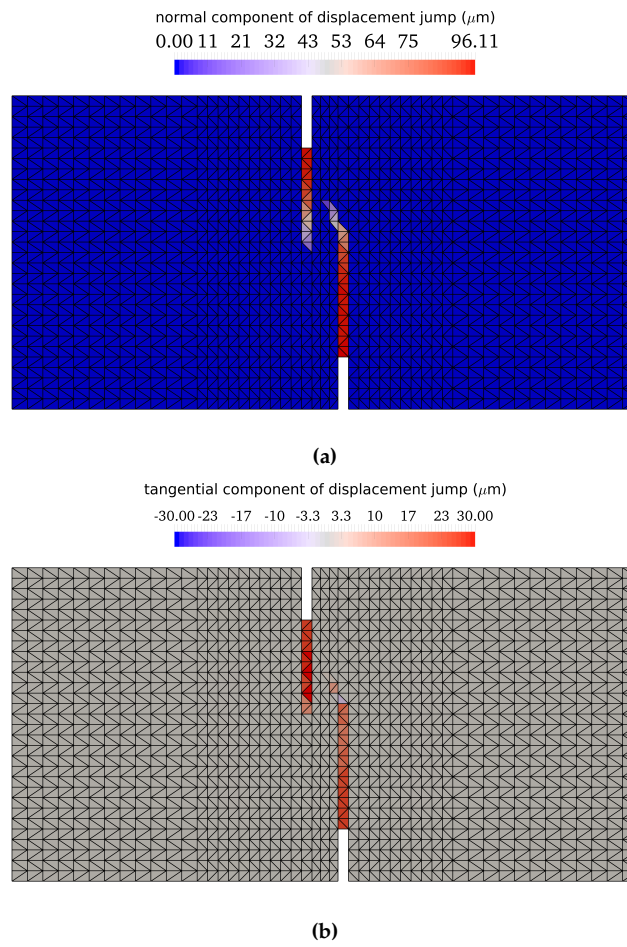


Figure 6.9: Distribution of $[[u]]_n$ (a) and $[[u]]_s$ (b) for the double notched specimen with eccentricity of 5 mm in the case of fine mesh at the end of the numerical test C_f

6.2 Shear wall tests

6.2.1 Description of the test

In this section, we simulate a shear wall under monotonic and non–reverse cyclic loading using the microplane microdamage model and the transition framework. The geometry and the reinforcement are considered according to the benchmark conducted by [RIVILLON and GABS, 2011]. The purpose of the benchmark is to determine the non–linear response and the crack patterns of the shear wall. But we focus here only on capturing the characteristic crack patterns of this test.

The specimen contains two beams and a shear reinforced concrete wall, with longitudinal and the transverse reinforcements (fig. 6.10). Here, the longitudinal reinforcement runs through all the components of the specimen connecting different components while the transverse reinforcement is present only in the shear wall. The beams are placed on the top and the bottom of the shear wall in order to impose the boundary conditions. Given the assumption of plane strain condition, the reinforcement in the shear wall of 0.15 m is normalized for a unit meter.

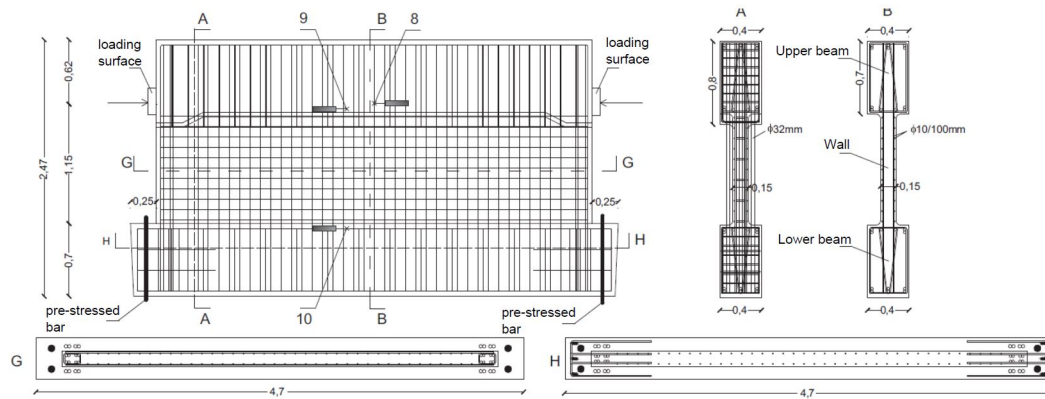


Figure 6.10: Geometry and reinforcement details of the shear wall specimen [RIVILLON and GABS, 2011]

6.2.2 Numerical simulations

The FE mesh of the specimen with unstructured CST elements is shown in fig. 6.11a. Total 2344 CST elements for modeling concrete and 1746 bar elements for modeling steel reinforcement are used.

In the experimental set up, two prestressed bars that run through the lower beam are used to prevent rotations of the specimen. For the sake of simplicity, these bars are not modeled but the equivalent boundary conditions are imposed on the lower beam as shown in fig. 6.11a. Also, during experiments, a force is applied on the loading surfaces on each side of the upper beam. However, in this work the loading is applied only on the left edge of the upper beam as Dirchlet boundary conditions, that is to say, the simulation is displacement driven. This consideration is because during the preliminary simulations, some convergence problems are encountered by imposing force on the loading surfaces. This in turn could be because it is difficult to follow the softening branch of the local constitutive law by applying an increasing force. Also, the self-weight of the shear wall is not taken into account.

The upper and the lower beams are assumed to behave in an elastic manner while the shear wall exhibits the non–linearity. In the case of reinforcement, each steel bar is modeled using 1D truss elements, that is, no extra degrees of freedom pertaining to the rotations of the bars are considered.

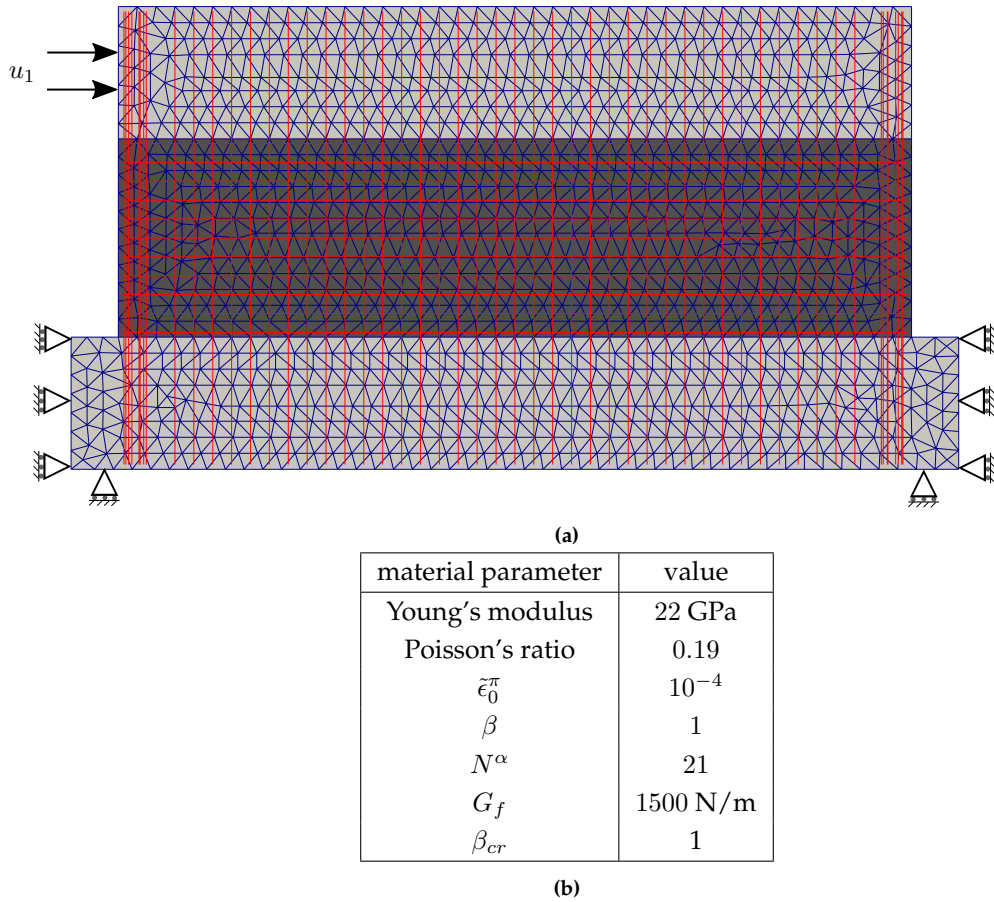


Figure 6.11: Finite element mesh of the shear wall, elastic beams and the reinforcement of the specimen (a) and the material parameters considered for the microplane microdamage model and the EFEM in the transition framework for the shear wall (b)

Here, we aim to restrict the material non-linearity only to the concrete. Hence, the reinforcement is assumed to behave in elasticity and the bond between the concrete and the steel is considered to be perfect. The material parameters of the microplane model and the traction-separation law of the EFEM are given in fig. 6.11b. For this test, the threshold for the transition criterion is assumed as 70% of g_f^π . Finally, the material parameters considered here are for illustration purposes only.

During the experiments, multiple cracking pattern is not observed for monotonic and the non-reverse cyclic loading, hence the number of cracks per element is restricted to 1 during these two tests. In the next sections, we present the global and local results of the numerical simulations performed under monotonic and non-reverse cycling loading conditions.

6.2.2.1 Monotonic loading

In the first case, monotonic loading is considered (i.e., load increases with respect to the pseudo-time). The evolution of the global and local quantities along with the cracking patterns at different time steps are described next.

Global results The global force-displacement curves of the shear wall under monotonic loading condition using microplane microdamage model and the transition methodology are com-

pared in fig. 6.12. Due to the presence of the reinforcement, no softening is observed in the global response. Similar to the previous case, there is a slight difference between the global responses of the shear wall using both the approaches which is mostly contributed due to the mixed mode behavior of the cracks.

Local results We show the anisotropic damage growth and the cracking patterns using the distributions of $\max_{\alpha} \omega^{\alpha}$ and $flag_{cr}$ (crack activation flag) respectively.

The damage growth starts in the region near the right edge of the specimen as shown in fig. 6.13 which depicts the distribution of $\max_{\alpha} \omega^{\alpha}$ before the initiation of the crack (A in fig. 6.12).

As the transition criterion reaches, the initiation of cracks takes place at the interface between the specimen and the top elastic beam near its right edge. This is shown in the distribution of $flag_{cr}$ at B (fig. 6.12) in fig. 6.14b. Meanwhile, the microdamage growth progresses to the center of the specimen (fig. 6.14a) along with its initiation at the left bottom edge of the specimen.

Now, as the transition criterion reaches in more finite elements, the diagonal cracks as well as the horizontal cracks at the center and the bottom left edge are initiated as shown in the distribution of $flag_{cr}$ at C (fig. 6.12) in fig. 6.15b. At this point, the microdamage has reached its peak in most of the elements (fig. 6.15a).

At the end of the test (D in fig. 6.12), crack initiates in even more finite elements bridging the cracks at the center with the cracks at the bottom left edge (fig. 6.16b). Also at this point, the microdamage growth takes place in few more elements at the top interface (fig. 6.16a).

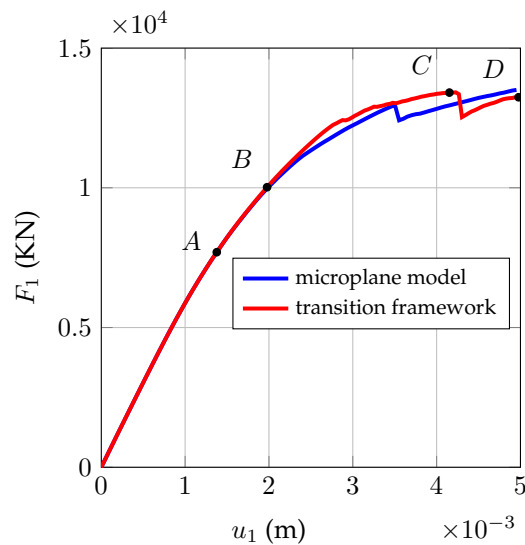


Figure 6.12: Comparison of the global responses of the shear wall specimen under monotonic loading using the microplane microdamage model and the transition methodology

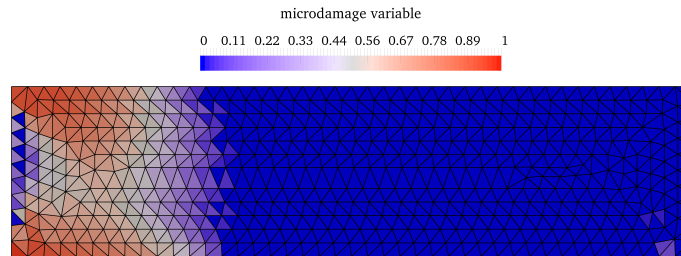


Figure 6.13: Distribution of $\max_{\alpha} \omega^{\alpha}$ for the shear wall specimen under monotonic loading before the initiation of crack at *A*

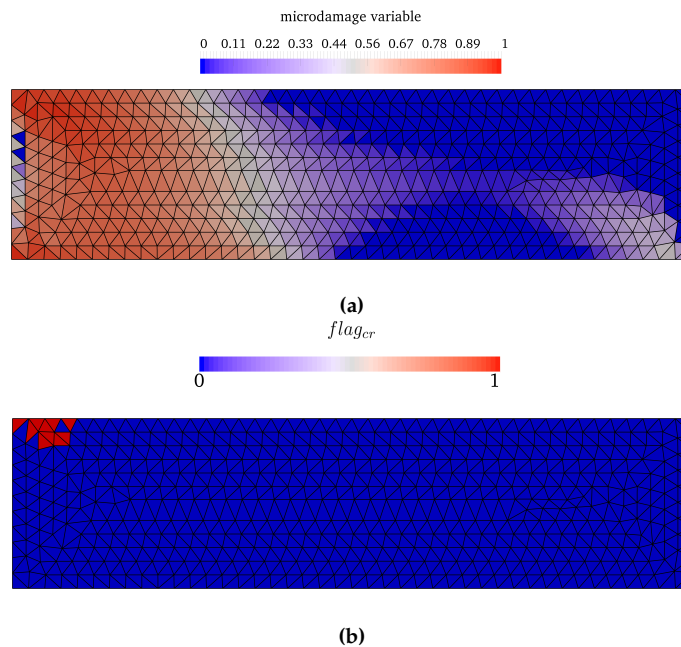


Figure 6.14: Distribution of $\max_{\alpha} \omega^{\alpha}$ (a) and $flag_{cr}$ (b) for the shear wall specimen under monotonic loading after the initiation of crack at *B*

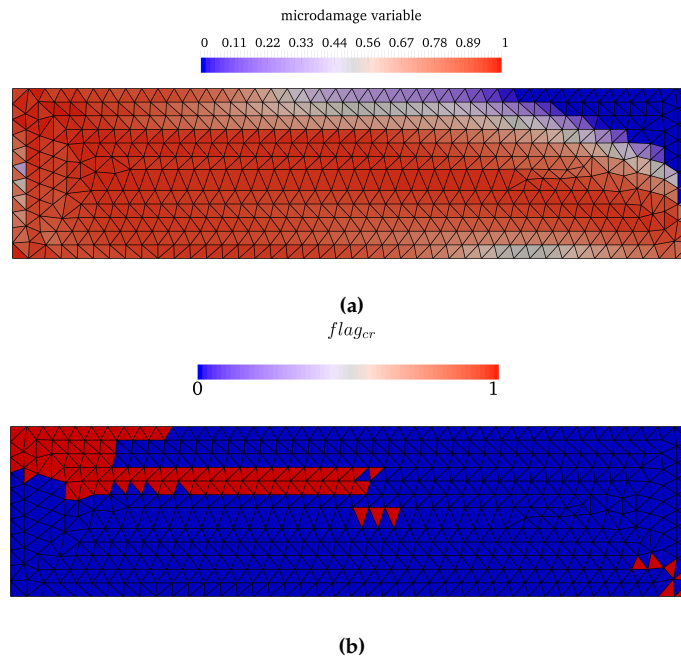


Figure 6.15: Distribution of $\max_{\alpha} \omega^{\alpha}$ (a) and $flag_{cr}$ (b) for the shear wall specimen under monotonic loading after the initiation of crack at C

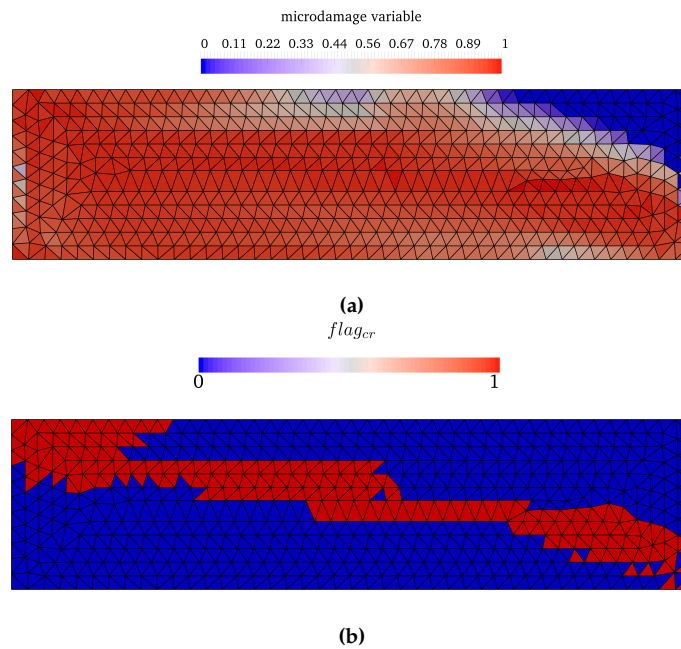


Figure 6.16: Distribution of $\max_{\alpha} \omega^{\alpha}$ (a) and $flag_{cr}$ (b) for the shear wall specimen under monotonic loading at the end of the numerical test D

The distributions of $[[u]]_n$ and $[[u]]_s$ are depicted in figs. 6.17a and 6.17b. From these figures, it can be observed that the cracks that are initiated at the later stage of the loading in the center portion of the specimen show more crack opening and crack sliding than the initial cracks at the interface between the specimen and the elastic beam.

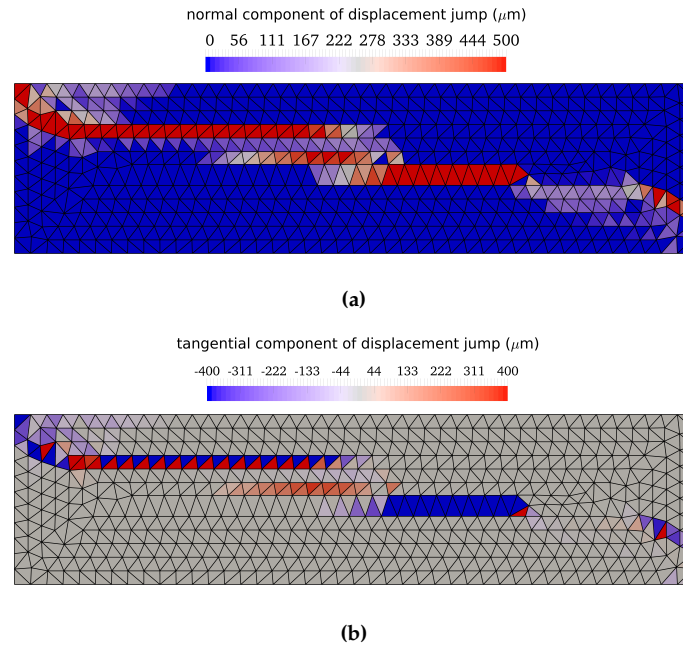


Figure 6.17: Distribution of $[[u]]_n$ (a) and $[[u]]_s$ (b) for the shear wall specimen under monotonic loading at the end of the numerical test D

6.2.2.2 Non–reverse cyclic loading

During this test, several cycles of loading, unloading and reloading are applied as shown in fig. 6.18 on the same (left) side of the upper elastic beam. The purpose of studying the non–reverse cyclic loading test is to illustrate the crack closure/re–opening during the load cycles.

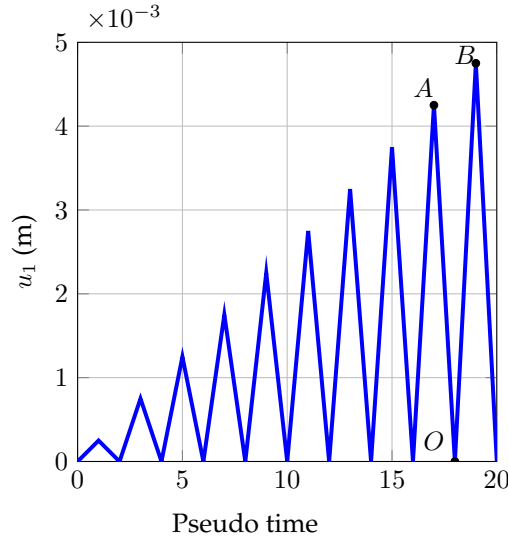


Figure 6.18: Time evolution of the applied displacement – shear wall specimen under non–reverse cyclic loading

Global results Similar to the previous case of monotonic loading, no softening is observed in the global force–displacement curves under non–reverse cyclic loading condition (fig. 6.19). It has to be noted that hysteresis loops are not exhibited since the internal frictional effects are not modeled. The difference between the global responses of the microplane microdamage model and the transition framework is less in this case than in the previous ones. However, the reduction of the global stiffness during unloading/reloading cycle is slightly more in the case of the transition framework than using the microplane microdamage model.

Local results It has to be noted that the distribution of $\max_{\alpha} \omega^{\alpha}$ in the present case is the same as in the case of monotonic loading. This is because the microdamage variable does not evolve during the unloading/reloading part of the cycle due to thermodynamic restrictions (4.32). Hence, we consider here the distributions of $flag_{cr}$, and the components of displacement jump in normal and tangential directions of the crack. The cracking patterns and crack closure/re–opening are illustrated here for the load cycle AOB (fig. 6.19).

In figs. 6.20a and 6.20b, we show the cracking patterns at starting and end of the load cycle (A and B respectively in fig. 6.19). They consist of the cracks at the interface along the upper-left edge and the horizontal/diagonal cracks in the center of the specimen. This is followed by the bridging between the cracks at the right bottom edge and cracks in the center of the specimen. These cracking patterns are in accordance with those in the case of the monotonic loading at this stage.

The closure of the crack and its reopening during the cycle AOB are illustrated using the depictions of $\llbracket u \rrbracket_n$ and $\llbracket u \rrbracket_s$ at A , O and B in figs. 6.21a to 6.21c and 6.22a to 6.22c respectively. It can be observed from figs. 6.21a to 6.21c (also figs. 6.22a to 6.22c) that the cracks that are opened at A are almost closed at the end of the unloading O in the global curve (fig. 6.19).

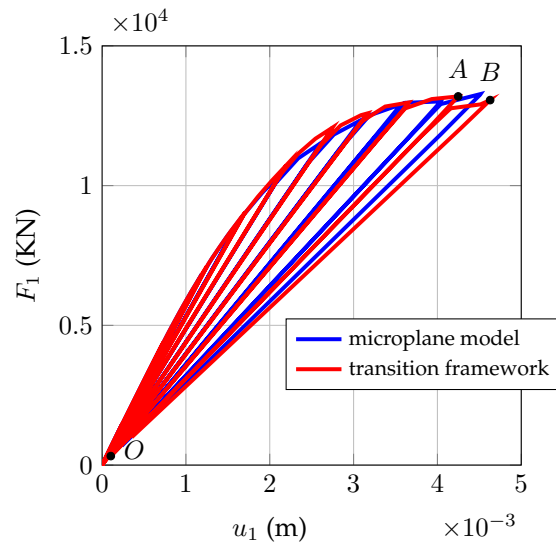


Figure 6.19: Comparison of the global responses of the shear wall specimen under non-reverse cyclic loading using the microplane microdamage model and the transition methodology

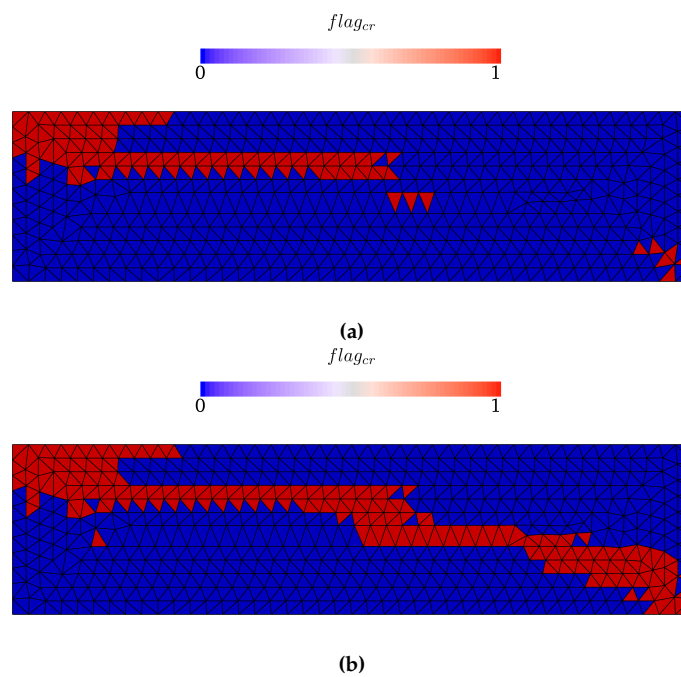


Figure 6.20: Distribution of $flag_{cr}$ for the shear wall specimen under alternate loading at start of the cycle A (a) and end of the cycle B (b)

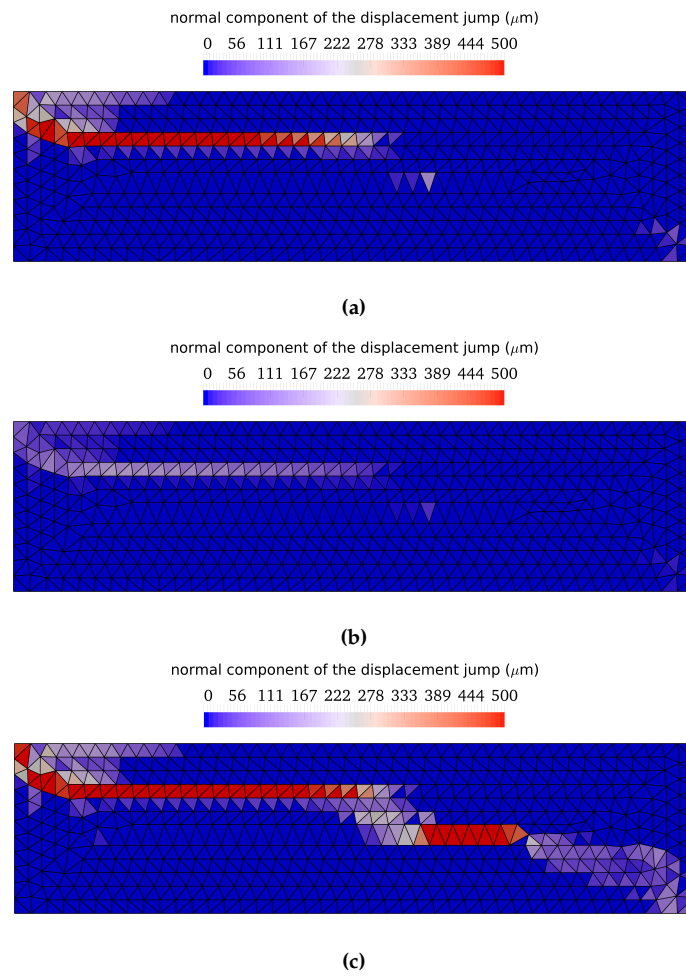


Figure 6.21: Distribution of $[[u]]_n$ for the shear wall specimen under alternate loading at the start of cycle *A* (a), end of unloading (b) and the end of cycle *B* (c)

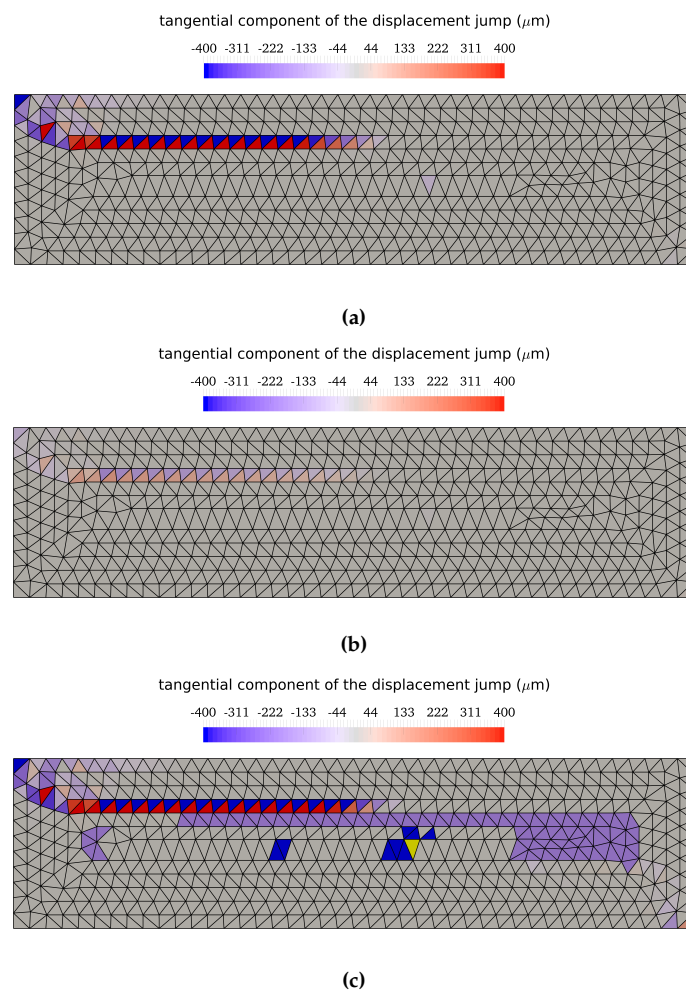


Figure 6.22: Distribution of $[[u]]_s$ for the shear wall specimen under alternate loading at the start of cycle *A* (a), end of unloading (b) and the end of cycle *B* (c)

6.3 Conclusions

The response of plain and reinforced concrete structures has been tested using the proposed formulations.

In the case of the double notched specimen, there is an acceptable match between the global responses of the microplane microdamage model and the damage-to-fracture transition methodology. However, it can be observed from both the global and local responses (cracking patterns) that the proposed energetic regularization of the microplane models does not allow to obtain fully mesh independent results, in terms of total dissipated energy and dependency of the crack pattern to the orientation of the finite element mesh.

In the case of the shear wall tests, the hardening trends of global responses during the monotonic and the non–reverse cyclic loading are well captured. Again, the robustness of the proposed transition methodology is proven from the global responses. The cracking patterns may not be exactly the same as that of the experimental ones but the trends are similar. Several types of cracks like interface cracks, diagonal cracks and bridging cracks are observed. In the case of the shear wall test under non–reverse cyclic loading, the crack closure and the reopening are well described.

In both the double notched specimen and shear wall tests studied here, the cracks exhibit mixed mode behavior. Common conclusion for both the test cases is that in order to compare the numerical results with that of the experimental ones we need to tune material parameters.

Here, we were able to simulate only the cases involving the initiation of a single crack. The cracking patterns involving multiple intersecting cracks are expected in the case of reverse cyclic loading of the shear wall specimen [RIVILLON and GABS, 2011, KISHTA, 2017]. However, during the preliminary simulations it is observed that it is difficult to obtain such crack patterns without crack tracking techniques [RICCARDI et al., 2017, OLIVER et al., 2002]. Also, the obtained global response of the shear wall under cyclic loading exhibits softening behavior which is not consistent for the behavior of reinforced concrete structures. This may be due to the modeling strategy used for the steel reinforcement and the steel-concrete bond. All these issues have to be tackled in the future work.

Conclusions

7.1 Conclusions

This thesis deals with numerical modeling of multiple cracks in concrete and reinforced concrete structures. Such a numerical tool is required to obtain the fine information of cracking which is essential to mitigate the issues related to durability and structural safety. Also, the developed models can be adapted to simulate the behavior of structures under severe loading conditions. The required ingredients to model the formation of multiple cracks in concrete are:

1. a numerical framework in which the multiple cracks in concrete can be modeled explicitly so that the fine information of cracking is obtained without resorting to any post-treatment techniques;
2. a constitutive model that takes into account the diffused damage phase in concrete and also capable of handling the induced anisotropy due to cracking;
3. a transition framework in which both the approaches can be coupled to model the complete strain localization process in quasi-brittle materials.

After a detailed state-of-the-art review, the approaches available in the literature for modeling cracking in concrete using either implicit or explicit descriptions of cracking are presented. It is shown that modeling discrete cracks in the continuum as strong discontinuities is advantageous because using this modeling strategy the information about cracking is obtained without any extra computational effort. Among several numerical frameworks that model the cracks as strong discontinuities, the EFEM is selected. In this framework, strong discontinuities are embedded inside a given finite element. First, the standard EFEM, which incorporates a single strong discontinuity per element, is studied. The discrete constitutive law that takes into account the mixed-mode cracking is considered. Rankine criterion is used to initiate the cracks. Later, this methodology is extended for the case of two intersecting strong discontinuities. In the extended EFEM, coupled traction continuity conditions are formulated by assuming that two crack surfaces are superposed. In this way, the local equilibrium at both the crack surfaces is satisfied. From the numerical tests, it is observed that the interaction between the cracks depends on the angle between them. Finally, it can be concluded that the extended EFEM allows for describing the initiation and propagation of orthogonal/non-orthogonal intersecting cracks. However, we consider here that the bulk remains elastic before the initiation of the cracks.

After developing the framework for modeling multiple cracks explicitly, we then focus on the diffused phase of cracking. The microplane models that provide the directional (anisotropic) description of cracking are selected for this purpose. The disk microplane system under plane strain assumption is used instead of a spherical one. This assumption leads to a computationally effective microplane model. The kinematic constraint expressions are presented in the case of the

disk microplane system. The stress tensor is then derived using both PVW and thermodynamic framework. Simple constitutive laws using a single microdamage variable are assumed. An internal variable defined using both the normal and tangential strain components is used to derive the microdamage variable on each microplane. Using the integration over the circle, the relation between the density of energy dissipation at the microplane level and at a unit volume is established. Later, the microplane elastic constants are also derived by equating the elastic stiffness matrices obtained from the microplane model and that of the Hooke's law. Also, the upper limit of the Poisson's ratio to ensure the positiveness of the energy dissipation on each microplane is determined. In terms of numerical implementation, a simple integration scheme over a semi-circle is employed to obtain the quantities at a unit volume (stress tensor, energy dissipation) from that of the microplane. Numerical localization analysis in the case of a uniaxial tensile test reveals that the loss of ellipticity of the rate equilibrium problem occurs only after certain microdamage is accumulated. As expected, the energy regularization technique gives mesh independent results if the assumed characteristic length is well determined.

Now that we have the microplane microdamage model for modeling initial phase of the strain localization process and the extended EFEM for tackling the multiple cracks, we next couple them with in a damage-to-fracture transition framework. First, the microplane microdamage model is used to describe the anisotropic damage in the localization band. Later, cracks are introduced as strong discontinuities in the extended EFEM. Now, the energy available for the crack is to be calculated by taking into account the energy dissipated in the localization band. For this purpose, we use the weak energy equivalence approach in which the energy dissipation of the body using the proposed models (separately) in the entire time domain is assumed to be equal. Following this approach, the residual energy available at the microplanes level is computed (at the transition instant) and then is dissipated at the crack surface. This is achieved by exploiting the anisotropic description of damage and energy dissipation of the microplane microdamage model.

The main interest of using the microplane microdamage model for modeling the response of the bulk material is that damage-to-fracture transition criteria can be written in terms of the quantities that are available on each microplane. Thus the induced anisotropy due to damage is taken into account. The selected transition criterion is based on the maximum energy dissipation on the microplane system. This proves to be an efficient one since the energy regularization technique is followed. Also, the same transition criterion is used for the initiation of the multiple cracks.

Finally, the capabilities of the proposed methodologies are illustrated by simulating plain and reinforced concrete specimens. Using the proposed transition methodology, the cracks are initiated in the localized damage zones in the specimen. The mixed mode behavior of the cracks is well described. However, in the case of reinforced concrete specimen the dissipation at the steel-concrete interface is not accounted for. The crack closure and reopening during non-reverse cyclic loading is well represented.

To conclude, the objective of developing a framework for modeling anisotropic damage and the formation of multiple cracks is achieved. Even though, we are able to illustrate the formation of a single crack in the case of structural level tests, the elementary level tests show several features of the proposed strategies for tackling multiple cracks.

7.2 Perspectives

The proposed framework can be improved in the following aspects:

- concerning the extended EFEM, we tackle here only the case of formation of two cracks. Although, such a consideration is subjective of the experimental/industrial case which is addressed by the proposed formulation. Some guidelines has to be developed for limiting the number of cracks to be considered in this framework. Even though the mixed mode

traction-separation law tackles the change in the behavior of crack from mode I to mixed mode, it could be interesting to formulate more complex crack initiation criteria (such as Mohr-Coloumb) for cracks that activates in mixed mode [WU and CERVERA, 2016]. During the simulations, several sensitivities related to the traction-separation law are encountered. A detailed numerical analysis on the convergence properties of the coupled traction continuity conditions is to be performed with an objective to remove these sensitivities.

- concerning the microplane microdamage model, we considered here only the positive part of the strain tensor for the projection operation. This is more suitable for tackling the mode I cracking. However, this formulation has to be improved to include the compression part of stress/strains as in several anisotropic damage models [ORTIZ, 1985, DESMORAT et al., 2007] Also, in order to handle the triaxial and hydrostatic cases, a volumetric–deviatoric split [BAŽANT and PRAT, 1988a] of the normal stress/strain may be required. In this case, a microdamage variable for each component of stress may be more suitable.
- concerning the transition approach, a method for enforcing the energy equivalence by using other than the energy regularization technique (e.g., nonlocal, gradient methods) for the microplane models has to be developed. The criteria used for the damage-to-fracture transition is to be improved by numerical experimentation techniques such as the virtual testing tools [DELAPLACE and DESMORAT, 2007] based on discrete element method fig. 7.1. The key question to address is, can an objective transition criterion be formulated? Also, another important point to clear is that how to separate the energy dissipation between initiated cracks? In this case, the possibility of the localization of the second crack is to be investigated. In the proposed transition formulation, we initiate both the cracks in the direction of the maximum principal stress. These aspects of the crack initiation direction and the orientation between the cracks also needs to be studied in detail.

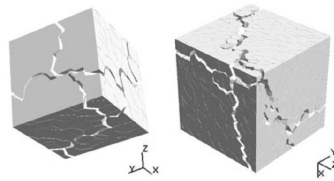


Figure 7.1: Virtual testing: cubic specimen under biaxial loading

Finally, during the structural case studies, it is shown that the crack patterns are well captured in the cases where single crack propagation occurs (double notched specimen, shear wall specimen in monotonic and non-reverse cyclic loading) without any need of crack tracking techniques. In these cases, we restrict the number of cracks to be initiated to one. However, in order to simulate the multiple intersecting crack patterns, it is essential to know a priori the set of elements in which multiple cracks has to be initiated. For this purpose, it is interesting to use the crack tracking techniques [RICCARDI et al., 2017, OLIVER et al., 2002] in order to identify the set of elements where multiple cracks intersect and to allow more than one crack to initiate. From the point of view of the structural applications, the computational efficiency of the proposed model can be further improved by taking advantage of the parallel computing technology. Parallel algorithms are employed in the case of the spherical microplane models in [NĚMEČEK et al., 2002] and future work has to be done to develop parallelization strategies for the disk microplane models as well. Also, studies has to be carried out with the perspective of incorporating the steel-concrete behavior in the both the microplane model and the traction-separation law.

This page is intentionally empty

Appendices

Elastic coefficients of the microplane microdamage model

Let us consider the stress tensor obtained from the components on each microplane and focus on the elastic response only:

$$\boldsymbol{\sigma} = \frac{1}{\pi} \int_{\Omega} (E_m \epsilon_m^\alpha \mathbf{M}^\alpha + E_l \epsilon_l^\alpha \mathbf{L}^\alpha) dS \quad (\text{A.1})$$

(A.1) can be rewritten in the component form as:

$$\sigma_{ij} = \frac{1}{\pi} \int_{\Omega} (E_m \epsilon_m^\alpha M_{ij}^\alpha + E_l \epsilon_l^\alpha L_{ij}^\alpha) dS \quad (\text{A.2})$$

Now substituting the expressions for ϵ_m^α (4.10) and ϵ_l^α (4.11) in eq. (A.2), we obtain:

$$\begin{aligned} \sigma_{ij} = & \frac{1}{\pi} \int_{\Omega} [E_m (\cos^2 \alpha \epsilon_{11} + \sin^2 \alpha \epsilon_{22} + 2 \sin \alpha \cos \alpha \epsilon_{12}) M_{ij}^\alpha] dS + \\ & \frac{1}{\pi} \int_{\Omega} [E_l (-\sin \alpha \cos \alpha \epsilon_{11} + \sin \alpha \cos \alpha \epsilon_{22} + 2(\cos^2 \alpha - \sin^2 \alpha) \epsilon_{12}) L_{ij}^\alpha] dS \quad (\text{A.3}) \end{aligned}$$

As a consequence σ_{11} reads ($M_{11} = \cos^2 \alpha$ and $L_{11} = -\sin \alpha \cos \alpha$) as:

$$\begin{aligned} \sigma_{11} = & \frac{1}{\pi} \int_0^{2\pi} [E_m (\cos^2 \alpha \epsilon_{11} + \sin^2 \alpha \epsilon_{22} + 2 \sin \alpha \cos \alpha \epsilon_{12}) \cos^2 \alpha] d\alpha + \\ & \frac{1}{\pi} \int_0^{2\pi} [E_l (-\sin \alpha \cos \alpha \epsilon_{11} + \sin \alpha \cos \alpha \epsilon_{22} + 2(\cos^2 \alpha - \sin^2 \alpha) \epsilon_{12}) (-\sin \alpha \cos \alpha)] d\alpha \\ = & \frac{1}{\pi} \int_0^{2\pi} [E_m (\cos^4 \alpha \epsilon_{11} + \sin^2 \alpha \cos^2 \alpha \epsilon_{22} + 2 \sin \alpha \cos^3 \alpha \epsilon_{12})] d\alpha + \\ & \frac{1}{\pi} \int_0^{2\pi} [E_l (\sin^2 \alpha \cos^2 \alpha \epsilon_{11} - \sin^2 \alpha \cos^2 \alpha \epsilon_{22} - 2(\sin \alpha \cos^3 \alpha - \sin^3 \alpha \cos \alpha) \epsilon_{12})] d\alpha \\ = & \frac{1}{\pi} \left[E_m \left(\frac{3\pi}{4} \epsilon_{11} + \frac{\pi}{4} \epsilon_{22} \right) + E_l \left(\frac{\pi}{4} \epsilon_{11} - \frac{\pi}{4} \epsilon_{22} \right) \right] d\alpha \\ = & \frac{1}{4} [E_m (3\epsilon_{11} + \epsilon_{22}) + E_l (\epsilon_{11} - \epsilon_{22})] d\alpha \end{aligned}$$

and σ_{22} reads ($M_{22} = \sin^2 \alpha$ and $T_{22} = \sin \alpha \cos \alpha$) as:

$$\begin{aligned}
\sigma_{22} &= \frac{1}{\pi} \int_0^{2\pi} [E_m(\cos^2 \alpha \epsilon_{11} + \sin^2 \alpha \epsilon_{22} + 2 \sin \alpha \cos \alpha \epsilon_{12}) \sin^2 \alpha] d\alpha + \\
&\quad \frac{1}{\pi} \int_0^{2\pi} [E_l(-\sin \alpha \cos \alpha \epsilon_{11} + \sin \alpha \cos \alpha \epsilon_{22} + 2(\cos^2 \alpha - \sin^2 \alpha) \epsilon_{12})(\sin \alpha \cos \alpha)] d\alpha \\
&= \frac{1}{\pi} \int_0^{2\pi} [E_m(\sin^2 \alpha \cos^2 \alpha \epsilon_{11} + \sin^4 \alpha \epsilon_{22} + 2 \sin^3 \alpha \cos \alpha \epsilon_{12})] d\alpha + \\
&\quad \frac{1}{\pi} \int_0^{2\pi} [E_l(-\sin^2 \alpha \cos^2 \alpha \epsilon_{11} + \sin^2 \alpha \cos^2 \alpha \epsilon_{22} + 2(\sin \alpha \cos^3 \alpha)] d\alpha - \\
&\quad \frac{1}{\pi} \int_0^{2\pi} [\sin^3 \alpha \cos \alpha \epsilon_{12}] d\alpha \\
&= \frac{1}{\pi} \left[E_m \left(\frac{\pi}{4} \epsilon_{11} + \frac{3\pi}{4} \epsilon_{22} \right) + E_l \left(-\frac{\pi}{4} \epsilon_{11} + \frac{\pi}{4} \epsilon_{22} \right) \right] \\
&= \frac{1}{4} [E_m(\epsilon_{11} + 3\epsilon_{22}) + E_l(-\epsilon_{11} + \epsilon_{22})]
\end{aligned}$$

and finally the shear stress σ_{12} is ($M_{12} = \sin^2 \alpha$ and $T_{12} = \frac{1}{2}(\cos^2 \alpha - \sin^2 \alpha)$) as:

$$\begin{aligned}
\sigma_{12} &= \frac{1}{\pi} \int_0^{2\pi} [E_m(\cos^2 \alpha \epsilon_{11} + \sin^2 \alpha \epsilon_{22} + 2 \sin \alpha \cos \alpha \epsilon_{12}) \sin \alpha \cos \alpha] d\alpha + \\
&\quad \frac{1}{\pi} \int_0^{2\pi} \left[\frac{E_l}{2} (-\sin \alpha \cos \alpha \epsilon_{11} + \sin \alpha \cos \alpha \epsilon_{22} + (\cos^2 \alpha - \sin^2 \alpha) \epsilon_{12}) (\cos^2 \alpha - \sin^2 \alpha) \right] d\alpha \\
&= \frac{1}{\pi} \int_0^{2\pi} [E_m(\sin \alpha \cos^3 \alpha \epsilon_{11} + \sin^3 \alpha \cos \alpha \epsilon_{22} + 2 \sin^2 \alpha \cos^2 \alpha \epsilon_{12})] d\alpha + \\
&\quad \frac{1}{\pi} \int_0^{2\pi} \left[\frac{E_l}{2} (-\sin \alpha \cos^3 \alpha \epsilon_{11} + \sin \alpha \cos^3 \alpha \epsilon_{22} + \sin^3 \alpha \cos \alpha \epsilon_{11}) \right] d\alpha - \\
&\quad \frac{1}{\pi} \int_0^{2\pi} [\sin^3 \alpha \cos \alpha \epsilon_{22} + (\cos^2 \alpha - \sin^2 \alpha)^2 \epsilon_{12}] d\alpha \\
&= \frac{1}{\pi} \int_0^{2\pi} [E_m(2 \sin^2 \alpha \cos^2 \alpha) \epsilon_{12}] d\alpha + \\
&\quad \frac{1}{\pi} \int_0^{2\pi} \left[\frac{E_l}{2} (\cos^4 \alpha - 2 \sin^2 \alpha \cos^2 \alpha + \sin^4 \alpha) \epsilon_{12} \right] d\alpha \\
&= \frac{1}{\pi} \left[E_m \left(\frac{\pi}{2} \epsilon_{12} \right) + E_l \left(\frac{3\pi}{4} - \frac{2\pi}{4} + \frac{3\pi}{4} \right) \epsilon_{12} \right] \\
&= \frac{1}{4} (2E_m + 2E_l) \epsilon_{12}
\end{aligned}$$

Using the expression for σ_{11} , σ_{22} and σ_{12} , the stress-strain relationship in matrix form is obtained as:

$$\begin{Bmatrix} \sigma_{11} \\ \sigma_{22} \\ \sigma_{21} \end{Bmatrix} = \frac{1}{4} \begin{bmatrix} 3E_m + E_l & E_m - E_l & 0 \\ E_m - E_l & 3E_m + E_l & 0 \\ 0 & 0 & 2(E_m + E_l) \end{bmatrix} \begin{Bmatrix} \epsilon_{11} \\ \epsilon_{22} \\ \epsilon_{21} \end{Bmatrix} \quad (\text{A.4})$$

Now the elastic constitutive model (Hooke's law) under plane strain conditions is given by:

$$\begin{Bmatrix} \sigma_{11} \\ \sigma_{22} \\ \sigma_{21} \end{Bmatrix} = \frac{E}{(1-\nu)(1-2\nu)} \begin{bmatrix} 1-\nu & \nu & 0 \\ \nu & 1-\nu & 0 \\ 0 & 0 & 1-2\nu \end{bmatrix} \begin{Bmatrix} \epsilon_{11} \\ \epsilon_{22} \\ \epsilon_{21} \end{Bmatrix} \quad (\text{A.5})$$

$$= \begin{bmatrix} \frac{E}{(1-2\nu)} & \frac{E\nu}{(1-\nu)(1-2\nu)} & 0 \\ \frac{E\nu}{(1-\nu)(1-2\nu)} & \frac{E}{(1-\nu)} & 0 \\ 0 & 0 & \frac{E}{(1-\nu)} \end{bmatrix} \begin{Bmatrix} \epsilon_{11} \\ \epsilon_{22} \\ \epsilon_{21} \end{Bmatrix} \quad (\text{A.6})$$

$$= \begin{bmatrix} \lambda + 2\mu & \lambda & 0 \\ \lambda & \lambda + 2\mu & 0 \\ 0 & 0 & 2\mu \end{bmatrix} \begin{Bmatrix} \epsilon_{11} \\ \epsilon_{22} \\ \epsilon_{21} \end{Bmatrix} \quad (\text{A.7})$$

where, E is the Young's modulus. Finally, the microplane constants can be computed by imposing the equality of the coefficients of the elastic stiffness matrices obtained from microplane model (eq. (A.4)) and the Hooke's law (eq. (A.7)):

$$3E_m + E_l = 4(\lambda + 2\mu) \quad (\text{A.8})$$

$$E_m - E_l = 4\lambda \quad (\text{A.9})$$

$$E_m + E_l = 4\mu \quad (\text{A.10})$$

So, one obtains the following expression for E_l :

$$E_l = 2(\mu - \lambda) \quad (\text{A.11})$$

Now, after substituting the expression for E_l (A.11) into the second identity (A.9) gives E_m as:

$$E_m = 4\lambda + 2\mu - 2\lambda = 2(\lambda + \mu) \quad (\text{A.12})$$

Using the expressions for E_m (A.12) and E_l (A.11), we can easily verify that the first identity is satisfied:

$$3E_m + E_l = 6(\lambda + \mu) + 2(\mu - \lambda) = 4\lambda + 8\mu = 4(\lambda + 2\mu) \quad (\text{A.13})$$

This page is intentionally empty

Modified traction-separation law

The traction-separation law formulated in section 3.4 is based on the condition that the internal variable evolves from 0 at the crack initiation. However, during the numerical studies involving both the elementary and structural test cases, we observed sensitivity with respect to the traction-separation law implemented following this condition. Hence, we follow the formulation presented in [ALFAIATE et al., 2001] and introduce a non-zero value of the internal variable κ_{cr}^0 at the crack initiation. In this formulation, the traction-separation law is given by,

$$\mathbf{t} = \frac{\partial \psi_S}{\partial [\mathbf{u}]} = (1 - d_{cr}) \mathbf{K} \cdot [\mathbf{u}] \quad (\text{B.14})$$

where, \mathbf{K} is given by [ALFAIATE et al., 2001]:

$$\mathbf{K} = \frac{f_t}{\kappa_{cr}^0} \mathbf{I} \quad (\text{B.15})$$

and the damage-like variable is rewritten as:

$$d_{cr} = 1 - \frac{\kappa_{cr}^0}{\kappa_{cr}} \exp\left(-\frac{f_t}{G_f} (\kappa_{cr} - \kappa_{cr}^0)\right) \quad (\text{B.16})$$

In this case, d_{cr} varies from 0 (no crack) to 1 (fully opened crack) instead from $-\infty$ in the previous case. Finally, the stiffness of the traction-separation law in the secant form is obtained as:

$$\mathbf{K}^s = (1 - d_{cr}) \frac{f_t}{\kappa_{cr}^0} \mathbf{I} \quad (\text{B.17})$$

Now, we give here the expressions of the stiffness matrices that are used to solve the linearized local equilibrium equations eqs. (3.98b) and (3.98c) in the presence of two cracks, that is to say, the coupled traction continuity conditions. First, we rewrite the expressions of $\mathbf{K}_{g_1 g_1}$, $\mathbf{K}_{g_1 g_2}$, $\mathbf{K}_{g_2 g_1}$ and $\mathbf{K}_{g_2 g_2}$ given in eqs. (3.102), (3.103), (3.106) and (3.107) at the iteration i in the case of CST as:

$$\mathbf{K}_{g_1 g_1}^i = \left. \frac{\partial \mathbf{t}_1}{\partial \mathbf{e}_1} \right|_{\mathbf{e}_1^i} - \mathbf{P}_1^\top \mathbf{C} \mathbf{G}_1 \quad (\text{B.18})$$

$$\mathbf{K}_{g_1 g_2}^i = -\mathbf{P}_1^\top \mathbf{C} \mathbf{G}_2 \quad (\text{B.19})$$

$$\mathbf{K}_{g_2 g_1}^i = -\mathbf{P}_2^\top \mathbf{C} \mathbf{G}_1 \quad (\text{B.20})$$

$$\mathbf{K}_{g_2 g_2}^i = \left. \frac{\partial \mathbf{t}_2}{\partial \mathbf{e}_2} \right|_{\mathbf{e}_2^i} - \mathbf{P}_2^\top \mathbf{C} \mathbf{G}_2 \quad (\text{B.21})$$

Now, one can replace the derivative of the traction-separation law appearing in eqs. (B.18) to (B.21) by a secant stiffness matrix, eq. (B.17). However, during numerical simulations it is observed that the constant penalized stiffness matrix (eq. (B.15)) has better performance in the far post-peak regime. Hence, even though the number of iterations required for the convergence of the linearized local equilibrium equations is increased, we use the constant penalized stiffness matrix to obtain the following stiffness matrices for solving the local system of equations in algorithm 2:

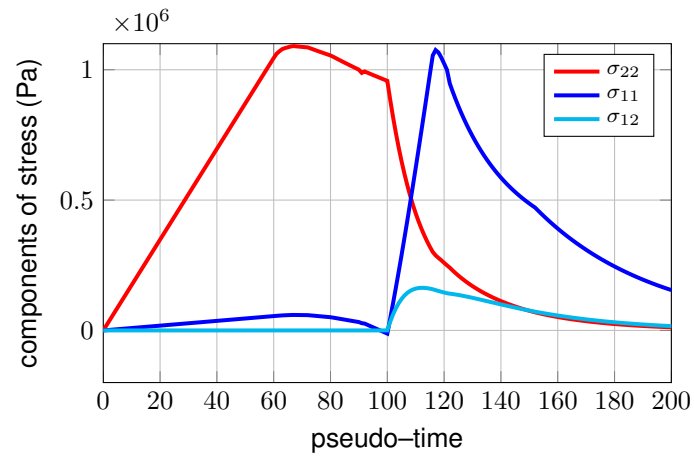
$$\mathbf{K}_{g_1 g_1}^i = \frac{f_t}{k_{cr}^0} \mathbf{I} - \mathbf{P}_1^\top \mathbf{C} \mathbf{G}_1 \quad (\text{B.22})$$

$$\mathbf{K}_{g_1 g_2}^i = -\mathbf{P}_1^\top \mathbf{C} \mathbf{G}_2 \quad (\text{B.23})$$

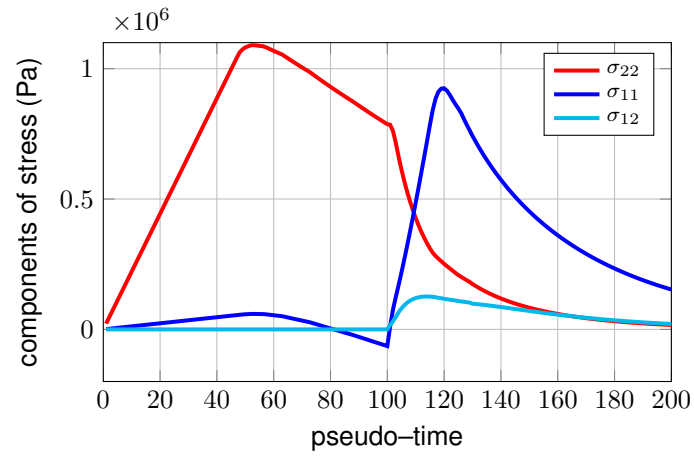
$$\mathbf{K}_{g_2 g_1}^i = -\mathbf{P}_2^\top \mathbf{C} \mathbf{G}_1 \quad (\text{B.24})$$

$$\mathbf{K}_{g_2 g_2}^i = \frac{f_t}{k_{cr}^0} \mathbf{I} - \mathbf{P}_2^\top \mathbf{C} \mathbf{G}_2 \quad (\text{B.25})$$

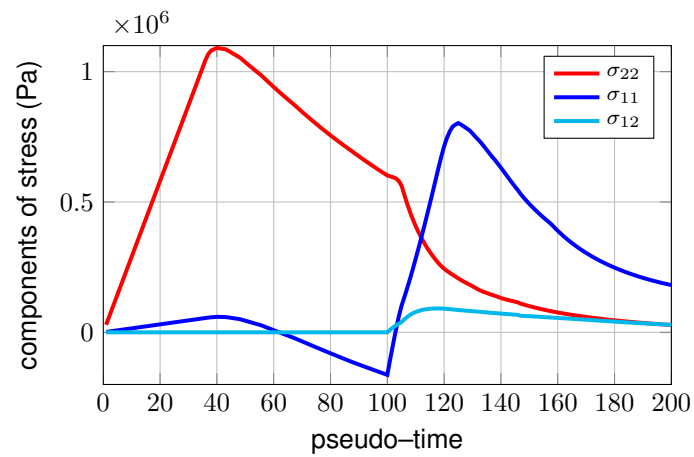
We repeat the William's like test performed in section 5.5.3.2 by using the modified traction-separation law and the global results for the threshold at 20%, 40% and 60% of g_f^π are presented in the figs. B1a to B1c respectively. It can be clearly seen that the global response is stabilized using the modified traction-separation law.



(a)



(b)



(c)

Figure B1: Time evolution of the components of stress - Willam's like loading test using transition approach for the threshold at 20% (a), 40% (b) and 60% (c) of g_f^π using modified traction-separation law

This page is intentionally empty

Bibliography

- [AKHAVAN et al., 2012] AKHAVAN, A., SHAFIATIAN, S., and RAJABIPOUR, F. (2012). Quantifying the effects of crack width, tortuosity, and roughness on water permeability of cracked mortars. *Cement and Concrete Research*, 42(2):313 – 320.
- [ALAM and LOUKILI, 2017] ALAM, S. Y. and LOUKILI, A. (2017). Transition from energy dissipation to crack openings during continuum–discontinuum fracture of concrete. *International Journal of Fracture*, 206(1):49–66.
- [ALFAIATE et al., 2001] ALFAIATE, J., WELLS, G., and SLUYS, L. (2001). On the use of embedded discontinuity elements with crack path continuity for mode-i and mixed-mode fracture. *International Journal for Solids and Structures*, 38:2933–2952.
- [ALLIX and LADEVÈZE, 1992] ALLIX, O. and LADEVÈZE, P. (1992). Interlaminar interface modelling for the prediction of delamination. *Composite structures*, 22(4):235–242.
- [ARMERO and EHRLICH, 2006] ARMERO, F. and EHRLICH, D. (2006). Finite element methods for the multi-scale modeling of softening hinge lines in plates at failure. *Computer methods in Applied Mechanics and Engineering*, 195(13):1283–1324.
- [ARMERO and GARIKIPATI, 1995] ARMERO, F. and GARIKIPATI, K. (1995). Recent advances in the analysis and numerical simulation of strain localization in inelastic solids. In Owen, O. and Hinton, E., editors, *Proceedings of Computational Plasticity IV*, pages 547–561. Barcelona. CIMNE.
- [BABUSKA and MELENK, 1997] BABUSKA, I. and MELENK, J. (1997). The partition of unity method. *International Journal for Numerical Methods in Engineering*, 40:727–758.
- [BATDORF and BUDIANSKY, 1949] BATDORF, S. and BUDIANSKY, B. (1949). A mathematical theory of plasticity based on the concept of slip. *NACA:TNI871*, 3(4):1672–1687.
- [BAŽANT, 1984] BAŽANT, Z. (1984). Microplane model for strain-controlled inelastic behaviour. *Mechanics of Engineering Materials*, 114(10):45–59.
- [BAŽANT, 1994] BAŽANT, Z. (1994). Nonlocal damage theory based on micromechanics of crack interactions. *Journal of Engineering Mechanics*, 120(3):593–617.
- [BAŽANT, 1996] BAŽANT, Z. (1996). Microplane model for concrete. i: Stress-strain boundaries and finite strain. *Journal of Engineering Mechanics*, 122(3):245–254.
- [BAŽANT and CANER, 2005a] BAŽANT, Z. and CANER, F. C. (2005a). Microplane model m5 with kinematic and static constraints for concrete fracture and anelasticity. i: Theory. *Journal of Engineering Mechanics*, 131(1):31–40.

- [BAŽANT and CANER, 2005b] BAŽANT, Z. and CANER, F. C. (2005b). Microplane model m5 with kinematic and static constraints for concrete fracture and anelasticity. ii: Computation. *Journal of engineering mechanics*, 131(1):41–47.
- [BAŽANT et al., 2000] BAŽANT, Z., CANER, F. C., CAROL, I., ADLEY, D., and AKERS, A. (2000). Microplane model m4 for concrete. i: Formulation with work-conjugate deviatoric stress. *Journal of Engineering Mechanics*, 122(9):944–953.
- [BAŽANT and di LUZIO, 2004] BAŽANT, Z. and di LUZIO, G. (2004). Nonlocal microplane model with strain-softening yield limits. *International Journal of Solids and Structures*, 41(24-25):7209–7240.
- [BAŽANT and GAMBAROVA, 1980] BAŽANT, Z. and GAMBAROVA, P. (1980). Rough cracks in reinforced concrete. *ASCE J Struct Div*, 106(4):819–842.
- [BAŽANT and OH, 1983] BAŽANT, Z. and OH, B. (1983). Crack band theory for fracture of concrete. *Matériaux et construction*, 16(3):155–177.
- [BAŽANT and OH, 1985] BAŽANT, Z. and OH, B. (1985). Microplane model for progressive fracture of concrete. *Journal of Engineering Mechanics*, 111(4):559–582.
- [BAŽANT and OH, 1986] BAŽANT, Z. and OH, B. (1986). Efficient numerical integration on the surface of a sphere. *ZAMM - Journal of Applied Mathematics and Mechanics / Zeitschrift für Angewandte Mathematik und Mechanik*, 66(1):37–49.
- [BAŽANT and PRAT, 1988a] BAŽANT, Z. and PRAT, P. (1988a). Microplane model for brittle-plastic material:i. theory. *Journal of Engineering Mechanics*, 114(10):1672–1687.
- [BAŽANT and PRAT, 1988b] BAŽANT, Z. and PRAT, P. (1988b). Microplane model for brittle-plastic material:ii. verification. *Journal of Engineering Mechanics*, 114(10):1689–1701.
- [BAŽANT et al., 1996] BAŽANT, Z., XIANG, Y., ADLEY, M. D., Prati, P. C., and Akers, S. A. (1996). Microplane model for concrete, ii: data delocalization and verification. *Journal of Engineering Mechanics*, 122(3):255–262.
- [BELYTSCHKO and BLACK, 1999] BELYTSCHKO, T. and BLACK, T. (1999). Elastic crack growth in finite elements with minimal remeshing. *International Journal for Numerical Methods in Engineering*, 45(5):601–620.
- [BELYTSCHKO et al., 2009] BELYTSCHKO, T., GRACIE, R., and VENTURA, G. (2009). A review of extended/generalized finite element methods for material modeling. *Modelling and Simulation in Materials Science and Engineering*, 17(4):043001.
- [BELYTSCHKO et al., 1996] BELYTSCHKO, T., KRONGAUZ, Y., ORGAN, D., FLEMING, M., and KYSL, P. (1996). Meshless methods: an overview and recent developments. *Computer methods in applied mechanics and engineering*, 139(1-4):3–47.
- [BELYTSCHKO and LASRY, 1989] BELYTSCHKO, T. and LASRY, D. (1989). A study of localization limiters for strain-softening in statics and dynamics. *Computers & structures*, 33(3):707–715.
- [BELYTSCHKO et al., 1994] BELYTSCHKO, T., LU, Y., and GU, L. (1994). Element-free galerkin methods. *International journal for numerical methods in engineering*, 37(2):229–256.
- [BRANCHERIE, 2003] BRANCHERIE, D. (2003). *Modèles continus et discrets pour les problèmes de localisation et de rupture fragile et/ou ductile*. Thèse de doctorat, Ecole Normale Supérieure de Cachan.
- [CANER and BAŽANT, 2000] CANER, F. C. and BAŽANT, Z. (2000). Microplane model m4 for concrete. ii: Algorithm and calibration. *Journal of Engineering Mechanics*, 126(9):954–961.

- [CANER and BAŽANT, 2005] CANER, F. C. and BAŽANT, Z. (2005). Microplane model m6f for fiber reinforced concrete. In ONATE, E., OWEN, D., PERIC, D., and SUAREZ, B., editors, *XI International Conference on Computational Plasticity. Fundamentals and Applications*.
- [CANER and BAŽANT, 2012] CANER, F. C. and BAŽANT, Z. (2012). Microplane model m7 for plain concrete. ii: Calibration and verification. *Journal of Engineering Mechanics*, 139(12):1724–1735.
- [CANER and BAŽANT, 2013] CANER, F. C. and BAŽANT, Z. (2013). Microplane model m7 for plain concrete. i: Formulation. *Journal of Engineering Mechanics*, 139(12):1714–1735.
- [CAROL and BAŽANT, 1997] CAROL, I. and BAŽANT, Z. (1997). Damage and plasticity in microplane theory. *International Journal for Solids and Structures*, 34:3807–3835.
- [CAROL et al., 2001a] CAROL, I., JIRÁSEK, M., and BAŽANT, Z. (2001a). A thermodynamically consistent approach to microplane theory. part-i: Free energy and consistent microplane stress. *International Journal for Solids and Structures*, 38:2921–2931.
- [CAROL et al., 2001b] CAROL, I., JIRÁSEK, M., and BAŽANT, Z. (2001b). A thermodynamically consistent approach to microplane theory. part i. free energy and consistent microplane stresses. *International Journal of Solids and Structures*, 38(17):2921–2931.
- [CAROL et al., 1992] CAROL, I., PRAT, P., and BAŽANT, Z. (1992). New explicit microplane model for concrete. *International Journal for Solids and Structures*, 29:1173–1191.
- [CAROL and WILLAM, 1996] CAROL, I. and WILLAM, K. (1996). Spurious energy dissipation/generation in stiffness recovery models for elastic degradation and damage. *International Journal of Solids and Structures*, 33(20-22):2939–2957.
- [CARPINTERI et al., 2003] CARPINTERI, A., CORNETTI, P., VALENTE, S., and BARPI, F. (2003). Cohesive crack model description of ductile to brittle size-scale transition: Dimensional analysis vs. renormalization group theory. *Engineering Fracture Mechanics*, 70(14):1809–1839.
- [CAZES et al., 2009] CAZES, F., CORET, M., COMBESCURE, A., and GRAVOUIL, A. (2009). A thermodynamic method for the construction of a cohesive law from a nonlocal damage model. *International Journal of Solids and Structures*, 46(6):1476–1490.
- [CAZES et al., 2016] CAZES, F., MESCHKE, G., and ZHOU, M. M. (2016). Strong discontinuity approaches: An algorithm for robust performance and comparative assessment of accuracy. *International Journal of Solids and Structures*, 96:355–379.
- [ČERVENKA et al., 2005] ČERVENKA, J., BAŽANT, Z., and WIERER, M. (2005). Equivalent localization element for crack band approach to mesh-sensitivity in microplane model. *International Journal for Numerical Methods in Engineering*, 62(5):700–726.
- [ČERVENKA, 1971] ČERVENKA, V. (1971). *Inelastic finite element analysis of reinforced concrete panels under inplane loads*. Ph.d. thesis, University of Colorado.
- [CHABOCHE, 1992] CHABOCHE, J. (1992). Damage induced anisotropy: on the difficulties associated with the active/passive unilateral condition. *International Journal of Damage Mechanics*, 1(2):148–171.
- [CHAMBON et al., 2001] CHAMBON, R., CAILLERIE, D., and MATSUCHIMA, T. (2001). Plastic continuum with microstructure, local second gradient theories for geomaterials: localization studies. *International Journal of Solids and Structures*, 38(46-47):8503–8527.
- [COMI, 2001] COMI, C. (2001). A non-local model with tension and compression damage mechanisms. *European Journal of Mechanics-A/Solids*, 20(1):1–22.

- [COMI et al., 2002] COMI, C., MARIANI, S., and PEREGO, U. (2002). From localized damage to discrete cohesive crack propagation in nonlocal continua. In *Proceedings of the Fifth World Congress on Computational Mechanics (WCCM V)*. Vienna University of Technology.
- [COMI et al., 2007] COMI, C., MARIANI, S., and PEREGO, U. (2007). An extended fe strategy for transition from continuum damage to mode i cohesive crack propagation. *International Journal for Numerical and Analytical Methods in Geomechanics*, 31(2):213–238.
- [COMI and PEREGO, 2001] COMI, C. and PEREGO, U. (2001). Fracture energy based bi-dissipative damage model for concrete. *International journal of solids and structures*, 38(36-37):6427–6454.
- [CORNELISSEN et al., 1986] CORNELISSEN, H., HORDIJK, D., and REINHARDT, H. (1986). Experimental determination of crack softening characteristics of normalweight and lightweight. *Heron*, 31(2):45.
- [CUSATIS and ZHOU, 2013] CUSATIS, G. and ZHOU, X. (2013). High-order microplane theory for quasi-brittle materials with multiple characteristic lengths. *Journal of Engineering Mechanics*, 140(7):04014046.
- [CUVILLIEZ et al., 2012] CUVILLIEZ, S., FEYEL, F., LORENTZ, E., and MICHEL-PONNELLE, S. (2012). A finite element approach coupling a continuous gradient damage model and a cohesive zone model within the framework of quasi-brittle failure. *Computer methods in applied mechanics and engineering*, 237:244–259.
- [de BORST, 1985] de BORST, R. (1985). Smearred crack analysis of reinforced concrete beams and slabs failing in shear. In *Proc. Int. Conf. on Computer Aided Analysis and Design of Concrete Struc.*, pages 261–273. Prineridge Press.
- [de BORST, 1987] de BORST, R. (1987). Computation of post-bifurcation and post-failure behavior of strain-softening solids. *Computers & Structures*, 25(2):211–224.
- [de BORST and MÜHLHAUS, 1992] de BORST, R. and MÜHLHAUS, H. (1992). Gradient-dependent plasticity: formulation and algorithmic aspects. *International Journal for Numerical Methods in Engineering*, 35(3):521–539.
- [de BORST and NAUTA, 1998] de BORST, R. and NAUTA, P. (1998). Non-orthogonal cracks in smearred finite element model. *Engineering Computations*, 124(8):842–851.
- [de BORST et al., 2004] de BORST, R., REMMERS, J., NEEDLEMAN, A., and ABELLAN, M. (2004). Discrete vs. smearred crack models for concrete fracture: bridging the gap. *International Journal for Numerical and Analytical Methods in Geomechanics*, 28(7-8):583–607.
- [DELAPLACE and DESMORAT, 2007] DELAPLACE, A. and DESMORAT, R. (2007). Discrete 3d model as complimentary numerical testing for anisotropic damage. *International Journal of Fracture*, 148(2):115.
- [DESMORAT et al., 2015] DESMORAT, R., GATUINGT, F., and JIRASEK, M. (2015). Nonlocal models with damage-dependent interactions motivated by internal time. *Engineering Fracture Mechanics*, 142:255–275.
- [DESMORAT et al., 2007] DESMORAT, R., GATUINGT, F., and RAGUENEAU, F. (2007). Non-local anisotropic damage model and related computational aspects for quasi-brittle materials. *Engineering Fracture Mechanics*, 74(10):1539–1560.
- [di LUZIO, 2007] di LUZIO, G. (2007). A symmetric over-nonlocal microplane model m4 for fracture in concrete. *International journal of solids and structures*, 44(13):4418–4441.

- [DOLBOW and BELYTSCHKO, 1999] DOLBOW, J. and BELYTSCHKO, T. (1999). A finite element method for crack growth without remeshing. *International Journal for Numerical Methods in Engineering*, 46(1):131–150.
- [DRAGON and MROZ, 1979] DRAGON, A. and MROZ, Z. (1979). A continuum model for plastic-brittle behaviour of rock and concrete. *International Journal of Engineering Science*, 17(2):121–137.
- [DUARTE et al., 2007] DUARTE, C., RENO, L., and SIMONE, A. (2007). A high-order generalized fem for through-the-thickness branched cracks. *International Journal for Numerical Methods in Engineering*, 72(3):325–351.
- [DUARTE and ODEN, 1996] DUARTE, C. and ODEN, J. (1996). An hp adaptive method using clouds. *Computer methods in applied mechanics and engineering*, 139(1-4):237–262.
- [DUFOR et al., 2011] DUFOR, F., LEGRAIN, G., PIJAUDIER-CABOT, G., and HUERTA, A. (2011). Estimation of crack opening from a two-dimensional continuum-based finite element computation. *International Journal for Numerical and Analytical Methods in Geomechanics*, 36(16):1813–1830.
- [DVORKIN et al., 1991] DVORKIN, E., ASSANELLI, A., and GIOIA, G. (1991). 2d finite elements with displacement interpolated embedded localization lines: The analysis of fracture in frictional materials. *Computer Methods in Applied Mechanics and Engineering*, 90:829–844.
- [DVORKIN et al., 1990] DVORKIN, E., CUITINO, A., and GIOIA, G. (1990). Finite elements with displacement interpolated embedded localization lines insensitive to mesh size and distortions. *International Journal for Numerical Methods in Engineering*, 30:541–564.
- [ETSE and NIETO, 2004] ETSE, G. and NIETO, M. (2004). Cosserat continua-based micro plane modelling. theory and numerical analysis. *Latin American applied research*, 34(4):229–240.
- [ETSE et al., 2003] ETSE, G., NIETO, M., and STEINMANN, P. (2003). A micropolar microplane theory. *International journal of engineering science*, 41(13-14):1631–1648.
- [FEENSTRA and de BORST, 1996] FEENSTRA, P. and de BORST, R. (1996). A composite plasticity model for concrete. *International Journal of Solids and Structures*, 33(5):707–730.
- [FERNANDES et al., 2008] FERNANDES, R., CHAVANT, C., and CHAMBON, R. (2008). A simplified second gradient model for dilatant materials: theory and numerical implementation. *International Journal of Solids and Structures*, 45(20):5289–5307.
- [FICHANT, 1996] FICHANT, S. (1996). *Endommagement et anisotropie induite du béton de structures: modélisations approchées*. PhD thesis, Cachan, Ecole normale supérieure.
- [GATUINGT and PIJAUDIER-CABOT, 2002] GATUINGT, F. and PIJAUDIER-CABOT, G. (2002). Coupled damage and plasticity modelling in transient dynamic analysis of concrete. *International journal for numerical and analytical methods in geomechanics*, 26(1):1–24.
- [GIRY et al., 2011] GIRY, C., DUFOR, F., and MAZARS, J. (2011). Stress-based nonlocal damage model. *International Journal of Solids and Structures*, 48(25-26):3431–3443.
- [GRANGER et al., 2001a] GRANGER, L., FLEURY, F., and TOURET, J. (2001a). Mechanical and leakrate predictions for nuclear power plant containments in accidental conditions. *Nuclear Engineering and Design*, 203(1):39 – 55.
- [GRANGER et al., 2001b] GRANGER, L., Rieg, C., Touret, J., Fleury, F., Nahas, G., Danisch, R., Brusa, L., Millard, A., Laborderie, C., Ulm, F., Contri, P., Schimmelpfennig, K., Barré, F., Firnhaber, M., Gauvain, J., Coulon, N., Dutton, L., and Tuson, A. (2001b). Containment evaluation under severe accidents (cesa): synthesis of the predictive calculations and analysis of the first experimental results obtained on the civaux mock-up. *Nuclear Engineering and Design*, 209(1):155 – 163.

- [GRASSL and JIRÁSEK, 2006] GRASSL, P. and JIRÁSEK, M. (2006). Damage-plastic model for concrete failure. *International journal of solids and structures*, 43(22-23):7166–7196.
- [GRASSL et al., 2002] GRASSL, P., LUNDGREN, K., and GYLLTOFT, K. (2002). Concrete in compression: a plasticity theory with a novel hardening law. *International Journal of Solids and Structures*, 39(20):5205–5223.
- [GUPTA and AKBAR, 1984] GUPTA, A. and AKBAR, H. (1984). Cracking in reinforced concrete analysis. *Journal of Structural Engineering*, 110(8):1735–1746.
- [HALM and DRAGON, 1998] HALM, D. and DRAGON, A. (1998). An anisotropic model of damage and frictional sliding for brittle materials. *European Journal of Mechanics-A/Solids*, 17(3):439–460.
- [HEGEN, 1996] HEGEN, D. (1996). Element-free galerkin methods in combination with finite element approaches. *Computer Methods in Applied Mechanics and Engineering*, 135(1):143–166.
- [HILL, 1958] HILL, R. (1958). A general theory of uniqueness and stability in elastic-plastic solids. *Journal of the Mechanics and Physics of Solids*, 6(3):236–249.
- [HILL, 1962] HILL, R. (1962). Acceleration waves in solids. *Journal of the Mechanics and Physics of Solids*, 10(1):1–16.
- [HILLERBORG et al., 1976] HILLERBORG, A., MODEER, M., and PETERSSON, P. (1976). Analysis of crack formation and crack growth in concrete by means of fracture mechanics and finite elements. *Cement and Concrete Research*, 6(6):773–781.
- [HUESPE and OLIVER, 2011] HUESPE, A. and OLIVER, J. (2011). Crack models with embedded discontinuities. In *Numerical Modeling of Concrete Cracking*, pages 99–159. Springer.
- [IMRAN and PANTAZOPOULOU, 2001] IMRAN, I. and PANTAZOPOULOU, S. (2001). Plasticity model for concrete under triaxial compression. *Journal of engineering mechanics*, 127(3):281–290.
- [INGRAFFEA and SAUOMA, 1985] INGRAFFEA, A. and SAUOMA, V. (1985). Numerical modeling of discrete crack propagation in reinforced and plain concrete. In *Fracture mechanics of concrete: structural application and numerical calculation*, pages 171–225. Springer.
- [JASON et al., 2006] JASON, L., HUERTA, A., PIJAUDIER-CABOT, G., and GHAVAMIAN, S. (2006). An elastic plastic damage formulation for concrete: Application to elementary tests and comparison with an isotropic damage model. *Computer methods in applied mechanics and engineering*, 195(52):7077–7092.
- [JASON and MASSON, 2014] JASON, L. and MASSON, B. (2014). Comparison between continuous and localized methods to evaluate the flow rate through containment concrete structures. *Nuclear Engineering and Design*, 277:146 – 153.
- [JIRÁSEK, 2016] JIRÁSEK, M. and Suárez, F. (2016). Localization properties of desmorat’s anisotropic damage model. *Computers & Structures*, 174:139–153.
- [JIRÁSEK, 2000] JIRÁSEK, M. (2000). Comparative study on finite elements with embedded discontinuities. *Computer Methods Applied Mechanics and Engineering*, 188:307–330.
- [JIRÁSEK, 2007] JIRÁSEK, M. (2007). Nonlocal damage mechanics. *Revue européenne de génie civil*, 11(7-8):993–1021.
- [JIRÁSEK, 2011] JIRÁSEK, M. (2011). Damage and smeared crack models. In *Numerical modeling of concrete cracking*, pages 1–49. Springer.

- [JIRÁSEK and BAUER, 2012] JIRÁSEK, M. and BAUER, M. (2012). Numerical aspects of the crack band approach. *Computers & structures*, 110:60–78.
- [JIRÁSEK and BELYTSCHKO, 2002] JIRÁSEK, M. and BELYTSCHKO, T. (2002). Computational resolution of strong discontinuities. In *In Proceedings of Fifth World Congress on Computational Mechanics*.
- [JIRÁSEK and GRASSL, 2008] JIRÁSEK, M. and GRASSL, P. (2008). Evaluation of directional mesh bias in concrete fracture simulations using continuum damage models. *Engineering Fracture Mechanics*, 75(8):1921–1943.
- [JIRÁSEK and ZIMMERMANN, 1998] JIRÁSEK, M. and ZIMMERMANN, T. (1998). Analysis of rotating crack model. *Journal of Engineering Mechanics*, 124(8):842–851.
- [JIRÁSEK and ZIMMERMANN, 2001] JIRÁSEK, M. and ZIMMERMANN, T. (2001). Embedded crack model. part ii: Combination with smeared cracks. *International Journal for Numerical Methods in Engineering*, 50(6):1291–1305.
- [JOUAN et al., 2017] JOUAN, G., SOUFFLET, M., KOTRONIS, P., and COLLIN, F. (2017). Second gradient models and concrete structures. In PAPANASTASIOU, P., PASTERNAK, E., and DYSKIN, A., editors, *Bifurcation and Degradation of Geomaterials with Engineering Applications*, pages 185–191. Springer International Publishing.
- [KACHANOV, 1958] KACHANOV, L. (1958). Time of the rupture process under creep conditions. *Izvestija Akademii Nauk SSSR, Otdelenie. Techniceskich Nauk*, 8:26–31.
- [KIM et al., 2011] KIM, D., DUARTE, C., and SOBH, N. (2011). Parallel simulations of three-dimensional cracks using the generalized finite element method. *Computational Mechanics*, 47(3):265–282.
- [KISHTA, 2017] KISHTA, E. (2017). *Anisotropic Cracking Model for Reinforced Concrete Structures with Enhanced Kinematics: Application to Bidimensional Elements Under Cyclic Loading*. PhD thesis, CEA Saclay, Direction des systèmes d’information.
- [KLISINSKI et al., 1991] KLISINSKI, M., RUNESSON, K., and STURE, S. (1991). Finite element with inner softening band. *Journal of Engineering Mechanics*, 117(3):575–587.
- [KRAJCINOVIC, 1985] KRAJCINOVIC, D. (1985). Continuous damage mechanics revisited: basic concepts and definitions. *Journal of Applied Mechanics*, 52:829–834.
- [KRAYANI et al., 2009] KRAYANI, A., PIJAUDIER-CABOT, G., and DUFOUR, F. (2009). Boundary effect on weight function in nonlocal damage model. *Engineering Fracture Mechanics*, 76(14):2217–2231.
- [KUHL and RAMM, 1998] KUHL, E. and RAMM, E. (1998). On the linearization of the microplane model. *Mechanics of Cohesive-frictional Materials: An International Journal on Experiments, Modelling and Computation of Materials and Structures*, 3(4):343–364.
- [KUHL and RAMM, 2000] KUHL, E. and RAMM, E. (2000). Microplane modelling of cohesive frictional materials. *European Journal of Mechanics - A/Solids*, 19:S121–S144.
- [KUHL et al., 2001] KUHL, E., STEINMANN, P., and CAROL, I. (2001). A thermodynamically consistent approach to microplane theory. part ii. dissipation and inelastic constitutive modeling. *International journal of solids and structures*, 38(17):2933–2952.
- [KUPFER et al., 1969] KUPFER, H., HILSDORF, H., and RUSCH, H. (1969). Behaviour of concrete under biaxial stresses. *ACI Journal*, 65(8):656–666.

- [LA BORDERIE, 1991] LA BORDERIE, C. (1991). *Phénomènes unilatéraux dans un matériau endommageable: modélisation et application à l'analyse de structures en béton*. Thèse de doctorat, Université Pierre et Marie Curie.
- [LADEVÉZE and LEMAITRE, 1984] LADEVÉZE, P. and LEMAITRE, J. (1984). Damage effective stress in quasi-unilateral material conditions. In *IUTAM Congress*.
- [LEBEDEV and LAIKOV, 1999] LEBEDEV, V. and LAIKOV, D. (1999). A quadrature formula for the sphere of the 131st algebraic order of accuracy. *Doklady Mathematics*, 59(3):477–481.
- [LECKIE and ONATE, 1981] LECKIE, F. A. and ONATE, T. (1981). Tensorial nature of damage measuring internal variables. In HULT, J. and LEMAITRE, J., editors, *Physical Non-linearities in Structural Analysis*, pages 140–155.
- [LEE and FENVES, 1998] LEE, J. and FENVES, G. (1998). Plastic-damage model for cyclic loading of concrete structures. *Journal of engineering mechanics*, 124(8):892–900.
- [LEE et al., 2004] LEE, S., SONG, Y., and HAN, S. (2004). Biaxial behavior of plain concrete of nuclear containment building. *Nuclear Engineering and Design*, 227(2):143–153.
- [LEGENDRE, 1984] LEGENDRE, D. (1984). *Prévision de la ruine des structures en béton par une approche combinée: mécanique de l'endommagement-mécanique de la rupture*. Thèse de doctorat, Université Paris 6.
- [LEMAITRE, 2012] LEMAITRE, J. (2012). *A course on damage mechanics*. Springer Science & Business Media.
- [LEMAITRE and CHABOCHE, 1990] LEMAITRE, J. and CHABOCHE, J. (1990). *Mechanics of Solid Materials*. Cambridge University Press.
- [LEMAITRE and MAZARS, 1982] LEMAITRE, J. and MAZARS, J. (1982). Damage mechanics applied to nonlinear behaviour up to failure of concrete structures.
- [LORENTZ and GODARD, 2011] LORENTZ, E. and GODARD, V. (2011). Gradient damage models: Toward full-scale computations. *Computer Methods in Applied Mechanics and Engineering*, 200(21-22):1927–1944.
- [LOTFI, 1992] LOTFI, H. (1992). *Finite element analysis of fracture in concrete and masonry structures*. Phd thesis, University of Colorado.
- [LUBARDA et al., 1994] LUBARDA, V., KRAJCINOVIC, D., and MASTILOVIC, S. (1994). Damage model for brittle elastic solids with unequal tensile and compressive strengths. *Engineering Fracture Mechanics*, 49(5):681–697.
- [LUBLINER et al., 1989] LUBLINER, J., OLIVER, J., OLLER, S., and ONATE, E. (1989). A plastic-damage model for concrete. *International Journal of solids and structures*, 25(3):299–326.
- [MANZOLI and SHING, 2004] MANZOLI, O. and SHING, P. (2004). Stress hybrid finite elements with multiple embedded cracks. *Proceedings of FraMCoS-5*, pages 123–130.
- [MATALLAH et al., 2010] MATALLAH, M., LA BORDERIE, C., and MAUREL, O. (2010). A practical method to estimate crack openings in concrete structures. *International Journal for Numerical and Analytical Methods in Geomechanics*, 34(15):1615–1633.
- [MAZARS, 1984] MAZARS, J. (1984). *Application de la mécanique de l'endommagement au comportement non linéaire et à la rupture du béton de structure*. Thèse de doctorat, Université Pierre et Marie Curie.

- [MAZARS, 1985] MAZARS, J. (1985). A model of a unilateral elastic damageable material and its application to concrete. In *Fracture toughness and fracture energy of concrete*. Elsevier, New York, N.Y.
- [MAZARS, 1986] MAZARS, J. (1986). A description of micro- and macroscale damage of concrete structures. *Engineering Fracture Mechanics*, 25(5/6):729–737.
- [MAZARS et al., 1990] MAZARS, J., BERTHAUD, Y., and RAMTANI, S. (1990). The unilateral behaviour of damaged concrete. *Engineering Fracture Mechanics*, 35(4/5):629–635.
- [MAZARS and PIJAUDIER-CABOT, 1989] MAZARS, J. and PIJAUDIER-CABOT, G. (1989). Continuum damage theory—application to concrete. *Journal of Engineering Mechanics*, 115(2):345–365.
- [MAZARS and PIJAUDIER-CABOT, 1996] MAZARS, J. and PIJAUDIER-CABOT, G. (1996). From damage to fracture mechanics and conversely: a combined approach. *International journal of solids and structures*, 33(20-22):3327–3342.
- [MELENK and BABUSKA, 1996] MELENK, J. and BABUSKA, I. (1996). The partition of unity finite element method: basic theory and applications. *Computer methods in applied mechanics and engineering*, 139(1):289–314.
- [MESCHKE et al., 1998] MESCHKE, G., LACKNER, R., and MANG, H. (1998). An anisotropic elastoplastic-damage model for plain concrete. *International Journal for Numerical Methods in Engineering*, 42:703–727.
- [MOES et al., 1999] MOES, N., DOLBOW, J., and BELYTSCHKO, T. (1999). A finite element method for crack growth without remeshing. *International Journal for Numerical Methods in Engineering*, 46:131–150.
- [MOHARRAMI and KOUTROMANOS, 2016] MOHARRAMI, M. and KOUTROMANOS, I. (2016). Triaxial constitutive model for concrete under cyclic loading. *Journal of Structural Engineering*, 142(7):04016039.
- [MÜHLHAUS and ALFANTIS, 1991] MÜHLHAUS, H. and ALFANTIS, E. (1991). A variational principle for gradient plasticity. *International Journal of Solids and Structures*, 28(7):845–857.
- [MURAKAMI, 1988] MURAKAMI, S. (1988). Mechanical modeling of material damage. *Journal of Applied Mechanics*, 55(2):280–286.
- [MURAKAMI and OHNO, 1981] MURAKAMI, S. and OHNO, N. (1981). A continuum theory of creep and creep damage. In PONTER, A. and HAYHURST, D., editors, *Creep in Structures*, pages 422–444. Springer Berlin Heidelberg.
- [NĚMEČEK et al., 2002] NĚMEČEK, J., PATZÁK, B., RYPL, D., and BITTNAR, Z. (2002). Microplane models: computational aspects and proposed parallel algorithm. *Computers & structures*, 80(27-30):2099–2108.
- [NGO and SCORDELIS, 1967] NGO, D. and SCORDELIS, A. (1967). Finite element analysis of reinforced concrete beams. *Journal of the American Concrete Institute*, 64:152–163.
- [NGUYEN, 2011] NGUYEN, G. D. (2011). A damage model with evolving nonlocal interactions. *International Journal of Solids and Structures*, 48(10):1544–1559.
- [NOUAILLETAS et al., 2015] NOUAILLETAS, O., LA BORDERIE, C., PERLOT, C., RIVARD, P., and BALLIVY, G. (2015). Experimental study of crack closure on heterogeneous quasi-brittle material. *Journal of Engineering Mechanics*, 141(11):04015041.

- [OHLSSON and OLOFSSON, 1997] OHLSSON, U. and OLOFSSON, T. (1997). Mixed-mode fracture and anchor bolts in concrete analysis with inner softening bands. *Journal of Engineering Mechanics*, 123(10):1027–1023.
- [OLIVER, 1989] OLIVER, J. (1989). A consistent characteristic length for smeared cracking models. *International Journal for Numerical Methods in Engineering*, 28(2):461–474.
- [OLIVER, 1996a] OLIVER, J. (1996a). Modeling strong discontinuities in solid mechanics via strain softening constitutive equations. part 1: Fundamentals. *International Journal for Numerical Methods in Engineering*, 39(21):3575–3600.
- [OLIVER, 1996b] OLIVER, J. (1996b). Modeling strong discontinuities in solid mechanics via strain softening constitutive equations. part 2: Numerical simulation. *International Journal for Numerical Methods in Engineering*, 39(21):3601–3623.
- [OLIVER, 2000] OLIVER, J. (2000). On the discrete constitutive models induced by strong discontinuity kinematics and continuum constitutive equations. *International Journal of Solids and Structures*, 37:7207–7229.
- [OLIVER et al., 1999] OLIVER, J., CERVERA, M., and MANZOLI, O. (1999). Strong discontinuities and continuum plasticity models: The strong discontinuity approach. *International Journal of Plasticity*, 15:319–351.
- [OLIVER et al., 2002] OLIVER, J., HUESPE, A., SAMANIEGO, E., and CHAVES, E. (2002). On strategies for tracking strong discontinuities in computational failure mechanics. In *Fifth World Congress on Computational Mechanics*, pages 7–12.
- [OLIVER et al., 2006] OLIVER, J., HUESPE, A., and SANCHEZ, P. (2006). A comparative study on finite elements for capturing strong discontinuities: E-fem vs x-fem. *Computer Methods in Applied Mechanics and Engineering*, 195(37):4732–4752.
- [OLIVER-LEBLOND et al., 2013] OLIVER-LEBLOND, C., ARNAUD, D., RAGUENEAU, F., and RICHARD, B. (2013). Non-intrusive global/local analysis for the study of fine cracking. *International Journal for Numerical and Analytical Methods in Geomechanics*, 37(8):973–992.
- [ORTIZ, 1985] ORTIZ, M. (1985). A constitutive theory for the inelastic behavior of concrete. *Mechanics of Materials*, 4(1):67–93.
- [ORTIZ et al., 1987] ORTIZ, M., YVES, L., and NEEDLEMAN, A. (1987). A finite element method for localized failure analysis. *Computer Methods in Applied Mechanics and Engineering*, 61(03):189–214.
- [OTTOSEN and SCORDELIS, 1977] OTTOSEN, N. and SCORDELIS, A. (1977). A failure criterion for concrete. *Journal of Engineering Mechanics*, 103(4):527–535.
- [OŽBOLT and BAŽANT, 1992] OŽBOLT, J. and BAŽANT, Z. (1992). Microplane model for cyclic triaxial behavior of concrete. *Journal of engineering mechanics*, 118(7):1365–1386.
- [PARK and KIM, 2003] PARK, H. and KIM, H. (2003). Microplane model for reinforced-concrete planar members in tension-compression. *Journal of Structural Engineering*, 129(3):337–345.
- [PEERLINGS et al., 1996] PEERLINGS, R., de BORST, R., BREKELMANS, W., and de VREE, J. (1996). Gradient enhanced damage for quasi-brittle materials. *International Journal for numerical methods in engineering*, 39(19):3391–3403.
- [PIETRUSZCZAK and MROZ, 1981] PIETRUSZCZAK, S. and MROZ, Z. (1981). Finite element analysis of deformation of strain-softening materials. *International Journal for Numerical Methods in Engineering*, 17(3):327–334.

- [PIJAUDIER-CABOT and BAŽANT, 1987] PIJAUDIER-CABOT, G. and BAŽANT, Z. (1987). Nonlocal damage theory. *Journal of engineering mechanics*, 113(10):1512–1533.
- [PIJAUDIER-CABOT and DUFOUR, 2010] PIJAUDIER-CABOT, G. and DUFOUR, F. (2010). Non local damage model: boundary and evolving boundary effects. *European Journal of Environmental and Civil Engineering*, 14(6-7):729–749.
- [PIJAUDIER-CABOT et al., 2004] PIJAUDIER-CABOT, G., HAIDAR, K., and DUBÉ, J. (2004). Non-local damage model with evolving internal length. *International journal for numerical and analytical methods in geomechanics*, 28(7-8):633–652.
- [RAGUENEAU et al., 2008] RAGUENEAU, F., DESMORAT, R., and GATUINGT, F. (2008). Anisotropic damage modelling of biaxial behaviour and rupture of concrete structures. *Computers and Concrete*, 5(4):417–434.
- [RAMTANI, 1990] RAMTANI, S. (1990). *Contribution à la modélisation multiaxiale du béton incluant les effets unilatéraux*. PhD thesis, Thèse de doctorat, Université Paris 6.
- [RASHID, 1968] RASHID, Y. (1968). Analysis of reinforced concrete pressure vessels. *Nuclear Engineering and Design*, 7:334–344.
- [RASTIELLO et al., 2014] RASTIELLO, G., BOULAY, G., DAL PONT, S., TAILHAN, J., and ROSSI, P. (2014). Real-time water permeability evolution of a localized crack in concrete under loading. *Cement and Concrete Research*, 56:20 – 28.
- [RASTIELLO et al., 2018] RASTIELLO, G., GIRY, C., GATUINGT, F., and DESMORAT, R. (2018). From diffuse damage to strain localization from an eikonal non-local (enl) continuum damage model with evolving internal length. *Computer Methods in Applied Mechanics and Engineering*, 331:650 – 674.
- [RASTIELLO et al., 2016] RASTIELLO, G., MOES, N., and COMI, C. (2016). Bi-dissipative thick level set (tls) damage model for quasi-brittle materials. In *9th International Conference on Fracture Mechanics of Concrete and Concrete Structures FraMCoS-9*, pages 1–9.
- [RASTIELLO et al., 2019] RASTIELLO, G., RICCARDI, F., and RICHARD, B. (2019). Discontinuity-scale path-following methods for the embedded discontinuity finite element modeling of failure in solids. *Computer Methods in Applied Mechanics and Engineering*, 349:431–457.
- [REINHARDT and CORNELISSEN, 1984] REINHARDT, H. and CORNELISSEN, H. (1984). Post-peak cyclic behaviour of concrete in uniaxial tensile and alternating tensile and compressive loading. *Cement and concrete research*, 14(2):263–270.
- [REYNOUARD, 1974] REYNOUARD, J. (1974). *Structures planes en béton armé élaboration d'un modèle de comportement jusqu'à la ruine et résolution numérique*. PhD thesis, Thèse de doctorat, Université Claude Bernard.
- [RICCARDI et al., 2017] RICCARDI, F., KISHTA, E., and RICHARD, B. (2017). A step-by-step global crack-tracking approach in e-fem simulations of quasi-brittle materials. *Engineering Fracture Mechanics*, 170:44–58.
- [RICE, 1976] RICE, J. (1976). Localization of plastic deformation. Technical report, Brown Univ. and Providence, RI (USA). Div. of Engineering.
- [RICHARD and RAGUENEAU, 2013] RICHARD, B. and RAGUENEAU, F. (2013). Continuum damage mechanics based model for quasi brittle materials subjected to cyclic loadings: Formulation, numerical implementation and applications. *Engineering Fracture Mechanics*, 98(01):383–406.

- [RICHARD et al., 2010] RICHARD, B., RAGUENEAU, F., CHRISTIAN, C., and LUCAS, A. (2010). Isotropic continuum damage mechanics for concrete under cyclic loading: Stiffness recovery, inelastic strains and frictional sliding. *Engineering Fracture Mechanics*, 77(8):1203–1223.
- [RICHARD et al., 2019] RICHARD, B., RASTIELLO, G., GIRY, C., RICCARDI, F., PAREDES, R., ZAFATI, E., KAKARLA, S., and LEJOUAD, C. (2019). Castlab: an object-oriented finite element toolbox within the matlab environment for educational and research purposes in computational solid mechanics. *Advances in Engineering Software*, 128:136–151.
- [RIVILLON and GABS, 2011] RIVILLON, P. and GABS, A. (2011). Projet national de recherche ceos.fr, axe 2–expérimentations.
- [RIZZI et al., 1995] RIZZI, E., CAROL, I., and WILLAM, K. (1995). Localization analysis of elastic degradation with application to scalar damage. *Journal of Engineering Mechanics*, 121(4):541–554.
- [ROTH et al., 2015] ROTH, S., LÉGER, P., and SOULAÏMANI, A. (2015). A combined xfem–damage mechanics approach for concrete crack propagation. *Computer Methods in Applied Mechanics and Engineering*, 283:923–955.
- [ROTS, 1988] ROTS, J. (1988). *Computational modeling of concrete fracture*. Phd thesis, Delft University of Technology.
- [ROTS and de BORST, 1987] ROTS, J. and de BORST, R. (1987). Analysis of mixed-mode fracture in concrete. *Journal of Engineering Mechanics*, 113(11):1739–1758.
- [ROTS et al., 1985] ROTS, J., NAUTA, P., KUSTER, G., and BLAAUWENDRAAD, J. (1985). Smearred crack approach and fracture localization in concrete. *HERON*, 30 (1), 1985.
- [ROTS, 1991] ROTS, J. G. (1991). Smearred and discrete representations of localized fracture. *Current Trends in Concrete Fracture Research*, Springer, 46:45–59.
- [SAKSALA et al., 2015] SAKSALA, T., BRANCHERIE, D., HARARI, I., and IBRAHIMBEGOVIC, A. (2015). Combined continuum damage-embedded discontinuity model for explicit dynamic fracture analyses of quasi-brittle materials. *International Journal for Numerical Methods in Engineering*, 101(3):230–250.
- [SAROUKHANI et al., 2013] SAROUKHANI, S., VAFADARI, R., and SIMONE, A. (2013). A simplified implementation of a gradient-enhanced damage model with transient length scale effects. *Computational Mechanics*, 51(6):899–909.
- [SHI et al., 2000] SHI, C., van DAM, A., van MIER, J., and SLUYS, B. (2000). Crack interaction in concrete. *Materials for buildings and structures*, 6:125–131.
- [SIMO and JU, 1987] SIMO, J. and JU, J. (1987). Strain-and stress-based continuum damage models—i. formulation. *International Journal of Solids and Structures*, 23(7)(7):821–840.
- [SIMO et al., 1993] SIMO, J., OLIVER, J., and ARMERO, F. (1993). An analysis of strong discontinuities induced by strain softening in rate-independent inelastic solids. *Computational Mechanics*, 12(09):277–296.
- [SIMO and RIFAI, 1990] SIMO, J. and RIFAI, M. (1990). A class of mixed assumed strain methods and the method of incompatible modes. *International Journal for Numerical Methods in Engineering*, 29:1595–1638.
- [SIMONE et al., 2003] SIMONE, A., WELLS, G., and SLUYS, L. (2003). From continuous to discontinuous failure in a gradient-enhanced continuum damage model. *Computer Methods in Applied Mechanics and Engineering*, 192(41-42):4581–4607.

- [SINHA et al., 1964] SINHA, B., GERSTLE, K., and TULIN, L. (1964). Stress-strain relations for concrete under cyclic loading. *ACI Structural Journal*, 61(2):195–211.
- [STEVENS and LIU, 1992] STEVENS, D. and LIU, D. (1992). Strain-based constitutive model with mixed evolution rules for concrete. *Journal of engineering mechanics*, 118(6):1184–1200.
- [STROUD, 1971] STROUD, A. (1971). Approximate calculation of multiple integrals. *Prentice Hall, Englewood Cliffs, New Jersey*, 29:296–302.
- [SUIDAN and SCHNOBRICH, 1973] SUIDAN, M. and SCHNOBRICH, W. (1973). Finite element analysis of reinforced concrete. *Journal of the Structural Division*, 99(st1).
- [SUKUMAR et al., 2001] SUKUMAR, N., CHOPP, D. L., MOES, N., and BELYTSCHKO, T. (2001). Modeling holes and inclusions by level sets in the extended finite-element method. *Computer methods in applied mechanics and engineering*, 190(46):6183–6200.
- [TAYLOR, 1938] TAYLOR, G. I. (1938). Plastic strain in metals. *Journal of the Institute of Metals*, 62:307–324.
- [TERRIEN, 1980] TERRIEN, M. (1980). Emission acoustique et comportement mécanique post critique d'un béton sollicité en traction. *BLPC*, 72:105:65.
- [VASSAUX et al., 2014] VASSAUX, M., RAGUENEAU, F., RICHARD, B., and MILLARD, A. (2014). Compressive behavior of a lattice discrete element model for quasi-brittle materials. *Computational Modelling of Concrete Structures*, 1:335–344.
- [VASSAUX et al., 2015] VASSAUX, M., RICHARD, B., RAGUENEAU, F., and MILLARD, A. (2015). Regularised crack behaviour effects on continuum modelling of quasi-brittle materials under cyclic loading. *Engineering Fracture Mechanics*, 149:18–36.
- [VERPEAUX and CHARRAS, 2011] VERPEAUX, P. and CHARRAS, T. (2011). Multiplicateur de lagrange, condensation statique et conditions unilatérales. In *10e colloque national en calcul des structures*.
- [WANG and WAISMAN, 2016] WANG, Y. and WAISMAN, H. (2016). From diffuse damage to sharp cohesive cracks: A coupled xfem framework for failure analysis of quasi-brittle materials. *Computer Methods in Applied Mechanics and Engineering*, 299:57–89.
- [WASHIZU, 1955] WASHIZU, K. (1955). On the variational principles of elasticity and plasticity. *Technical Report 25-18, Aeroelastic and Structures Research Laboratory, MIT Press, Cambridge*, 46:131–150.
- [WELLS and SLUYS, 2000] WELLS, G. and SLUYS, L. (2000). Application of embedded discontinuities for softening solids. *Engineering Fracture Mechanics*, 65:263–281.
- [WELLS and SLUYS, 2001] WELLS, G. and SLUYS, L. (2001). Three-dimensional embedded discontinuity model for brittle fracture. *International Journal of Solids and Structures*, 38(5):897–913.
- [WESTERGAARD, 1939] WESTERGAARD, H. (1939). Bearing pressures and cracks. *Journal of Applied Mechanics*, 61(A):49–53.
- [WILLAM et al., 1989] WILLAM, K., PRAMONO, E., and STURE, S. (1989). Fundamental issues of smeared crack models. In *Fracture of concrete and rock*, pages 142–157. Springer.
- [WILLAM and WARNKE, 1975] WILLAM, K. and WARNKE, E. (1975). Constitutive model for the triaxial behaviour of concrete. *IABSE Seminar on Concrete Structures Subjected to Triaxial Stress, Bergamo, Italy*, page 1–31.

- [WU and CERVERA, 2016] WU, J.-Y. and CERVERA, M. (2016). A thermodynamically consistent plastic-damage framework for localized failure in quasi-brittle solids: Material model and strain localization analysis. *International Journal of Solids and Structures*, 88:227–247.
- [WU et al., 2014] WU, L., BECKER, G., and NOELS, L. (2014). Elastic damage to crack transition in a coupled non-local implicit discontinuous galerkin/extrinsic cohesive law framework. *Computer Methods in Applied Mechanics and Engineering*, 279:379–409.
- [XENOS and GRASSL, 2014] XENOS, D. and GRASSL, P. (2014). Comparison of nonlocal and crack-band damage-plasticity approaches for modelling the failure of reinforced concrete structures. In Bićanić, N., H., M., G., M., and de BORST, R., editors, *Computational modelling of concrete structures*.
- [YAZADANI and SCHREYER, 1990] YAZADANI, S. and SCHREYER, H. (1990). Combined plasticity and damage mechanics model for plain concrete. *Journal of engineering mechanics*, 116(7):1435–1450.
- [ZREID and KALISKE, 2018] ZREID, I. and KALISKE, M. (2018). A gradient enhanced plasticity–damage microplane model for concrete. *Computational Mechanics*, 62(5):1239–1257.

Titre : Modélisation de la multi-fissuration des matériaux quasi-fragiles par couplage d'un modèle d'endommagement anisotrope microplan et d'une formulation des discontinuités fortes dans la méthode des éléments finis enrichis

Mots clés : fissuration multiple, microplan, éléments finis à discontinuité intégrée, transition endommagement-fissuration

Résumé : Dans un contexte d'évaluation des structures en béton armé, il est d'usage d'estimer la durabilité à l'échelle du matériau, l'aptitude au service et enfin, la tenue structurale qui définit la performance de l'ouvrage considéré. Toutefois, évaluer la performance d'un élément de structure nécessite le recours à des approches numériques permettant la description voire la prédiction des principaux mécanismes dissipatifs. Par ailleurs, il est attendu de cette description que des quantités locales caractérisantes la fissuration soient accessibles numériquement, on peut citer la tortuosité, l'espacement ou encore les ouvertures associées à la fissuration. Le principal objectif de ces travaux de thèse consiste à proposer une approche permettant la description de la fissuration sous chargement cyclique. Pour cela, l'approche proposée

permet de décrire le processus complet de localisation des déformations depuis l'apparition de l'endommagement jusqu'à l'initiation et la propagation de fissures multiples dans des matériaux quasi fragiles. Pour cela, la stratégie adoptée repose d'une part sur l'utilisation du modèle microplan permettant ainsi de décrire le caractère anisotrope de la fissuration et d'autre part, sur la particularisation de la méthode aux éléments finis à discontinuités intégrées. Ces deux piliers sont couplés à l'aide d'une technique de transition entre endommagement diffus et fissuration localisée. L'approche proposée est illustrée à l'aide de plusieurs exemples élémentaires. Enfin, quelques cas tests à l'échelle de l'élément de structure sont étudiés.

Title : From anisotropic damage to multiple cracks by coupling a microplane model and a strong discontinuity formulation in the Embedded Finite Element Method

Keywords : multiple cracks, microplane model, EFEM, damage-to-fracture transition

Abstract : The performance aspects of large scale civil engineering structures like containment facilities such as durability, serviceability and structural safety are assessed from time to time to avert any catastrophes. Also, in the cases of extreme loading, different cracking mechanisms contribute to each other ultimately leading to the failure. This creates the need for devising certain regulatory measures. In order to achieve this, it is essential to predict the information like crack opening displacements, crack spacing and tortuosity. The purpose of this thesis is to develop numerical tools to model multiple intersecting cracks. In particular, the complete strain localization process from the onset of damage to the

initiation and propagation of multiple cracks. Two main ingredients are used. The microplane model allows to describe the anisotropic damage phase and Embedded Finite Element Method (EFEM) introduces cracks as multiple strong discontinuities in the damaged continuum. First, the standard EFEM is extended in the context of multiple cracks. Later, the microplane microdamage model is formulated in a thermodynamic framework using simple constitutive laws. Finally, these two approaches are coupled using a transition methodology. The proposed methodologies are illustrated using several elementary and structural test cases that involve complex stress-strain states.